

Mechanisms of boundary layer transition induced by isolated roughnes

Ye, Qingqing

DOI

[10.4233/uuid:b1b5332a-33d5-4fd4-b386-3acc48e12003](https://doi.org/10.4233/uuid:b1b5332a-33d5-4fd4-b386-3acc48e12003)

Publication date

2017

Document Version

Final published version

Citation (APA)

Ye, Q. (2017). *Mechanisms of boundary layer transition induced by isolated roughnes*. [Dissertation (TU Delft), Delft University of Technology]. <https://doi.org/10.4233/uuid:b1b5332a-33d5-4fd4-b386-3acc48e12003>

Important note

To cite this publication, please use the final published version (if applicable).
Please check the document version above.

Copyright

Other than for strictly personal use, it is not permitted to download, forward or distribute the text or part of it, without the consent of the author(s) and/or copyright holder(s), unless the work is under an open content license such as Creative Commons.

Takedown policy

Please contact us and provide details if you believe this document breaches copyrights.
We will remove access to the work immediately and investigate your claim.

**MECHANISMS OF BOUNDARY LAYER
TRANSITION INDUCED BY ISOLATED
ROUGHNESS**

MECHANISMS OF BOUNDARY LAYER TRANSITION INDUCED BY ISOLATED ROUGHNESS

Proefschrift

ter verkrijging van de graad van doctor
aan de Technische Universiteit Delft,
op gezag van de Rector Magnificus prof.ir.K.C.A.M. Luyben;
voorzitter van het College voor Promoties,
in het openbaar te verdedigen op
donderdag 15 juni 2017 om 15:00uur

door

Qingqing YE

Bsc in Aerospace Engineering
Beijing Institute of Technology, Beijing, China,
geboren te Tangshan, China

Dit proefschrift is geodgekeurd door de

Promotor: Prof. dr. F. Scarano

Copromotor: Dr. ir. F. F. J. Schrijer

Samenstelling promotiecommissie

| | |
|----------------------------|---|
| Rector Magnificus, | voorzitter |
| Prof. dr. F. Scarano, | Technische Universiteit Delft, promotor |
| Dr. ir. F. F. J. Schrijer, | Technische Universiteit Delft, copromotor |

Onafhankelijke leden:

| | |
|-------------------------|-----------------------------------|
| Prof. J. H. M. Fransson | KTH Royal Institute of Technology |
| Prof. dr. S. Hickel | Technische Universiteit Delft |
| Dr. E. B. White | Texas A&M University |
| Dr. ir. G. E. Elsinga | Technische Universiteit Delft |
| Dr. Z. Sun | City, University of London |

Reservelid

| | |
|-----------------------|-------------------------------|
| Prof. dr. D. Casalino | Technische Universiteit Delft |
|-----------------------|-------------------------------|

Keywords: isolated roughness, boundary layer, transition, stability, vortical structures.

Cover designed by: Qingqing Ye

Copyright ©2017 by Qingqing Ye.

ISBN: 978-94-6186-822-0

An electronic version of this dissertation is available at

<http://repository.tudelft.nl>

Summary

Boundary layer transition is a relevant phenomenon in many aerodynamic and aero-thermodynamic problems and has been extensively investigated from the past century till recent times. Among the factors affecting the transition process, surface roughness plays a key role. When a roughness element with sufficiently large height (h) compared to the boundary layer thickness (δ) is immersed in a laminar boundary layer, it will produce spanwise varying disturbances with the potential to accelerate the transition process. In the thesis, a fundamental study is carried out to understand the physical mechanism of isolated roughness element induced transition. Experiments are performed in incompressible flow regime covering both critical and supercritical conditions. Tomographic particle image velocimetry (PIV) is employed as the main experimental diagnostic technique, returning the three-dimensional velocity and vorticity field of the flow.

The three-dimensional wake flow behaviour is firstly identified behind roughness element of micro-ramp geometry. The micro-ramp produces a pair of counter-rotating streamwise vortices in the wake, transporting low momentum fluid away from the wall by the central upwash motion, and sweeping the high momentum flow towards the near-wall region sideward. The shear layer around the central low-speed region is related to the growth of Kelvin-Helmholtz (K-H) instability. The active range of the primary vortices and the central low-speed region in the streamwise direction is associated to the selection of the dominant instability mechanism, which decreases with the increase of roughness-height based Reynolds number (Re_h).

The instantaneous flow field reveals that the earliest unstable structures featuring hairpin shape are caused by the K-H instability at the separated shear layer. The evolution of K-H vortices is strongly influenced by Re_h . At $Re_h = 1170$, the K-H vortices are lift up under the upwash motion effect of the quasi-streamwise vortices, following by paring, distortion and finally breakdown. The active region of K-H vortices is separated from the inception of turbulent wedge, where early stage transition occurs. When Re_h decreases approaching the critical value, the K-H vortices progressed gradually until the overall shear layer is destabilized, indicating the correlation between K-H instability and transition. The POD analysis yields the symmetric (K-H) and asymmetric mode. The disturbance energy associated to the symmetric modes changes with Re_h . At higher Re_h , the disturbance energy of the symmetric modes quickly decays, having a comparable contribution as the asymmetric modes. When $Re_h < 1000$, the symmetric modes produce a remarkably higher level of disturbance energy until the onset of transition, indicating its dominance.

The effectiveness of roughness element on promoting transition is strongly influenced by its geometry. The bluff-front roughness elements induce horseshoe vortices due to upstream separation. The different rotation direction of these

Summary

vortices compared to the micro-ramp leads to early inception of sideward growth of fluctuations, and more rapid transition process. While for the slender micro-ramp, significant longer distance is required to for the onset of transition.

Samenvatting

Grenslaagtransitie is een belangrijk aspect in veel aerodynamische en aerothermodynamische toepassingen waardoor er in het verleden en in het heden uitgebreid onderzoek gedaan wordt naar dit onderwerp. Verschillende factoren beïnvloeden het transitieproces, een hiervan is de oppervlakte ruwheid welke een belangrijke rol in neemt. Als een ruwheidselement met voldoende hoogte (h) ten opzichte van de grenslaagdikte (δ) in een laminaire grenslaag geplaatst wordt, zullen er in spanwijdte variërende verstoringen optreden welke het potentieel hebben het transitieproces te versnellen. Dit proefschrift beschrijft een fundamenteel onderzoek wat als doel heeft meer inzicht en begrip te verschaffen in het fysische mechanisme waarmee een enkel ruwheidselement grenslaagtransitie kan veroorzaken. Daartoe zijn experimenten uitgevoerd in een onsamendrukbare stroming voor kritische en superkritische condities. Tomographic particle image velocimetry (PIV) is gebruikt als belangrijkste meettechniek, waarmee het driedimensionale snelheidsveld en vortciteitsveld van de stroming kan worden gemeten.

Allereerst is het gedrag van de driedimensionale stroming in het zog van een ruwheidselement in de vorm van een micro-ramp in kaart gebracht. De micro-ramp veroorzaakt een paar tegen elkaar indraaiende en in stromingsrichting georiënteerde (primaire) wervels. In het midden wordt lucht met lage impuls weg van de wand verplaatst door de centrale opwaartse afbuiging van de stroming en aan de zijkant wordt lucht met hoge impuls naar de wand toe getransporteerd. Rond het zog van de micro-ramp bevindt zich een afschuiflaag waarin Kelvin-Helmholtz (K-H) instabiliteiten groeien. De grootte van het gebied waarin de primaire wervels en het zog actief zijn, bepaalt in belangrijke mate de selectie van het dominante instabiliteitsmechanisme. Dit gebied wordt kleiner naar mate het Reynoldsgetal gebaseerd op de hoogte van het ruwheidselement (Re_h) toeneemt.

In het instantane stromingsveld is te zien dat de eerste onstabiele haarspeldachtige structuren worden veroorzaakt door K-H instabiliteit in de losgelaten afschuiflaag. De ontwikkeling van de K-H wervels wordt sterk beïnvloed door de grootte van Re_h . Voor $Re_h = 1170$ worden de K-H wervels eerst opgetild door de opwaartse stroming, gevolgd door "pairing", vervorming en uiteindelijk breken ze op. Het gebied waarin de K-H wervels actief zijn komt niet overeen met de locatie waar de turbulente wig ontstaat (begin van transitie). Als Re_h verlaagd wordt en de kritieke waarde nadert, dan verloopt de K-H instabiliteit meer geleidelijk totdat de volledige afschuiflaag gedestabiliseerd is. Dit duidt op een correlatie tussen K-H instabiliteit en transitie. Door middel van een POD analyse kunnen de symmetrische (K-H) en asymmetrische modes worden geïdentificeerd. De energie van de symmetrische verstoringen varieert met Re_h . Voor hoge waarden van Re_h neemt de energie van de symmetrische modes stroomafwaarts sterk af, uiteindelijk wordt de bijdrage even hoog als die van de asymmetrische modes. Voor $Re_h < 1000$ is het energie niveau van de symmetrische modes opmerkelijk hoog tot aan de transitie locatie, wat duidt op het belang voor het transitieproces.

De effectiviteit van ruwheidselementen in het bevorderen van transitie wordt sterk beïnvloed door de geometrie. Stompe ruwheidselementen veroorzaken hoefijzerwervels doordat de stroming loslaat stroomopwaarts van het element. De draairichting van deze wervels zorgt ervoor dat de fluctuaties snel groeien in zijwaartse richting en dat het transitieproces wordt bespoedigd. Daarentegen is er voor de slanke micro-ramp (zonder loslating stroomopwaarts) een beduidend langere afstand nodig voordat transitie begint.

Content

| | |
|---|-----|
| Summary..... | III |
| Samenvatting..... | V |
| Content | VII |
| 1 Introduction..... | 1 |
| 1.1 Historical background..... | 2 |
| 1.2 Relevance of boundary layer transition in aerospace..... | 3 |
| 1.2.1 Civil transport aircraft..... | 4 |
| 1.2.2 Turbomachinery | 5 |
| 1.2.3 Hypersonic flight | 6 |
| 1.3 Effect of roughness element on transition..... | 8 |
| 1.4 Prediction of roughness induced transition..... | 11 |
| 1.5 Scope of the thesis and outline..... | 13 |
| 2 Fundamentals of roughness induced transition..... | 15 |
| 2.1 Fundamentals of boundary layer theory | 16 |
| 2.1.1 Boundary layer properties..... | 16 |
| 2.1.2 Paths to turbulence | 18 |
| 2.2 Mechanisms of roughness induced transition..... | 19 |
| 2.3 Isolated roughness induced transition | 23 |
| 2.3.1 Roughness-height based Reynolds number | 23 |
| 2.3.2 Roughness geometry..... | 24 |
| 2.4 Wake flow of the roughness element..... | 29 |
| 2.4.1 Streamwise vortices | 29 |
| 2.4.2 Hairpin vortices and Kelvin-Helmholtz instability | 32 |
| 2.4.3 Turbulent wedge..... | 35 |
| 2.5 Research questions and objectives | 37 |
| 3 Experimental techniques and arrangements..... | 39 |
| 3.1 Flow facility | 40 |
| 3.2 Wind tunnel model and flow conditions..... | 40 |
| 3.3 Laminar boundary layer characterization..... | 42 |

Content

| | |
|---|----|
| 3.4 Roughness geometry..... | 42 |
| 3.5 Particle image velocimetry..... | 44 |
| 3.5.1 Tracer particle..... | 45 |
| 3.5.2 Particle imaging..... | 46 |
| 3.5.3 Image analysis..... | 48 |
| 3.6 Tomographic PIV..... | 49 |
| 3.6.1 Working principle..... | 49 |
| 3.6.2 System calibration..... | 50 |
| 3.6.3 Volume reconstruction..... | 52 |
| 3.7 Experiment arrangement..... | 54 |
| 3.7.1 Tomographic PIV setup..... | 54 |
| 3.7.2 Data analysis..... | 55 |
| 3.8 Uncertainty analysis..... | 57 |
| 3.9 Data reduction..... | 58 |
| 3.9.1 Proper Orthogonal Decomposition..... | 58 |
| 3.9.2 Vortex detection..... | 60 |
| 4 Transition scenario at supercritical Re_h | 63 |
| 4.1 Introductory remarks..... | 64 |
| 4.2 Mean flow organization..... | 66 |
| 4.3 Momentum deficit and log-layer..... | 68 |
| 4.4 Instantaneous flow organization..... | 71 |
| 4.4.1 Evolution of K-H vortices..... | 72 |
| 4.4.2 Formation of turbulent wedge..... | 75 |
| 4.4.3 Transition mechanisms..... | 77 |
| 4.5 Turbulent properties..... | 78 |
| 4.5.1 Velocity fluctuations..... | 78 |
| 4.5.2 Turbulence production..... | 82 |
| 4.6 Conclusion..... | 85 |
| 5 Reynolds number dependence of roughness-induced transition..... | 87 |
| 5.1 Introductory remarks..... | 88 |
| 5.2 Time-averaged flow topology..... | 89 |
| 5.3 Instantaneous flow organisation..... | 92 |

| | |
|---|-----|
| 5.4 Disturbance energy and growth..... | 96 |
| 5.5 POD analysis..... | 98 |
| 5.5.1 Pattern of POD modes..... | 99 |
| 5.5.2 Symmetry of disturbance energy..... | 103 |
| 5.5.3 Spatial development of secondary vortex structure: low order model..... | 106 |
| 5.6 Reynolds number effect on transition mechanism..... | 109 |
| 6 Roughness geometry effect on transition..... | 111 |
| 6.1 Introductory remarks..... | 112 |
| 6.2 Near wake flow topology..... | 112 |
| 6.3 Roughness induced velocity fluctuations..... | 118 |
| 6.4 Instantaneous vortical structures..... | 121 |
| 6.4.1 Wake flow of the cylinder and the diamond..... | 122 |
| 6.4.2 Wake flow of the hemisphere..... | 125 |
| 6.4.3 Features of turbulent wedge..... | 128 |
| 6.5 Geometry effect on the route to transition..... | 128 |
| 7 Conclusions and outlooks..... | 131 |
| 7.1 Transition mechanisms..... | 132 |
| 7.1.1 Dominant flow feature..... | 132 |
| 7.1.2 Reynolds number effect..... | 133 |
| 7.1.3 Geometry effect..... | 133 |
| 7.2 Outlooks in incompressible flow regime..... | 134 |
| 7.2.1 Mechanism-based transition criterion..... | 134 |
| 7.2.2 Effect of freestream turbulence..... | 135 |
| 7.2.3 Numerical simulation of roughness induced transition..... | 135 |
| 7.3 Outlook towards the high speed regimes..... | 135 |
| 7.3.1 Flow Conditions..... | 136 |
| 7.3.2 Experimental arrangement..... | 137 |
| 7.3.3 Micro-ramp flow topology at Mach 6..... | 140 |
| References..... | 143 |
| Acknowledgements..... | 155 |
| Publications..... | 157 |
| Curriculum Vitae..... | 159 |

1

Introduction

1.1 Historical background

The phenomenon of laminar to turbulent transition was firstly noticed in 1883, when Osborne Reynolds (1883) visualized the flow changes from a well-ordered condition to a chaotic mixing state at sufficiently large incoming flow velocity in a circular pipe. The former coloured filament flow visualization was later repeated at the University of Manchester, as exhibited in Fig. 1.1. A non-dimensional parameter, Reynolds number, was introduced, being the ratio of inertial forces to viscous forces within fluid flow. A self-similar principle with respect to Reynolds number ($Re = u_m d / \nu$) was proposed, where u_m = volume flux (Q)/pipe cross-sectional area (A), d is the pipe diameter, and ν is the kinematic viscosity. Reynolds found that the laminar flow will become turbulent when the Reynolds number increases above the critical value of 2300. Below that, the flow remains laminar.



Fig. 1.1. Repetition of Reynolds experiment by Johannesen and Lowe at the University of Manchester, pipe flow from left to right, the photo redrawn from Van Dyke (1982).

Later, it was discovered that the transition process from laminar to turbulent can also occur in boundary layer over solid body. The simplest boundary layer transition process is represented by the flow over a flat plate of zero angle of attack when the external disturbance is infinitesimal, referred to as *natural transition*. The unsteadiness of the flow starts from the amplification of two-dimensional Tollmien-Schlichting (TS) waves, superimposing on the laminar boundary layer. The visualization of the TS wave is provided in Fig. 1.2 using coloured fluid in water. After exponentially growth to a certain amplitude downstream (usually 1-2% of the freestream velocity), the TS waves show spanwise variation, becoming three-

dimensional disturbances. At this stage, 'Λ' shape vortex structure forms, exhibiting different types. Klebanoff et al. (1962) found the 'Λ' vortices aligned in phase with and of similar wave length as TS wave, referred to as *K-type* vortices after Klebanoff. Others also observed the 'Λ' vortices distributed in a staggered pattern with a longer wavelength with respect to TS wave. The latter is a subharmonic unstable wave, referred to as *C-type* after Craik (1971) or *H-type* after Herbert (1983). The 'Λ' vortices break down downstream and are replaced by the formation of turbulent spot, as shown in Fig. 1.3, initiating the transition from laminar to turbulent. The fully turbulent boundary layer establishes after the coalescence of turbulent spots.

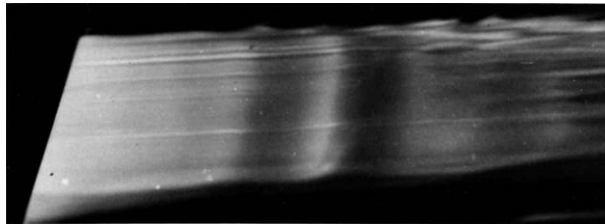


Fig. 1.2. Photograph of two-dimensional Tollmien-Schlichting wave in a flat plate boundary layer, flow from left to right (Werlé 1981).

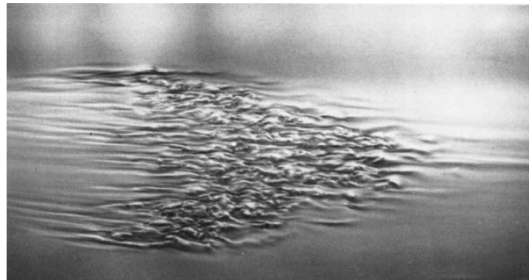


Fig. 1.3. Visualization of Emmons turbulent spot by aluminium flakes in a water channel, flow from left to right (Cantwell et al. 1978).

In practice, it is hard to experience infinitesimal external disturbances and the flow conditions vary from case to case. A variety of factors, such as freestream disturbances, pressure gradient, surface roughness, Mach number etc., can modify the transition process. The paths to turbulence will be detailed in sec. 2.1.2

1.2 Relevance of boundary layer transition in aerospace

The interest on understanding, predicting and controlling boundary layer transition maintains from the past century till recent (Kachanov 1994). The major motivation is the significant impact of laminar to turbulent transition on the aerodynamic and aero-thermodynamic problems, such as surface heat transfer, drag, and flight vehicle maneuverability.

1.2.1 Civil transport aircraft

In subsonic and supersonic flow, the development of civil transport aircraft faces the challenges of being energy saving and environmentally friendly. Reducing the total drag is one of the main targets to achieve fuel economy and to decrease harmful emission (pollution) and noise from engines. Drag reduction can also increase the aircraft speed and cruise range, improving aerodynamic performance.

For a subsonic transport aircraft, it has been shown that the skin friction drag occupies about 50% of the total drag (Thibert et al. 1990). In the cruise condition of supersonic aircraft, the skin friction drag also contributes sufficiently to the total drag, taking up to 40% (Vermeersch et al. 2015). While the lift induced drag, wave drag due to volume and other components (parasitic, interference etc.) take up 35%, 20% and 5% respectively. The skin friction and surface heating of the turbulent flow are remarkably higher than that of laminar condition, as the boundary layer profile is much fuller, leading to higher velocity gradient $(\partial u/\partial y)_{y=0}$ at the wall. An example is shown by the infrared thermography measurement over swept wing under inflight condition in Fig. 1.4. It is obvious desirable to enlarge the laminar flow range by delaying transition. It was reported that laminarization of the flow over Airbus A340 result in a drag reduction of 14% (Robert 1992). In fact, transition delay will also be beneficial to reducing takeoff gross weight, operating empty weight, block fuel for a given mission, and to improve cruise lift-to-drag (L/D) ratio (Joslin 1998). As reported by Kirchner (1987), the laminar flow over subsonic transport aircraft by using natural laminar flow concept (NLF), hybrid laminar flow control technique (HLFC) and laminar flow control technique (LFC) can lead to the great potential of fuel saving, as illustrated in Fig. 1.5. The level of fuel saving due to larger laminar flow range increases with the cruise range of the aircraft, indicating its benefit in long-range transport aircrafts.

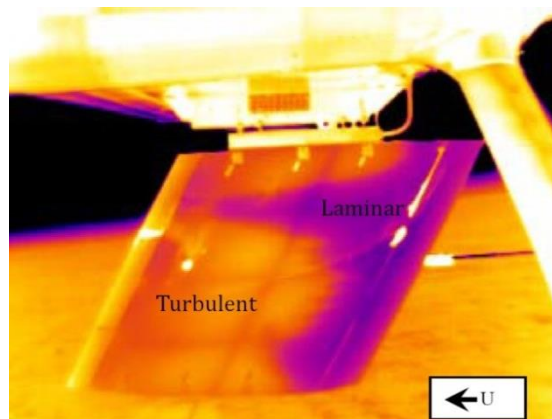


Fig. 1.4. Surface temperature over swept wing in flight testing in subsonic condition in Texas AM, the surface of the wing is cooled during test, darker (low temperature) and lighter (high temperature) colour for laminar and turbulent region respectively (Crawford et al. 2013).

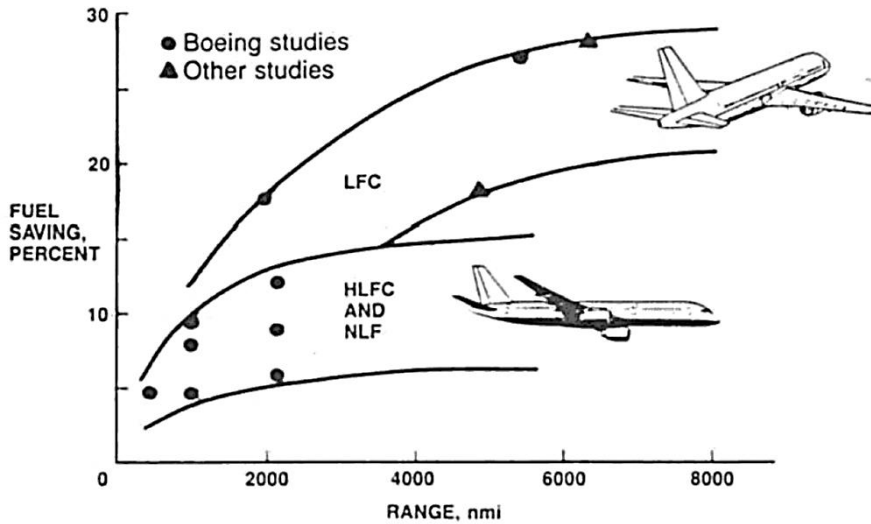


Fig. 1.5. Benefit of increased laminar flow range over subsonic transport aircraft (Kirchner 1987).

1.2.2 Turbomachinery

For the periodic unsteady flow over high-lift low-pressure (LP) turbine blades, boundary layer transition and separation are of great research interest due to its significant impact on the blade efficiency (Hodson and Howell 2005). The LP turbine usually has blades of large aspect ratio, lying in the range of 3:1 to 7:1. The resulted large adverse pressure gradient over the suction surface is vulnerable to boundary layer separation, as shown in Fig. 1.6. For a given blade profile, the suction side of the blade produces 60% of the losses, which mostly attributes to boundary layer separation (Howell et al. 2000). To reduce the downstream flow separation while keeping high lift remains to be a big challenge for the designers. Many boundary layer control methods have been put forward. The idea is to promote transition and to reach turbulent flow condition before the separation bubble using active techniques, such as plasma actuator (Huang et al. 2006) and pulsed injection vortex generator jets (Rizzetta and Visbal 2005), or passive type, like roughness element (Zhang et al. 2005).

In the flow around LP blades, the predominant source of unsteadiness is the upstream blade rows. The convected upstream wake disturbances, both random (wake turbulence) and periodic (wake velocity defect and pressure fields) interact with the boundary layer along the suction surface, which can also cause transition. For the detailed process and loss control using wake unsteadiness, the readers can refer to the review article by Hodson and Howell (2005).

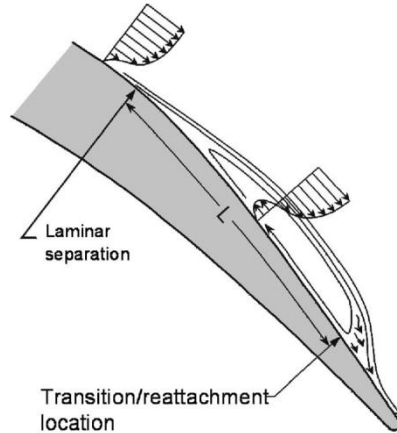


Fig. 1.6. Schematic representation of boundary layer separation on the suction side of LP turbine blade (Praisner and Clark 2004).

1.2.3 Hypersonic flight

Typically, the hypersonic flight is the flight regime where the Mach number ($Ma = u_\infty/a_\infty$) is higher than 5. The capabilities of the hypersonic flight are limited by the technical challenges associated with aero-thermodynamics and propulsion system.

1.2.3.1 Re-entry vehicle

When developing re-entry vehicles, the aero-thermodynamic issue becomes critical in the design loop. The designers have to balance the aerodynamic performance against the requirement on the aerodynamic heating. The dramatic increase in surface heat load and skin friction caused by boundary layer transition during ascent, cruise and re-entry has first order impact on the design of thermal protection system (TPS). Typically, when flow turns from laminar to turbulence, the surface heat flux will increase by a factor of more than 3, as shown in Fig. 1.7 (Horvath et al. 2004, Schneider 2004). Consequently, accurate prediction of laminar/turbulent transition is of significant importance for hypersonic re-entry vehicle, in consideration of safety, as well as the weight and operation and maintenance of the vehicle.

Current engineering prediction tools for hypersonic transition mostly rely on the flight test data and wind tunnel experiments. The transition location is estimated by limited number of parameters (eg. Reynolds number and Mach number). The accuracy is questioned when changing vehicle geometry and flight condition. Furthermore, during the wind tunnel test, transition process is affected by the freestream noise radiated from the wall of test facility, making it difficult to offer precise data and fair comparison with inflight test result (Schneider 2001). The development of numerical simulation gives more insight to instability mechanisms leading to transition. New correlation methods has been proposed taking the transition mechanisms into account, including the first and second mode instability

(Schneider 2015). However, as each of them only considers one factor and new hypersonic boundary layer transition mechanisms is still needed to be identified, general transition prediction method is not available.

As a result, for the consideration of flight safety, designers usually follow the conservative philosophy and employ oversized TPS, leading to significant increase of the vehicle overall mass, and degrade in vehicle performance.

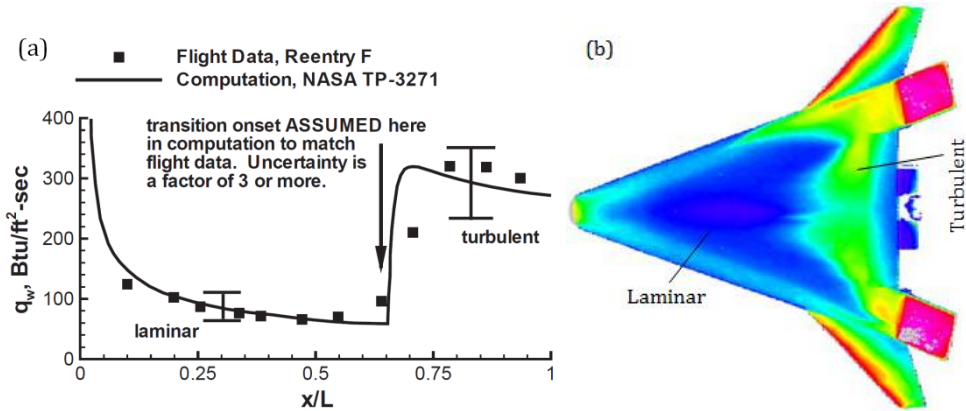


Fig. 1.7. Surface heat load distribution for transition, (a) heat flux (q_w) along the cone for reentry F (Schneider 2004); (b) non-dimensional heat flux distribution of X-33 windward surface at $Ma = 6$, $Re_{unit} = 2.6 \times 10^7$, $AOA = 30^\circ$ (Berry et al. 2001).

1.2.3.2 Air-breathing vehicle

The challenge of boundary layer transition is also faced in designing hypersonic air-breathing vehicle, such as X-43A (Hyper-X), which is of a slender configuration (Lau 2008), as shown in Fig. 1.8. The forebody of the vehicle consists of discrete flat ramps, providing multiple non-isentropic flow compression. The flow will be preconditioned when passing the forebody of the vehicle before entering the scramjet. For the purpose of achieving uniform flow distribution and preventing boundary layer separation in the intake of scramjet, turbulent flow is desired. According to the hypersonic boundary layer transition prediction performed in NASP program, the flow will remain laminar before the engine inlet at Mach 7. Forced transition using boundary layer trip is typically required (Berry et al. 2001). Nevertheless, the transition onset needs to be accurately controlled. Otherwise a longer range of turbulent flow along the forebody will cause unwanted increase of skin friction and heat loads, increasing the requirement on TPS.

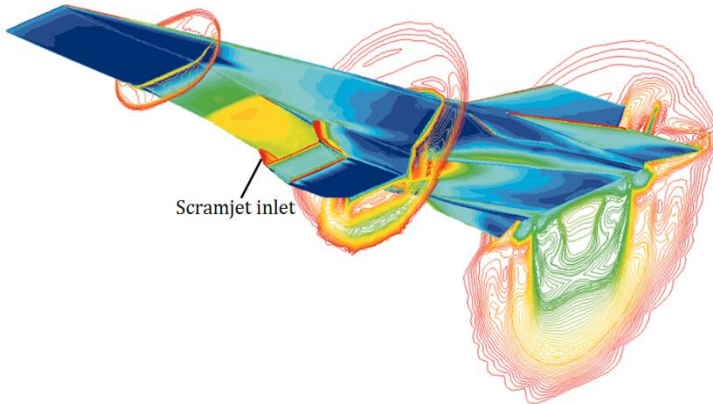


Fig. 1.8. CFD image of surface heat transfer on X-43A and flow field contour shown by local Mach number, the test condition at Mach 7 with engine operating, reproduced from NASA website.

1.3 Effect of roughness element on transition

Successful prediction of transition relies on an indepth understanding of the physical mechanism leading to transition. Despite the intensive experimental and numerical researches on the topic, many questions on the physical mechanisms of boundary layer transition are still to be answered (Kachanov 1994, Fedorov 2011, Zhong and Wang 2012). The presence of many relevant factors including freestream disturbances, pressure gradient, Mach number, compressibility, surface curvature and surface roughness can greatly influence the transition process. Among all the factors, surface roughness plays a key role. The transition process can either be accelerated or delayed by the roughness element, depending on the flow condition and roughness properties.

Usually, when a roughness element with sufficiently large height (h) compared to the boundary layer thickness (δ) is immersed in a laminar boundary layer, it will produce a disturbance with the potential to accelerate the transition process (Reshotko 2001). The supercritical roughness element can have different applications. On one side, the accelerated transition results in unexpected increase in both drag and surface heat load. Such roughness element can appear as localized gap filler protruding on the surface of space shuttle Discovery as shown in Fig. 1.9. During hypersonic re-entry test, high localized surface temperature is produced by unknown origin and wing protuberance of space shuttle, as shown in Fig. 1.10. The increased heat load can cause fatal damage to the thermal protection system (TPS), associated with exceeding bond-line temperature limits, burn through, or thermos-structural breakup. Sometimes spacewalk is needed before re-entry to remove the protuberance on the vehicle surface. On the other hand, transition can also be artificially promoted by the roughness element to increase the near-wall momentum and prevent unwanted separation in the flow. In this case, the roughness element has been put over suction side of compressor blades (Van Rooij and Timmer 2003,

Montomoli et al. 2010) and airfoil (Lin 2002) to achieve high lift. Or at supersonic condition, in which separation is mostly resulted from shock wave boundary layer interaction, roughness element is applied to avoid unstart problem of scramjet (Giepmans et al. 2016). A successful separation control using zigzag trip to promote early transition at Mach 1.7 is shown Fig. 1.11, in which the reverse flow region is eliminated. For the application of boundary layer trip, an accurate prediction of transition onset location is essential, as transition and turbulent flow should occur upstream of the separation bubble.

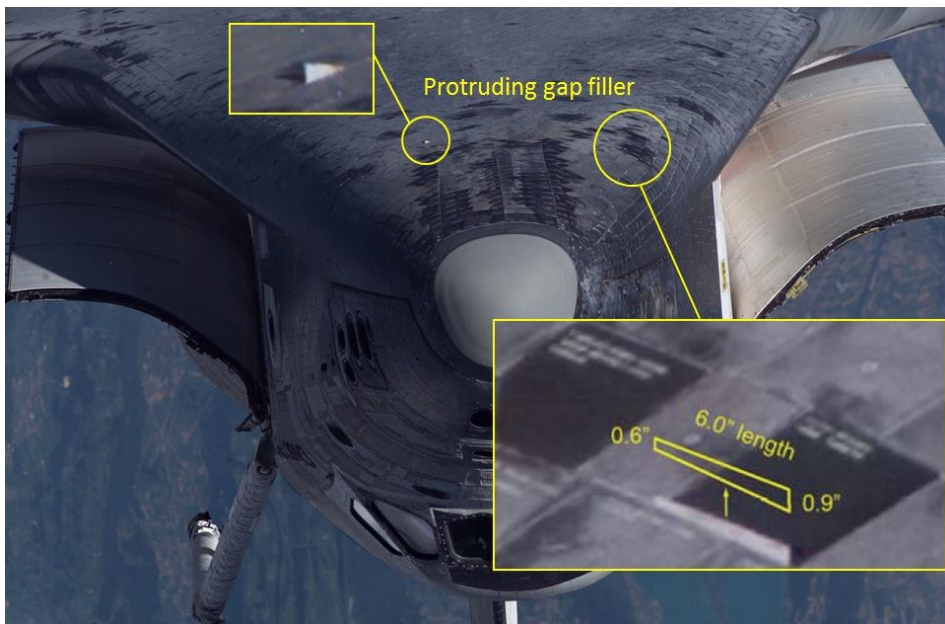


Fig. 1.9. Surface of space shuttle Discovery, with protruding gap filler, photo taken by John Philips at International Space Station (ISS) (Source: SI Website, ISS011-E-11074 and NASA Website).

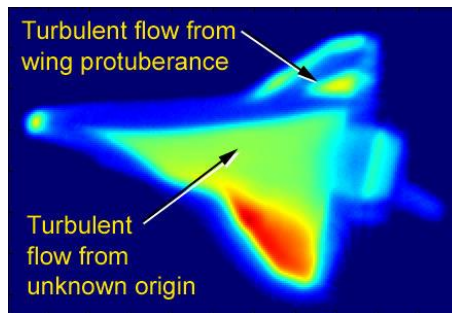


Fig. 1.10. Surface temperature distribution over space shuttle during Return-to-Flight, STS-119, at Mach 8.4 (Horvath et al. 2010).

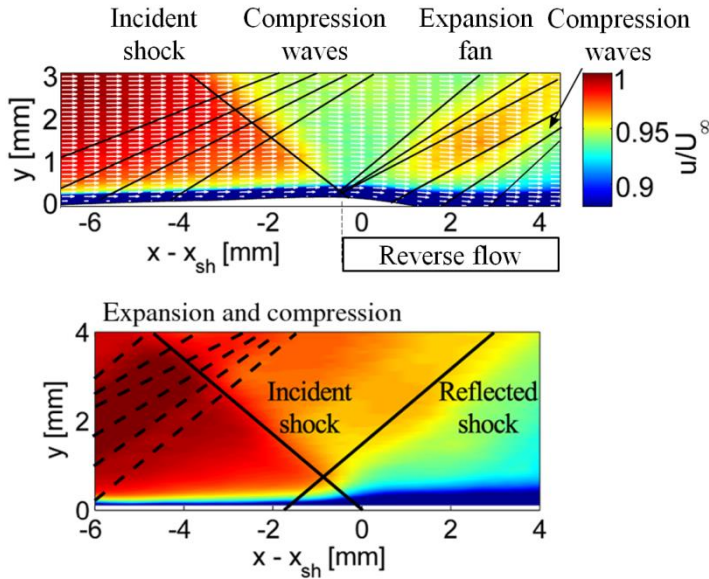


Fig. 1.11. Control of flow separation caused by SWBLI using boundary layer trip; top: undisturbed condition, bottom: with zigzag trip. (Giepmans et al. 2016)

On the other hand, under subcritical condition, the roughness element can produce stable velocity streak of moderate amplitude in the wake (Fransson et al. 2004). The stable streaks are able to reduce the growth of artificially generated TS waves, therefore yielding the potential to delay the natural transition process (Cossu and Brandt 2004, Fransson et al. 2006, Shahinfar et al. 2012). As shown in Fig. 1.12 (Fransson et al. 2006), external forcing is produced in the freestream to trigger transition after the exponential growth of TS waves on the bottom half. Under the same forcing condition, boundary layer remains laminar on the top half under the control of a spanwise array of cylindrical roughness element. The physical mechanism behind the transition delay is provided by the perturbation energy equation. The stable velocity streak produces a negative spanwise production term, Reynolds stress $-\overline{uw}$ on $\partial u/\partial z$. Together with the viscous dissipation, the former negative term compensates the positive wall-normal production term $-\overline{uv}$ on $\partial u/\partial y$ (Cossu and Brandt 2004). Although promising, the successful stabilization of TS wave relies on the selection roughness parameters, such as roughness height, shape and spacing, under limited flow conditions (low turbulence flow). Once the velocity streak amplitude is larger than the critical value, roughness element will produce unstable wake flow, leading to upstream movement of transition until the roughness location.

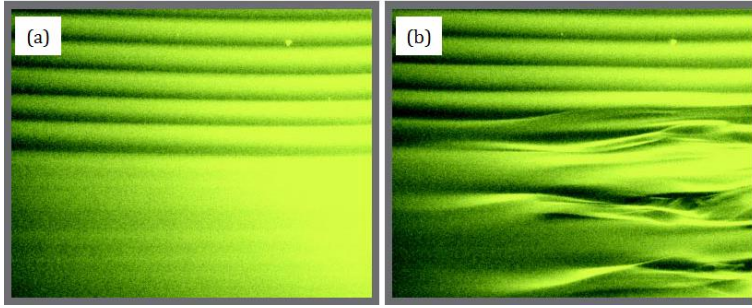


Fig. 1.12. Smoke flow visualizations of two-dimensional boundary layer with (up) and without (bottom) roughness induced velocity streaks, (a) no external forcing (b) subject to external forcing (Fransson et al. 2006).

1.4 Prediction of roughness induced transition

Reynolds number is widely accepted as an important tool to predict laminar to turbulent transition. For the smooth flat plate of zero angle of attack, natural transition occurs at a distance (x_t) from the leading edge. The critical Reynolds number relating to the streamwise position is given by

$$Re_t = u_\infty x_t / \nu \quad (1.1)$$

ranging from 3.5×10^5 to 10^6 (Schlichting and Krause 2003), where u_∞ is the freestream velocity.

When the surface roughness is placed inside the boundary layer, one major effect is to promote transition. In this case, the transition process induced by roughness element is estimated by the roughness-height based Reynolds number, defined as

$$Re_h = u_h h / \nu \quad (1.2)$$

where h is the roughness height and u_h is the streamwise velocity at that height (Van Driest and Mccauley 1960, Tani 1969, Fedorov 2011). At low speed, transition induced by three-dimensional roughness is typically predicted by the critical value of Re_h obtained by experiments (Tani 1969). Below the critical Re_h , transition is not accelerated comparing with natural transition case. The flow in the wake of the roughness element remains stable and returns to the homogeneous laminar conditions after a certain distance. Instead, when exceeding the threshold, transition will rapidly move upstream until the roughness location, as shown by the relation between Re_t and Re_h behind cylindrical roughness element in Fig. 1.13. The condition when transition occurs at the roughness location is called 'effective', as the roughness trips the boundary layer as effective as possible. Further increase of Re_h does not move transition upstream. Tani et al. (1962) proposed an empirical estimate of the critical Re_h for three-dimensional isolated roughness with aspect ratio of unity, lying

in the range between 600 and 1000 for incompressible flows. In a more recent study on $Re_{h,crit}$ by Klebanoff et al. (1992), lower critical Re_h of 450 was found for a roughness element of same geometry and aspect ratio. Von Doenhoff and Braslow (1961) obtained the correlation between the critical Re_h and the aspect ratio of roughness element, scaling with $(h/c)^{2/5}$, indicating transition can occur at lower Re_h when the span width of roughness increases. Since the occurrence of transition depends on a multitude of parameters (roughness geometry, freestream disturbance level and local pressure gradient), significant variations of the $Re_{h,crit}$ have been observed, rendering a limited range on its application. Furthermore, the physical transition process is not directly taken into account in this correlation.

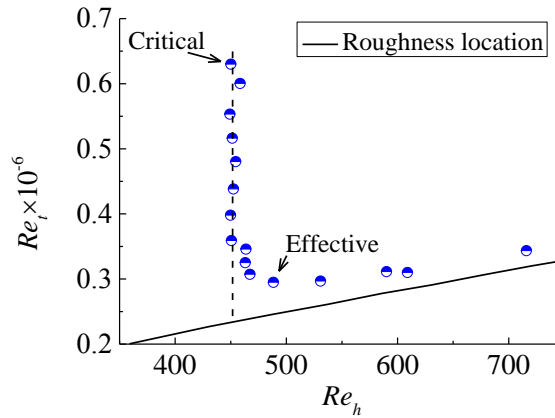


Fig. 1.13. Variation of transitional Reynolds number Re_t with Re_h behind cylindrical roughness element, redrawn from Klebanoff et al. (1992).

In hypersonic flow, early experiments (Dryden 1953, Van Driest and Mccauley 1960) also suggest the importance of Re_h in the transition process. As in compressible flow, the Mach number and surface temperature becomes more influential, Re_h alone is not sufficient to predict roughness induced boundary layer transition. Based on the inflight and wind tunnel test, a popular transition criterion, referred to as *Shuttle criterion*, was developed within the US space flight program (Berry et al. 1998, 2001) as

$$(Re_\theta / Ma_e)_{tr} = C(h / \delta_{99})^{-1} \quad (1.3)$$

where Re_θ is the Reynolds number based on boundary layer momentum thickness, Ma_e is the Mach number at the edge of boundary layer, h/δ_{99} is the ratio between roughness height and boundary layer thickness. The critical limit of the constant C is estimated to be 200 by LATCH method for shuttle orbiter (Berry et al. 2006), when transition happens downstream of the roughness location, as shown in Fig. 1.14. For

the effective condition, the constant C increases to 310. However, the constant value can vary significantly (approximately 50%) when using a different computation method, increasing the level of uncertainty during application.

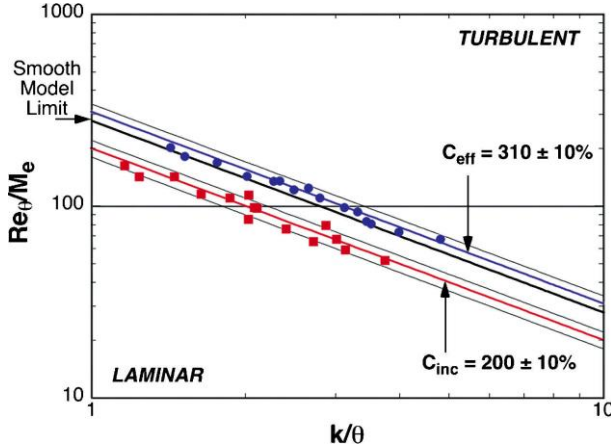


Fig. 1.14. Correlation for shuttle orbit by LATCH code (Berry et al. 2006).

The availability of direct numerical simulation (DNS) allows more detailed study on roughness induced transition, increasing the parametric range to perform accurate correlation. Redford et al. (2010) used DNS to study the influence of the Mach number and thermal condition at the wall on isolated roughness induced transition. A smooth bump shape roughness with an aspect ratio of 2 was considered. A linear relation between the parameter $M_h T_\infty / T_w$ and Re_h was found to distinguish the steady laminar case from the transitional case. Based on the numerical research behind cubic shape roughness at different Mach number, Bernardini et al. (2012) proposed a modified roughness-height based Reynolds number $Re_h^* = u_h h / \nu_w$ by using the kinematic viscosity at the wall. The critical value of 460 was suggested. In a more recent parametrical study, Bernardini et al. (2014) estimated the critical Reynolds number based on the momentum deficit produced by the roughness element. The latter parameter depends strongly on the roughness geometry. Details of the former criterion will be given in sec. 2.3.2.

1.5 Scope of the thesis and outline

Boundary layer transition induced by roughness elements is an important phenomenon relating to the design of subsonic and supersonic civil transport aircraft, hypersonic flight vehicle and the blades of turbomachinery. Understanding the transition mechanism behind roughness elements is essential for the accurate prediction of aerodynamic forces and surface heat load. The current investigation focuses on the fundamental transitional flow features behind isolated roughness elements. The study is carried out using the approach of wind tunnel experiments. A

three-dimensional measurement technique namely tomographic particle image velocimetry (PIV) is employed.

1

Chapter 2 provide a detail overview of the fundamentals of boundary layer theory and roughness induced transition based on available literature. The parametric effect on transition process and roughness wake flow features is addressed. The open research questions and research objectives are proposed and elaborated.

In Chapter 3, the flow facilities and test conditions are discussed. The working principles of particle image velocity and experimental arrangement are presented in detail. One important aspect is to set up high spatial resolution measurement system which enables the detection of vortical structures down to half of the roughness height. The data reduction techniques including Proper Orthogonal Decomposition (POD) and vortical detection methods used in the thesis are explained.

Chapter 4 opens the investigation on boundary layer transition mechanisms induced by a single micro-ramp in the incompressible regime. The main target is to understand the early stage of three-dimensional laminar to turbulent transitional flow feature at supercritical Re_h . Both time-averaged and unsteady instantaneous flow organisations are inspected. The instantaneous flow organisation elucidates the mechanism of transition along its stages. A connection between unsteady vortical structure and wake flow instability is proposed, revealing the dominant mechanism leading to transition.

In Chapter 5, the research on micro-ramp induced transition continues with the influence of roughness-height based Reynolds number. The variation of transitional flow features when the Reynolds number decreasing down to the critical regime is investigated. Proper Orthogonal Decomposition (POD) of the velocity field is applied to highlight the dominant unstable flow feature from the obtained eigenmodes. Re_h is found to be the key factor determining the importance mode type.

Roughness geometry has been long recognized as an important parameter influencing transition process. The main target of Chapter 6 is to compare the different flow topologies and study the effect of the element geometry on accelerating boundary layer transition. Four different geometries, including cylinder, diamond, hemisphere and micro-ramp, are considered maintaining constant height and span of the element. A main flow behaviour distinction is observed between the bluff-front elements and the slender-shaped micro-ramp. A common mechanism of sideward propagation for the turbulent wedge among all elements is proposed.

The thesis concludes in Chapter 7, summarising the most important findings. Outlooks for the future development are given, offering potential research perspectives.

2

Fundamentals of roughness induced transition

2.1 Fundamentals of boundary layer theory

A brief introduction to the classical boundary layer quantities and non-dimensional parameters used in the thesis is given in this section. The paths to turbulence under different flow condition is described following the road map proposed by Morkovin (1988) and Reshotko (2008).

2.1.1 Boundary layer properties

Prandtl introduced the concept of boundary layer, which is the thin layer close to the surface of a solid body where viscosity must be taken into account. The velocity of the boundary layer starts from zero at the surface and increases with the wall-normal distance (y) from the surface. The velocity profile ($u(y)$) is sketched in Fig. 2.1. The edge of the boundary layer is considered as the point where the velocity reaches the freestream value. Due to the continuous velocity change inside the boundary layer, the precise location of the edge cannot be identified. In practice, the boundary layer thickness is defined as the distance from the point where the velocity reaches a certain percentage of the freestream value, which is typically 99% (δ_{99}). The thickness of boundary layer over zero-incidence flat plate increases monotonically with the distance from the leading edge (x). The exact solution of the laminar boundary layer thickness can be obtained by the Blasius similarity (White and Corfield 2006), as

$$\delta_{99}(x) = 5 \sqrt{\frac{\nu x}{u_\infty}} \quad (2.1)$$

In the current study, the Blasius solution for laminar boundary layer is used as a reference for comparison with the measured boundary layer velocity profile, validating the laminar condition of the undisturbed incoming flow.

The wall shear stress can also be estimated from the velocity gradient at the wall, as

$$\tau_w(x) = \mu \left(\frac{\partial u}{\partial y} \right)_w \quad (2.2)$$

The skin friction coefficient is

$$c_f = \frac{\tau_w(x)}{\rho u_\infty^2 / 2} \quad (2.3)$$

When the flow undergoes laminar to turbulent transition, the boundary layer thickness increases significantly, with a much fuller velocity profile (see Fig. 2.1). The

increased velocity gradient at the wall leads to larger skin friction, which increases by a factor of 3 or more.

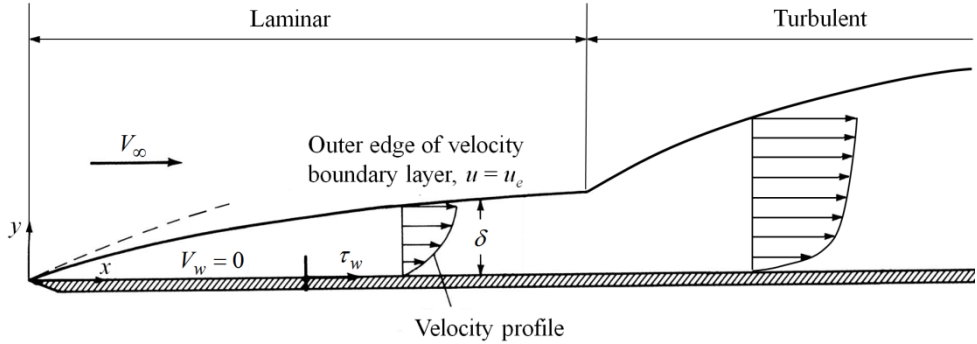


Fig. 2.1. Boundary layer properties over a flat plate of zero angle of attack, redrawn from Anderson (2010).

Another two important parameters of the boundary layer are the displacement thickness (δ^*) and momentum thickness (θ), highlighting the difference between the viscous velocity profile inside the boundary layer with the inviscid velocity profile. The displacement thickness is defined as the mass flux defect, as

$$\delta^* = \int_{y=0}^{\infty} \left(1 - \frac{\rho u}{\rho_{\infty} u_{\infty}}\right) dy \quad (2.4)$$

suggesting the distance by which the streamline lines is displaced upward by the boundary layer comparing to the inviscid flow condition. The momentum thickness indicates the momentum defect introduced by the boundary layer, defining as

$$\theta = \int_{y=0}^{\infty} \frac{\rho u}{\rho_{\infty} u_{\infty}} \left(1 - \frac{u}{u_{\infty}}\right) dy \quad (2.5)$$

The shape factor (H) of boundary layer is the ratio between the displacement thickness (δ^*) and momentum thickness (θ). The value of shape factor increases with the adverse pressure gradient of the flow. Moreover, in the process of boundary layer transition, significant decrease of the shape factor occurs. For a laminar boundary layer, the shape factor (H) equals to 2.59 according to the Blasius solution. When reaching the turbulent condition, shape factor (H) decreases to approximately 1.4.

2.1.2 Paths to turbulence

Boundary layer transition results from the nonlinear response of the undisturbed laminar boundary layer to different type of external disturbances (Saric et al. 2002). The disturbances in the freestream, such as sound, vorticity, temperature and entropy, enter the boundary layer and determine the initial conditions of disturbance amplitude, phases and frequencies. This process is defined as receptivity (Morkovin 1969). The instability wave is generated when the perturbations amplify to a certain value. Due to the variation of the initial conditions, including Reynolds number, wall curvature, surface roughness, and sweep, different types of instabilities can occur. The paths to turbulence are summarized by Reshotko (2008) and are shown schematically in Fig. 2.2.

At a low disturbance environment, transition is explained by the linear stability theory. In this condition, modal growth of the unstable disturbances, such as first mode instability (exhibited by the well-known TS wave), crossflow instability and Görtler vortices, is dominant. The breakdown to turbulence is caused by nonlinear secondary instabilities when the disturbance amplitude is large enough, as already explained in sec. 1.1. This is the traditional path to transition, referred to as ‘*path A*’ in Fig. 2.2.

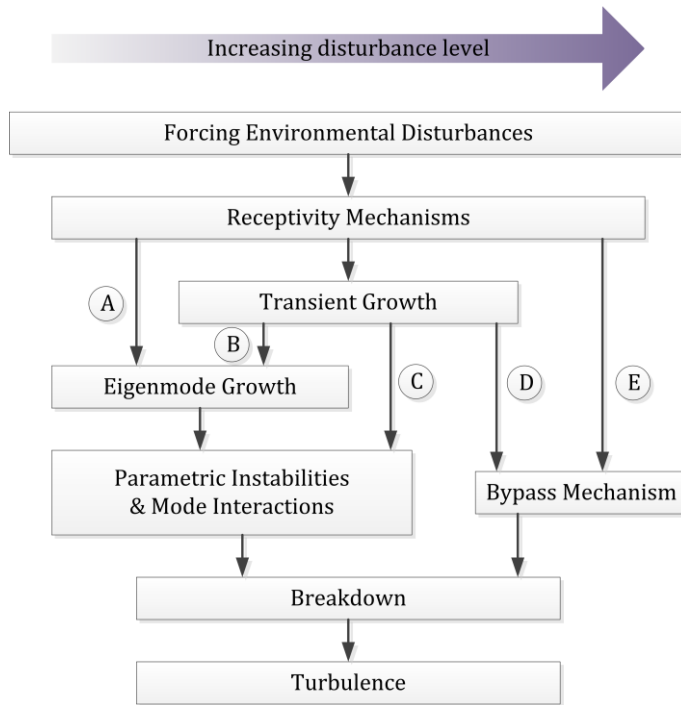


Fig. 2.2. Paths to turbulence in boundary layers (Reshotko 2008).

With the increase of the disturbance amplitude, transient growth occurs due to the non-orthogonal nature of the Orr-Sommerfeld and Squire eigenfunctions (Schmid and Henningson 2001). Although the solutions of both eigenfunctions damp slightly in time, the non-orthogonal superposition of highly oblique T-S and Squire modes leads to the algebraic growth before exponential decay. To emphasize, transient growth is also linear. Through weak transient growth, higher initial disturbance amplitude for the growth of eigenmodes can be achieved, shown as '*path B*' in Fig. 2.2. In the spatial growth theory, the optimal transient disturbances are stationary vortices, providing spanwise varying inhomogeneity in the mean flow (Reshotko and Tumin 2001). The scenario of transient growth can also be described by the 'lift-up' mechanism proposed by Landahl (1990). Nevertheless, the largest modal growth occurs with traveling transverse disturbances at low speed, or traveling oblique disturbances at supersonic speed. The coupling mechanism between streamwise and transverse disturbances is not clear yet. Strong transient growth can directly lead to secondary or subcritical instabilities in *path C*, or direct bypass (*path D*).

The bypass transition has no linear growth regime, reaching the nonlinear process directly. When the freestream disturbances are sufficiently large, usually at 1%-4% of freestream velocity (Wu et al. 2014), the linear growth of disturbances is bypassed, shown as '*path E*'. The transition process is dominated by the streamwise elongated streaks of alternating positive and negative sign of disturbance velocities. With the growth of disturbance amplitude in the streamwise direction, localized turbulent spots occur, indicating the onset of transition.

2.2 Mechanisms of roughness induced transition

For a two-dimensional roughness element without spanwise variation, including the forward facing step, 2D gap and wire, the transition process has been well documented and understood. The natural transition is promoted by amplification of Tollmien-Schlichting (TS) waves at the downstream separation and recovery region of the roughness (Klebanoff and Tidstrom 1972). The nature of eigenmode growth is modified along '*path A*' in Fig. 2.2. Increasing Re_h leads to the growth of TS wave amplitude (Saric et al. 2002), thus moving the transition location upstream gradually, closer to the roughness element (Perraud et al. 2004).

The three-dimensional roughness elements are typically classified into two types, isolated and distributed. The isolated roughness includes gaps, steps, joints, local flaws due to limited manufacturing tolerance (rivet head), and trip elements. The distributed roughness appears in the form of randomly dispersed small imperfections, such as sand-grain trips and screw threads, which are left on the metal surface by machining and ablation in hypersonic flows. The simplified types of isolated and distributed roughness elements are shown in Fig. 2.3 as cylinder or diamond shape and random grit respectively. The research in the current thesis focuses on the isolated roughness type, which produces a localized disturbance source. The transition scenario behind isolated roughness element is easier to

2. Fundamentals of roughness induced transition

understand compared with distributed type. The latter is complex in geometry, increasing the number of descriptive parameters.

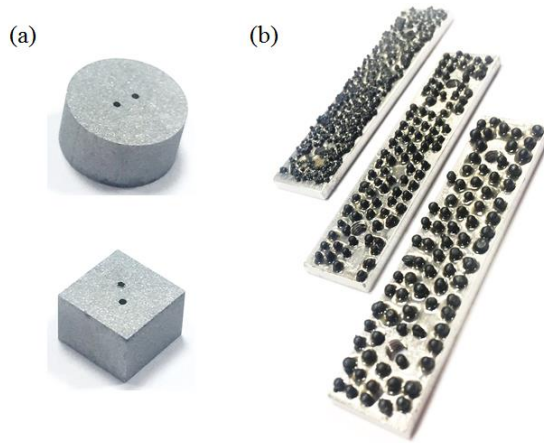


Fig. 2.3. Examples of isolated and distributed roughness element, (a) isolated cylinder and diamond, (b) random grit.

The explanation on how three-dimensional roughness influence boundary layer transition is not as clear as the two-dimensional type. The transition process cannot be explained by the enhancement of TS wave (Reshotko 1984, Morkovin 1990), as three-dimensional roughness introduces a localized spanwise deflection of the streamlines without strong downstream flow separation. Comparing with two-dimensional roughness element, Re_h plays a more important role in determining the effect of three-dimensional isolated roughness element on transition, as explained in sec. 1.4. Early work mostly focussed on determining the transition onset location, in order to increase the database used for the development of empirical correlations (Klebanoff et al. 1955, Tani et al. 1962). In more recent experiments, the flow features upstream and downstream of isolated roughness as well as the induced disturbances are measured in more detail. For example, Fransson et al. (2004, 2005, 2006) performed a series of hot-wire measurements downstream of a spanwise periodic array of cylindrical roughness elements at low speed. An important observation was the formation of streamwise elongated velocity streaks in the wake, which are produced by the streamwise vortices, as sketched in Fig. 2.4. The streamwise vortices induce an upwash motion on the side, transporting low momentum fluid away from the wall. On the other side, they sweep high-momentum fluid towards the wall, resulting in the formation of low- and high-speed streaks, which modulate the surface shear along the wall-normal and spanwise direction. The magnitude of the streaks depends on the streamwise vorticity, which increase in the near wake, followed by a fast decay when moving further downstream. The initial purpose of implementing isolated roughness is to delay the amplification of TS waves using steady velocity streaks. However, they observed the onset of transition

when the streak amplitude increases beyond a critical level. For the latter condition, the wake flow becomes inviscid unstable due to the presence of inflection points in wall-normal and spanwise directions, which can promote laminar to turbulent transition.

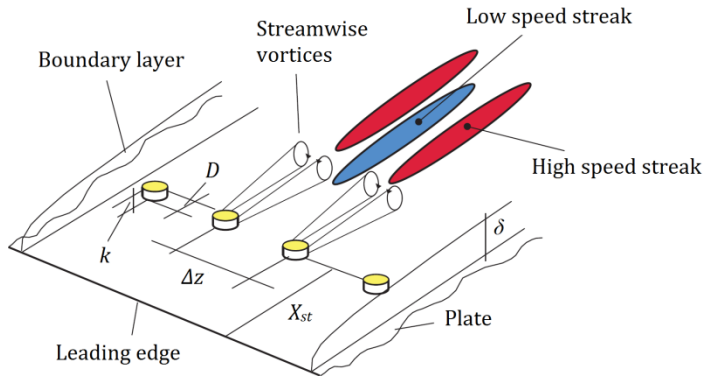


Fig. 2.4. Flow topology around cylindrical roughness element (Fransson et al. 2004).

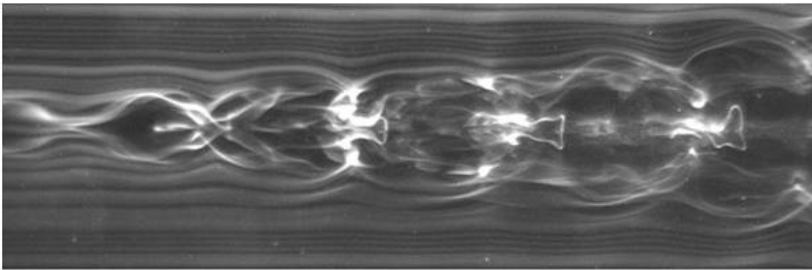
Ergin and White (2006) experimentally studied the spatial evolution of disturbances behind cylindrical roughness. The spanwise variation of the flow decays rapidly in the near wake. They stated that the transition process is governed by a competition between the growth of fluctuations and the relaxation of spanwise non-parallel flow towards laminar condition. Transition occurs when the unsteady disturbances reach the critical amplitude before the base flow can return to Blasius state.

The development of transient growth theory offers the first theoretical guidance to the research on roughness induced transition. The connection is based on that the stationary streamwise vortices produced by three-dimensional roughness are qualitatively similar to the optimal disturbances, which undergoes maximum energy growth over finite temporal and spatial distance in transient growth (Andersson et al. 1999). Following the transient growth theory, the streamwise velocity disturbances produced by roughness element, although being stable in the content of linear stability theory, can lead to transition (Reshotko 2001, Reshotko and Tumin 2004). The transition process forced by three-dimensional roughness element can be categorized in 'path D' in Fig. 2.2 at supercritical condition (Downs et al. 2008). For the quantitative discrepancy between optimal disturbances and the roughness induced velocity streaks, the reader can refer to Fransson et al. (2004) and White et al. (2005). When Re_h reaches the effective level, the disturbances produced by roughness element can lead to direct bypass transition, following 'path E'.

Similarly, in the bypass transition process, the formation of velocity streaks through the 'lift-up' mechanism takes over the role of TS waves in the process of the growth of the perturbations (Landahl 1990). Once the streak amplitude exceeds a critical value, the streak will be subject to a secondary instability, with either sinuous or varicose modulation, and finally breaks down to turbulence (Andersson et al. 2001).

Andersson et al. (2001) studied the secondary instability of the velocity streaks in the bypass transition process using DNS. Two types of instability modes, varicose (symmetric) and sinuous (asymmetric), can be sustained. The definition of the instability modes is based on the appearance of the low-speed streaks. The critical streak amplitude for the excitation of sinuous instability is 26% of the freestream velocity. Varicose instability is more unstable when the streak amplitude is larger than 37% of the freestream velocity. By a well control of freestream disturbances, Asai et al. (2002) experimentally investigated the three-dimensional shear layer instability around the low-speed streaks. They found that the growth of varicose mode is related to the inflectional velocity profile in the wall-normal direction, which is prone to Kelvin-Helmholtz (K-H) instability. The induced hairpin-shape vortical structure is visualized in Fig. 2.5(a). The sinuous mode is caused by the instability at the spanwise shear layer. The velocity streaks exhibit meandering motion, which evolve into quasi-streakwise vortices with alternating vorticity sign, as shown in Fig. 2.5(b).

(a)



(b)

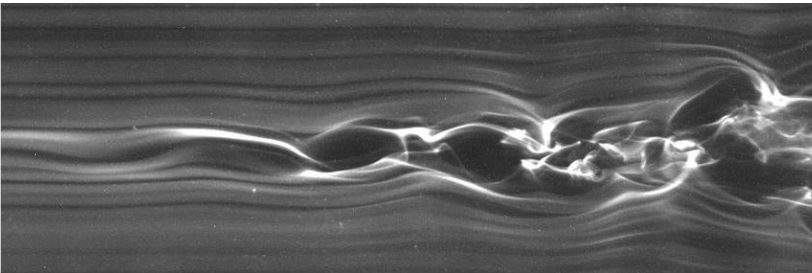


Fig. 2.5. Visualization of varicose (a) and sinuous (b) mode, produced by artificial disturbances at low speed, flow from left to right (Asai et al. 2002).

In the wake of isolated roughness element in both incompressible and compressible flow regime, the varicose and sinuous instability mode are found in the global stability analysis based on DNS result (De Tullio et al. 2013, Loiseau et al. 2014, Citro et al. 2015, Shin et al. 2015). The contour of streamwise velocity disturbances for these two modes is shown in Fig. 2.6. The spatial distribution of the disturbances reaches qualitative agreement with the scenario in bypass transition process. Different from what proposed by Asai et al. (2002), Loiseau et al. (2014) and De Tullio et al. (2013) found that the varicose mode extract energy from both wall-normal and lateral shear layer. As a result, the former mode becomes a instability of the three-dimensional shear layer as a whole, instead of only in wall-normal direction.

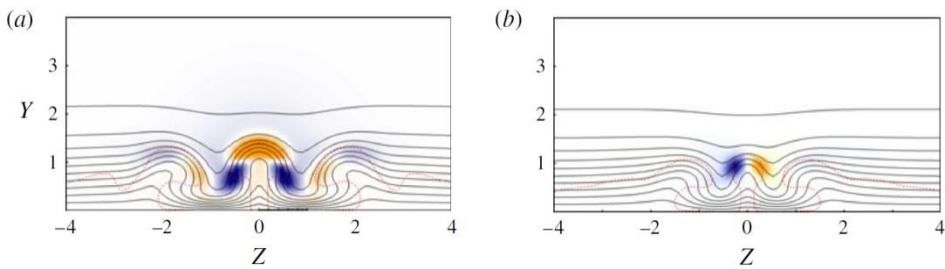


Fig. 2.6. Contour of streamwise velocity disturbances of varicose (a) and sinuous (b) mode behind cylindrical roughness at low speed, superimposed by streamwise velocity contour lines (Loiseau et al. 2014).

2.3 Isolated roughness induced transition

Despite the intensive researches on roughness induced transition, no general transition mechanism has been proposed, as the transition process is still influenced by many factors, including Reynolds number, roughness size, and roughness geometry. The effect of these factors will be detailed in the following sections.

2.3.1 Roughness-height based Reynolds number

As described in sec. 1.4, roughness-height based Reynolds number ($Re_h = u_h h / \nu$) takes the effect of both roughness height (h) and disturbance parameter into account. The latter is represented by the velocity at the roughness tip u_h . The importance of Re_h is revealed by its influence on the growth of the velocity perturbations in the wake of roughness element (Fransson et al. 2004, 2005, White et al. 2005, Denissen and White 2008, 2009). The maximum transient growth of the roughness produced streamwise velocity perturbations scales with Re_h^2 . Ergin and White (2006) studied the transitional flow over a spanwise array of cylindrical roughness element using hot-wire anemometry at various Re_h , ranging from subcritical ($Re_h = 202$ and 264) to supercritical conditions ($Re_h = 334$). They found that the exponential growth rate of the unsteady disturbances increases rapidly with the increase of Re_h . At supercritical

condition, the unsteady disturbances undergo transient growth and spread laterally along the wake span, leading to transition to turbulence. On the other hand, in the subcritical condition, the unsteady disturbances are damped before transition can occur, returning a restabilized laminar flow.

The variation of Re_h can modulate velocity streak distribution and amplitude, which influence the physical mechanism towards transition. Typically, a low speed region around the symmetry plane is produced behind the roughness element (Joslin and Grosch 1995, Ergin and White 2006, Cherubini et al. 2013, Loiseau et al. 2014). The most unstable instability mode associates with the magnitude and the active range of central low-speed region. In the compressible flow regime, Choudhari et al. (2010) and Kegerise et al. (2012) studied the flow over diamond-shaped roughness at Mach 3.5 both numerically and experimentally at various Re_h . They found that the counter-rotating vortex pairs in the wake of diamond induce low- and high-speed regions. Increasing Re_h leads to longer streamwise persistence of the central low speed region. Compared to shear layer (K-H) instability, the streak instability corresponding to sinuous mode sustains over longer streamwise distance, which dominates the process of transition with final breakdown to turbulence at lower Re_h . Whereas shear layer instability undergoes fast growth and leads to the onset of transition at high Re_h .

In hypersonic flow condition, the influence of Re_h is also dramatic. In most research cases, Re_h changes simultaneously with Mach number, with an opposing trend. Iyer and Mahesh (2013) performed DNS analysis on the transitional flow feature around hemisphere at three Re_h (also Mach number). No transition can be detected at the lowest Re_h of approximately 9000. Similar to incompressible flow regime, increasing Re_h moves transition upstream, closer to the roughness element, as shown by the example in Fig. 2.7. The transition promotion by increasing Re_h has also been observed by other numerical studies (Redford et al. 2010, Bernardini et al. 2014, Subbareddy et al. 2014). Iyer and Mahesh (2013) identified three sources of unsteadiness, including upstream vortex system, upstream shock induced unsteadiness and unstable downstream separated shear layer. The strength of the unsteadiness strongly depends on Re_h . At median Re_h , the shear layer unsteadiness is dominant. Whereas at higher Re_h , both upstream vortex system and downstream shear layer are strongly unstable.

2.3.2 Roughness geometry

One application of the isolated roughness element is to effectively trip boundary layer transition. The effectiveness of a roughness element in promoting transition depends not only on Reynolds number (Tani 1969) and roughness size (Ergin and White 2006), but also on strongly its shape (Klebanoff et al. 1992), as different vortical patterns can be introduced in the wake, which modulate the amplitude and distribution of velocity streaks (Acarlar and Smith 1987, Fransson et al. 2006, Fransson and Talamelli 2012).

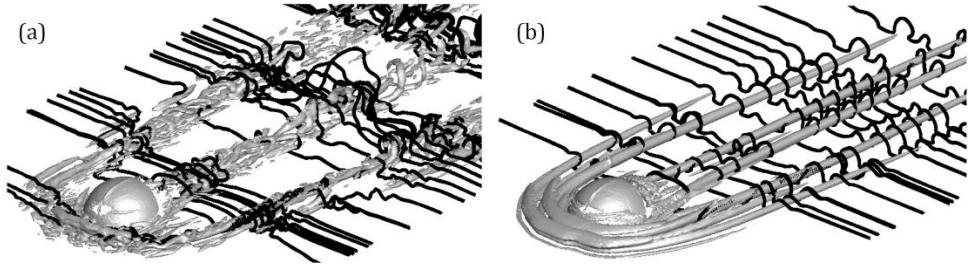


Fig. 2.7. Instantaneous vortical structure detected by Q criterion, superimposed by the vortex lines, (a) $Ma = 3.37$, $Re_h = 16831$, (b) $Ma = 5.26$, $Re_h = 14190$ (Iyer and Mahesh 2013).

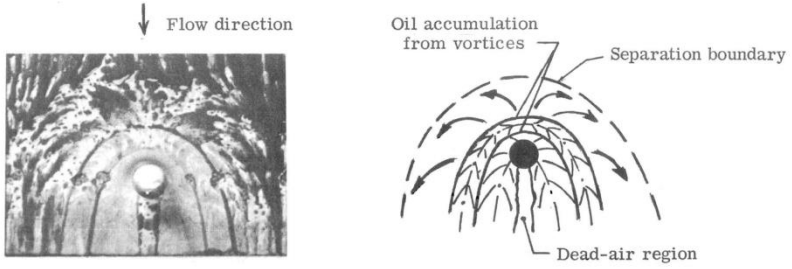
The early awareness of the roughness geometry effect on transition was when studying the transition onset location and the critical Re_h . Behind an array of spherical roughness with the aspect ratio of unity in low speed flow, Klebanoff et al. (1955) obtained a critical Re_h of 577, which slightly deviates from the range of 600 to 1000 behind cylinder of the same aspect ratio measured by Tani et al. (1962). Later on, Klebanoff et al. (1992) measured the critical Re_h behind both cylinder and hemisphere with $h/c = 0.5$. A higher critical value of 425 was obtained for cylinder compared with that of 325 for hemisphere.

Two major types of roughness geometry are considered in the previous researches: bluff-front and slender-front. The bluff-front roughness element, such as cylinder, can produce strong upstream separation and a system of spanwise vortices in the separation area. The flow patterns around bluff-front roughness element, including sphere, cylinder, triangular prism and pinhead, have been visualized by Whitehead (1969) at $Ma = 6.9$, as shown in Fig. 2.8. Compared with bluff-front type, the upstream separation introduced by the slender-front roughness element, such as micro-ramp, is significantly weaker. Consequently, no spanwise vortex system is produced in this case.

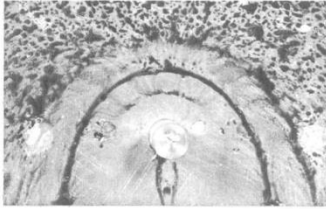
Most studies comparing the roughness tripping efficiency have been conducted directly in the most relevant high-speed regime. Hicks and Harper (1970) compared the effectiveness of sphere and triangular shape roughness at supersonic speed at three Mach numbers. The transition location (x_t) behind two roughness types at different roughness-height based Reynolds number Re_h is measured based on the inception of the turbulent wedge, as plotted in Fig. 2.9. Under the same flow condition, early transition was observed for triangular roughness, reaching effective condition at $Re_h \cong 6000$. For sphere, the effective Re_h is approximately 8000.

Tirtey et al. (2011) experimentally studied the surface footprint of the mean flow structure induced by different roughness elements (cylinder, diamond, hemisphere and micro-ramp) using oil-flow visualization and infrared thermography at Mach 6. The streamwise evolution of the surface heat transfer in the symmetry plane of the wake of different roughness elements was compared, revealing that the diamond shape is the most efficient in promoting transition, whereas the micro-ramp shows the lowest efficiency.

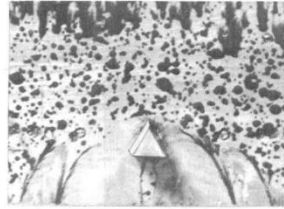
2. Fundamentals of roughness induced transition



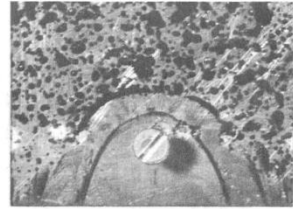
a) Sphere



b) Cylinder



c) Triangular prism



d) Pinhead

Fig. 2.8. Flow visualization around different roughness element (Whitehead 1969).

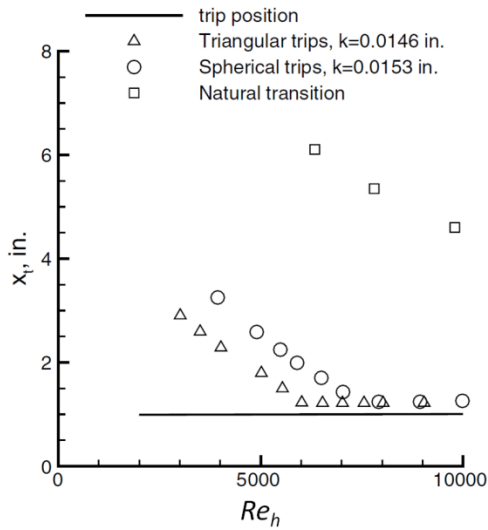


Fig. 2.9. Effect of roughness-height based Reynolds number and roughness geometry on transition location (Hicks and Harper 1970).

In order to find the controlling parameter of roughness geometry effect on transition, Bernardini et al. (2014) performed parametric study of roughness induced transition from supersonic to hypersonic regime using DNS. Three roughness geometries, namely hemisphere, cubic and cylinder of various sizes, were considered at different flow conditions. As one major feature of the roughness wake is the low-speed streaks with streamwise momentum deficit, they implemented a new control parameter, the momentum defect, into the existing Reynolds number to account for roughness geometry effect. The new Reynolds number can be linked to the previous used roughness-height based Reynolds number in compressible flow, Re_h^* , as

$$Re_Q = Re_h^* \cdot (h/c)^{-1/2} \cdot F(shape) \quad (2.6)$$

where

$$F(shape) = \int_0^1 \frac{y}{h} \cdot \frac{w(y)}{c} d\left(\frac{y}{h}\right) \quad (2.7)$$

$w(y)$ is defined as the width of the roughness, which can change with the wall-normal position y and reveals the cross-sectional shape of the roughness. The new correlation represents the roughness geometry effect through the aspect ratio and cross-sectional shape. Transition occurs when Re_Q is larger than 200 to 280. However, the correlation is based only on bluff front roughness element. While the slender-front roughness type, such as micro vortex generator, is not considered, limiting its range of application.

A DNS study later conducted by Van Den Eynde and Sandham (2015) expanded the considered roughness geometries. Besides bluff-front (cylinder, cubic and diamond) and slender-front (ramp-up) roughness, they also included smooth bump and ramp-down geometry, vary the roughness aft-section. They found the importance of the roughness streamwise profile in transition efficiency. For the roughness types with bluff-front, diamond shape is the most effective in promoting transition, followed by cylinder and cubic. Transition also occurs behind ramp-up roughness geometry but with some delay. For the smooth-bump and ramp-back geometry, transition was not tripped under the same external disturbance level. It seems that the area reduction of backward separation delays the transition process. As a result, they suggested that the backward section of the roughness can lead to different wake flow behaviour, affecting the transition scenario. The detailed feature needs to be further characterized.

The comparison of the efficiency of the aforementioned roughness geometries on promoting transition is summarized in Tab. 2.1.

Tab. 2.1. Transition promotion efficiency of isolated roughness elements

| | Roughness geometry | | | Flow condition |
|----------------------------------|---------------------------------|---|----------------------------------|----------------------|
| | Bluff-front | > | Slender-front > Slender-back | |
| Klebanoff et al. (1992) | Cylinder > hemisphere | | | $u_\infty = [0, 27]$ |
| Hicks and Harper (1970) | Triangular > Sphere | | | Ma = [1.6, 2.2, 2.9] |
| Tirtey et al. (2011) | Diamond > cylinder > hemisphere | > | Micro-ramp | Ma = 6 |
| Bernardini et al. (2012) | Hemisphere > cubic > cylinder | | | Ma = [1.1, 2, 4, 6] |
| Van Den Eynde and Sandham (2015) | Diamond > cylinder > cubic | > | Ramp-up > Ramp-down, smooth bump | Ma = 6 |

2.4 Wake flow of the roughness element

Besides the statistical analysis of disturbance growth and stability analysis of roughness induced transition discussed in the previous section of this chapter, another important aspect is to understand the wake flow features of the isolated roughness. A review of the previous researches will be given in this section, addressing two main types of vortical structures, the streamwise vortices and the hairpin vortices. Significant difference in vortical topology is found when changing roughness geometry. The related instability mechanism is discussed. The final breakdown to turbulence initiating by the formation of turbulent wedge is elaborated.

2.4.1 Streamwise vortices

A general feature of the roughness wake flow is the multiple streamwise vortices and the produced low- and high- speed streaks. The origin and evolution of the streamwise vortices induced by both bluff- and slender-front roughness elements is addressed.

2.4.1.1 Bluff-front roughness

The bluff-front roughness elements, including cylinder, diamond, cubic, and hemisphere, are mostly studied in transitional boundary layer considering flow topology (Gregory and Walker 1956, Whitehead 1969, Fransson et al. 2004, Iyer and Mahesh 2013, Doolittle et al. 2014, Subbareddy et al. 2014). The initial visualization was obtained by Gregory and Walker (1956) behind a cylinder at low speed, as shown in Fig. 2.10. The flow upstream of the cylinder rolls up and forms the spanwise vortices, which wrap around the obstacle and turns into streamwise rotating direction when traveling downstream. The lateral upwash motion produced by the legs of the horseshoe vortices lead to two low-speed regions at the spanwise side. Similar flow topology around cylinder was proposed by Fransson et al. (2004), revealing the predominance of horseshoe vortices and their impact on the wake flow features (see Fig. 2.4). One of the most complete investigations of the laminar horseshoe vortex was conducted by Baker (1979). A system of two, four or six spanwise vortices forms upstream of the cylinder. The number of spanwise vortices and the level of unsteadiness increase with the increase of the freestream velocity and the aspect ratio of the obstacle. In the numerical simulation of Rizzetta and Visbal (2007), the generation of a four-vortex-system was observed upstream of the cylinder at both subcritical and supercritical Re_h . At hypersonic flow condition, the horseshoe vortex system is also detected upstream of hemispherical (Danehy et al. 2009) and cylindrical (Danehy et al. 2010, Avallone et al. 2016) roughness elements by the recently performed experimental researches. The unsteadiness of the horseshoe vortices plays an important role in the downstream transition process (Danehy et al. 2009, 2010, Iyer and Mahesh 2013, Subbareddy et al. 2014).

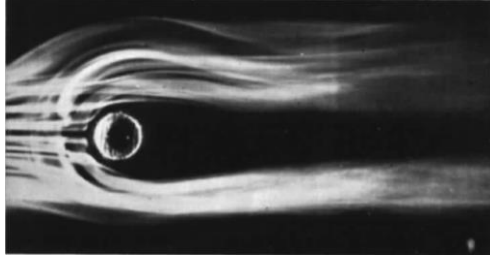


Fig. 2.10. Smoke flow visualization around cylindrical roughness element at low speed, $h/\delta = 0.7$. (Gregory and Walker 1956)

Another counter-rotating streamwise vortex pair in the wake of the bluff front roughness is produced at the backward separation area, as shown by the white line in Fig. 2.11. Contrary to the rotating direction of the legs of the horseshoe vortices, this vortex pair induces a central upwash and lateral downwash motion. As a result, a low-speed region is produced close to the roughness symmetry plane (Joslin and Grosch 1995, Ergin and White 2006, Loiseau et al. 2014). The strength of the central vortex pair and low-speed region is highly related to the Reynolds number, aspect ratio and the geometry of the roughness element. The shear layer around the central low-speed region is prone to the growth of Kelvin-Helmholtz instability. Loiseau et al. (2014) claimed that the streamwise distance of the central low-speed region influences the dominant mode of instability leading to transition.

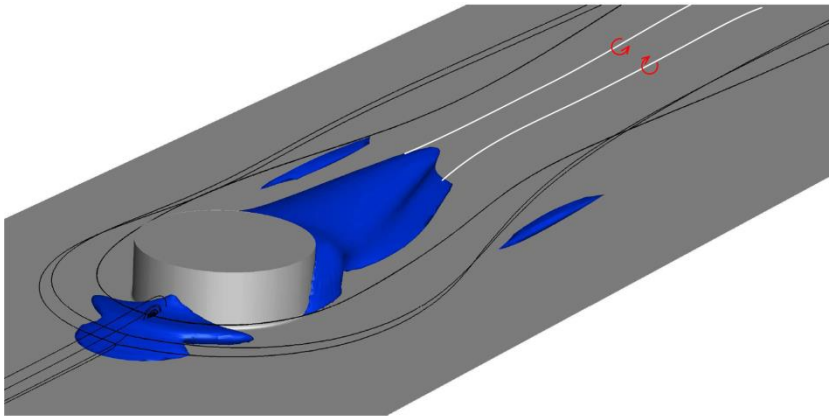


Fig. 2.11. Visualization of the vortical topology of the cylinder using streamlines, the upstream and downstream separation shown by blue iso-surfaces, redrawn from Loiseau et al. (2014).

2.4.1.2 Slender-front roughness

As no streamwise vortices originated from upstream horseshoe vortex system is produced, the vortical structures in the wake of slender-front roughness element are more compact.

Among the slender-front roughness, micro-ramp has received most attention as a vortex generator and it has demonstrated effectiveness in reducing flow separation caused by shock wave boundary layer interaction (SWBLI) (Dolling 2001, Babinsky et al. 2009, Giepman et al. 2014). Recent investigations have dealt with the flow topology over a micro-ramp immersed in supersonic turbulent boundary layers. Babinsky et al. (2009) studied the effect of ramp height and described a baseline surface flow topology. The wake consists of multiple counter rotating vortex pairs, including one dominant primary pair and several secondary pairs as shown in Fig. 2.12(a). The primary vortex pair ejects low momentum fluid away from the wall in the region around the symmetry plane and entrains high momentum fluid downwards from the sides, as shown in Fig. 2.12(b). In the later experimental study, Sun et al. (2012) visualized the full three-dimensional flow organization using tomographic PIV. Only the primary counter-rotating vortex pair was observed.

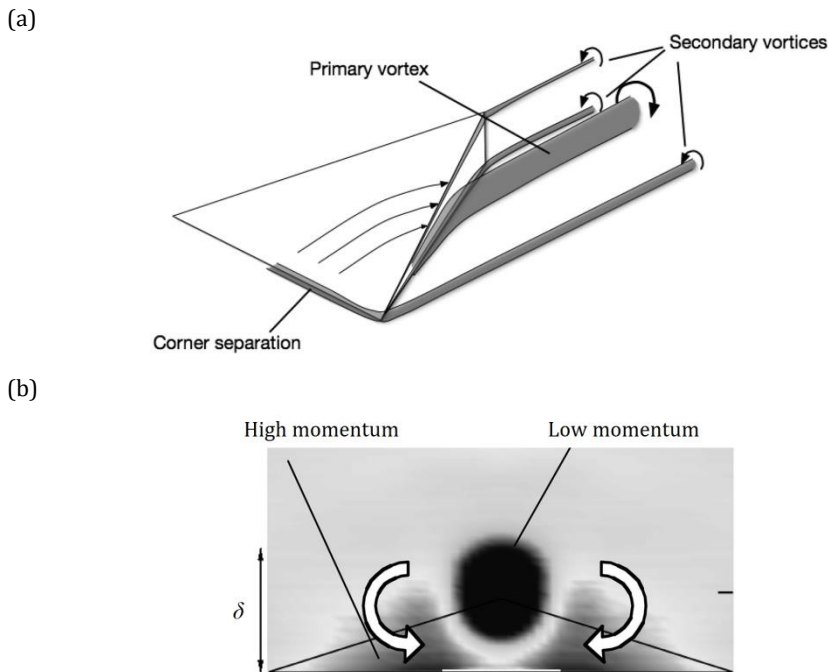


Fig. 2.12. Mean flow features around micro-ramp, (a) flow topology with primary and secondary vortices, (b) momentum transport effect of the streamwise vortices (Babinsky et al. 2009).

Similar vortical structures are detected in laminar flow regime, where the transition scenario is clearer. Choudhari et al. (2009) performed DNS investigation behind a micro-ramp with laminar incoming boundary layer at Mach 6 and observed similar velocity streak distribution in the wake. Tirtey et al. (2011) studied the transitional flow over micro-ramp in the hypersonic flow regime both numerically

and experimentally at the same Mach number, revealing the presence of two pairs of counter rotating vortices close to the symmetry plane. The secondary vortex structures were observed at the outer side of the primary vortices. The fast spreading behaviour of the secondary vortex pair downstream was conjectured to the onset of turbulent wedge (see Fig. 2.13).

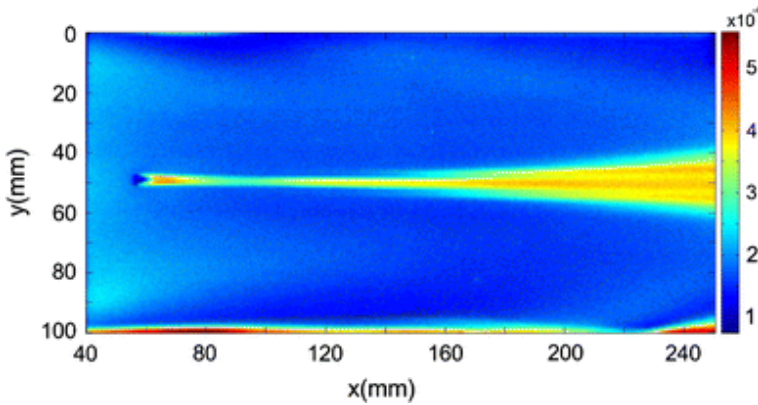


Fig. 2.13. Distribution of modified Stanton number around micro-ramp geometry (Tirtey et al. 2011).

2.4.2 Hairpin vortices and Kelvin-Helmholtz instability

In low-speed flows, the onset of hairpin-shape vortices shedding behind isolated roughness element has been generally associated to the process of early boundary layer transition (Acarlar and Smith 1987, Klebanoff et al. 1992, Ergin and White 2006). Acarlar and Smith (1987) characterized the shedding phenomenon and flow pattern in the separated shear layer behind a hemispherical element using flow visualization techniques and hot-film anemometry. The shedding of hairpin vortices occurs when Re_h is higher than 120. The formation of hairpins results from the lift-up of low momentum fluid behind the hemisphere, leading to inflectional velocity profile, which is favourable to the growth of Kelvin-Helmholtz instability. The development of the hairpin vortices at two streamwise stages is shown in Fig. 2.14, which moves away from the wall, being elongated and stretched when convecting downstream. The shedding phenomenon of the hairpin vortices is characterized by Strouhal number $St = fh/u_h$, where f is the shedding frequency. The Strouhal number increases from 0.05 to 0.2-0.4 with the rising of Re_h when $Re_h < 1200$. At sufficiently high Re_h , the hairpin vortices become unstable. Further increase of Re_h does not influence the Strouhal number. The boundary layer undergoes transition and breakdown to turbulence under the effect of shear layer instability. The Strouhal numbers obtained by Klebanoff et al. (1992) behind a hemisphere fall in the similar range. Besides, Klebanoff et al. (1992) found the boundary layer displacement thickness at the roughness location is a more appropriate characteristic length comparing with roughness height for Strouhal number. A linear

relation was obtained between vortex shedding frequency (f), displacement thickness at roughness location (δ^*) and velocity at roughness height (u_h) as

$$\frac{f\delta^*}{u_h} = \text{const} \quad (2.8)$$

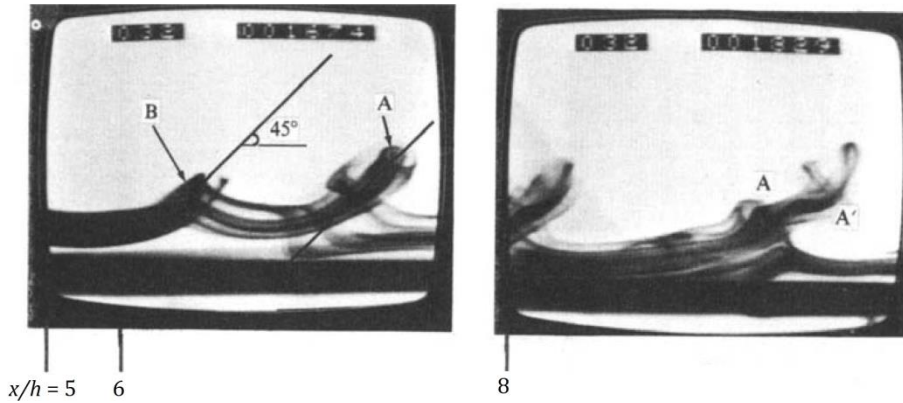


Fig. 2.14. Development of hairpin vortices in the near wake of hemisphere (Acarlar and Smith 1987).

The self-sustained vortex shedding was also observed in the wake of a cylinder by Choudhari and Fischer (2005) using numerical simulation. Furthermore, Ergin and White (2006) performed measurements in the wake of an array of cylinders by means of hot-wire anemometry for various Reynolds numbers. Due to the good agreement between the inflection point location in the velocity profile and the location of maximum velocity fluctuation intensity, they concluded that the velocity fluctuations leading to transition are ascribed to Kelvin-Helmholtz instability and associated hairpin vortex structures. Under the same flow condition as the experiment of Ergin and White (2006), the DNS analysis of the flow past a single cylinder performed by Rizzetta and Visbal (2007) indicates that the transition process is greatly influenced by hairpin vortex structure. The unstable shear layer is produced close to the roughness element, leading to the amplification of K-H instability. The hairpin rollers form at the separated shear layer, as shown in Fig. 2.15 by the isosurface of streamwise vorticity magnitude $|\omega_x|$. The hairpin vortices evolve from large-scale regular and periodical condition into a small-scale distributed and chaotic state, indicating the breakdown to turbulence.

In the stability analysis of Loiseau et al. (2014) and Cherubini et al. (2013), by superimposing the varicose type of disturbances to the mean flow field, the nonlinear evolution process is also featured by the birth of symmetric hairpin vortices. On the other hand, the occurrence of hairpin vortices induced by sinuous type disturbances is not general, as only being observed by Loiseau et al. (2014).

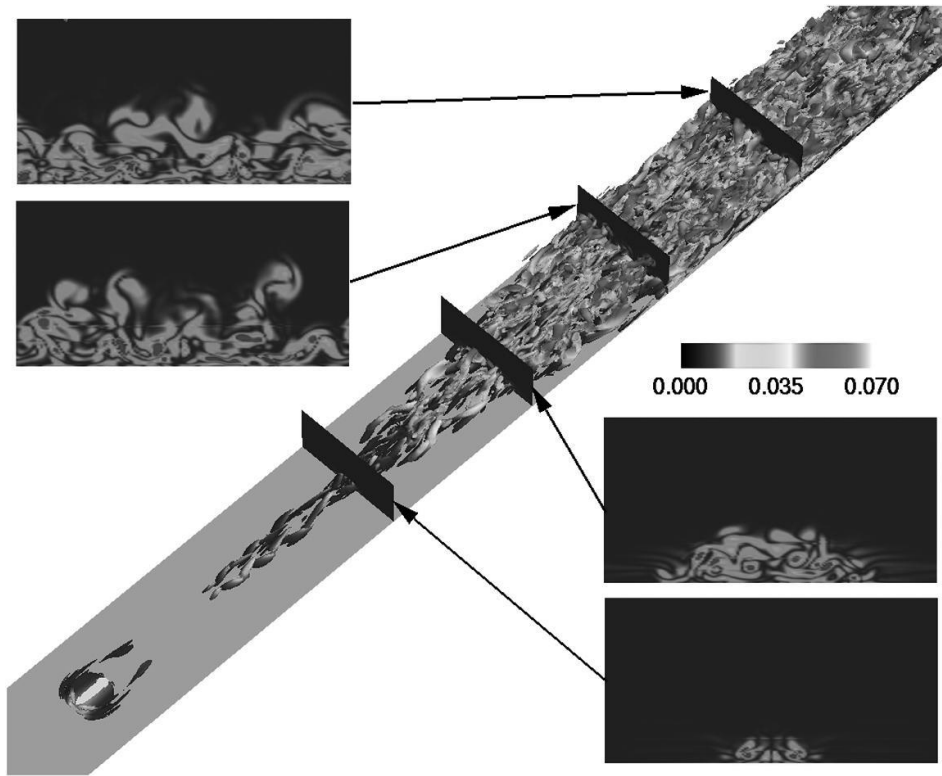


Fig. 2.15. Instantaneous wake flow behind cylinder at $Re_h = 334$, visualized by the isosurface and cross-sectional contour of streamwise vorticity magnitude $|\omega_x|$. (Rizzetta and Visbal 2007)

The relation between Kelvin-Helmholtz instability and boundary layer transition is also addressed in hypersonic boundary layer condition. In the recent DNS computations behind isolated roughness in hypersonic flow, such as hemisphere (Iyer and Mahesh 2013, Bernardini et al. 2014), cylinder (Subbareddy et al. 2014), cubic (Bernardini et al. 2012) and smooth bump (Redford et al. 2010), the formation of counter-rotating streamwise vortex pair close to the symmetry plane was observed, which perturb the steady shear flow in the wake of the roughness. The high magnitude perturbations induce the formation of hairpin vortices at different Mach number, as shown by the isosurface of swirling strength in Fig. 2.16. The vortex shedding phenomenon at the separated shear layer is again considered to be closely related to the transition mechanism.

However, the role of K-H instability and hairpin vortices on transition remains controversial. As discussed in sec. 2.3, the dominant instability mechanism strongly depends on Re_h . By varying Re_h , the streaky instability related to lateral shear layer of the flow can induce faster growth of disturbances comparing to K-H instability, reaching high disturbance amplitude, leading to boundary layer transition

(Choudhari et al. 2010, Kegerise et al. 2012, Loiseau et al. 2014). Further numerical or experimental evidence is necessary to understand the transition mechanism induced by isolated roughness.

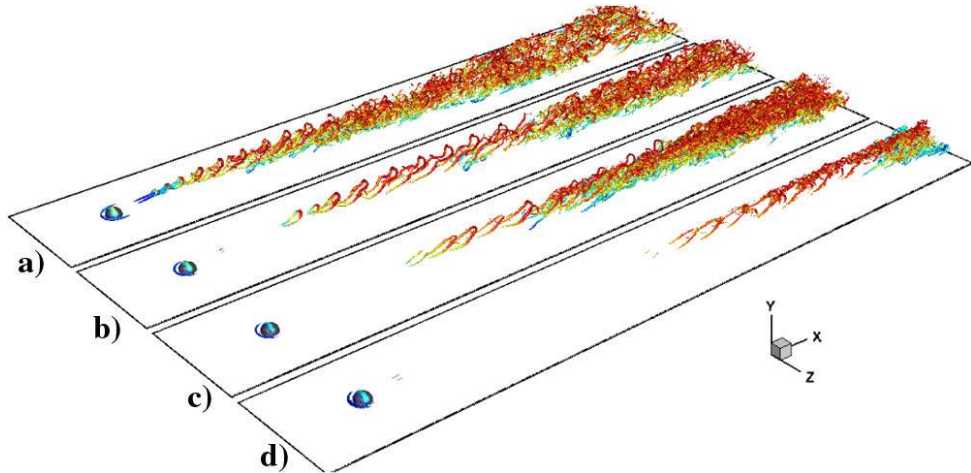


Fig. 2.16. The formation of hairpin vortices induced by hemisphere at various flow condition, visualizing by swirling strength, a) $Ma = 1.1$, b) $Ma = 2$, c) $Ma = 4$, d) $Ma = 6$. (Bernardini et al. 2014)

2.4.3 Turbulent wedge

The transition to turbulence is initiated by the formation and growth of localized turbulent regions. In the bypass transition process, when the flow is subject to high amplitude freestream disturbances, the localized turbulence appears in the form of turbulent spot (see Fig. 1.3). When transition is forced by an isolated roughness element, wedge shape turbulent region forms downstream, referred to as turbulent wedge. Turbulent wedge and spot share a lot of common features, as the global pattern of a train of spots follows a wedge shape (Henningson et al. 1987). The typical structure of the turbulent wedge is shown in Fig. 2.17. As proposed by Schubauer and Klebanoff (1956) and Zhong et al. (2003), the turbulent wedge consists of a fully turbulent core, bounded by an intermittent turbulent region. As shown by the hot-film measurement signal in Fig. 2.17, the turbulence level decreases when moving away from the symmetry plane of the wedge, approaching laminar condition near the edge. A widely accepted lateral spreading angle of turbulent wedge of 6.4° for fully turbulent core was reported by Schubauer and Klebanoff (1956) behind a spherical shape roughness element. The angle increases to 10.4° when taking the intermittent region into account. However, the spreading angle can vary due to the change of roughness geometry and Reynolds number (Zhong et al. 2003) which will be detailed in Chap. 5 and 6.

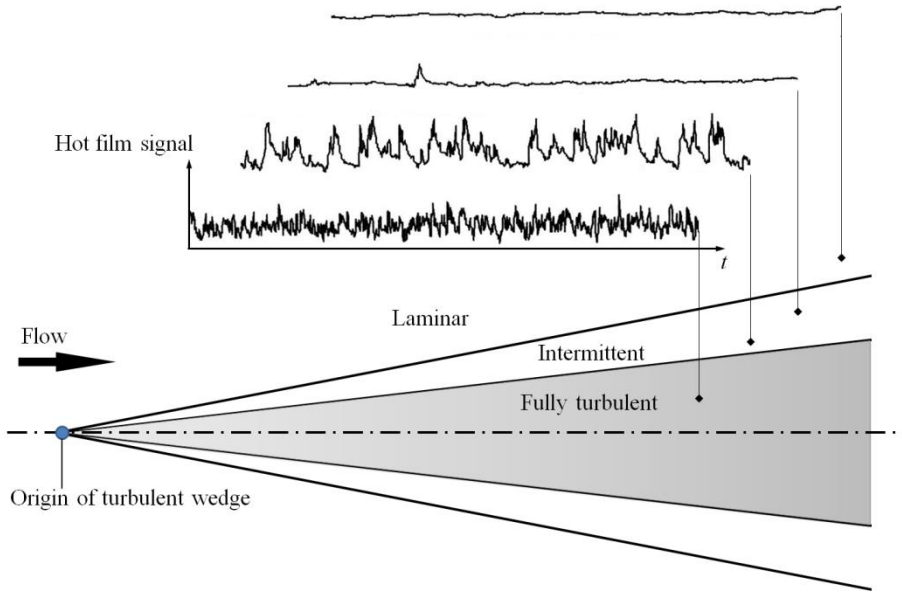


Fig. 2.17. Turbulent wedge structure, redrawn from Schubauer and Klebanoff (1956) and Zhong et al. (2003).

The growing and merging of the localized turbulent region complete the formation of fully turbulent boundary layer. Gad-El-Hak et al. (1981) studied the spanwise growth of turbulent wedge and spot using dye flow visualization. They found the spanwise propagation of localized turbulent region into undisturbed laminar boundary is caused by a destabilization process. The surrounding laminar flow breaks down through the strong disturbance produced by the turbulent region. This disturbance was hypothesised to associate with wake-like structures. In the later three dimensional investigations of the turbulent spot using DNS (Henningson et al. 1987, Singer and Joslin 1994, Singer 1996) and tomographic PIV (Schröder et al. 2008), the dominant vortex structure is identified to be hairpin-shape and quasi-streamwise vortices, as shown in Fig. 2.18. The destabilization process evolving the regeneration of hairpin vortices along the spanwise edge of the turbulent spot has been emphasized by many researchers (Krishnan and Sandham 2006, Redford et al. 2012, Brinkerhoff and Yaras 2014). The vortex tilting and stretching at the edge of the spot produces quasi-streamwise vortices, which induces sideward lift-up motion and is prone to the growth of inflectional instability. Besides the destabilization mechanism, Redford et al. (2012) suggested that the movement of the existing hairpin vortices in the spanwise direction through lateral ejection also assists the spreading of turbulent spot. Further quantitative experimental characterization of the spanwise growth mechanism of localized turbulent region is elaborated in the current research.

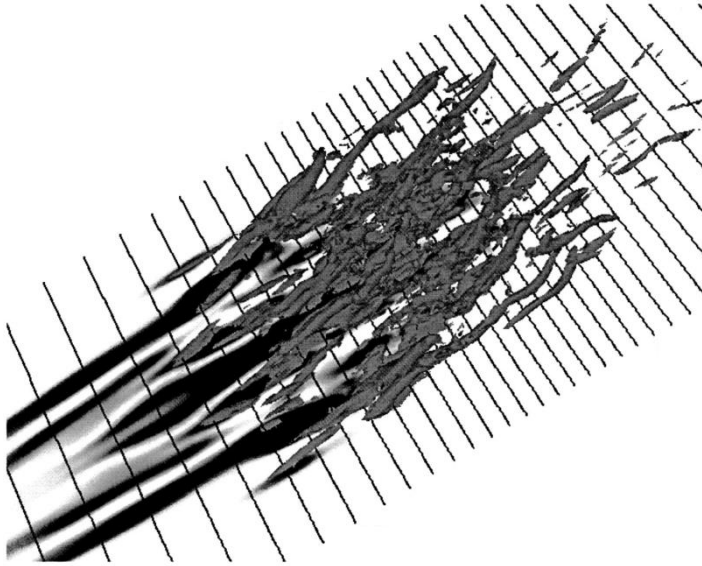


Fig. 2.18. Turbulent spot structure visualized by iso-surface of streamwise vorticity (Singer 1996).

2.5 Research questions and objectives

Despite the attention devoted to the topic, the physical mechanism of boundary layer transition induced by isolated roughness is still not fully understood. Although high fidelity numerical simulation gives an insight to the unstable vortical structures induced by isolated roughness element, the experimental studies that link the existence of streamwise vortices and hairpin vortices with the boundary layer instability are based either on two-dimensional flow visualization or statistical analysis from point-wise measurements. Therefore, more detailed experimental investigation is necessary to characterize the three-dimensional flow features behind isolated roughness, consolidating the understanding of transition process. Moreover, the aforementioned experimental studies mostly focus on the near wake region (within 20 micro-ramp heights), whereas the vortex evolution process leading to transition would require observations in the far wake, where the turbulent regime is established.

The main objective here is to identify transition process by detecting the three-dimensional unsteady wake. For this aim, tomographic particle image velocimetry is employed, as it is a volumetric measurement technique, which can describe the information of instantaneous velocity and vorticity field with high spatial resolution. The experiments are performed in the low-speed regime, where compressibility effect do not play a role and the topology of the flow can be studied in its details to determine the transitional flow pattern. This case, although simplistic, would represent the reference scenario for boundary layer transition induced by isolated roughness elements to which further studies in the compressible or turbulent regime

may refer. In particular, the study of the thesis is to answer the following important questions.

1. What is the main unstable flow feature developing the wake of roughness element?
2. Is it possible to identify the vortical structure which may contribute to the instability mechanism, leading to transition?
3. How does Reynolds number affect the transition process, especially flow feature and dominant instability mode?
4. What is the influence of roughness geometry on the wake flow topology and transition effectiveness?

In the current thesis, four different isolated roughness geometries (micro-ramp, cylinder, diamond, and hemisphere) are considered. The investigation starts from the supercritical Reynolds number ($Re_h = 1170$, Chap. 4 and 6), which decreases until reaching critical regime ($Re_h = 730$ and 460 , Chap. 5). The measurement domain covers a large streamwise range till the onset of the turbulent flow regime in order to follow the evolution of vortical structures along the complete transition process. The dynamic behaviour of the flow is investigated and related to transition mechanism. The influence of Reynolds number and roughness geometry is specified in Chap. 5 and 6.

3

Experimental techniques and arrangements

The experimental techniques used in the thesis are described in this chapter, starting with the specifications of the flow facility. The flow conditions of the research are introduced. A detailed description of the working principle of planar and tomographic particle image velocimetry is provided, following by the experimental arrangement. A large portion of material on particle image velocimetry is retrieved from the existing literature (Elsinga et al. 2006, Raffel et al. 2007, Scarano 2013). The uncertainty analysis of the measurement is provided. The chapter closes with the explanation on data reduction techniques associated to Proper Orthogonal Decomposition (POD) and the flow structure detection method.

3.1 Flow facility

The experiments were carried out in the low-speed open test section wind tunnel (W-tunnel) of the Aerodynamics Laboratories of the Aerospace Engineering Faculty at TU Delft, as shown in Fig. 3.1. The W-tunnel operates at room temperature and pressure. During operation, the flow passes through a plenum and centrifugal fan into the diffuser. After the settling chamber, the flow is accelerated in the nozzle with a contraction ratio of 9:1. The test section has an area of $0.4 \times 0.4 \text{m}^2$. The maximum operating velocity of the tunnel is 35m/s and the turbulence level in the freestream is below 0.5%.



Fig. 3.1. Photo of W-tunnel in the Aerodynamics Laboratories at TU Delft.

3.2 Wind tunnel model and flow conditions

In the experiment, an aluminium flat plate of 700mm long and 20mm thick was installed in the mid-plane of the test section of W-tunnel, spanning its entire width (400mm). The top view of the model arrangement is shown in Fig. 3.2. The plate was equipped with a modified super ellipse leading edge (Lin et al. 1992), with no

curvature discontinuity and preventing laminar flow separation. The plate terminates with a sharp trailing edge at a surface angle of 11.3° with respect to the freestream direction. The plate surface was covered by black-matt adhesive foil to reduce laser reflection during the tomographic PIV measurements. Details of the tomographic PIV will be discussed in sec. 3.6 and 3.7. The roughness elements were oriented along the centreline at $x_r = 290\text{mm}$ downstream from the leading edge. The origin of the coordinate system (O) is located at the wall, at the centre of the roughness elements (see Fig. 3.5). The coordinate axes x, y, z correspond to the streamwise, wall-normal and spanwise directions respectively. The measurement domain extends from 5mm to 150mm behind the roughness ($x/h = [2.5, 75]$).

The experiments are carried out at freestream velocity u_∞ of 10, 7 and 5m/s. At the roughness location, the undisturbed laminar boundary layer thickness (δ_{99}) is measured to be 3.26, 3.88 and 4.52mm respectively. The properties of the undisturbed boundary layer at the roughness location are summarized in Tab. 3.1.

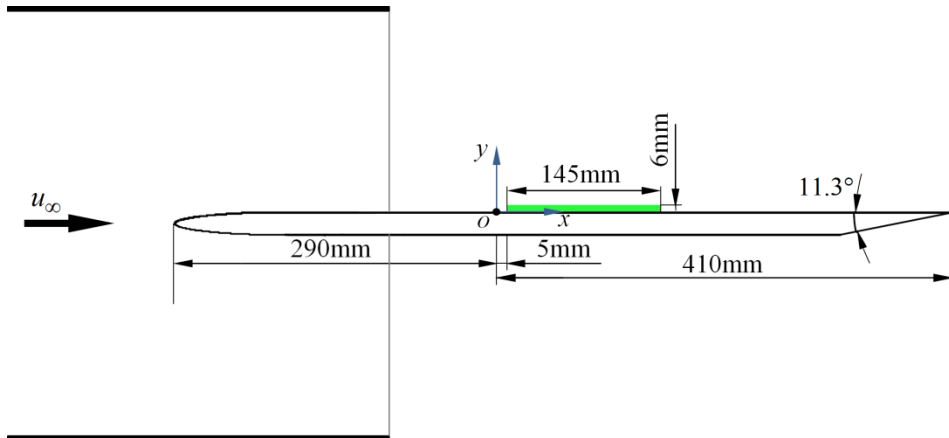


Fig. 3.2. Schematic of model arrangement from the top view.

Tab. 3.1. Incoming flow conditions.

| $u_\infty(\text{m/s})$ | 10 | 7 | 5 |
|--------------------------|--------------------|--------------------|--------------------|
| $\delta_{99}(\text{mm})$ | 3.26 | 3.88 | 4.52 |
| $\delta^*(\text{mm})$ | 1.14 | 1.38 | 1.63 |
| $\theta(\text{mm})$ | 0.44 | 0.53 | 0.62 |
| H | 2.59 | 2.61 | 2.64 |
| Re_x | 2.13×10^5 | 1.50×10^5 | 1.06×10^5 |
| Re_θ | 302 | 258 | 214 |

3.3 Laminar boundary layer characterization

The boundary layer developing along the flat plate without the roughness element is characterized by its velocity profile obtained from an average of 200 uncorrelated tomographic PIV measurement samples. The results are analysed at the most downstream location of the measurement domain $x/h = 70$ (430mm from the leading edge) in order to verify that the boundary layer develops in the laminar regime along the entire domain of interest. The velocity profile is compared with the theoretical solution based on Blasius self-similarity (White and Corfield 2006), yielding a good agreement, which confirms the laminar regime of the undisturbed boundary layer (see Fig. 3.3). Near the wall ($\eta < 0.1$) the measured velocity profile deviates from the theoretical result due to the limited spatial resolution (Kähler et al. 2012). The RMS fluctuations of the streamwise velocity component do not exceed 2% of the freestream velocity, which also gives an indication of the current measurement noise level. The shape factor along the range of $x/h = [-5, 75]$ reveals a relative constant value of 2.59 ± 0.05 along the measurement domain (see Fig. 3.4), indicating a laminar regime of the flow.

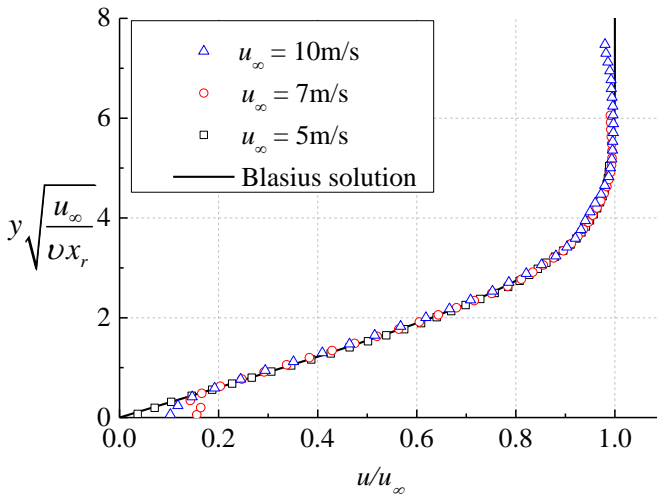


Fig. 3.3. Undisturbed boundary layer at $x/h = 70$ (430mm from the leading edge) and comparison with Blasius solution.

3.4 Roughness geometry

Four roughness geometries were used in the thesis, including micro-ramp, cylinder, diamond and hemisphere, with a height (h) of 2mm and span width (c) of 4mm, as schematically shown in Fig. 3.5. The length (l) of micro-ramp was 4.5mm, resulting in an incidence angle (β) and half sweep angle (α) of 24° . The geometry of the micro-ramp follows the optimization study by Anderson et al. (2006) and is one of the most reported in the literature (Babinsky et al. 2009, Herges et al. 2010, Sun et

al. 2012, Giepman et al. 2014). The corresponding roughness-height based Reynolds number ($Re_h = u_h \times h / \nu$) is 1170, 730 and 460, respectively. The resulting ratio between roughness height and boundary layer thickness is $h/\delta = 0.44, 0.52$ and 0.62 . Based on the roughness aspect ratio (c/h) of 2, the critical Re_h ranges from 455 to 682, indicating critical and supercritical conditions for the current experiments (Klebanoff et al. 1955, Von Doenhoff and Braslow 1961). The roughness related properties are summarized in Tab. 3.2.

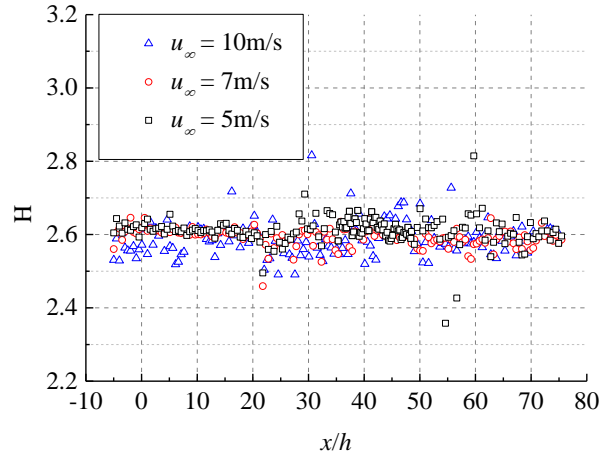


Fig. 3.4. Streamwise evolution of the shape factor at all flow conditions.

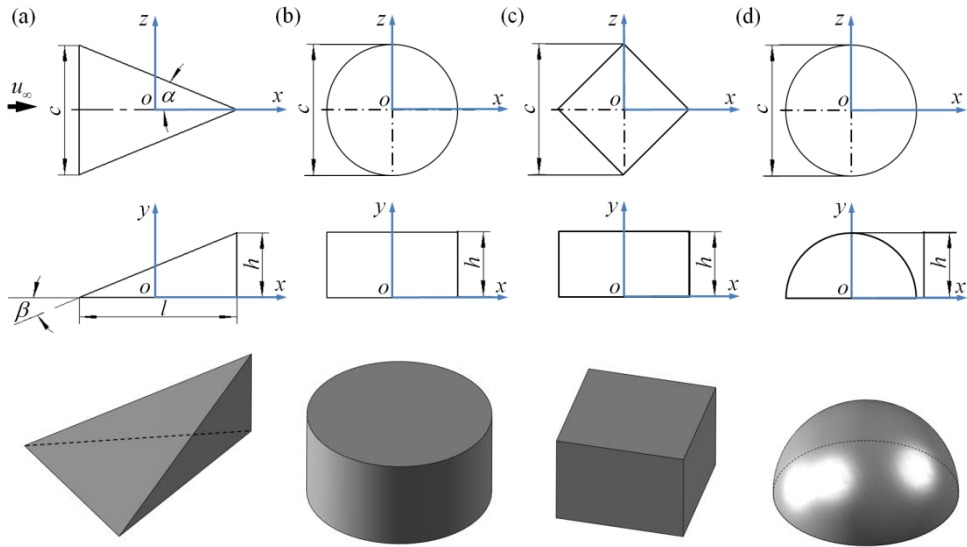


Fig. 3.5. Geometry of the roughness elements, top and side view, (a) micro-ramp, (b) cylinder, (c) diamond, (d) hemisphere, $h = 2\text{mm}$, $c = 4\text{mm}$, $\alpha = \beta = 24^\circ$.

Tab. 3.2. Roughness properties.

| u_∞ (m/s) | 10 | 7 | 5 |
|------------------|------|------|------|
| h/δ | 0.61 | 0.52 | 0.44 |
| Re_h | 1170 | 730 | 460 |

3.5 Particle image velocimetry

Particle image velocimetry is a non-intrusive technique being able to measure the instantaneous velocity field of the flow. The principal of PIV is based on tracking the movement of small particles immersed in fluid. The tracer particles are illuminated by a pulsed light source (typically laser) within a thin light sheet for two times with short separation Δt . The light scattered by the particles at each illumination is recorded in two sequential image frames by a charge couple device (CCD). The typical experimental arrangement of PIV is shown in Fig. 3.6, reproduced from Raffel et al. (2007).

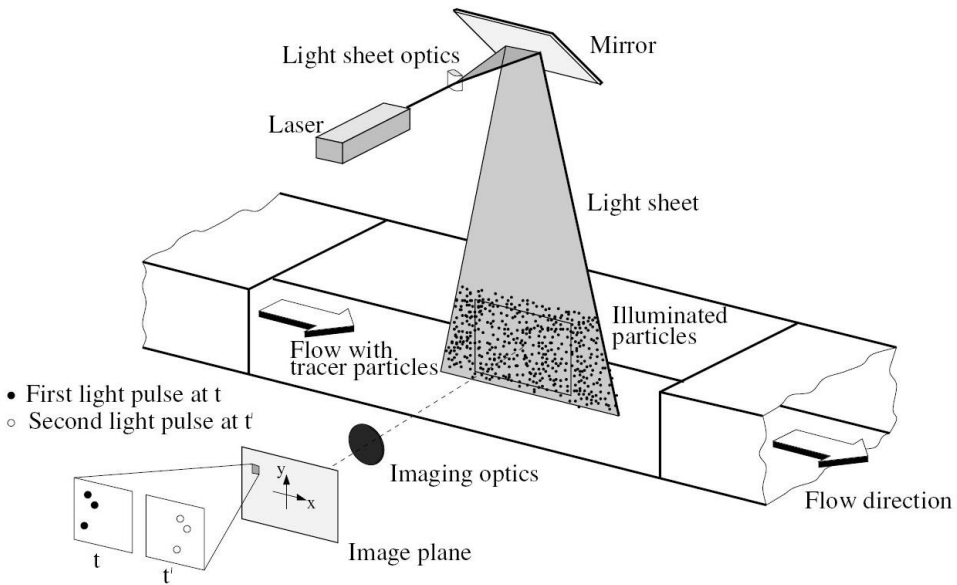


Fig. 3.6. Typical planar PIV arrangement (Raffel et al. 2007).

The velocity of the flow $u_f(x,t)$ is measured indirectly by the particle displacement $\Delta x(x,t)$ in a finite time separation $\Delta t = t_2 - t_1$ between the laser pulses as (Westerweel 1997):

$$\Delta x(x, t_1, t_2) = \int_{t_1}^{t_2} u_p(x, t) dt \tag{3.1}$$

where $u_p(x,t)$ is the particle velocity, which can be obtained by the first order term of the Taylor expansion of equation (3.1) as

$$u_p(x,t_0) = \lim_{\Delta t \rightarrow 0} \frac{\Delta x(x,t_1,t_2)}{\Delta t} \cong \frac{\Delta x(x,t_1,t_2)}{\Delta t} = \frac{x(t_2) - x(t_1)}{\Delta t} \quad (3.2)$$

The particle velocity $u_p(x,t)$ should be identical to the fluid velocity $u_f(x,t)$ for the ideal tracers. However, in practice, the tracer particles always have a velocity slip comparing with the surrounding fluid. The associated error is usually negligible. In addition, the displacement obtained from equation (3.1) only provides the average velocity along the trajectory over the separation time.

3.5.1 Tracer particle

The fidelity of PIV measurement requires the tracer particle to accurately follow the motion of the fluid and not change the fluid properties. Moreover, the particle should also scatter sufficient light to be distinguished from the image background. As a result, a correct choice of seeding size and material is critical and requires the knowledge of the mechanical properties of small particles immersed in fluid flows.

The small particle is modelled as a sphere with a diameter of d_p . The dynamics of the particle is dominated by the Stokes drag (Melling 1997). The external forces, such as gravitational and electrostatic forces, can be considered negligible. The velocity difference (u_s , slip velocity) between the particle and the fluid can be estimated as (Raffel et al. 2007),

$$u_s = u_p - u_f = d_p^2 \frac{(\rho_p - \rho_f)}{18\mu} \frac{du_p}{dt} \quad (3.3)$$

where μ is the fluid dynamic viscosity, ρ_p and ρ_f are the density of particles and fluid respectively. From equation (3.3), one can find the accurate tracking can only be achieved when particles reach the neutral buoyant condition, $(\rho_p - \rho_f)/\rho_f \ll 1$. In liquid flow, finding particles with matching density is not hard. On the other hand, in the gas flow, the neutral buoyant condition is not possible to be achieved as the typical level of density ratio is in the order of $O(10^3)$.

The response of the particle velocity follows the exponential law of decaying process when the density ratio is large, as

$$u_p = u_f [1 - e^{(-t/\tau_p)}] \quad (3.4)$$

where the relaxation time τ_p is defined as

$$\tau_p = d_p^2 \frac{\rho_p}{18\mu} \quad (3.5)$$

Low relaxation time is always desired in order to have the particles tracking the flow faithfully. As a result, particles with low density and small diameter are usually implemented in the PIV measurement. The tracer particle fidelity is quantitatively assessed by particle Stokes number S_k , defining as the ratio between particle relaxation time and characterization time of the flow, as

$$S_k = \tau_p / \tau_f \quad (3.6)$$

When $S_k < 0.1$, an acceptable tracing accuracy of error lower than 1% is obtained (Samimy and Lele 1991). In the gas flow experiment at low speed, the oil droplets have been widely used as tracer particles, which have the non-toxic character. For a common used oil of $1\mu\text{m}$ diameter and 10^3kg/m^3 density under current experiment conditions, the Stokes number yields the order of 10^{-2} , considering suitable for the PIV measurement.

3.5.2 Particle imaging

When viewing the illuminated particle (considered as a distance point source) through an aberration-free lens mounted on the camera, the particle does not appears as a point, but forms a Fraunhofer diffraction pattern with a circular disk shape, which is known as Airy disk. The particle image diameter is determined by the first zero of the Airy function. The particle imaging system is featured by the objective focal length f , the ratio between the focal length and the length aperture diameter $f_\#$, and the image magnification factor M . The focus criterion of the lens is

$$\frac{1}{f} = \frac{1}{d_i} + \frac{1}{d_o} \quad (3.7)$$

where d_o is object distance and d_i is image distance, as shown schematically in Fig. 3.7. The magnification factor M is defined as,

$$M = \frac{d_i}{d_o} \quad (3.8)$$

The diffracted minimum image diameter is given by

$$d_{diff} = 2.44\lambda(1+M)f_\# \quad (3.9)$$

If the lens aberration can be neglected, the particle image diameter can be estimated by

$$d_\tau = \sqrt{(Md_p)^2 + (d_{diff})^2} \quad (3.10)$$

where Md_p is the particle image geometric diameter. Note that for typical optical parameters in PIV, d_{diff} is significantly larger than Md_p . Therefore, the diffraction limit dominates the particle image diameter, which remains constant despite the change in d_p . Nevertheless, one should keep in mind that the particle image intensity I strongly depends on d_p , as $I \propto d_p^2$.

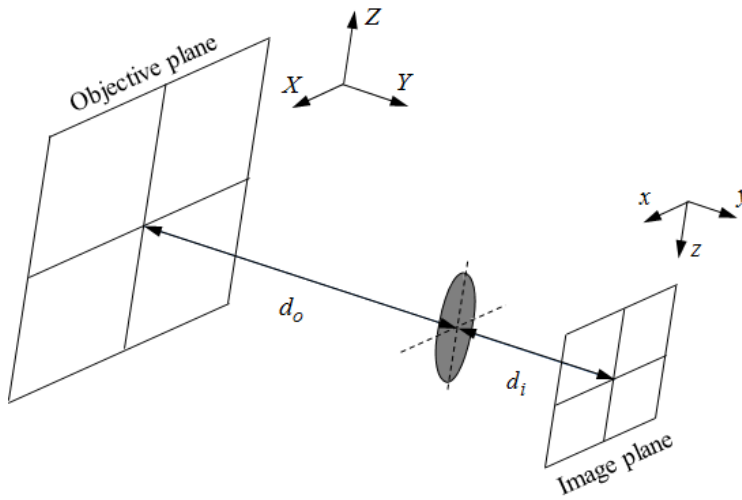


Fig. 3.7. Optical arrangement of the PIV image system.

Considering the sampling theory, one requirement is that particle image diameter d_τ should not be smaller than the sensor's pixel size. When the particle image diameter is smaller than the pixel size, the particles are under-sampled. As the particles are imaged as discrete pixels, the accuracy of the particle motion estimation will be limited to pixel level, leading to the displacement error up to 0.5pixels. The particle position information and its light distribution are irreversibly lost. The condition is referred to as *peak locking* (Westerweel 1997). In order to avoid peak locking error, the particle image diameter can be modified to the optimum size of 2-3pixels by changing $f_\#$ (see equation (3.9)). The example of recorded particle image in the current experiment is shown in Fig. 3.8.

Besides, $f_\#$ also determines the focal depth δz , representing the volume thickness in which the particles are in focus, given by

$$\delta z = 4.88\lambda f_{\#}^2 \left(\frac{M+1}{M} \right)^2 \tag{3.11}$$

To make all the illuminated particles in proper focus, the focal depth should be at least equal the laser sheet thickness.

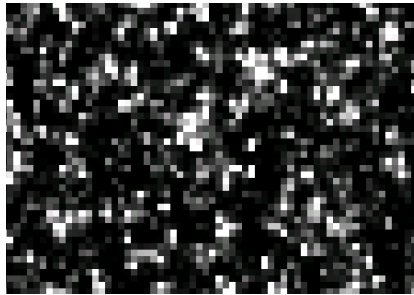


Fig. 3.8. Recorded particle image at optimum size of 2-3pixels using LaVision pro LX.

3.5.3 Image analysis

In the acquired particle images, the instantaneous locations of the tracer particles are shown as distinct peaks of light intensity. The original image is divided into small cells (interrogation window), spaced regularly. Each interrogation window contains a number of particles (typically 10-20). The averaged particle displacement of one interrogation window is evaluated by the cross-correlation technique, which finds the degree of matching between the particles of two image frames at t and $t+\Delta t$ based on the pixel intensity level. The cross-correlation procedure is shown in Fig. 3.9, reproduced from Raffel et al. (2007).

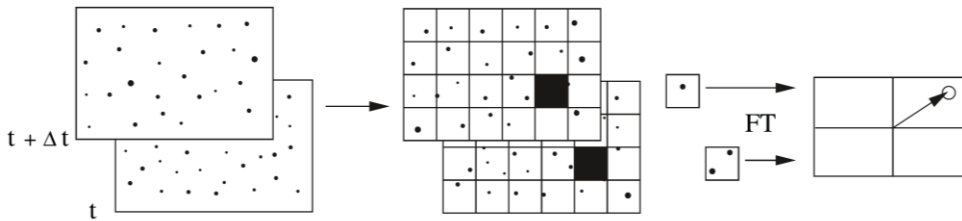


Fig. 3.9. Procedure of digital PIV cross-correlation (Raffel et al. 2007).

The light intensity distribution at each interrogation window is defined as $I_1(i, j)$ and $I_2(i, j)$ at t and $t+\Delta t$. i and j represent the pixel location. The product of the overlapping light intensities at each spatial shift $(\delta x, \delta y)$ are summed up through

$$C(\delta x, \delta y) = \sum_{i=0}^M \sum_{j=0}^N [I_1(i, j) - \bar{I}_1][I_2(i + \delta x, j + \delta y) - \bar{I}_2] \quad (3.12)$$

where \bar{I}_1 and \bar{I}_2 are the average intensity I_1 and I_2 . $M \times N$ is the size of the interrogation area. The correlation function is normalized using intensity standard deviation of each window,

$$c(\delta x, \delta y) = \frac{C(\delta x, \delta y)}{\sqrt{\sigma_1} \sqrt{\sigma_2}} \quad (3.13)$$

where

$$\sigma(x, y) = \sum_{i=0}^M \sum_{j=0}^N [I(i, j) - \bar{I}]^2 \quad (3.14)$$

The largest peak in the correlation map represents the most probable displacement within each interrogation window. With knowledge of the time separation Δt , the velocity vector field can then be determined.

3.6 Tomographic PIV

Despite the successful development of conventional particle image velocimetry, only two (planar) or three (stereoscopy) velocity components within a two-dimensional measurement plane can be captured. In order to overcome the measurement limitation and to capture 3D instantaneous flow field, tomographic particle image velocimetry is developed by Elsinga et al. (2006) as a novel 3D measurement technique based on the principles of optical tomography, enabling the understanding of unsteady coherent structures. The tomography concept has been widely used in medical imaging such as CT scan, in which the sectional images are taken through a body by the moving X-ray source.

3.6.1 Working principle

In the tomographic PIV measurement system, as shown in Fig. 3.10, tracer particle are dispersed and illuminated in a measurement volume for two sequence times by a pulsed light source. The volume light is usually generated by expanding the thickness of the laser sheet using cylindrical optical lens. The light scattered by the particles is recorded by several CCD cameras (usually 3-6) simultaneously, viewing the field of view from different directions. In order to keep all the particles within the illuminated volume in focus, longer focal depth δz needs to be obtained by decreasing the aperture of the objective lens, until the focal depth slightly exceed the level of laser sheet thickness. Furthermore, cameras are complied with the Scheimflug adapters to align the focus plane with the mid-objective plane, decreasing

the required focal depth δz . As the light intensity is inversely proportional to the light sheet thickness and the light captured by the camera sensor is proportional to the aperture area, a strong signal reduction occurs with the increase of volume thickness, limiting the possible scale of the measurement volume.

The 3D particle distribution in the objective space is reconstructed as a 3D light intensity distribution from its projection on the camera sensor using multiplicative algebraic reconstruction technique (MART). The particle motion is analysed by the 3d cross-correlation algorithm, using iterative multigrid window (volume) deformation technique (Scarano and Riethmuller 2000).

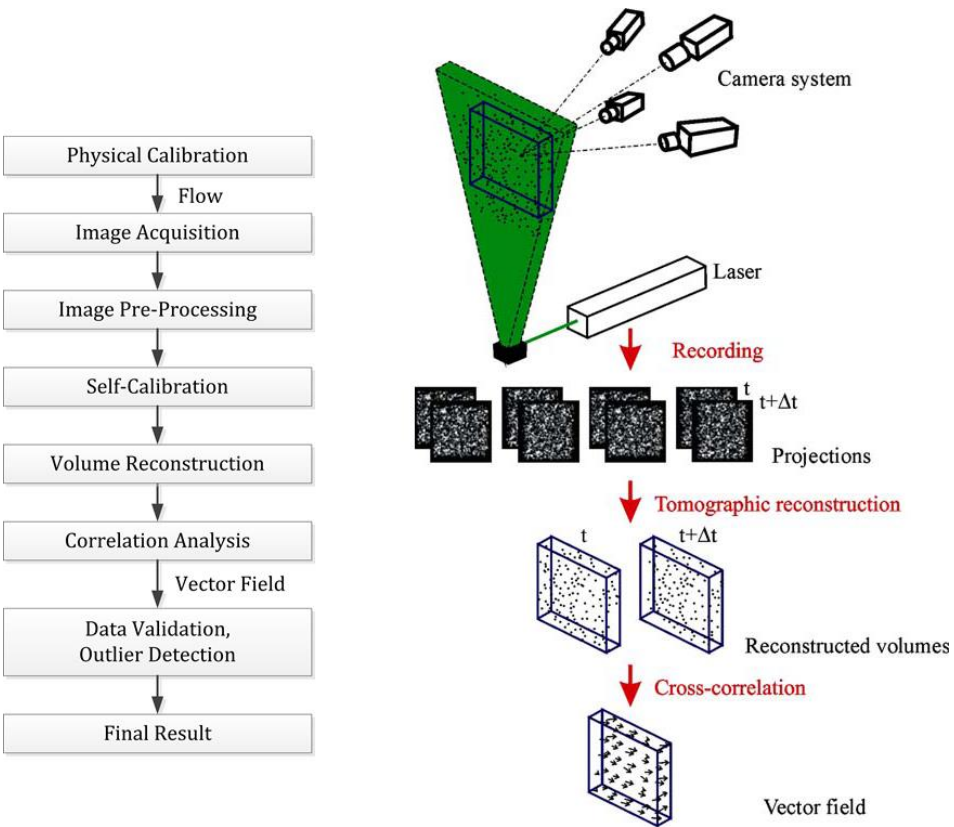


Fig. 3.10. Working principal of tomographic PIV, left: flow chart of the experimental procedure, adapted from Lynch (2015), right: schematic illustration of experimental setup and procedure reproduced from Elsinga et al. (2006)

3.6.2 System calibration

In the tomographic PIV experiment, the relation between the 3D objective space (x, y, z) and the image coordinates (x', y') is established by the calibration procedure.

As the tomographic reconstruction quality relies on the accurate triangulation between the physical space and image planes, high precision calibration is required. The tomographic PIV calibration typically consists of two steps: physical calibration and self-calibration, similar to that of stereoscopic PIV.

A calibration target with dots or crosses on a regular grid is used in physical calibration. The calibration target can be either 2D, as the crosses and dots locates at a single plane, or 3D, which has two planes with known distance in the volume depth direction. The calibration target is recorded by each camera at 2 to 9 positions through the measurement volume depth. The most popular type of physical calibration is to fix the calibration target on a translation unit, obtaining coplanar equal distance views, as shown in Fig. 3.11. The mapping function between the physical space and image space can be obtained by either pinhole model (Tsai 1987) or third-order polynomial model (Soloff et al. 1997). The later model has better performance under optical distortions conditions, which is selected in the following experiment.

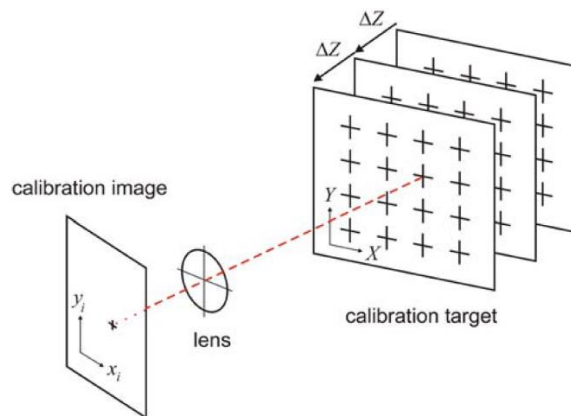


Fig. 3.11. Schematic illustration of multi-plane physical calibration (Elsinga 2008).

After the initial establishment of the calibration mapping function, further correction procedure is needed to reduce the misalignment of the lines of sight from each camera. The error of physical calibration can exceed 1pixel due to the inaccurate calibration caused by limited number of markers, incorrect volume depth transformation, slight movement of the cameras caused by the time different between physical calibration and image acquisition, or even the aero-optical distortions. The volume self-calibration procedure proposed by Wieneke (2008) can detect and correct the calibration misalignment to less than 0.1pixel. The former procedure is based on the triangulation of 2D particle positions recorded by each camera to 3D particle locations. For each detected particle in 3D space, if the lines of sight of all the cameras intersect in a point, the mapping function is accurate resulting in a zero disparity, $d_i = (d_{ix}, d_{iy}) = (x'_i, y'_i) - (x_i, y_i)$ (see Fig. 3.12). When the

mapping function is not perfect, the disparity map is generated by detecting the most probable disparity vector to correct the mapping function and minimize the disparity distance $|(x_i', y_i') - (x_i, y_i)|$. Iterative self-calibration procedure can be performed until reaching the required accuracy of volume reconstruction. In the current experiment, the calibration error decreases from 0.5pixel to 0.05 after self-calibration, as shown in the disparity vector in Fig. 3.13.

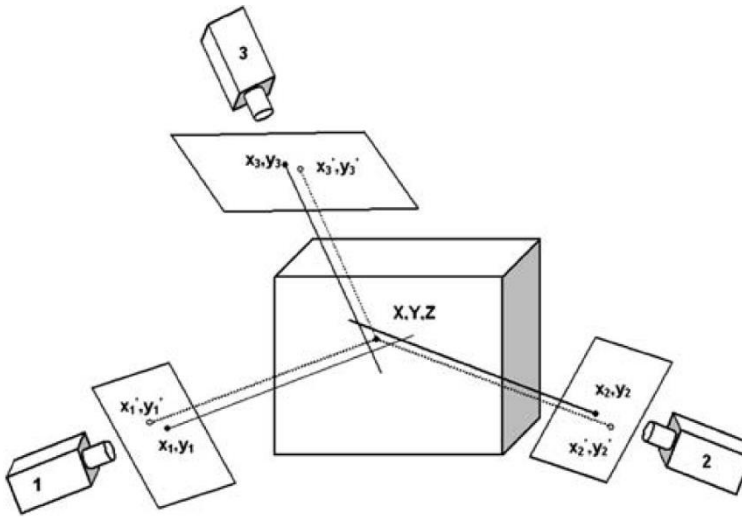


Fig. 3.12. Triangulation disparities due to calibration errors (Wieneke 2008).

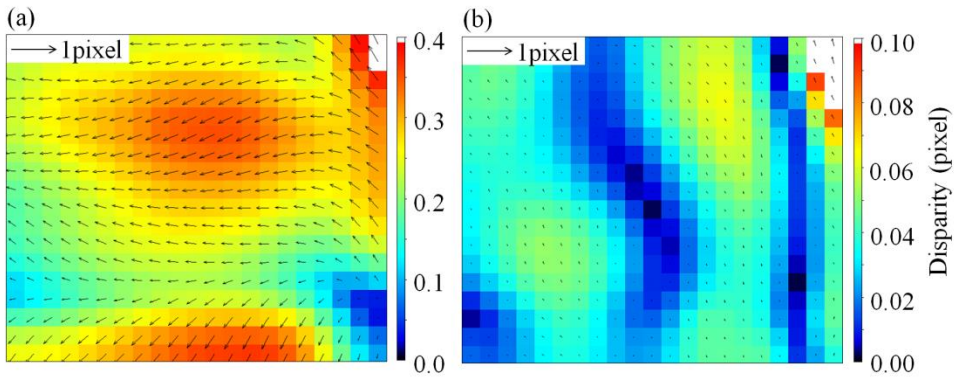


Fig. 3.13. Disparity vector of volume self-calibration for the initial (a) and final step (b).

3.6.3 Volume reconstruction

Using the mapping function between the physical space and image planes, the 3D intensity distribution $E(X, Y, Z)$ in the discretized cubic voxel elements can be

obtained. The projection of the light intensity $E(X, Y, Z)$ on each image pixel (x_i, y_i) returns the image light intensity distribution $I(x_i, y_i)$ of each camera. A linear relation between E and I is given by

$$\sum_{j \in N_i} w_{i,j} E(X_j, Y_j, Z_j) = I(x_i, y_i) \quad (3.15)$$

where i and j represent the number index of pixels in the image field and voxels in the objective space. $w_{i,j}$ is the weighting coefficient indicating the contribution of j th voxel intensity to i th pixel intensity. N_i is the number of voxels intersecting with the line of sight of pixel i , shown by the shaded area in Fig. 3.14. The weighting function $w_{i,j}$ ranges from 0 to 1, depending on the intersected volume between the pyramid from the pixel in the direction of line of sight and the cubic voxel, and the distance from the voxel centre to the line of sight, illustrated in Fig. 3.14. The calculation of the intersection between pyramid and cubic is challenging. For the ease of practical application, the estimation is performed based on the assumption that the line of sight is cylinder and the voxel is sphere.

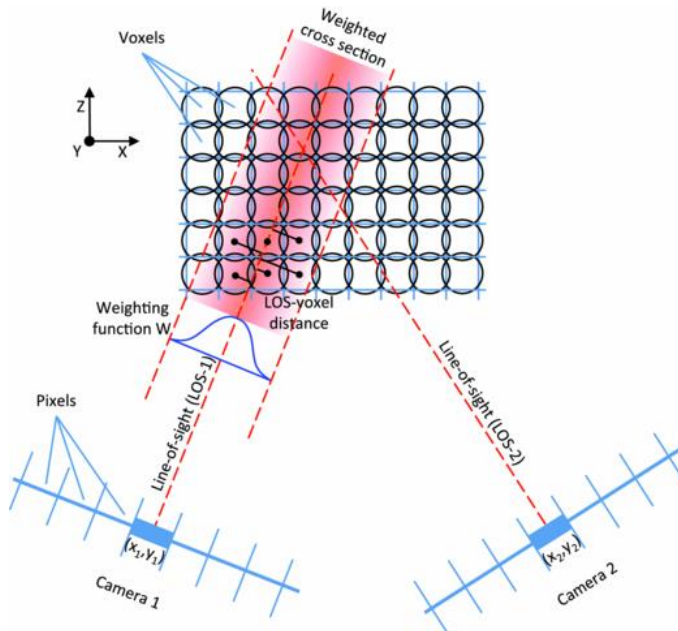


Fig. 3.14. Schematic representation of the image model of tomographic reconstruction, viewing from the top, cylinder shape line of sight and sphere voxel shape, voxels fall in the shaded area has a non-zero weighting coefficient $w_{i,j}$. (Scarano 2013)

To solve equation (3.15), an iterative reconstruction technique MART (Herman and Lent 1976) is employed. Elsinga et al. (2006) proved that MART algorithm is a

suitable approach for tomographic PIV images, which later becomes widely applied. The MART algorithm starts the operation with an initial guess of $E(X, Y, Z)^0$ and updates $E(X, Y, Z)$ based on the ratio between the measured image pixel intensity and the projection from objective voxel intensity as

$$E(X_j, Y_j, Z_j)^{k+1} = E(X_j, Y_j, Z_j)^k \left(\frac{I(x_i, y_i)}{\sum_{j \in N_i} w_{i,j} E(X_j, Y_j, Z_j)} \right)^{\mu w_{i,j}} \quad (3.16)$$

where μ is a scalar relaxation parameter with a value smaller than one. It is ensured by the exponent that only the elements in $E(X, Y, Z)$ affecting the i th pixel are updated. Moreover, another requirement of the multiplicative MART scheme is that E and I are definite positive. The iterative loop ends when reaching convergence.

Besides the calibration accuracy, the tomographic reconstruction quality is also influenced by many other factors, including particle density, camera arrangement, the maximum camera aperture and the number of cameras (Elsinga et al. 2006). A synthetic review on the aforementioned dependence factors is given by Scarano (2013).

3.7 Experiment arrangement

3.7.1 Tomographic PIV setup

Tomographic particle image velocimetry was adopted in the present investigation for its ability to describe the instantaneous three-dimensional distribution of velocity and vorticity.

The flow was seeded with a SAFEX fog machine, which generates water-glycol droplets of approximately $1\mu\text{m}$ diameter. The particle concentration was carefully adjusted at approximately 4 particles/ mm^3 . Pulsed illumination is obtained with a *Quantel CFR PIV-200* Nd: YAG laser (200mJ/pulse, 532nm wavelength, 9ns pulse duration). The pulse separation time was set to 30, 43 and 60 μs , corresponding to the freestream velocity of 10, 7 and 5m/s. The resulted particle displacement is 10pixels in the freestream at all flow conditions. An array of four LaVision Imager Pro LX interline CCD cameras (4872 \times 3248pixels, 7.4 μm /pixel) was arranged subtending an arc to simultaneously record the images of the light scattered by the tracers in the illuminated region, as shown in Fig. 3.15. Although a linear arrangement of viewing directions yields lower reconstruction accuracy in comparison to a 2D camera arrangement (Scarano 2013), the current choice of a maximum aperture angle of $\beta = 60^\circ$ mitigates this disadvantage and returns a reconstruction quality comparable to that obtained subtending a solid angle. Each camera was equipped with an objective of 105mm focal length mounted at an angle to comply with the Scheimpflug condition (Prasad and Jensen 1995). The numerical aperture was set to $f_\# = 11$, resulting in a focal depth of 8.4mm. The sensor was

cropped in the vertical direction resulting in an active sensor region of 4872×1500 pixels. The corresponding measurement volume size is $145(x) \times 6(y) \times 45(z)$ mm³ ($72.5h \times 3h \times 23h$). The resulting digital image resolution is 33.6 pixels/mm corresponding to 35.4 voxels/mm in the object space. The wall-normal depth of illumination was ranging from the wall to three ramp-heights ($y/h = [0, 3]$), which is sufficient to encompass the boundary layer thickness at the roughness position. The dataset consists of 200 snapshots acquired at 1.5 Hz rate. The measurement parameters are summarized in Tab. 3.3.

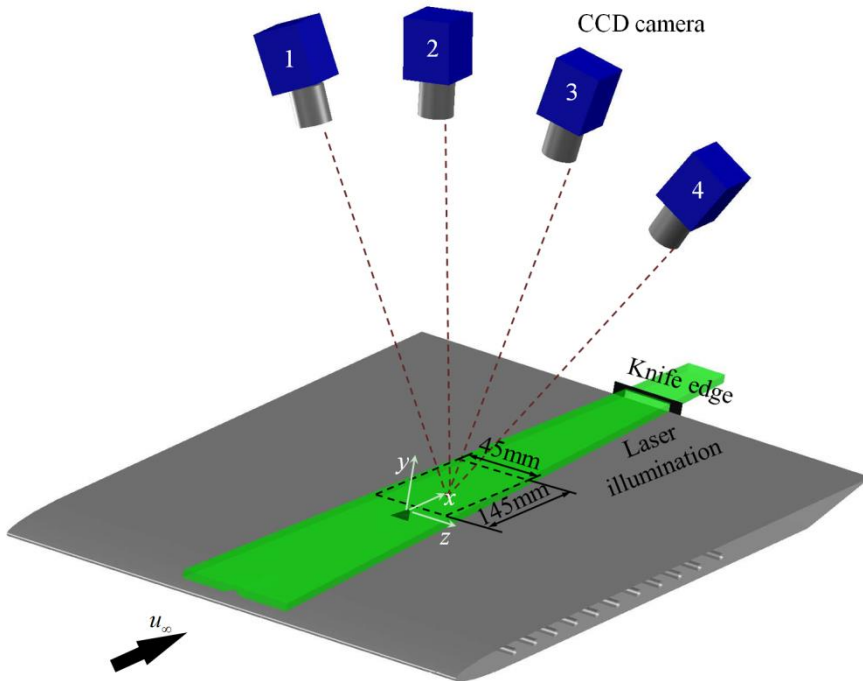


Fig. 3.15. Schematic illustration of experimental configuration and tomographic PIV setup.

3.7.2 Data analysis

System synchronization, data acquisition and processing were performed using LaVision Davis 8 software. The 3D physical calibration of the tomographic image was performed to establish the relation between the three-dimensional domain (object space) and its projection onto the camera sensor (image space). The space mapping is based on third order polynomial functions and the coefficients are obtained with a calibration target translated along the wall-normal direction at three positions with 1 mm interval. After the experiment, it was found that the coordinate system associated to the calibration was slightly rotated with respect to the model surface

by an angle of less than 1° along the x axis. Such misalignment was corrected by applying a rotation to the 3D calibration coordinate system with a custom built in procedure in Davis 8. The resulting measurement grid was realigned to the model system of coordinates to within 0.1° . After the physical calibration, volume self-calibration (Wieneke 2008) is used to reduce the residual calibration disparity to less than 0.1pixels. In order to further optimize the quality of the particle recordings, the raw images were pre-processed by subtracting the time-minimum intensity at each pixel, and subtracting the local minimum calculated on a kernel of 31×31 pixels. Finally, the intensity is normalized over the entire field of view and among different cameras using the local average over a kernel of 51×51 pixels. The measurement volume was reconstructed by using the CSMART algorithm which is similar to SMART (simultaneous implementation of multiplicative algebraic reconstruction techniques) (Atkinson and Soria 2009), but with reduced reconstruction time compared with conventional MART. The light intensity profile of the reconstructed three-dimensional objects from a single snapshot is shown in Fig. 3.16(a), indicating the signal to noise ratio of approximately 4. The position of the wall was inferred within approximately 30microns by detecting a peak of intensity corresponding to a few reflection points at the surface. The surface reflection peak is shown in Fig. 3.16(b) obtained by reconstructing time-minimum image, without seeding.

Volume cross-correlation was based on three-dimensional cross-correlation with iterative multi-grid volume deformation algorithm and implemented in a custom software (FLUERE)(Lynch 2015). The size of the final interrogation volume is $40 \times 20 \times 40$ voxels ($1.13 \times 0.56 \times 1.13 \text{mm}^3$), with an overlap of 75%. The resulting spatial resolution enables the detection of coherent vortices down to a scale of half a roughness height. A small fraction of data outliers was detected by using median filter (Westerweel and Scarano 2005) and replaced by linear interpolation of surrounding data points.

Tab. 3.3. Tomographic PIV parameters.

| Parameter | Value |
|-----------------------------|---|
| Laser pulse separation | 30, 43, 60 μs ($u_\infty = 10, 7, 5 \text{ m/s}$) |
| Active sensor size | 4872 \times 1500pixels |
| Magnification | 0.25 |
| Digital imaging resolution | 33.6pixels/mm |
| Object focal length, $f_\#$ | 105mm, 11 |
| Measurement volume | 145 \times 6 \times 45 mm^3 |
| Interrogation volume | 40 \times 20 \times 40voxels ($1.13 \times 0.56 \times 1.13 \text{mm}^3$) |
| Overlap factor | 75% |
| Vector pitch | 0.28mm (x and z axis), 0.14mm (y axis) |
| Grid of measured vectors | 495 \times 44 \times 115 |

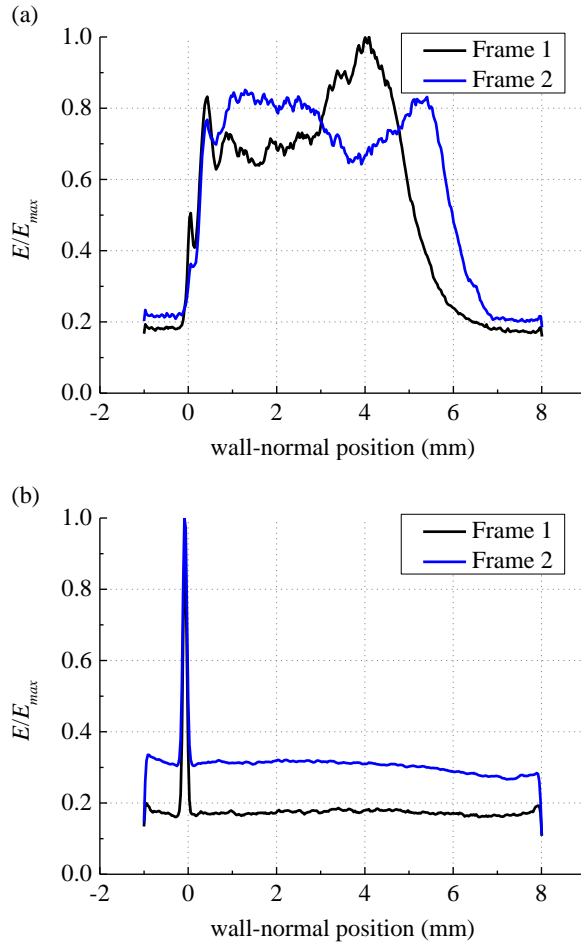


Fig. 3.16. Reconstruction light intensity profiles, (a) from a single snapshot, (b) detection of wall position by surface reflection.

3.8 Uncertainty analysis

The experimental uncertainty arising from the measurement error is associated to tomographic PIV measurement. The ensemble data size and the cross-correlation analysis are the most important factors influencing the measurement uncertainty. The dataset consists of 200 uncorrelated instantaneous snapshots. The uncertainty on the mean velocity can be estimated from the expression below:

$$\varepsilon_u = \frac{\sigma_u}{\sqrt{M}} \quad (3.17)$$

where ε_u is the relative uncertainty, σ_u is the typical level of streamwise velocity fluctuations ($\langle u' \rangle / u_\infty$) and M is the number of uncorrelated snapshots.

The uncertainty on the RMS of velocity fluctuations is estimated according to the expression below:

$$\varepsilon_{\langle u \rangle} = \frac{\sigma_u}{\sqrt{2(M-1)}} \quad (3.18)$$

where $\varepsilon_{\langle u \rangle}$ is the relative uncertainty on the streamwise velocity fluctuations normalized by the freestream value.

The uncertainty of the Reynolds shear stress can be estimated from

$$\varepsilon_{\overline{u'v'}} = \frac{\sqrt{1 + R_{uv}^2} \sigma_u \sigma_v}{\sqrt{M-1}} \quad (3.19)$$

where $\varepsilon_{\overline{u'v'}}$ is the relative uncertainty of Reynolds shear stress, R_{uv} is the correlation coefficient of u' and v' determined by

$$R_{uv} = \frac{\sigma_{uv}}{\sigma_u \sigma_v} \quad (3.20)$$

σ_v and σ_{uv} is the typical level of wall-normal velocity fluctuations ($\langle v' \rangle / u_\infty$) and Reynolds shear stress ($-\overline{u'v'} / u_\infty^2$) respectively.

The error due to the reconstruction and cross-correlation algorithm also influence the accuracy of the measured velocity field. Following Lynch and Scarano (2015), an error of 0.3voxel on displacement is considered, which is in the order of 3% on 10voxels freestream particle displacement. Other sources of error such as model vibration and system calibration, are considered negligible after the self-calibration procedure (Wieneke 2008) is applied. The uncertainty parameters are summarized in Tab. 3.4.

3.9 Data reduction

3.9.1 Proper Orthogonal Decomposition

Proper orthogonal decomposition (POD) is a well-established procedure introduced into fluid mechanics to statistically identify dominant coherent structures in complex flows (Lumley 1967). The POD method decomposes the fluctuating component of the velocity field into limited number (N) of time-independent orthogonal modes $\varphi_n(x,y,z)$ and time-dependent orthonormal amplitude coefficients $\alpha_n(t)$, as expressed in equation (3.21)

$$u'(x, y, z, t_i) = \sum_{n=1}^N \alpha_n(t_i) \varphi_n(x, y, z) \quad (3.21)$$

Tab. 3.4. Summary of measurement uncertainty parameters

| Re_h | 1170 | 730 | 460 |
|--|------------|-------|-------|
| Reconstruction and cross-correlation uncertainty ε_{cc} | 0.3 voxels | | |
| Instantaneous velocity ε_{cc} ($\times 10^2$) | 3 | | |
| Typical level of $\langle u' \rangle / u_\infty$ | 0.1 | 0.1 | 0.08 |
| Typical level of $\langle v' \rangle / u_\infty$ | 0.05 | 0.05 | 0.04 |
| Typical level of $-\overline{u'v'} / u_\infty^2$ | 0.015 | 0.002 | 0.003 |
| Mean velocity ε_u ($\times 10^2$) | 0.7 | 0.7 | 0.6 |
| RMS velocity fluctuations $\varepsilon_{\langle u' \rangle}$ ($\times 10^2$) | 0.5 | 0.5 | 0.4 |
| Reynolds shear stress $\varepsilon_{\overline{u'v'}}$ ($\times 10^2$) | 0.041 | 0.038 | 0.025 |

POD has been widely applied as data reduction method for PIV experiments, yielding either a simplified representation of the structure containing high fluctuation energy or supporting a reduced order reconstructed models based on a limited number of modes (Van Oudheusden et al. 2005, Legrand et al. 2011). The snapshot POD method, which was proposed by Sirovich (1987), is applied to the current tomographic PIV experiment. The suitability of POD to the treatment of 3D data issued from tomographic PIV has been already shown in past works (Violato and Scarano 2013, Morton et al. 2016). Its first application to investigate the three-dimensional pattern resulting from the roughness induced transition is given in the present study. The three velocity fluctuation components are arranged in the matrix below (equation (3.22)), taking their correlation into account.

$$U = \begin{bmatrix} (u')_1^1 & (u')_1^2 & \cdots & \cdots & (u')_1^M \\ (v')_1^1 & (v')_1^2 & \cdots & \cdots & (v')_1^M \\ (w')_1^1 & (w')_1^2 & \cdots & \cdots & (w')_1^M \\ \vdots & \vdots & \vdots & \vdots & \vdots \\ \vdots & \vdots & \vdots & \vdots & \vdots \\ (u')_p^1 & (u')_p^2 & \cdots & \cdots & (u')_p^M \\ (v')_p^1 & (v')_p^2 & \cdots & \cdots & (v')_p^M \\ (w')_p^1 & (w')_p^2 & \cdots & \cdots & (w')_p^M \end{bmatrix} \quad (3.22)$$

where M is the number of snapshots, and p is the number of positions in each snapshot. Each POD mode is written as a linear combination of snapshots, as

$$\varphi_n(x, y, z) = \sum_{i=1}^M \psi_n(t_i) u'(x, y, z, t_i) \quad (3.23)$$

where ψ_n is the eigenvector of the autocovariance matrix, $R = U^T U / M$. The corresponding eigenvalue of each modes λ_n represents its contribution to the total disturbance energy, sorting in the descending order. The POD modes are normalized such that $||\varphi_n||=1$.

The instantaneous snapshot can be reconstructed using low-order model incorporating the mean flow and only limited number (K) of POD modes which represent the dominant part of the fluctuation field as

$$u_{LOM}(x, y, z, t_i) = \bar{u}(x, y, z, t_i) + \sum_{k=1}^K \alpha_k(t_i) \varphi_k(x, y, z) \quad (3.24)$$

The low-order reconstruction acts as a spatial filter, removing the small-scale fluctuations and random measurement noise. The predominant large-scale coherent structure in the flow will be clarified.

3.9.2 Vortex detection

Tomographic PIV measurement enables the detection of three velocity components and the corresponding velocity gradient. The derivatives of velocity is exhibited as

$$\nabla \cdot V = \begin{bmatrix} \frac{\partial u}{\partial x} & \frac{\partial u}{\partial y} & \frac{\partial u}{\partial z} \\ \frac{\partial v}{\partial x} & \frac{\partial v}{\partial y} & \frac{\partial v}{\partial z} \\ \frac{\partial w}{\partial x} & \frac{\partial w}{\partial y} & \frac{\partial w}{\partial z} \end{bmatrix} \quad (3.25)$$

The velocity gradient is calculated using least square difference method as

$$\begin{aligned} \frac{\partial V}{\partial x} &= - \frac{2V(i+2, j, k) + V(i+1, j, k) - V(i-1, j, k) - 2V(i-2, j, k)}{10\Delta x} \\ \frac{\partial V}{\partial y} &= - \frac{2V(i, j+2, k) + V(i, j+1, k) - V(i, j-1, k) - 2V(i, j-2, k)}{10\Delta y} \\ \frac{\partial V}{\partial z} &= - \frac{2V(i, j, k+2) + V(i, j, k+1) - V(i, j, k-1) - 2V(i, j, k-2)}{10\Delta z} \end{aligned} \quad (3.26)$$

where i, j, k represent the grid index of x, y, z direction in the vector field.

The transitional wake of roughness element is predominated by large-scale vortex structures. The detection of the vortices is firstly realized by vorticity, which is defined mathematically as the curl or rotation of the velocity field,

$$\omega = \nabla \times V \quad (3.27)$$

where $\nabla = (\frac{\partial}{\partial x}, \frac{\partial}{\partial y}, \frac{\partial}{\partial z})$ in Cartesian coordinate. Each vorticity component can be written as,

$$\begin{bmatrix} \omega_x \\ \omega_y \\ \omega_z \end{bmatrix} = \begin{bmatrix} \frac{\partial w}{\partial y} - \frac{\partial v}{\partial z} \\ \frac{\partial u}{\partial z} - \frac{\partial w}{\partial x} \\ \frac{\partial v}{\partial x} - \frac{\partial u}{\partial y} \end{bmatrix} \quad (3.28)$$

The use of the λ_2 criterion (Jeong and Hussain 1995), or equivalently of the Q-criterion (Hunt et al. 1988) is well accepted and fairly widespread in the fluid mechanics community to identify unambiguously vortices in turbulent flows. With respect to vorticity iso-surfaces the λ_2 criterion offers the advantage that it selects only the regions dominated by solid body rotation and not by shear. This approach is based on the detection of pressure minimum across the vortex using the symmetric 3×3 tensor,

$$S^2 + \Omega^2 \quad (3.29)$$

where S and Ω are the symmetric and asymmetric component of ∇u , expressing as

$$S = \frac{1}{2} \left(\frac{\partial u_i}{\partial x_j} + \frac{\partial u_j}{\partial x_i} \right), \quad \Omega = \frac{1}{2} \left(\frac{\partial u_i}{\partial x_j} - \frac{\partial u_j}{\partial x_i} \right) \quad (3.30)$$

The eigenvalues of $S^2 + \Omega^2$ are λ_1, λ_2 and λ_3 , sorting in a magnitude decreasing order ($\lambda_1 \geq \lambda_2 \geq \lambda_3$). The region where $\lambda_2 < 0$ corresponds to a vortex core. λ_2 is found to be a robust representation of the vortex geometry and widely applied in the study of vortical structure in transitional (Schlatter et al. 2008, Duguet et al. 2012, Hack and Zaki 2014) and turbulent (Zhou et al. 1999, Schlatter et al. 2014) boundary layer.

4

Transition scenario at supercritical Re_h

In this chapter, the early stage of three-dimensional laminar to turbulent transition behind a micro-ramp is studied in the incompressible regime using tomographic PIV. Experiments are conducted at supercritical micro-ramp-height h based Reynolds number $Re_h = 1170$. The mean flow topology reveals the underlying vortex structure of the wake flow with multiple pairs of streamwise counter-rotating vortices visualized by streamwise vorticity. The primary pair generates a vigorous upwash motion in the symmetry plane with a pronounced momentum deficit. A secondary vortex pair is induced closer to the wall. The tertiary and even further vortices maintain a streamwise orientation, but are produced progressively outwards of the secondary pair and follow a wedge-type pattern. The instantaneous flow pattern reveals that the earliest unstable mode of the wake features arc-like Kelvin-Helmholtz vortices in the separated shear layer. The K-H vortices are lifted up due to the upwash induced by the quasi-streamwise vortex pair, while they appear to undergo pairing, distortion and finally breakdown. Immediately downstream, a streamwise interval of relatively low vortical activity separates the end of the K-H region from the formation of new hairpin vortices close to the wall. The latter vortex structures originate from the region of maximum wall shear, induced by the secondary vortex pair causing strong ejection events which transport low-speed flow upwards. The whole pattern features a cascade of hairpin vortices along a turbulent non-turbulent interface. The wedge-shape cascade signifies the formation of a turbulent wedge. Inside the wedge region, the velocity fluctuations approach quasi-spanwise homogeneity, indicating the development towards a turbulent boundary layer. The wedge interface is characterized by a localized higher level of velocity fluctuations and turbulence production, associated to the deflection of the shear layer close to the wall and the onset of coherent hairpin vortices inducing localized large-scale.

4.1 Introductory remarks

The general understanding of the transitional flow features behind isolated roughness elements can be retrieved from the literature review in sec. 2.4. An isolated roughness element produces a low-speed region in the wake close to the symmetry plane. The unstable separated shear layer leads to the formation of hairpin-shape vortex structures, which relate to the onset of transition.

Most previous researches focused on the bluff-front roughness elements (cylinder, diamond and sphere), which produce horseshoe vortices by upstream flow separation (Baker 1979). Less effort has been put to the slender-front roughness element, such as micro-ramp, which introduces mild modulation to the mean flow, possibly following different route towards transition. The micro-ramp geometry has been widely used as the flow control device to enhance boundary layer transition and avoid unwanted separation (Berry et al. 2001, Lin 2002). In the special area of separation control caused by shock wave boundary layer interaction (SWIBLI), Anderson et al. (2006) suggested the micro-ramp geometry offers the advantages of strongly minimizing the transformed shape factor H_{tr} of the boundary layer (Fukuda et al. 1975) and structural ruggedness. As a result, micro-ramp received the most

research interest when immersed in supersonic turbulent boundary layer. The mean flow topology featuring multiple pairs of counter-rotating vortices has been explained in sec. 2.4.1.2.

Blinde et al. (2009) investigated the instantaneous flow organization past an array of micro-ramps using stereo PIV along wall-parallel planes. The presence of instantaneous counter-rotating vortices at the side of each element wake was ascribed to the leg portion of hairpin vortices, which agrees with observations in low-speed flows (Acarlar and Smith 1987, Klebanoff et al. 1992). The LES study by Li and Liu (2010) reports a train of vortex rings produced in the highly sheared region of the wake. This vortex ring is further explained as a product of K-H instability, with a highly intermittent nature (Lu et al. 2010, Wang et al. 2012). Sun et al. (2012) experimentally visualized the full three-dimensional flow organization using tomographic PIV. The instantaneous flow organization shows the presence of a train of arc-shaped vortices at the edge of the wake due to the K-H instability. In the downstream wake region of the micro-ramp, K-H instability at the upper shear layer further develops with the onset of vortex pairing (Sun et al. 2014). In a more recent numerical study, Sun et al. (2014) also investigated the temporal evolution of the latter vortices, concluding that the onset of arc-like vortices pairing and connection at the bottom in the downstream region contributes to the distortion of the streamwise counter rotating vortex pair.

The resulting unsteady flow behaviour downstream of the micro-ramp is therefore to be connected to the presence of the micro-ramp in combination with the incoming boundary layer turbulence which in turn affects the stability of the overall wake structure. This interaction partly masks the mechanism of the wake evolution and the onset of instability. In this respect, studies in the laminar regime potentially yield a clearer scenario of transition and the instability mechanisms behind submerged isolated micro-ramp.

The current chapter focuses on the three-dimensional representation of the flow feature behind micro-ramp of 2mm height and 4mm span (Fig. 3.5) immersed in a laminar incoming boundary layer at supercritical roughness-height based Reynolds number $Re_h = 1170$. The details of the micro-ramp geometry and incoming flow condition have been explained in sec. 3.2 and 3.4. The ratio between micro-ramp height and boundary layer thickness (h/δ) is 0.61. The tomographic PIV measurement domain encompasses 6 ramp widths spanwise and 73 ramp heights streamwise. The mean flow organization (sec. 4.2 and 4.3) identifies the streamwise vortical structures and the induced spanwise and wall normal velocity variation. The details of unsteady flow activity are inspected by instantaneous visualization in sec. 4.4, with the aid of the vortex detection λ_2 criterion (Jeong and Hussain 1995). The statistical analysis of velocity field fluctuations and turbulence production are given in sec. 4.5, aiming at a quantitative characterization of the wake turbulent structure and yielding the edge of turbulent non-turbulent interface along with its spreading angle.

4.2 Mean flow organization

The topology of the time-average flow is obtained by analysing the mean velocity and vorticity fields, which in turn provide a baseline for interpreting the instantaneous flow pattern. The mean velocity and vorticity fields are obtained by averaging 200 instantaneous uncorrelated snapshots. The cross-flow velocity is inspected at three $y-z$ planes positioned downstream of the micro-ramp at $x/h = 5$, 15 and 53. The result is illustrated in Fig. 4.1, where the projection of the streamlines on the $y-z$ plane is visualized along with the colour contours of the non-dimensional streamwise velocity (u/u_∞).

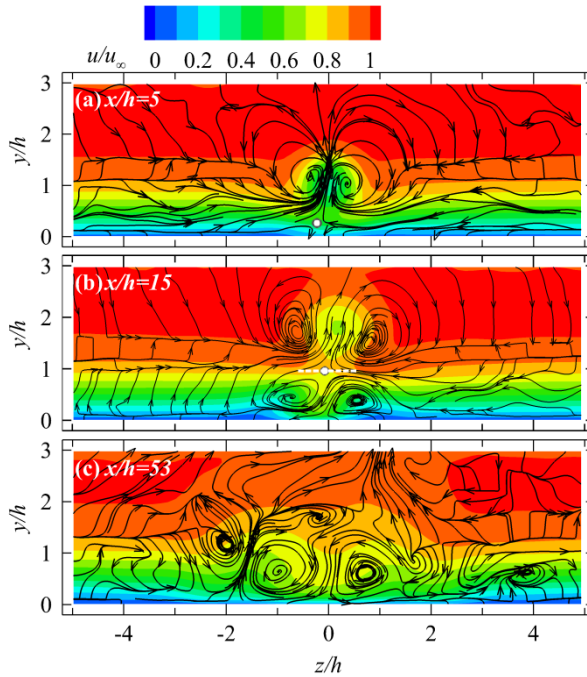


Fig. 4.1. Time averaged streamwise velocity (colour contours) and flow topology (streamtraces) in the $y-z$ plane at three streamwise locations. The stagnation point in (a)(b) highlighted with white dot, the 'neck' region in (b) shown with white-dash line.

In the near wake region ($x/h = 5$), the micro-ramp induces a pair of counter rotating vortices (primary streamwise vortex pair), which produce a central upwash motion and a lateral downwash at $z/h = \pm 0.6$ (shown with the projected streamlines in Fig. 4.1(a)). This pattern has been reported in numerous studies conducted in supersonic turbulent boundary layers (Babinsky et al. 2009, Sun et al. 2012). The pronounced upwash motion induced by this primary vortex pair causes a mushroom-shaped velocity deficit region around the symmetry plane ($z/h = 0$) and the formation of a saddle point at approximately $y/h = 0.2$ (shown as the white dot).

The flow in the region below the saddle point is directed towards the wall where it stagnates. The wall-normal position of the vortex core appears at $y/h = 1.2$ for $x/h = 5$ (Fig. 4.1(a)) and is lifted up to $y/h = 1.8$ downstream at $x/h = 15$ (Fig. 4.1(b)) as a result of the self-induced velocity (Crow 1970). With the primary vortex pair being lifted up ($x/h = 15$), the stagnation point emerges away from the wall to approximately one micro-ramp height. A second pair of counter-rotating vortices is formed (approximately at $z/h = \pm 0.7$), with opposite rotation direction with respect to the primary pair. Secondary vortices were also observed by Tirtety et al. (2011) in the hypersonic laminar micro-ramp wake. The presence of this vortex pair induces a downwash motion at the symmetry plane close to the wall, which tends to flatten the velocity profile (see Fig. 4.3(b)). As a result, high momentum fluid is directed downwards below the stagnation point with a twofold increase of the velocity close to the wall (Fig. 4.3(b), $y/h = [0.1, 0.2]$, $x/h = 15$). The high-speed region between the secondary vortices also emphasizes the formation of a neck region (indicated by a white dashed line) at approximately $y/h = 1.0$ ($x/h = 15$, Fig. 4.1(b)). Lateral upwash produced by the secondary vortex pair generates low-speed regions and associated velocity deficit at the side. The large increase in wall shear, in combination with the inflectional velocity profile ($y/h = 0.5$, $z/h = \pm 1$) is ascribed to determine triggering conditions for the instability mechanism leading to flow transition, which is further circumstantiated in sec. 4.4. At $x/h = 53$ (Fig. 4.1(c)), the strength of the primary vortex can no longer be detected by the streamlines as they appear to have risen beyond the upper boundary of the measurement domain. From Fig. 4.2, it appears that the primary vortices do remain at a constant height close to the measurement boundary, but with a significant decay of the peak vorticity. The foci of the secondary vortex pair have moved outwards in spanwise direction widening the high-speed region close to the wall. Two low-speed regions are formed at the spanwise location of the latter vortex pair. A weaker tertiary vortex pair is induced aside the secondary pair with the same sense of rotation as the primary one (see Fig. 4.2). The combined effect of secondary and tertiary vortices causes focused ejections of low-speed fluid above the wall, which is associated to the formation of unstable hairpin structures as will be discussed in the remainder of the study.

The time-averaged vortex topology is rendered in Fig. 4.2 through the spatial distribution of non-dimensional streamwise vorticity ($\omega_x^* = \omega_x \times h / u_\infty$). Close to the micro-ramp, two pairs of counter-rotating structures corresponding to the primary and secondary vortex pair are clearly identified. The vortex system persists downstream with decreasing strength. The lift-up and diffusion process of the primary vortices is evident from the side view (Fig. 4.2(b)). The secondary vortex pair appears to be active from the most upstream measurement location. The tertiary system of vortices makes its first appearance outwards at approximately $x/h = 25$. It is hypothesized here that the tertiary vortex structure might be the precursor to the laminar to turbulence transition as it produces together with the secondary vortex pair the two saddle points close to the wall with upwash regions potentially generating unsteady ejection events. This hypothesis is further elaborated in the discussion of the statistical flow properties (sec. 4.5). Further downstream, even a

fourth ($x/h = 40$) and a fifth ($x/h = 54$) vortex pair are observed outwards of the tertiary vortex pair. These vortices are ascribed to the mutual induction effect of the neighbouring vortices. The whole vortical pattern follows the shape of a wedge, in analogy to that shown in turbulent spots.

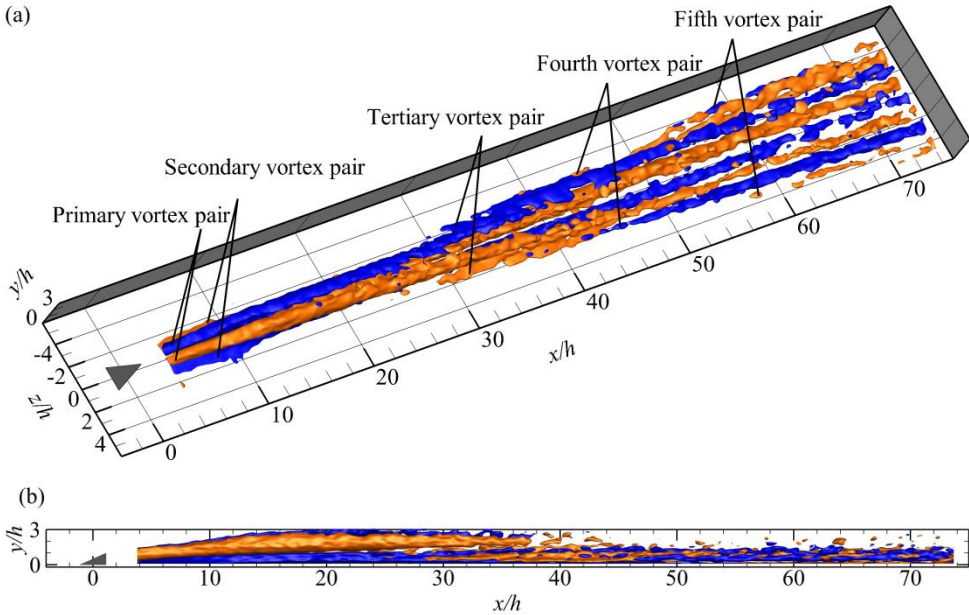


Fig. 4.2. Three-dimensional rendering of time-averaged streamwise vorticity (blue for anticlockwise rotation vortices, $\omega_x^* = -0.04$; red for clockwise rotation vortices, $\omega_x^* = 0.04$). Perspective (a) and side (b) view.

4.3 Momentum deficit and log-layer

Previous studies of the micro-ramp wake have dealt with the streamwise evolution of the momentum deficit and characterized its turbulent recovery (Ghosh et al. 2010, Sun et al. 2014). In the present case, the momentum deficit and the properties of the shear layer induced by the micro-ramp pertain to the laminar regime and the velocity profile in the symmetry plane ($z/h = 0$) is compared with that of the undisturbed boundary layer.

The situation is illustrated at four streamwise positions ($x/h = 5, 15, 40$ and 70) in Fig. 4.3. The micro-ramp wake exhibits an overall deficit with respect to the laminar reference of approximately $0.6u_\infty$ at $x/h = 5$ with a minimum velocity located at $y/h = 1.2$. Two shear layers bound the region of reduced momentum. The upper shear layer emanates from the trailing edge of the micro-ramp, which eventually becomes unstable with the formation of Kelvin-Helmholtz vortices (Acarlar and Smith 1987). The bottom shear layer is produced by the combined action of the

primary and secondary vortex pair transporting high momentum fluid towards the symmetry plane. As the streamwise velocity locally exceeds that of the undisturbed boundary layer, a higher near wall shear is produced. The rapid decrease of the velocity deficit ($0.3u_\infty$ at $x/h = 15, y/h = 1.8$) indicates a recovery process dominated by the large-scale mixing across the shear layer. At $x/h = 40$ and 70 (Fig. 4.3(c)(d)), no velocity minimum can be observed in the profile, which is ascribed to the combined effect of the diffusion of the wake induced by shear layer mixing and the upward motion of the primary vortex pair approaching the upper boundary of the measurement domain. However, the local velocity deficit observed at the edge of the undisturbed boundary layer is considered to cause by the strong upward motion of the secondary and tertiary vortices. This effect is confined in a limited spanwise range ($z/h = [-5, 5]$) and outside of it, the full freestream velocity is observed (see Fig. 4.1).

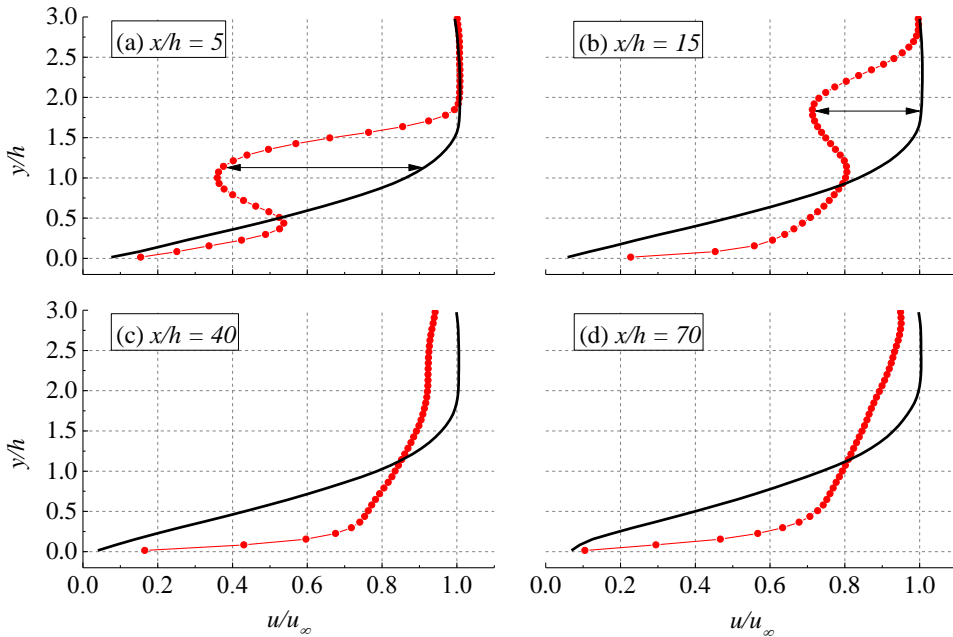


Fig. 4.3. Streamwise evolution of time averaged velocity profile in the symmetry plane (red line-circle) and comparison with undisturbed boundary layer profile (black line).

The wake recovery is quantified by following the streamwise evolution of the maximum momentum deficit. A rapid decreasing rate of maximum velocity deficit $(u_{BL}(y) - u(y))_{max}/u_\infty$ (where $u_{BL}(y)$ is the velocity of undisturbed boundary layer) from 0.6 to 0.1 occurs within the range of $x/h < 35$. Past this range, the velocity deficit is confined to the upper region of the boundary layer and stays constant at approximately $0.1u_\infty$. Sun et al. (2014) observed that the streamwise evolution of the maximum velocity deficit follows a power-law type decay in a supersonic turbulent

boundary layer. In the present case the validity of the power-law decay is confirmed by the acceptable fit to velocity deficit profile (Fig. 4.4) in the range $x/h = [7, 27]$, where the wake recovery is dominated by the K-H vortex structures. A detailed analysis of the latter is given in the sec. 4.4. The power law relation reads as:

$$\frac{(u_{BL}(y)-u(y))_{\max}}{u_{\infty}} = 4.5\left(\frac{x}{h}\right)^{-1.06} \quad (4.1)$$

The recovery rate of 1.06 is considerably larger than the values of 0.73 - 0.78 reported by Sun et al. (2014), indicating a more efficient momentum mixing. The latter is ascribed to the longer persistence of coherent large-scale flow structures occurring in the laminar regime, as opposed to the more rapid breakdown in the turbulent boundary layer.

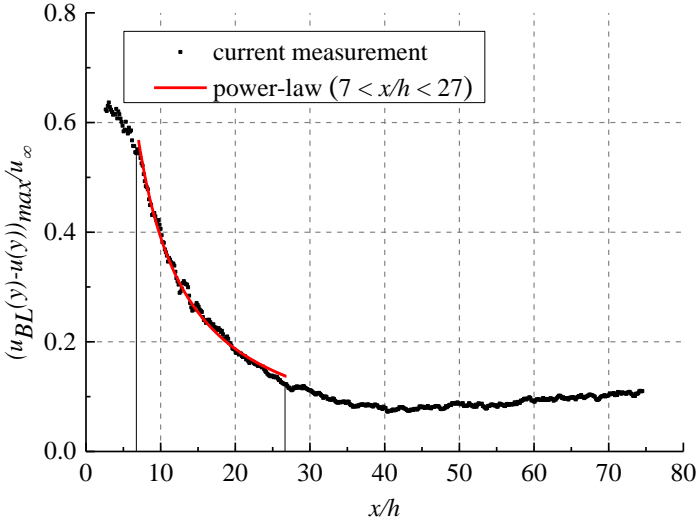


Fig. 4.4. Streamwise evolution of maximum velocity deficit $(u_{BL}(y)-u(y))_{\max}/u_{\infty}$.

In order to establish the onset and development of the turbulent regime, the velocity profile is plotted in the semi-logarithmic scale enabling a direct comparison with the log law fit. Fig. 4.5 illustrates the streamwise development of non-dimensional velocity u/u_{∞} versus $u_{\infty}y/\nu$ along the symmetry plane. The logarithmic equation characterizing the overlap layer of turbulent boundary layer reads as (Kline et al. 1969):

$$u^+ = \frac{1}{\kappa} \ln y^+ + B \quad (4.2)$$

where $\kappa=0.41$, $B=4.0$. Substituting $u_\tau / u_\infty = (\frac{1}{2} c_f)^{1/2}$ into equation (4.2) yields

$$\frac{u}{u_\infty} = A \ln\left(\frac{u_\infty y}{\nu}\right) + C \quad (4.3)$$

where $A = \frac{1}{\kappa} (\frac{1}{2} c_f)^{1/2}$ and $C = (\frac{1}{2} c_f)^{1/2} [\frac{1}{2\kappa} \ln(\frac{1}{2} c_f) + B]$.

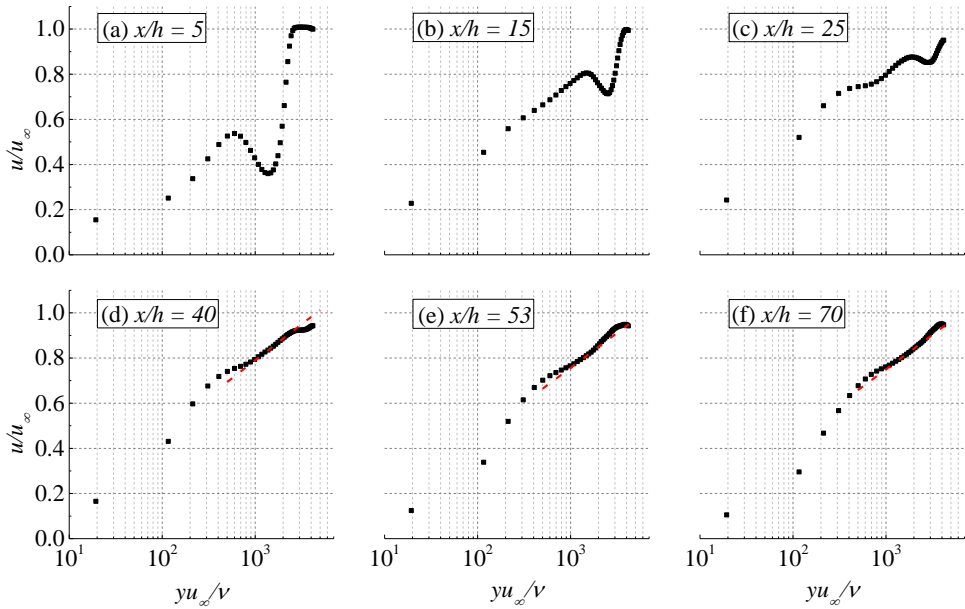


Fig. 4.5. Wall-normal semi-log profile of u/u_∞ developing streamwise along the symmetry plane (black squares). Log-law region highlighted with dashed red line.

At $x/h = 5, 15$ and 25 , the lower part of the profile features the large momentum defect region due to the wake. At $x/h = 40, 53$ and 70 , a linear range of $u_\infty y/\nu = [1 \times 10^3, 2 \times 10^3]$ in the upper part of the profile indicates the presence of an overlap layer complying with the log law. By using equation (4.3), the skin friction c_f is determined by a linear fit in the log region, shown as the red dashed line in Fig. 4.5. Consequently, the flow exhibits turbulent regime from $x/h = 40$.

4.4 Instantaneous flow organization

The formation and growth of unstable oscillations past the isolated roughness elements have been associated in the past to one of the driving mechanisms forcing boundary layer transition. Extensive discussion is found in the literature that focuses

on shear layer instability past isolated roughness elements of various geometries, such as circular cylinders (Ergin and White 2006) and hemispherical cap (Acarlar and Smith 1987, Citro et al. 2015). This instability is conjectured to act as precursor to the onset of transition. In the case of micro-ramps, the onset of shear layer instability was also observed in supersonic turbulent boundary layers (Li and Liu 2010, Sun et al. 2012). On the other side, different conclusions were drawn by Choudhari et al. (2009), who examined the role of both shear layer and streak instabilities in supersonic boundary layer. The latter were associated to spanwise high-shear layer of the flow, undergoing a more rapid growth compared to shear layer instability away from the roughness element and triggering final breakdown to turbulence. The current experiments visualize the instantaneous three-dimensional structure of velocity and vorticity fluctuations, from which the pattern of Kelvin-Helmholtz vortices can be observed along with their evolution in the wake. The instantaneous vortex structure is highlighted from the three-dimensional iso-surface of a vortex detection criterion by λ_2 (Jeong and Hussain 1995). The iso-surface in Fig. 4.6 is colour-coded by streamwise velocity to better distinguish between the portions of flow at high speed and at low speed.

4.4.1 Evolution of K-H vortices

In the very near wake of the micro-ramp ($x/h < 4$), the shear layer on top of the wake exhibits a quasi-steady behaviour with no evidence of shear layer fluctuations. The baseline flow is dominated by the primary streamwise vortex pair (see Fig. 4.2). Downstream of the very near wake region, unstable waves in the shear layer due to K-H instability are observed, leading to large scale quasi-periodic fluctuations at the upper shear layer. Very similar wavy structure has been observed in numerous studies dealing with a turbulent boundary layer upstream of the micro-ramp (Li and Liu 2010, Sun et al. 2012). Moreover, the presence of K-H vortices producing shear layer fluctuations is consistent with the inflection point in the mean velocity profile immediately downstream of the micro-ramp (see Fig. 4.3 at $x/h = 5$).

The arc-shape vortices within the shear layer emanating from the micro-ramp trailing edge can be clearly observed in Fig. 4.6(a). The low-momentum fluid ejection event (Q2, $u' < 0, v' > 0$) associated with an arc-vortex is visualized with iso-surface of $u'v'/u^2_\infty = -0.002$ (coloured black). The sweep events (Q4, $u' > 0, v' < 0$) are also identified as iso-surface of $u'v'/u^2_\infty = -0.002$ (coloured green). Q2 events focus within the leg portion and upstream region of the arc-vortex head (Zhou et al. 1999), whereas the sweeping motions (Q4) are more broadly distributed in the region downstream of the vortex head and mildly shown along the sides of legs (Adrian and Liu 2002). More downstream, the vortices develop a quasi-streamwise leg-like portion (Robinson 1991), which elongate under the shearing motion between the head and the near wall region. The overall pattern features a train of hairpin-like vortices. The spanwise rotation of the head portion induces an inclination angle around $35^\circ - 60^\circ$ of the leg portion to the x axis, which agrees fairly well with the hairpin vortex organization investigated by Adrian et al. (2000). Moving downstream, the K-H vortices lift up, due to the upwash motion induced by the leg

portion and form an inclined shear layer. At $x/h = 15$, the K-H vortices appear to grow in size and to increase their azimuthal range due to self-induction of the legs. Eventually, the leg pairs connect at the bottom to produce full ring vortices, as shown in Fig. 4.6(b) and observed in previous studies (Sun et al. 2014, Yan et al. 2014). The random traces of small-scale vortices near the wall ($y/h < 0.5$), is solely ascribed to the effect of measurement noise.

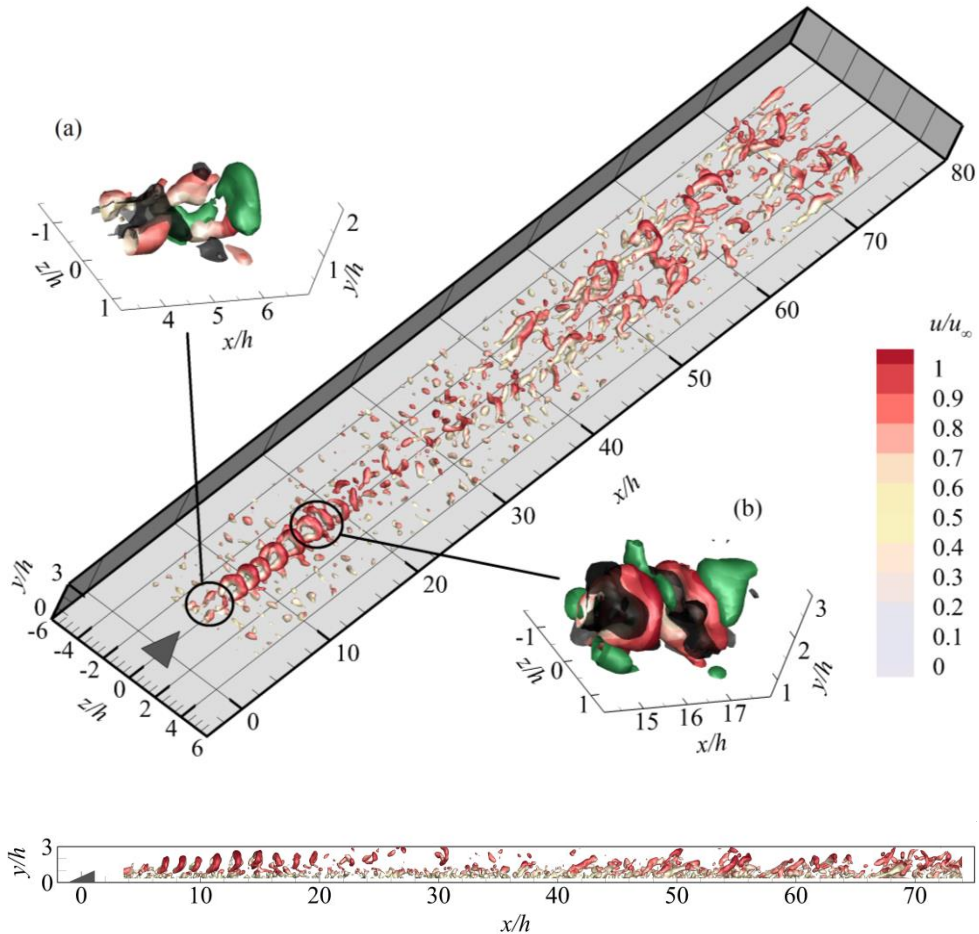


Fig. 4.6. The instantaneous flow pattern detected by λ_2 criterion ($\lambda_2 = -0.07$) colour coded by u/u_∞ , perspective (top) and side (bottom) view, (a)(b) ejection (black) and sweep (green) events are shown by $u'v'/u^2_\infty = -0.002$.

The wavelength of the shear layer fluctuations induced by the K-H vortices is defined as the interval between adjacent vortices. A statistical analysis by means of the spatial auto-correlation function is applied to the instantaneous spanwise vorticity field (ω_z). The region over which the spatial auto-correlation is evaluated is

$6.4h$ in the streamwise direction. The ensemble averaged wavelength is evaluated over a set of 100 instantaneous snapshots in the range of $x/h = [4, 20]$, as shown in Fig. 4.7. The vortices are spaced at regular intervals of approximately $\lambda_0/h = 1.45$ in the range of $x/h = [4, 6]$, which is the initial wavelength (see Fig. 4.6, side view). The convection velocity of the vortices can be inferred invoking Galilean decomposition with respect to the local streamwise velocity (Adrian et al. 2000). The initial convection velocity estimated from the vortex centre is to $u_{c0} = 0.69u_\infty$. The resulting frequency of vortex shedding is then estimated to be $f_{s0} = u_{c0}/\lambda_0 = 2,430\text{Hz}$ corresponding to a Strouhal number of $St_0 = f_{s0}h/u_\infty = 0.48$. Klebanoff et al. (1992) reported that the Strouhal number in the wake of roughness elements strongly depends on their size, shape and Reynolds number. Several studies (Acarlar and Smith 1987, Klebanoff et al. 1992) investigating the shedding phenomenon from roughness elements report Strouhal numbers varying from 0.2 to 0.5. The current experiment falls near the upper end of the range.

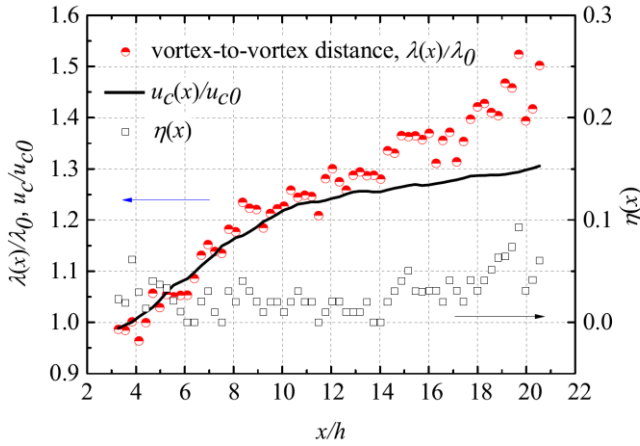


Fig. 4.7. Streamwise evolution of vortex-to-vortex distance. Non-dimensional convective velocity u_c/u_{c0} (black solid line), non-dimensional wavelength λ/λ_0 of experimental result (red circles) and the vortex pairing probability $\eta(x)$ (square).

The streamwise evolution of the wavelength is compared with the increase of the convective velocity u_c of the K-H vortices, in order to determine the occurrence of vortex pairing. In the range of $x/h = [4, 14]$, the convective velocity increases from $u_{c0} = 0.69u_\infty$ to $u_c = 0.85u_\infty$ ($1.26u_{c0}$). The wavelength has the same growth rate as the convective velocity, indicating that no vortex pairing takes place. However, in the later stage ($x/h = [14, 18]$), the growth of wavelength departs from the convective velocity and exhibits a steeper increase than the convective velocity, leading to $\lambda/\lambda_0 = 1.4$. In this stage, neighbouring ring vortices are observed to occasionally approach each other and undergo a rapid pairing. The example of the pairing process can be observed in the zoomed view of instantaneous vortex structure in Fig. 4.8. One can also refer to Ye et al. (2016) for the videos of 20 uncorrelated instantaneous

snapshots. The swirling pattern of velocity vectors becomes evident when displaying it after subtracting a convective velocity of $0.85u_\infty$. The pairing process is observed to occur intermittently. Therefore it does not lead, on average, to a doubling of the wavelength as evaluated from statistical cross-correlation analysis. In the range of $x/h = [18, 20]$, the interval of the vortices further increases to approximately $\lambda/\lambda_0 = 1.5$. As the convective velocity has remained relatively unaltered, the increased spatial separation signifies an increased occurrence of pairing in the downstream region. A simplified model is given here which describes the streamwise evolution of vortex-to-vortex distance, where the convective velocity u_c and the probability of vortex pairing are considered:

$$\lambda(x) = \lambda_0 \frac{u_c(x)}{u_{c0}} (1 + \eta(x)) \quad (4.4)$$

In the above equation $\eta(x)$ is the pairing probability. The equation does not account for multiple pairing. As shown in Fig. 4.7, the evolution of the vortex pairing probability $\eta(x)$ starts to increase from $x/h = 14$, leading to the deviation of wavelength evolution from that of the convective velocity.

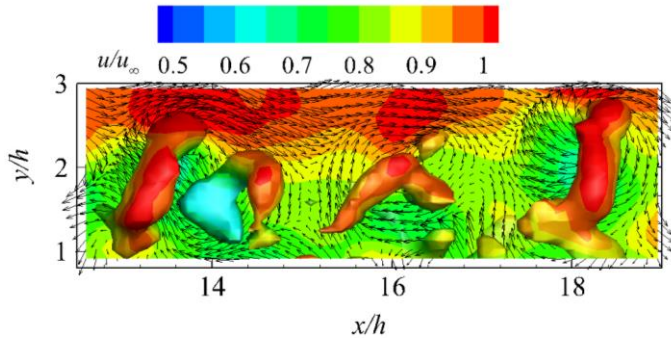


Fig. 4.8. Occurrence of vortex pairing detected by λ_2 criterion ($\lambda_2 = -0.07$) colour coded by u/u_∞ . The streamwise velocity contour in the symmetry plane shown with swirling vector field after subtracting a convective velocity of $0.85u_\infty$.

4.4.2 Formation of turbulent wedge

In the near wall region, newly formed vortex structures are observed starting from $x/h = 35$. These structures have a hairpin shape with head (spanwise rotation) and leg (quasi-streamwise rotation) portions. Instead of holding spanwise symmetry, the hairpins are more frequently observed in a 'cane' shape (Guezennec et al. 1989). Unlike the flow topology near the micro-ramp, the vortex structures do not develop following constant spanwise position ($z/h = 0$). Furthermore, the hairpin vortices appear more frequently shifted away from the symmetry plane and develop downstream with a spanwise spreading, as illustrated in Fig. 4.9. The position of first

4. Transition scenario at supercritical Re_h

occurrence of these vortex structures coincides with the range where the tertiary vortex pair is detected in the system of time-averaged streamwise vortices (see Fig. 4.2). However, the inception of such hairpin vortices varies significantly streamwise ($x/h = [30; 50]$), indicating an intermittent behaviour. The newly formed hairpins stay at a relatively constant wall-normal position, and no clear periodicity can be inferred from their pattern. Moreover, near the symmetry plane, lower to no activity of large-scale coherent vortex structures is observed, indicating the flow is developing into fully turbulent regime.

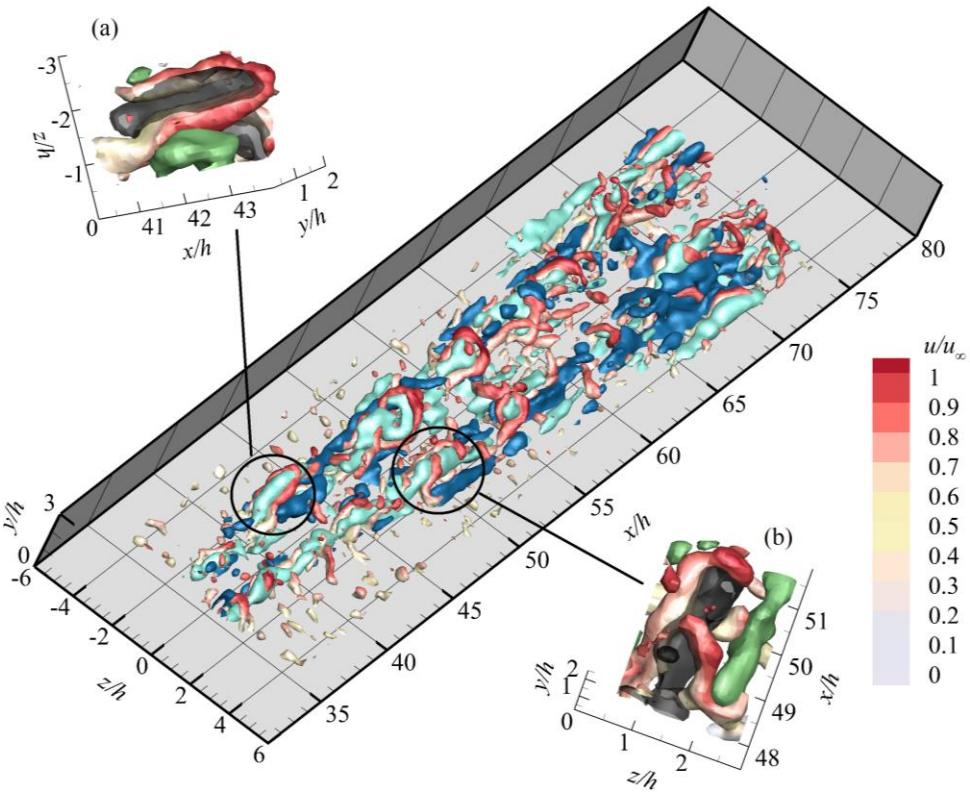


Fig. 4.9. Instantaneous flow pattern at the wedge region. Vortices visualized by iso-surfaces of $\lambda_2 = -0.07$, colour coded by u/u_∞ ; low-speed regions (light blue $u' = -0.13u_\infty$) and high-speed regions (dark blue $u' = 0.1u_\infty$); (a)(b) details of ejection (black) and sweep (green) are shown by $u'v'/u_\infty^2 = -0.005$.

Singer (1996) discussed the conditions governing the formation of hairpin vortices in a zero-pressure gradient vorticity field and found that it requires strong upward ejections. A study on the correlation between the newly formed hairpin vortices, low- and high-speed regions and ejection and sweep events is necessary to further understand the evolution of instantaneous vortex structure in the downstream region. The low-speed region is characterized by a negative component

of the streamwise velocity fluctuation $u' = -0.13u_\infty$, shown as the light blue iso-surface in Fig. 4.9. The majority of the hairpin structures are observed enclosing the elongated low-speed regions. The upward motion induced in the middle of the legs transports low-speed fluid from the wall to the upper part of the boundary layer. Such ejection events (iso-surface of $u'v'/u_\infty^2 = -0.005$, $u' < 0$, $v' > 0$) take place at the low-speed region, as shown in Fig. 4.9(a)(b). Comparably mild high-speed regions appear on the outside of the legs and upstream of the head region. These features are highlighted with (dark-blue) iso-surfaces of positive streamwise velocity fluctuations ($u' = 0.1u_\infty$). The sweep event (iso-surface of $u'v'/u_\infty^2 = -0.005$, $u' > 0$, $v' < 0$) in this region moves the high momentum flow from the upper boundary layer to the lower part. The global scenario of entangled hairpin vortices in range of $x/h = [35, 75]$ resembles a wedge shape, indicating a spanwise development of the vortical structures moving downstream.

In fact, the process is very similar to that observed for the development of turbulent spots, where low-speed regions provide a favourable condition for perturbations to trigger flow instabilities, ultimately leading to transition (Singer 1996, Durbin and Wu 2007). Furthermore, hairpin vortices have been reported as an ubiquitous phenomenon in turbulent spots (Ovchinnikov et al. 2008, Wu and Moin 2009). Consequently, the formation of a turbulent wedge can be confirmed in the current experiment, denoting the onset of boundary layer transition. By measuring the streamwise distance from the onset location of the newly formed hairpin vortices to the most downstream one in the measurement domain, the spreading angle is estimated to 4.5° . A detailed analysis based on the statistical properties of the turbulent fluctuations is given in sec. 4.5.1.

4.4.3 Transition mechanisms

In summary, the evolutonal flow pattern from the micro-ramp to boundary layer transition can be qualitatively divided into the following stages: 1) steady shear flow in presence of streamwise vortices; 2) formation and growth of K-H vortices; 3) pairing and breakdown of hairpin or ring-shape vortices; 4) onset of new hairpin vortices close to the wall; 5) spanwise propagation of the turbulent interface bounding a wedge-like region.

The turbulent wedge appears downstream of the lift-up and breakdown process of K-H vortex structure. However, no evident relation is found between the arc-shape vortices emanating from the micro-ramp trailing edge and the onset of these new hairpin vortices. Moreover, at the inception point of the latter structure, the fragmented K-H vortices can barely detected within the domain of interest and the distance between these two regions suggests no interaction taking place between them. The above discussion leads to the conclusion that the fluctuations occurring in the unstable shear layer past the micro-ramp trailing edge are not playing a role in the mechanism of transition.

It is instead conjectured, following the mean flow organization, that the inception of turbulent fluctuations is due to the near-wall secondary streamwise

vortex pair, following the detachment of the primary pair. The boundary layer transition is associated to the excess wall shear induced by the secondary vortex pair, in combination with the inflectional velocity profile produced by the interaction with the tertiary vortex pair. The latter hypothesis is further discussed in the remainder of the study, and supported by the statistical analysis of the velocity field and its fluctuations.

4.5 Turbulent properties

The generation of turbulent fluctuations following a wedge-like pattern in the instantaneous results indicates that the onset of laminar to turbulent transition falls in the range of $x/h = [30, 50]$, which is captured within the current measurement domain. The evolution of the turbulence properties is investigated by analysing the RMS fluctuations of streamwise and wall-normal velocity (u' , v') and turbulence production (P).

4.5.1 Velocity fluctuations

The two reference states of the boundary layer are the fully laminar condition and the fully developed turbulent regime which can be characterized by a well-known distribution of streamwise velocity fluctuations. The analysis of the velocity fluctuations in the wake of micro-ramp focuses on its development starting from the conditions of the undisturbed boundary layer.

The streamwise and wall-normal velocity fluctuations ($\langle u' \rangle / u_\infty$, $\langle v' \rangle / u_\infty$) are illustrated in Fig. 4.10 and Fig. 4.11. Colour contours of y - z cross-sections are selected at six streamwise locations $x/h = 5, 15, 25, 40, 53, 70$ and one x - y cross-section at the symmetry plane ($z/h = 0$). The y - z cross-sectional contours are superimposed with contour lines of time-averaged streamwise velocity. The location of the streamwise vortices is depicted by the selected projected streamlines. The upper and bottom inflection points of the streamwise velocity profile in the y direction are plotted in the x - y cross-plane (see Fig. 4.11) to signify the edge of the near-wake ($x/h < 27$), where the upwash induced by the primary vortex pair contributes to strong streamwise and wall-normal velocity fluctuations at the wake centre and interface of the wake and the freestream (also see Fig. 4.10(a)(b), $x/h = 5$ and 15). The maximum of the streamwise velocity fluctuations progressively lifts up and decreases in magnitude when travelling downstream, with a significant decay in the vortex-breakdown region ($x/h > 20$) and a rapid wake recovery. From $x/h = 30$ onwards, the velocity fluctuations in this region of the flow are considered to be negligible, or at least, they merge within the noise level of the measurement.

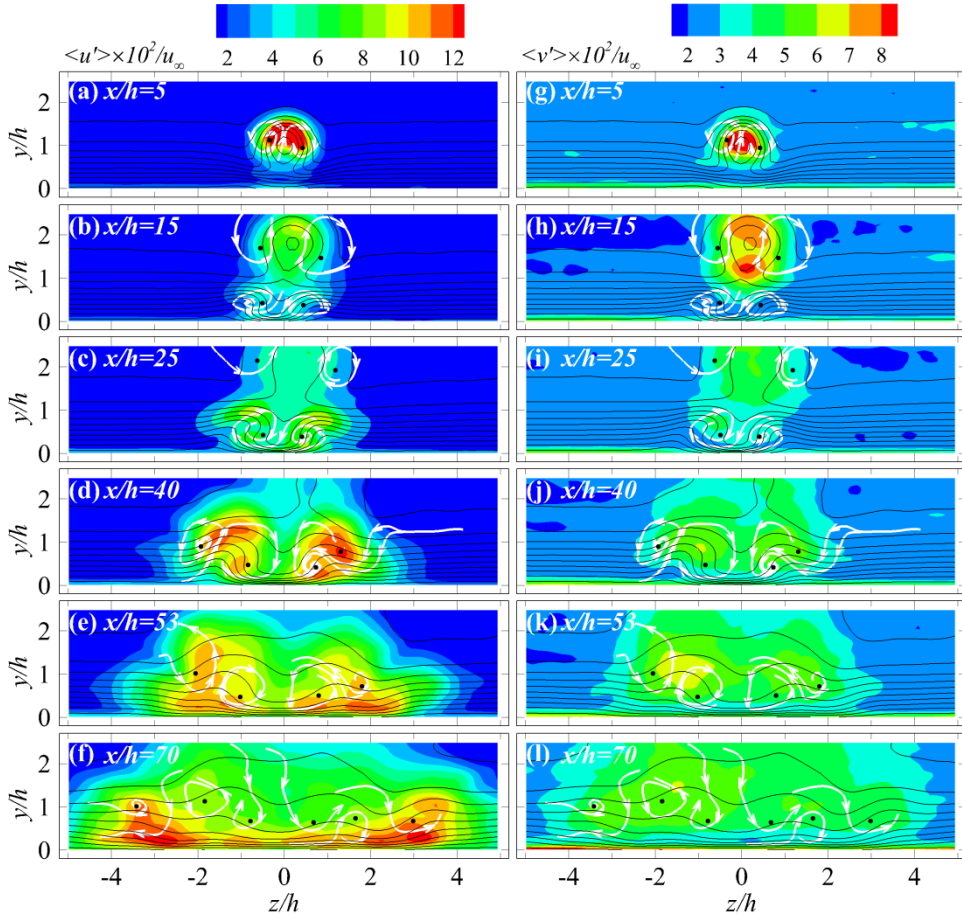


Fig. 4.10. $y - z$ cross-sectional contour of velocity fluctuations ((a)-(f): $\langle u' \rangle / u_\infty$; (h)-(l): $\langle v' \rangle / u_\infty$), with contour lines of u / u_∞ ; selected projected streamlines; approximate location of time-averaged streamwise vortices, black dots: the vortex core.

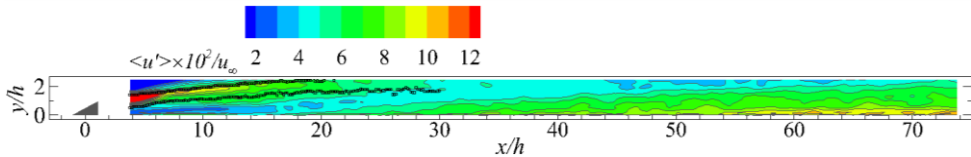


Fig. 4.11. $-y$ cross-sectional contour ($z/h = 0$) of streamwise velocity fluctuation, $\langle u' \rangle / u_\infty$; y axis scaled by a factor of 1.2 for clarity.

Beneath the wake region, the downwash motion produced by the secondary vortex pair transports high momentum fluid towards the wall. This effect is already visible at $x/h=15$ (Fig. 4.10(b)) where the contour lines near the wall in the symmetry plane are significantly bent downwards, resulting in a higher wall shear at that location. As a result, an increased level of streamwise velocity fluctuations is produced. Away from the symmetry plane, the secondary vortex pair induces ejection events, which produce low-speed regions, where upward bent of the contour lines can be observed (also see Fig. 4.1(b), $x/h = 15$). A tertiary vortex pair is formed that produces jointly with the secondary pair a streamwise velocity profile exhibiting an inflection point. Unlike the decaying process of the inflectional profile ($u - y$ profile) induced in the near wake past the micro-ramp, the latter persists until the most downstream measurement location and is considered to be the physical condition sustaining the cascade of fluctuations that lead to transition. As a result, the onset of a turbulent wedge is observed (corresponding with the formation of tertiary vortex pair) in this range (Fig. 4.10(b)-(f)). In fact, in this case, the inflection point is significantly closer to the wall. The turbulent momentum mixing at the turbulent non-turbulent interface results in a local maximum of streamwise velocity fluctuations ($\langle u' \rangle / u_\infty$) on top of the low-speed blob at $y/h = 1$, $z/h = \pm 0.7, \pm 1.2$ and ± 1.7 , corresponding to $x/h = 25, 40$ and 53 in figure Fig. 4.10(c)-(e). These local maxima are ascribed to the formation of large-scale hairpin-like coherent structures as also visualized in Fig. 4.6 and Fig. 4.9. The wall-normal velocity fluctuations are less revealing. Their amplitude is approximately half of the streamwise fluctuations (Fig. 4.10(g)-(l)). However, the spatial distribution of $\langle v' \rangle / u_\infty$ also returns a maximum in the near wake corresponding to the arc/ring vortices (Fig. 4.10(g)-(h), $x/h = 5$ and 15) and two symmetrical peaks at the turbulent non-turbulent interface tracing the boundaries of the turbulent wedge (Fig. 4.10(i)-(k), $x/h = 25, 40$ and 53). Also these statistical properties are in agreement with the hairpin vortex structures, especially the strong ejections at the hairpin head portion. In contrast, the flow region near the symmetry plane exhibits a comparatively lower level of fluctuations. The cross-sectional area occupied by turbulent fluctuations increases linearly in spanwise direction due to the formation of the turbulent wedge. It is not yet understood whether the system of streamwise vortices emerging from the time-averaged analysis, which also features a wedge-like pattern, has an active role in this scenario, or is solely the statistical result of the staggered occurrence of hairpin vortices in the wedge.

Nearing the downstream edge of the investigated domain (Fig. 4.10(f) and (l), $x/h = 70$), the flow exhibits a more homogeneous distribution of the streamwise velocity fluctuations. However, the symmetrical peak of velocity fluctuations at the border of the turbulent wedge ($y/h = 1, z/h = \pm 3.5$) can still be distinguished, indicating the persistence of the hairpin vortices propagating towards the undisturbed boundary layer. Brinkerhoff and Yaras (2014) observed that the regeneration of wavepackets of hairpin vortices at the edge the turbulent spot dominates its lateral spreading. It is hypothesized here that the sidewise propagation of the turbulent non-turbulent interface occurs by the formation of these large

coherent hairpin structures rather than small-scale isotropic turbulent fluctuations. Further evidence is given in the following section by the analysis of turbulence production.

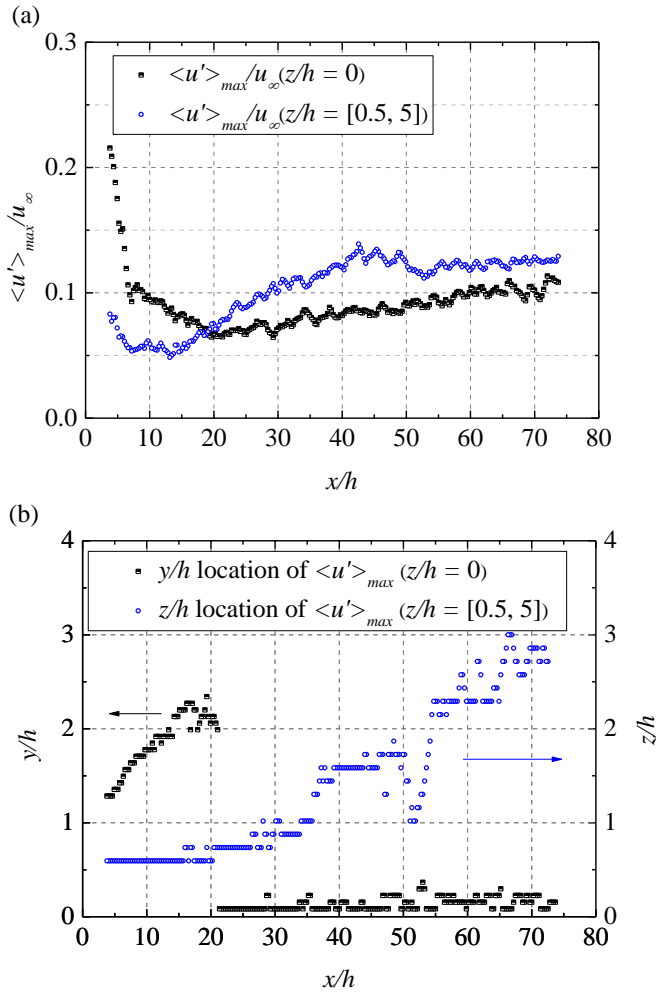


Fig. 4.12. Maximum streamwise velocity fluctuation ($\langle u' \rangle_{\max} / u_{\infty}$) evolution at $z/h = 0$ (half-solid black square) and $z/h = [0.5, 5]$ (open blue circle). (a) maximum velocity fluctuation magnitude at the symmetry plane and its sides, (b) corresponding location of maxima along wall-normal (y/h) and spanwise (z/h) direction.

The amplitude of the streamwise velocity fluctuations $\langle u' \rangle$ is further evaluated by characterizing the evolution of its maximum both in the symmetry plane ($z/h = 0$) and away from it ($z/h = [0.5, 5]$). Fig. 4.12 shows that in the upstream region $x/h = [3, 20]$, the streamwise velocity fluctuations are dominated at the symmetry plane by

the shear layer instability, as confirmed by the location of the maximum ($y/h > 1$). The amplitude is rapidly decreasing in combination with the upward motion of the shear layer from upstream to downstream in this range. Beyond $x/h = 20$, the near wall fluctuations intensify more rapidly along the wedge boundary rather than in the symmetry plane. This is followed by a spanwise dilation of the turbulent region indicating that hairpin vortices at the turbulent non-turbulent interface dominate the velocity fluctuations. At the most downstream location, the distribution of streamwise velocity fluctuations tends to become more homogeneous and the maximum at the symmetry plane approaches the value at the wedge boundary around $0.12u_\infty$. Although the values are distributed more homogeneously within the wedge in the spanwise direction, they are still in excess of values reported in turbulent boundary layers (Klebanoff et al. 1955, Spalart 1988).

As the laminar to turbulent transition starts with the growth of a turbulent region, its spatial development is characterized by the spreading angle of the turbulent wedge (Schubauer and Klebanoff 1956), which is an important aspect to be further characterised. The RMS of the streamwise velocity component ($\langle u' \rangle / u_\infty$) at a chosen $x - z$ plane ($y/h = 0.4$) is shown in Fig. 4.13, where the turbulent wedge exhibits a marked increase of streamwise velocity fluctuations compared with the laminar region. Schubauer and Klebanoff (1956) described the turbulent wedge as consisting of a fully turbulent core bounded by an intermittent region. De Tullio et al. (2013) studied the development of turbulent wedge using direct numerical simulation (DNS) and found that in the intermittent region, the TKE decreases sharply in comparison with the turbulent core. In the current study, a dramatic decrease of velocity fluctuation level can also be observed when moving from the turbulent core towards the boundary of turbulent wedge. The area of steep velocity fluctuation decrease is assumed to correspond to the intermittent region. A half spreading angle of approximately 4.6° is found, which agrees fairly with 5.2° reported in the numerical simulation of Brinkerhoff and Yaras (2014), where a micro-jet in cross-flow was used for triggering transition.

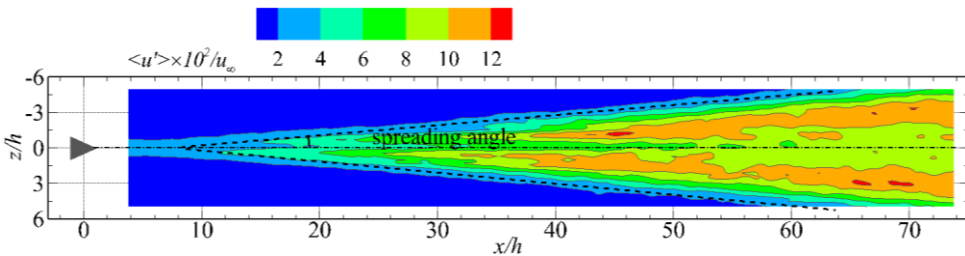


Fig. 4.13. $x - z$ cross-sectional contour ($y/h = 0.4$) of streamwise velocity fluctuation, $\langle u' \rangle / u_\infty$.

4.5.2 Turbulence production

The source of velocity fluctuations is characterized here with the production of turbulent kinetic energy, which provides the energy extracted by the mean flow

through the interaction of turbulent fluctuations and the shearing motion. Hereafter, the discussion focuses on the relation between coherent hairpin vortex structures and the production of turbulent kinetic energy. The production term follows the turbulent kinetic energy budget (Kundu and Cohen 1990) as

$$P = -\overline{u_i' u_j'} \frac{\partial \overline{u_j}}{\partial x_i} \quad (4.5)$$

The turbulence production term is expressed in non-dimensional form P^* by normalization with $(u_\infty)^3/h$. The spatial distribution of P^* is illustrated in Fig. 4.14 by colour-contours in $y-z$ cross-sections at six streamwise locations $x/h = 5, 15, 25, 40, 53$ and 70 . Contour lines of the streamwise velocity fluctuation and the approximate location of time-average streamwise vortices are added to ease the interpretation of results.

In the near wake (Fig. 4.14(a)(b), $x/h = 5$ to 15), a maximum is attained within the upper shear layer dominated by the arc-shaped K-H vortices. At $x/h = 15$, a secondary peak of production is observed at the bottom shear layer in the region where K-H vortices form a ring shape. Following the wake recovery process, the production strength located both at the upper and bottom shear layer decreases rapidly and becomes negligible from $x/h = 25$ (Fig. 4.14(c)).

Close to the wall (Fig. 4.14(b), $x/h = 15$), a peak of production near the symmetry plane is identified initiated by the excess wall shear. At the same location two side peaks are observed slightly outwards and above the secondary vortices. The persistence of secondary vortices induces the tertiary vortex pair, contributing to sidewise ejections, which in turn sustain the sidewise shear layer. The latter is ascribed to be the feeding mechanism for the onset of velocity fluctuations, ultimately transferring mean flow energy into turbulent kinetic energy. The current experiment shows that the strength of turbulent production intensifies moving downstream and concentrates along the turbulent wedge boundary with a pattern becoming relatively complex as it features several maxima. The first peak value is associated to the region of flow ejection with maximum upwash motion (Fig. 4.14(b), $x/h = 15, y/h = 0.7, z/h = \pm 0.7$). Another peak of turbulence production is observed close to the wall (more clearly resolved at $x/h = 25$ and 40 , Fig. 4.14(c)(d)), displaced towards the symmetry plane in comparison with the previous one. This maximum is ascribed to the increased wall-shear induced by the secondary pair of streamwise vortices in the upstream region. At $x/h = 40$, the sideward movement of the turbulence production peaks is observed accompanying the spanwise propagation of the turbulent wedge. The location of turbulence production coincides with the boundary of the turbulent wedge, where a high occurrence of coherent hairpin vortex structures is found. This pattern is observed further downstream (Fig. 4.14(e), $x/h = 70$), indicating a self-similar behaviour for the turbulent wedge front. At $x/h = 70$ also the turbulence production becomes relatively homogeneous with

4. Transition scenario at supercritical Re_h

peak value close to the wall due to excess wall-shear produced together by the secondary and tertiary vortices.

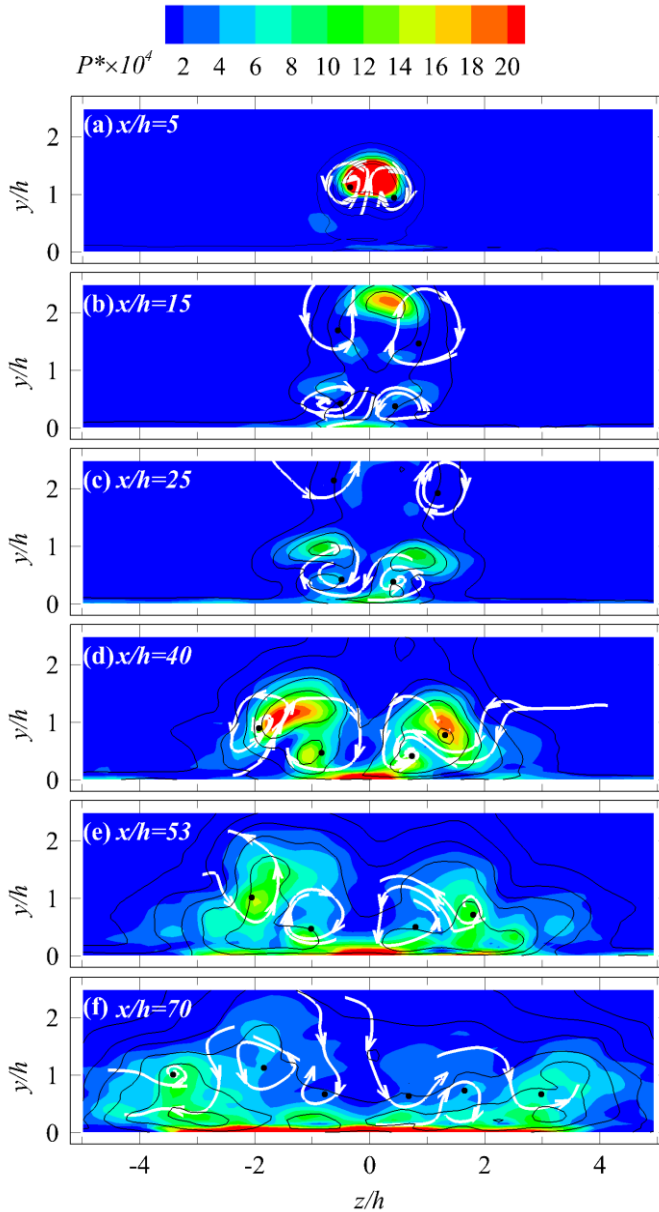


Fig. 4.14. Spatial distribution ($y-z$ cross-sections) of the turbulence production P^* by color contours. Solid-black contour lines represent the streamwise velocity fluctuation $\langle u' \rangle / u_\infty$. Projected streamlines (white) indicate approximate location of time-averaged streamwise vortices, black dots: the vortex core.

From the above scenario it can be concluded that the inception of turbulence production is given in the near-wake region by the secondary streamwise vortices with the combined effect of flow ejection and increased wall shear. Once established, the pattern is no longer dependent upon the secondary vortices as a cascade is produced along the edge of the turbulent wedge, where large-scale hairpin vortex structures are active in transferring mean flow kinetic energy into turbulence. The latter conduces to the propagation of turbulent fluctuations to the non-turbulent region.

4.6 Conclusion

The present study investigates the instantaneous three-dimensional organization of the flow undergoing laminar-turbulent transition induced by a micro-ramp at supercritical roughness-height based Reynolds number (Re_h).

The mean flow behind the micro-ramp exhibits a first pair of streamwise counter-rotating vortices as the dominant flow structure emanating from the ramp trailing edge and generating an upwash motion which induces a pronounced velocity deficit. The inflectional boundary layer profile preludes to the occurrence of Kelvin-Helmholtz (K-H) instability in the wake. A secondary pair of vortices is formed close to the wall, in turn inducing a tertiary vortex pair in the downstream region. The overall mean topology features several other quasi-streamwise vortices arranged in alternation and developing sidewise following a wedge shape, which is illustrated with the conceptual sketch in Fig. 4.15.

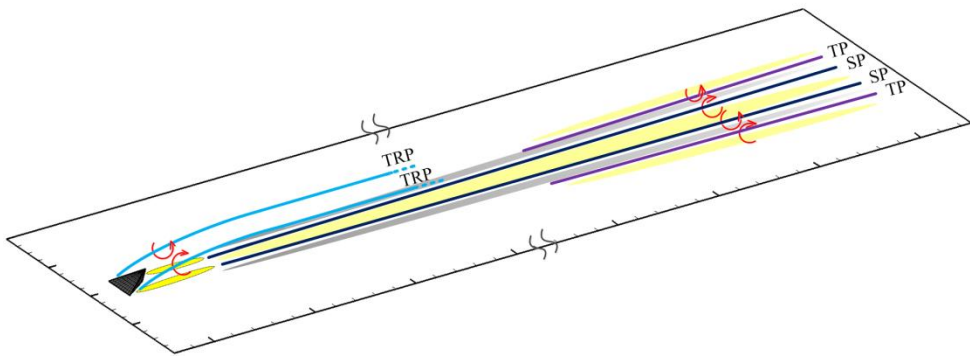


Fig. 4.15. Conceptual sketch of the flow topology in the wake of micro-ramp at supercritical Re_h . TRP, SP, and TP: trailing edge, secondary and tertiary vortex pair; blue and yellow projections: low- and high-speed regions.

Unlike the mean flow field, the instantaneous flow organization in the near wake is dominated by the K-H vortices in the separated shear layer, where they develop from arc-shape to hairpin and finally to ring shape (see Fig. 4.16). The vortex-to-vortex distance indicates the occurrence of vortex pairing prior to their disruption due to three-dimensional instabilities. Despite their intensity and

4. Transition scenario at supercritical Re_h

coherence, the fluctuations due to K-H instability rapidly travel upwards, losing contact with the near wall region, where the onset of transition is later observed. It is therefore concluded that for micro-ramp at current supercritical Re_h , the K-H vortices do not play an important role in the physical mechanism of forced transition.

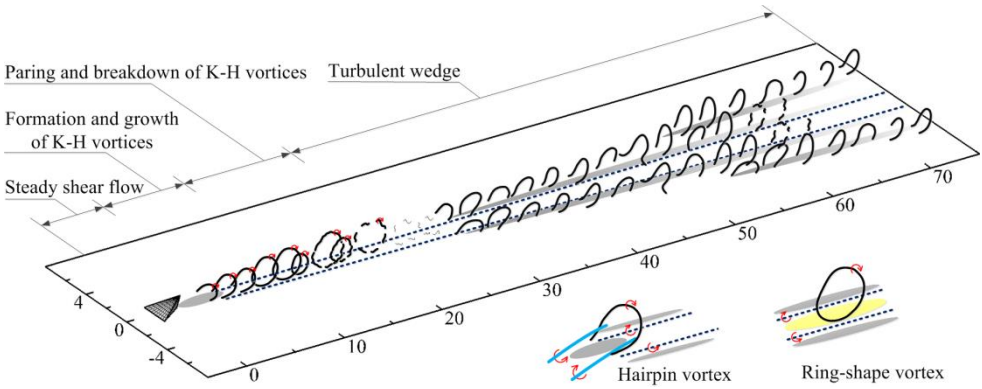


Fig. 4.16. Conceptual model of the transitional flow organization in the wake of micro-ramp; low- and high-speed region: grey and yellow projections; blue solid lines: TRP, dark blue dash lines: SP.

The generation of large-scale hairpin-like vortices in the downstream region is concentrated along the sides of a wedge-type region, which is confirmed as turbulent wedge. The global scenario depicts a cascade of hairpin vortices spreading spanwise with the wedge inner region characterized by small scale turbulent fluctuations. The highest values of turbulent kinetic energy as well as turbulence production are concentrated at the turbulent non-turbulent interface.

The inception point of these hairpins coincides with the region where secondary and tertiary streamwise vortices produce an asymmetric upwash motion (ejection), which acts as precursor to the formation of the first large-scale hairpin vortices. From the present observations it is therefore concluded that the secondary and tertiary streamwise vortices determine the mean flow conditions for the growth of unstable fluctuations leading to the generation of hairpin vortices, which the transition mechanism is associated to.

5

Reynolds number dependence of roughness- induced transition

Part of this chapter has been presented in *18th International Symposium on the Application of Laser and Imaging Techniques to Fluid Mechanics* (Ye et al. 2016).

The variation of transitional flow features past a micro-ramp when the Reynolds number is decreased approaching the critical regime is investigated. The experiments are performed in the incompressible regime at lower supercritical and critical roughness-height based Reynolds number ($Re_h = 730$ and 460) with tomographic PIV. Comparisons are made with the flow behaviour at $Re_h = 1170$. The time-averaged flow organization features with multiple counter-rotating vortex pairs. The primary vortex pair and induced central low-speed region is active over longer range when decreasing Re_h . In the instantaneous flow, at $Re_h < 1000$, the hairpin vortices induced by Kelvin-Helmholtz (K-H) instability progress gradually from close to the micro-ramp into the region where the overall shear layer is destabilized, indicating the correlation between the K-H instability and the onset of transition. The breakdown of K-H vortices as observed at $Re_h = 1170$, does not occur at lower Re_h . Decreasing Re_h , the secondary vortex structures make the first appearance significantly downstream, postponing the formation of sideward disturbances, which destabilize the local shear layer by ejection events. Proper Orthogonal Decomposition (POD) yields two major types of eigenmodes with symmetric and asymmetric spatial distribution of velocity fluctuations in the near wake, corresponding to the presence of vortex shedding and a sinuous wiggling motion respectively. Re_h is the key factor determining the importance symmetric mode. At $Re_h = 1170$, the disturbance energy of the symmetric mode decays before the onset of transition, indicating its insignificance. However, decreasing Re_h to 730 and 460 , the symmetric mode produces continuous growth of high level disturbance energy, leading to transition.

5.1 Introductory remarks

As addressed in sec. 2.3.1, the roughness-height-based Reynolds number has a first order impact on laminar to turbulent transition forced by surface roughness. Despite the intensive research on the effect of Re_h , most attention has been paid to the statistical analysis of perturbation growth and modal analysis in incompressible flow. Detailed analysis of the instantaneous flow organization depending upon the Reynolds number is necessary to consolidate the understanding of transition process. The previous chapter only dealt with the supercritical condition of micro-ramp induced transition. The unsteady flow behaviour closer to critical Re_h needs to be explored. Furthermore, it is particularly desired to identify the vortical structures that may contribute to the instability mechanism, leading to the interest in applying Proper Orthogonal Decomposition (POD), which is an efficient tool for data reduction in the field of fluid mechanics (Lumley 1967). The obtained eigenmode can shed light on the dominant flow features and facilitate the reduced order description of the flow field.

The present investigation employs tomographic PIV to capture the three-dimensional aspects of the evolution process towards transition in the wake behind a micro-ramp. Besides at $Re_h = 1170$, the current chapter also includes experiments conducted covering both lower supercritical and critical Re_h flow conditions ($Re_h = 730$ and 430). The flow conditions and boundary layer properties can be retrieved

from sec. 3.2. The system of streamwise vortices as well as the induced velocity distribution is identified in the time-averaged flow topology (sec. 5.2). The influence of Re_h on the instantaneous flow organization is visualized by the iso-surface of λ_2 criterion and non-dimensional streamwise vorticity (sec. 5.3). The full chapter corroborates the analysis with a statistical characterization of the velocity fluctuations (sec. 5.4). The POD analysis returns the most energetic spatial modes, which are later identified the symmetric and asymmetric components of the growing velocity fluctuations (sec. 5.5). The reduced-order model consisting of selected POD modes clarifies development of secondary vortex structures, giving rise to the lateral growth of perturbations.

5.2 Time-averaged flow topology

The time-averaged flow topology behind the micro-ramp is examined with the iso-surfaces of non-dimensional streamwise vorticity ($\omega_x^* = \omega_x \times h / u_\infty$) at $Re_h = 730$ and 460, shown in Fig. 5.1. A counter-rotating vortex pair, which induces a focussed upwash motion, emanates from the micro-ramp trailing edge at both flow conditions. From the side view, one can observe that this primary pair of vortices (VP1) is lifted up when moving downstream by the self-induced velocity (Crow 1970).

At $Re_h = 1170$ (Fig. 4.2), as discussed in Chap. 4, after the rapid lift-up, the primary vortex pair decreases its intensity due to the momentum mixing caused by Kelvin-Helmholtz vortices. As a result, the self-induced velocity decays and the pair remains at a constant wall-normal position of $y/h = 2$ from $x/h = 18$. Furthermore, this vortex system can no longer be distinguished from $x/h = 40$ (see Fig. 4.2(b)). The secondary vortex pair (VP2) is formed beneath the primary pair and appears to be already present at the most upstream region of the measurement domain. This vortex pair has opposite rotation and induces a focussed downwash fluid motion. Moreover, this vortex pair remains in contact with the wall due to its downward induced velocity. At $x/h = 25$, a tertiary vortex pair (VP3) is detected. Together with even further vortex pairs appearing at the spanwise side, the wake in the downstream region globally resembles a wedge shape. The upwash and downwash motions produced by the adjacent vortices expand spanwise the streaky velocity distribution.

When decreasing Re_h to 730 and 460 (Fig. 5.1(a)(b)), the primary vortex pair appears to be initially lifted up and then continues downstream with no significant reduction of its intensity. The rate of lift-up decreases with Re_h as expected, due to the lower initial vorticity magnitude and wall-normal velocity. When moving downstream, each vortex of the primary pair bifurcates into three branches distributed vertically. The first bifurcation appears at $x/h = 8$ and 10 for $Re_h = 730$ and 460 respectively (shown as B1 in Fig. 5.1(a)(b) side view). These two branches later re-connect into a single vortex again at $x/h = 26$ and 38. Starting from $x/h = 18$ and 28, a second bifurcation (B2) emerges. A subsidiary branch with lower vorticity magnitude appears on top of the major one. The former branch moves away from the wall with decreasing intensity, fading out completely at $x/h = 36$ and 48 without

uniting with the major branch. A secondary pair of counter-rotating vortex appears from $x/h = 8$ and 14 at $Re_h = 730$ and 460 respectively at the spanwise side of the primary pair instead of beneath, and with opposite rotation direction. The formation of a tertiary vortex pair outwards of the secondary one is significantly delayed with respect to the case at $Re_h = 1170$ as they appear from $x/h = 30$ and 45 . The overall vortical structure, although similar to the previous case, has an inverted sign for the vorticity in the downstream region, which is due to the persistence of the primary vortex pair as opposed to them lifted away from the wall at $Re_h = 1170$. The formation of a wedge shape region is also delayed and only a tertiary pair is observed within the present measurement domain.

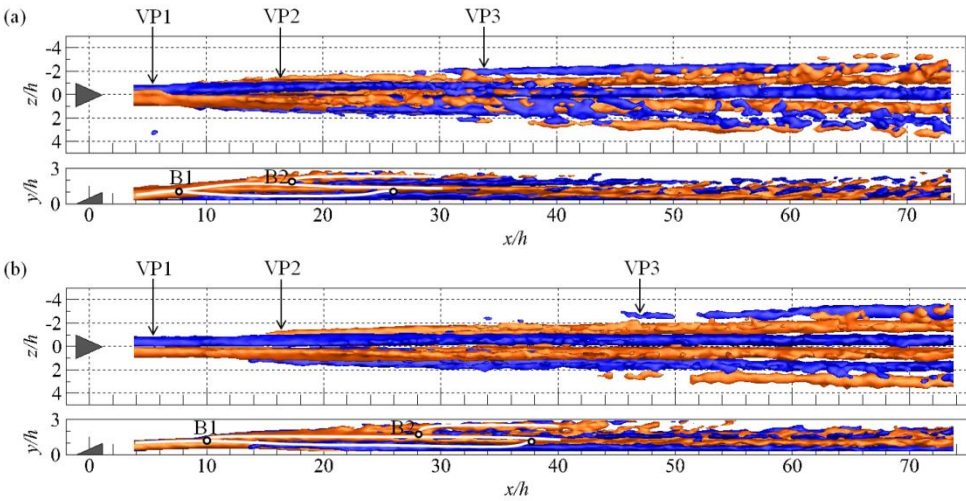


Fig. 5.1. Three-dimensional rendering of time-averaged streamwise vorticity (red and blue for clockwise and anticlockwise rotation vortices, $\omega_{x^*} = \pm 0.04$). (a) $Re_h = 730$, (b) $Re_h = 460$. Top (top) and side (bottom) view, the vortex bifurcation (B1) and reconnection (B2) points highlighted with white dots in the side view.

The spanwise modulation of momentum caused by the action of the streamwise vortices determines the spatial distribution of the low- and high-speed regions in the wake of the micro-ramp. The difference between the time-averaged streamwise velocity (u/u_∞) and the undisturbed boundary layer (u_{bl}/u_∞) is considered here as $u_d/u_\infty = (u - u_{bl})/u_\infty$. This approach allows to visualize the regions with lowered momentum (deficit) and those where the momentum is increased (exceed) as typically due to downwash motion or turbulent mixing. The analysis is shown at four $y-z$ cross planes located at $x/h = 5, 25, 52$ and 70 in Fig. 5.2. The contour lines of streamwise velocity and selected projected streamlines are superimposed on the colour contours of the non-dimensional streamwise velocity difference (u_d/u_∞).

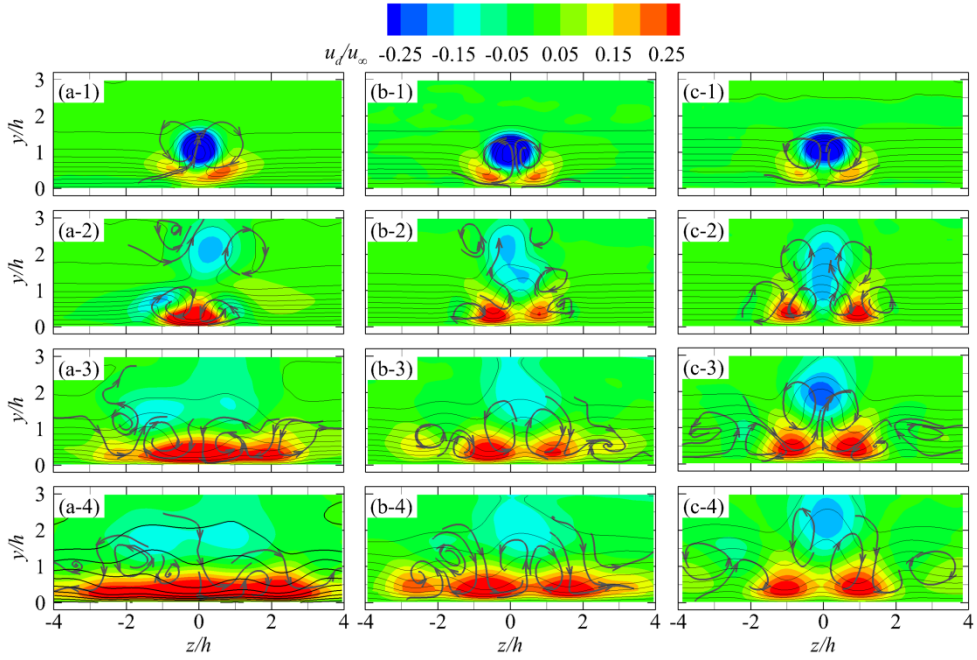


Fig. 5.2. Streamwise velocity difference u_d/u_∞ at $y-z$ cross planes, with contour lines of $u/u_\infty = [0, 1]$ of 0.1 interval; flow topology shown with selected streamlines; (a) $Re_h = 1170$, (b) $Re_h = 730$, (c) $Re_h = 460$; 1: $x/h = 5$, 2: $x/h = 25$, 3: $x/h = 52$, 4: $x/h = 70$.

Close to the micro-ramp ($x/h = 5$) a pronounced low-speed region is present around the symmetry plane bounded by two high-speed regions close to the wall. This effect is seen irrespective of the Re_h and is produced by the central upwash and lateral downwash motion of the primary vortices. The magnitude of the velocity difference u_d along low- and high-speed regions shows small variation with the change of Re_h , which is $u_{d,min}/u_\infty = [-0.60, -0.61, -0.57]$, and $u_{d,max}/u_\infty = [0.24, 0.23, 0.20]$ corresponding to $Re_h = [1170, 730, 460]$. Similarly, Fransson and Talamelli (2012) reported that the velocity streak amplitude $(u_{d,max} - u_{d,min})/2$ behind the micro-ramp remains at a relatively constant value when Re_h is above the critical value. A rapid decrease in magnitude of the central low-speed region is observed at $Re_h = 1170$ (Fig. 5.2(a)), which lifts up and cannot be detected beyond $x/h = 52$. A connection of the high-speed regions occurs at the most upstream region due to the fast lift-up process of the primary vortices and the early appearance of the secondary pair. The former regions merge at $x/h = 25$, leading to an increased velocity exceed magnitude of $0.51u_\infty$. Two newly formed sideward low-speed regions can be observed at this streamwise location, due to the sideward upwash motion produced by the secondary vortices. Further downstream at $x/h = 52$ and 70 , as the flow becomes turbulence, the wake exhibits a relatively homogenous distribution of the high-speed region close to the wall, due to turbulent transportation. Nevertheless, two low-speed regions can still be detected on top of it with lower magnitude, indicating the

persistence of sideward upwash motion. On the other hand, at $Re_h = 730$ and 460 , the central low-speed region as well as the induced inflectional velocity profile persist till the most downstream measurement location due to the more stable action of primary vortex pair, in favour of the amplification of turbulent fluctuations. The increase in magnitude of the high-speed regions (to $u_{d,max} = 0.35u_\infty$ and $0.33u_\infty$ for $Re_h = 730$ and 460 respectively, at $x/h = 25$) is slower due to the late inception of secondary vortex pair and weaker downwash motion. The connection of high-speed regions is postponed downstream to $x/h = 25$ and 52 , without the appearance of merging. Aside of the high-speed regions, two low-speed region with rather weak intensity can also be observed due to the upwash motion induced by the joint action secondary and tertiary vortex pair. The global active area of velocity streaks is comparable smaller at lower Re_h .

5.3 Instantaneous flow organisation

The interaction between the micro-ramp and the laminar boundary layer produces a separated shear layer at all flow condition considered, where the velocity exhibits an inflectional profile susceptible to Kelvin-Helmholtz (K-H) instability. The latter instability leads to the formation and growth of hairpin-like vortices in regular succession. The importance of K-H instability on the overall transition process highly depends on Reynolds number (Choudhari et al. 2010). At $Re_h = 1170$, K-H vortices lose the spatial connection with the onset of the turbulent wedge in the wake of micro-ramp, indicating that K-H instability does not play a role in transition (Chap. 4). In the current experiments, when Re_h approaches the critical value, a different pattern and evolution process of K-H vortices is observed in the wake. The instantaneous organization of vortices is visualized by the iso-surface of a vortex detection criterion based on the second eigenvalue of the velocity gradient tensor λ_2 (Jeong and Hussain 1995) and the non-dimensional instantaneous streamwise vorticity (ω_x^*), as shown in Fig. 5.3 and Fig. 5.4.

The similarity in flow behaviour at $Re_h = 730$ and 460 pertains not only to the time-averaged flow pattern but also to the instantaneous organization of vortex structures. In comparison with $Re_h = 1170$, the shear layer emanating from the trailing edge exhibits relatively steady state conditions within a finite streamwise range ($x/h < 6$ and 8 at $Re_h = 730$ and 460 respectively). The primary streamwise vortex pair is formed immediately after the ramp as shown in Fig. 5.3. Downstream, the train of K-H vortices forming in the separated shear layer exhibits a strain dominated hairpin-like shape, with approximately 40° and 25° initial inclination angle in the head region at $Re_h = 730$ and 460 respectively. These vortices are spaced at regular intervals with a wavelength at inception of approximately $\lambda/h = 2.1$ at $Re_h = 730$ and 3.5 at $Re_h = 460$, which varies consistently with the increased vorticity thickness of the shear layer (Lesieur 2012). Unlike the rapid distortion process occurring at $Re_h = 1170$, the K-H vortices here appear to persist over a significantly longer streamwise distance. The first marked difference is that the K-H vortices are not fully lifted up under the effect of the self-induced upward motion of the primary vortex pair. This is particularly marked at $Re_h = 460$, where the K-H vortices are

significantly stretched becoming elongated in the streamwise direction. At $Re_h = 730$, vortex pairing is observed starting from $x/h = 14$. Instead at critical Re_h , no evidence of the occurrence of pairing is found.

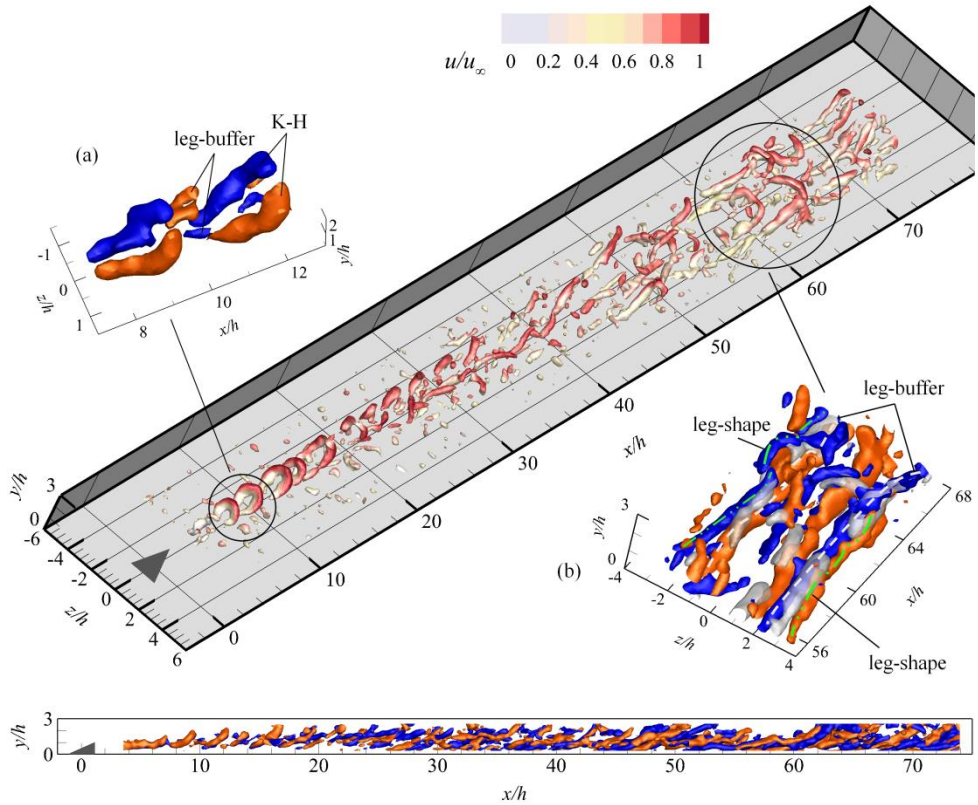


Fig. 5.3. The instantaneous flow pattern at $Re_h = 730$, perspective view detected by λ_2 criterion ($\lambda_2 = -0.07$) colour-coded by u/u_∞ . (a)(b) and side view: streamwise vorticity, red and blue for clockwise and anticlockwise rotation vortices, $\omega_x^* = \pm 0.3$; (b) grey iso-surface: low-speed regions shown by $u'/u_\infty = -0.15$, leg-buffer and leg-shape vortices highlight with white dash and green dash-dot lines.

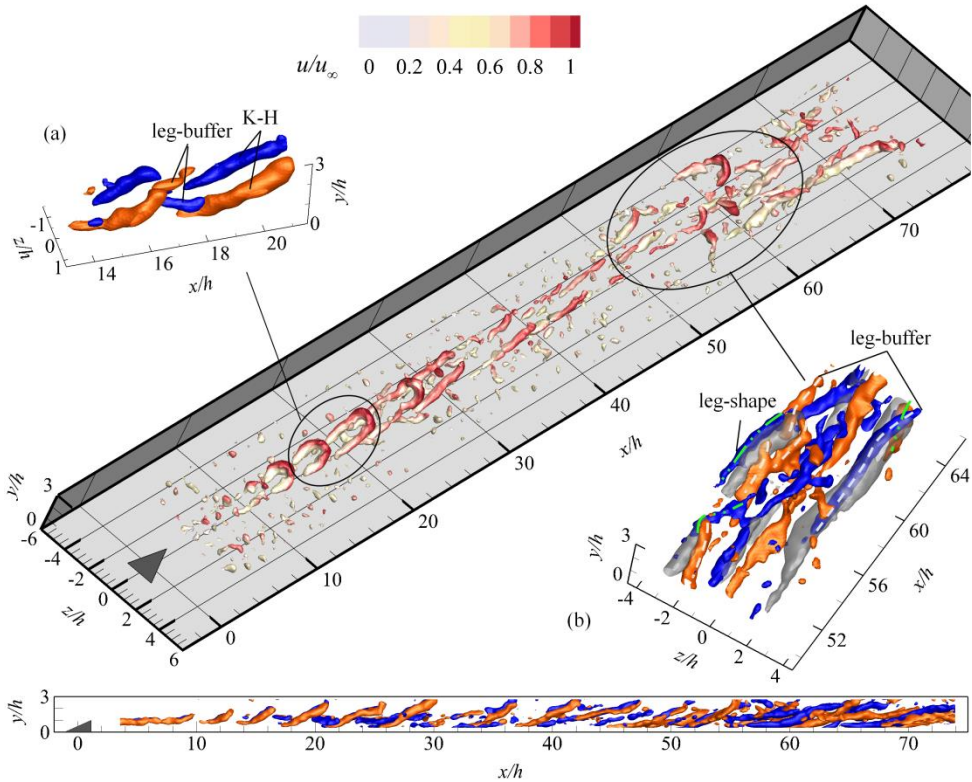


Fig. 5.4. The instantaneous flow pattern at $Re_h = 460$, perspective view detected by λ_2 criterion ($\lambda_2 = -0.06$) color-coded by u/u_∞ . (a)(b) and side view: streamwise vorticity, red and blue for clockwise and anticlockwise rotation vortices, $\omega_x^* = \pm 0.3$; (b) grey iso-surface: low-speed regions shown by $u'/u_\infty = -0.15$, leg-buffer and leg-shape vortices highlight with white dash and green dash-dot lines.

Here, only the flow behaviour at $Re_h = 460$ is examined in detail for conciseness. The K-H vortices being intensively stretched while convecting downstream lead to a significantly elongation of the leg portion and a gradually decreased inclination angle. The elongated leg portion of the K-H vortex tends to move towards the wall. On the other hand the head portion is lifted up and eventually detaches from the legs. In the present experiments, the hairpin heads cannot be followed in their full evolution as they leave the measurement domain from $x/h = 30$. A plateau is formed in the hairpin leg in the range of $x/h = [20, 35]$, as shown in the side view in Fig. 5.4. Head and Bandyopadhyay (1981) explained the presence of this plateau region as a condition of equilibrium between two opposing effects, namely the shear layer imposing a rotation towards the wall and the upward induced velocity by the two legs that concur with the primary vortex pair.

The gap between two neighbouring hairpins legs sees the onset of an additional small structure, denoted here as *leg-buffer* with opposite rotation direction due to

the mutual induction effect of the legs, as shown by the iso-surface of streamwise vorticity ω_x^* in Fig. 5.4 (a). The leg-buffer vortices draw vorticity from the bifurcated shear layer, leading to the growth in length and width. They move away from the symmetry plane and are aligned at the spanwise side of the K-H vortices. The action of the leg-buffer structures is coherent with that of the time-averaged secondary vortex pair discussed in the mean flow organisation. It has been conjectured that the secondary vortex pair emerges as an artefact of temporal averaging of leg-buffer vortices and does not occur in the instantaneous flow organisation (Elsinga and Westerweel 2012). The further intensity increase of the leg-buffer vortices gives rise to another unique large *leg-shape* vortex structure outwards (Fig. 5.4(b)). The strong sideward ejection event, induced by the combined motion of the former vortices, transports low momentum flow to the outer boundary layer. The resulted sideward low speed region (highlighted with grey iso-surface of negative streamwise velocity fluctuations, $u'/u_\infty = -0.15$) and inflection points are susceptible to the further growth of perturbation. The local high-shear layer at the sideward low speed regions produces the spanwise vorticity, which roll up and connect with the leg-buffer or leg-shape streamwise vortices (Fig. 5.4, $x/h = 60$, $z/h = [-4, -2]$). As a result, new hairpin vortices are generated away from the symmetry plane. The leg-buffer and leg-shape vortices produce a wedge shape vortex pattern globally due to their spanwise movement, resembling the structure of turbulent wedge as observed at $Re_h = 1170$. At $Re_h = 460$, due to the late inception of the sideward hairpin vortices, only the very early stages of the turbulent wedge are intermittently captured. The U-shape vortex packets consisting the neighbouring leg-shape, leg-buffer vortices and the K-H roller appear occasionally at the early stage of turbulent wedge (Fig. 5.4(b)), indicating the onset of transition (Singer and Joslin 1994).

In summary, at $Re_h = 730$ and 460 , the primary vortex pair of time-averaged flow as well as the K-H rollers in the instantaneous flow persist over a longer streamwise range compared with $Re_h = 1170$. However, the onset of secondary and tertiary vortex pair is postponed downstream when decreasing Re_h . The transition process is significantly delayed, showing as the late inception of turbulent wedge. The onset location and relevant properties of the aforementioned vortical structures at all three Re_h are summarized in Tab. 5.1.

Tab. 5.1. Comparison between vortical structures at different Re_h .

| Re_h | 1170 | 730 | 460 |
|---|---------|---------|----------|
| Streamwise range of primary vortices (x/h) | < 40 | < 75 | < 75 |
| Onset of the secondary vortices (x/h) | 4 | 8 | 14 |
| Onset of the tertiary vortices (x/h) | 25 | 30 | 45 |
| Wavelength of K-H vortices at inception (λ/h) | 1.45 | 2.10 | 3.50 |
| Streamwise range of K-H vortices (x/h) | [5, 25] | [6, 75] | [10, 75] |

5.4 Disturbance energy and growth

The values of Re_h selected within this work span from around to above the critical level. Therefore the perturbation imparted by the micro-ramp is expected to trigger boundary layer transition even at the lowest $Re_h = 460$. The evolution of velocity fluctuations introduced by the micro-ramp is quantitatively characterized with the integrated disturbance energy, following the definition of Ergin and White (2006), as

$$\varepsilon_{rms}(x) = \iint_{S_{wake}} (\langle u'(x, y, z) \rangle / u_\infty)^2 d\left(\frac{y}{h}\right) d\left(\frac{z}{h}\right) \quad (5.1)$$

where $\langle u' \rangle / u_\infty$ is the non-dimensional RMS fluctuations of the streamwise velocity component. S_{wake} is the area of the micro-ramp wake region, in which $\langle u' \rangle / \langle u' \rangle_{max} \geq 0.3$. An example of wake boundary at selected cross-plane ($x/h = 70$, $Re_h = 1170$) is shown by the contour line of $\langle u' \rangle / u_\infty = 0.06$ in Fig. 5.5. The maximum RMS fluctuations $\langle u' \rangle_{max} / u_\infty = 0.06$ in this case. In the work of Ergin and White (2006), the spanwise extent of the velocity fluctuation region remains constant along the streamwise direction after the flow becomes turbulent due to the limited spanwise distance between neighbouring roughness elements. In the present case, the region of active fluctuations evolves downstream following a wedge-like distribution. For a full comparison with the above work, the disturbance energy is also evaluated by the mean value over the active wake region (referred to as *local disturbance energy*, $\varepsilon_{local} = \varepsilon_{rms} / S_{wake}$).

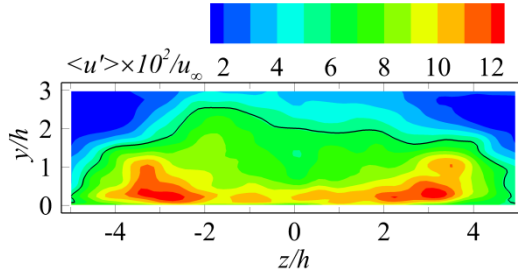
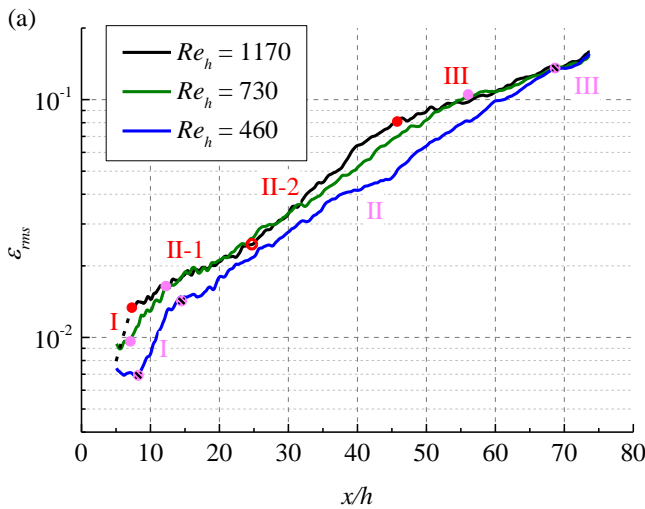


Fig. 5.5. y - z cross-plane contour of $\langle u' \rangle / u_\infty$ at $x/h = 70$, $Re_h = 1170$; superimposed with the contour line of $\langle u' \rangle / u_\infty = 0.06$.

The streamwise evolution of ε_{rms} at all Re_h is shown in Fig. 5.6(a). The range of reliable data begins from approximately $x/h = 7$. Upstream of that point spurious fluctuations are ascribed to the decreased tomographic accuracy close to the edge of the reconstructed domain (Elsinga et al. 2006). As a result, the initial energy growth produced by K-H instability is not captured at $Re_h = 1170$. The dashed line indicates the expected trend of this stage (stage I) as inferred from the analysis of high-resolution planar PIV experiments. Downstream in the range of $x/h = [7, 25]$ (stage

II-1), the integrated disturbance energy undergoes exponential growth, followed by a further intensification in $x/h = [25, 46]$ (stage II-2). The streamwise location of the turning point coincides with the inception of tertiary vortex pair in the mean flow field. The former vortex pair is considered as the precursor to turbulent wedge leading to spanwise propagation of disturbance (also sec. 4.2). Further downstream ($x/h > 46$, stage III), the growth of ε_{rms} is retarded. The range of stage III agrees with that of turbulent wedge (see Tab. 5.1), indicating the establishment of turbulent flow. Different from the observation of Ergin and White (2006), in which the growth of energy is saturated, the spanwise spreading of turbulent wedge lead to linear growth of ε_{rms} . The local disturbance energy (ε_{local}) is calculated in the range of $x/h > 25$ (shown in Fig. 5.6(b)), from which on the tertiary vortices are formed (see Tab. 5.1). The ε_{local} reaches a plateau in stage III, confirming the turbulent condition.

Decreasing the Re_h to 730 and 460, the magnitude of ε_{rms} reached is comparable or lower in the same streamwise range, suggesting that the wake of micro-ramp is more stable at lower Re_h . The initial exponential growth of K-H instability is well measured (stage I). The second stage of lower growth rate persists in a longer streamwise range until $x/h = 56$ and 68 at $Re_h = 730$ and 460 respectively, in consistence with the active area of the primary vortex pair. Downstream, as the flow becomes turbulent, the ε_{rms} also follows the linear area growth of the turbulent wedge (stage III), corresponding to a saturation of the local disturbance energy ε_{local} (Fig. 5.6(b)). The integrated disturbance energy reaches the same level in stage III at all flow conditions. The late inception of the former stage indicates that the onset of transition is delayed gradually with the decrease of Re_h , which agrees with the observations in the instantaneous flow organisation (sec. 5.3).



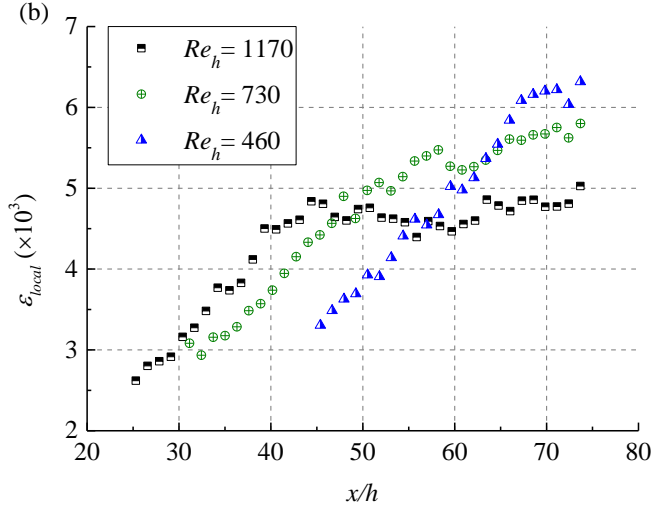


Fig. 5.6. Streamwise evolution of integrated (a) and local (b) disturbance energy; the measurement noise level: (a) 4×10^{-3} , (b) 1.4×10^{-4} .

5.5 POD analysis

The snapshot POD method is applied to the three-dimensional velocity field to reveal the statistical pattern of the most energetic fluctuations as well as its contribution to the growth of disturbance, which possibly leads to the laminar to turbulent transition. The analysis is performed in a limited streamwise range before the start of fully turbulent flow at all Re_h ($x/h < 45, 55$ and 65 for $Re_h = 1170, 730$ and 460 respectively), as the latter contains mostly uncorrelated turbulent fluctuations (Wu and Moin 2009, Sayadi et al. 2014), making the modal decomposition less efficient and would mask the features in the laminar and transitional state. The spanwise range of the domain is also truncated to the wake region to remove the effect of the measurement noise at the edge of the domain. At all the flow conditions, an ensemble size of 200 snapshots is used to perform the snapshot POD analysis, following the procedure described in sec. 3.9.1.

Contribution of the first 45 modes to the total disturbance energy is demonstrated in Fig. 5.7. Different from the POD analysis in the wake flow of the blunt body (Van Oudheusden et al. 2005) or jet flows (Kirby et al. 1990), in which the largest amount of energy is captured by a small number of eigenmodes (usually first two modes), small energy variation between low- and high order modes is observed in the current analysis. This is due to the presence of multi-flow-scales structures that play a role in the development of transitional wake, which requires a large number of modes to be reliably reconstructed. Similar ‘flat’ energy distribution has also been observed in the transitional boundary layer developing along a swept wing, in which crossflow instability plays an important role (Serpieri and Kotsonis 2016) and the unsteady base flow at supersonic condition (Humble et al. 2007). As the unsteadiness of the micro-ramp wake is stronger at higher Re_h , the decrease of

energy towards higher POD modes becomes moderate, resulting in 24% of the total energy being captured by the first 20 eigenmodes, lower than 30% and 36% at $Re_h = 730$ and 460, respectively.

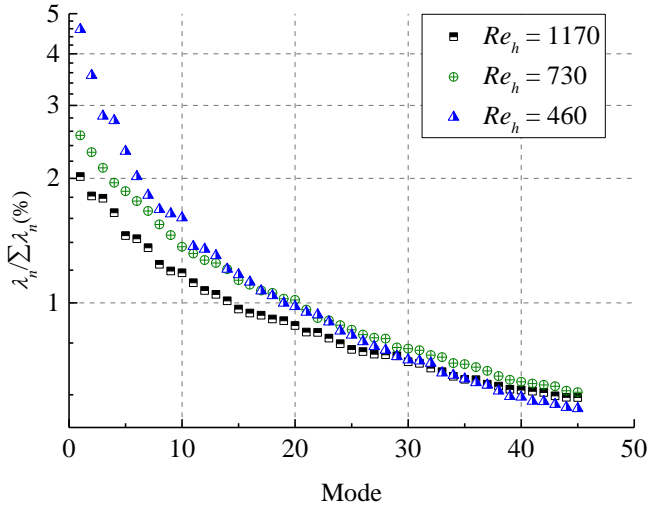


Fig. 5.7. Relative energy distribution of the first 45 POD modes.

As a result, the relative disturbance energy of each single mode does not directly represent its importance to the coherent structure. On the other hand, the correspondence between the pattern of POD modes and the development of specific flow instability becomes critical in identifying the contribution of the modes to transition. In the current experiments, one dominant feature is the vortex shedding phenomenon at all flow conditions, featuring K-H vortices that convect downstream. The latter vortices introduce high amplitude velocity fluctuations. Pair of POD modes is expected to be achieved with $\pi/2$ phase shift to describe the convection behaviour (Van Oudheusden et al. 2005, Lengani et al. 2014). Another general flow pattern is the formation of the turbulent wedge in the downstream region featuring spanwise inclined hairpin vortices. Both flow features can be an important criterion in the selection of dominant POD modes. Due to the similarity in the flow topology as well as the transition process at $Re_h = 730$ and 460, only the latter case will be discussed.

5.5.1 Pattern of POD modes

5.5.1.1 Supercritical condition: $Re_h = 1170$

At $Re_h = 1170$, the first three POD modes are selected to depict the dominant unsteady flow features. The iso-surface of normalized streamwise velocity fluctuation component ($\varphi_{n,u}/u_\infty = \pm 1.2 \times 10^{-4}$) is shown in Fig. 5.8.

Mode 1 and 2 are clearly coupled, as demonstrated by the similar spatial distribution of velocity fluctuations. They appear in phase quadrature and therefore, they combine into a travelling wave. In the range of $x/h = [7, 18]$, the iso-surfaces of velocity fluctuations form distinct patches of alternating sign. Each single patch consists of two portions: an arch-shape structure close to the symmetry plane tilting upstream and two downstream inclined leg-shape structures. The initial wavelength ($\lambda_{0,s}$) of this wavy structure is 1.45, in relation with that observed for the K-H vortices from instantaneous flow topology (Lengani et al. 2014). The visualization through these modes allows a clearer definition of the region dominated by the K-H rollers ($x/h = [7, 18]$). The velocity patch exhibits good spanwise symmetry with respect to the mid-span plane (referred to as *symmetric mode*). The symmetrical distribution of the perturbation is consistent with the varicose-type mode in the wake of roughness element issued from stability analysis (Choudhari et al. 2010, De Tullio et al. 2013, Loiseau et al. 2014), contributing to the periodic shedding of hairpin vortices. As reported by Loiseau et al. (2014), although the varicose mode appears initially at the wake centre, it propagates spanwise and occupies the whole domain width. However, in the present POD analysis, the velocity fluctuation patches in mode 1 and 2 remains confined within a limited spanwise range ($z/h = [-0.5, 0.5]$). The intensity of the patches attenuates rapidly in the range $x/h = [16, 20]$ and becomes negligible beyond $x/h = 22$. To some surprise, the vortex pairing observed in the instantaneous snapshots that leads to stronger ring vortices and a longer distance between subsequent vortices (sec. 4.4.1) is not captured within this modal decomposition. This may be due to the small energy and coherence of this regime along with the intermittent behaviour of vortex pairing.

Moving downstream to $x/h = 28$ in mode 1, elongated structures appear close to the wall, away from the symmetry plane, with alternate positive and negative sign. These structures are oblique to the streamwise direction and point inwards by approximately 30° , with a wavelength of approximately $5h$. They correspond to the inception of the second amplification of turbulent fluctuations. The oblique patches spread in the spanwise direction and resemble a wedge shape with a scenario similar to that reported for the growth of the laminar-turbulent interface of turbulent spot (Duguet and Schlatter 2013, Couliou and Monchaux 2016), featuring oblique velocity streaks. Consequently, the oblique patches are regarded as the preliminary feature of the turbulent wedge in the current condition, preserving the spanwise growth of turbulent fluctuations.

In mode 3 (Fig. 5.8(c)), a different pattern is exhibited in the near wake ($x/h = [8, 20]$). The patches of alternating sign have weaker amplitude compared with the previous two modes and tend to distribute in a more staggered pattern, losing the spanwise symmetry (referred to as *asymmetric mode*). Only the upstream inclined arch-shape structure appears in the patch. Their inception is postponed to $x/h = 8$. No pair of eigenmode arises in this case. As observed in the sinuous instability mode (Asai et al. 2002, Loiseau et al. 2014), the asymmetric mode is assumed to modulate the flow field into a sinuously wiggling pattern. However, as the magnitude of the asymmetric patches in mode 3 is remarkably lower than the symmetric mode (1 and

2), the sinuous modulation to the K-H vortices is found in the instantaneous flow. Starting from $x/h = 21$, larger oblique patches are observed close to the wall, resembling the spatial distribution to that in mode 1 and 2, with higher fluctuation intensity and longer wavelength of approximately $10h$.

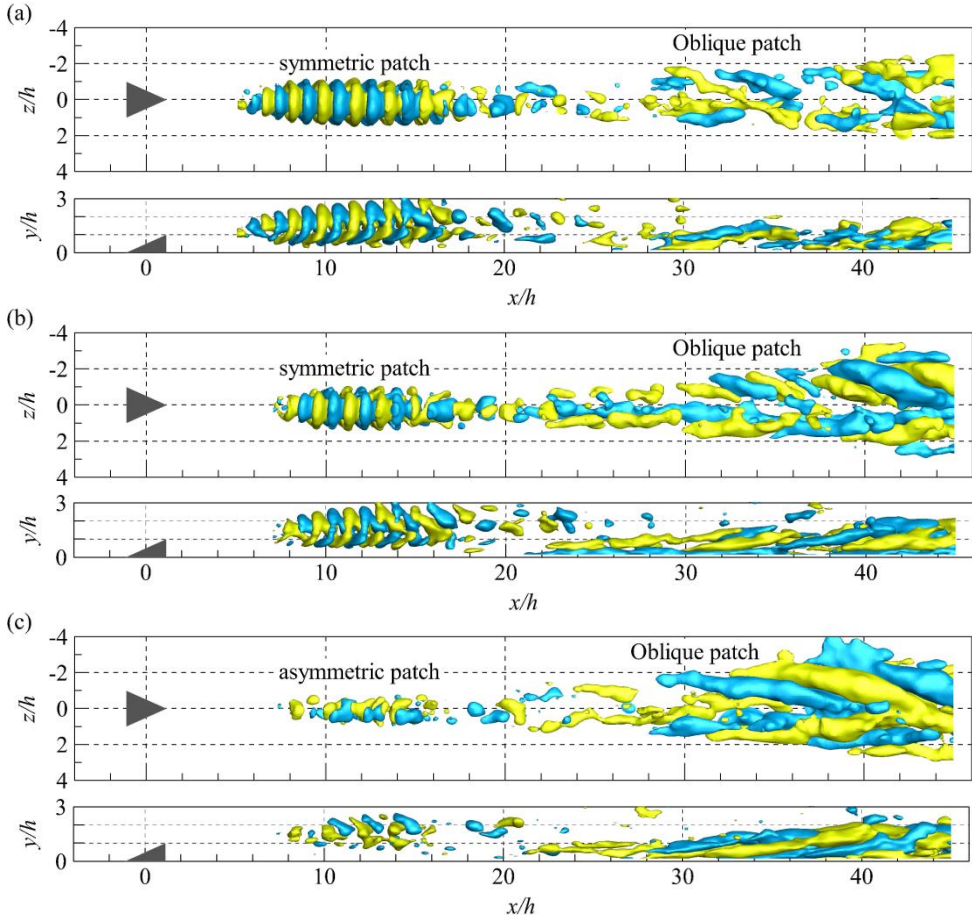


Fig. 5.8. Streamwise velocity fluctuation component of POD modes at $Re_h = 1170$ ($\varphi_{n,u}/u_\infty = \pm 1.2 \times 10^{-4}$), (a)(b)(c): mode 1, 2 and 3.

5.5.1.2 Critical condition: $Re_h = 460$

Both symmetric and asymmetric modes are found at critical Re_h . The differences in pattern and evolution of the streamwise velocity fluctuations are characterized by the selected POD modes 1, 2, 4 and 5, as shown in Fig. 5.9. In this flow condition, mode 1 converts into an asymmetric spatial distribution (Fig. 5.9(a)). A more pronounced spanwise shift of velocity fluctuation patches of alternating sign can be observed around the symmetry plane compared with the asymmetric mode

(mode 3) at $Re_h = 1170$, indicating a stronger sinuous modulation to the central low-speed region as well as the hairpin vortices by this mode. Similarly, no coupled POD mode appears. The active range of the velocity patches extends from $x/h = 10$ until 40, continuing with the streamwise velocity streaks downstream. Instead of remaining close to the symmetry plane, the asymmetric mode spreads in the spanwise direction by inducing positive and negative velocity fluctuation streaks sideward, contributing to the growth of unsteadiness at the spanwise shear layer between neighbouring low- and high-speed regions in the mean flow (see Fig. 5.2). The velocity fluctuation streaks persist till the downstream end of the domain, maintaining high amplitude. The structures resemble a wedge shape globally. The oblique patches do not emerge in this mode.

The symmetric mode pair in quarter phase shift are detected as mode 4 and 5 (Fig. 5.9(c)(d)). The coupled range appears in $x/h = [8, 45]$, featuring downstream inclined hairpin-shape velocity fluctuation patches. The initial wavelength λ_{s0}/h of the former modes is $3.5h$, which is also identical to that of K-H vortices. As a result, this mode pair contributes to the shedding phenomenon of the K-H vortices. The inclination angle of the patches becomes smaller at lower Re_h , which agrees with the stability analysis in the wake of bump (Cherubini et al. 2013). The shape variation of the velocity fluctuation patch is similar to the hairpin vortices, which is stretched and elongated, with the lift-up of the head portion and the extension of the leg portion towards the wall. The spanwise propagation of the patches is initiated by the generation of velocity fluctuation filaments close to the wall, with increasing magnitude developing downstream. From $x/h = 45$, elongated patches away from the symmetry plane of spanwise symmetric can be detected, with larger size compared with the feature at $Re_h = 1170$. It is conjectured that the former patches are induced by the fluctuation filaments after they reach certain large magnitude. These patches exhibit a different pattern compared with the oblique structures observed at $Re_h = 1170$. The features of these elongated patches is particularly evident in mode 2 (Fig. 5.9(b), $x/h > 40$), where the hairpin component is less dominant. The symmetric elongated patches are connected by a large-scale velocity fluctuation blob close to the symmetry plane, resembling a 'A' shape as a whole. Unlike the spatial separation observed in $Re_h = 1170$, the elongated patches downstream and the upstream symmetric patches appear to be entangled. Moreover, no interruption of the fluctuation amplitude is observed, indicating a strong correlation between the K-H vortices regime and the onset of the turbulent wedge.

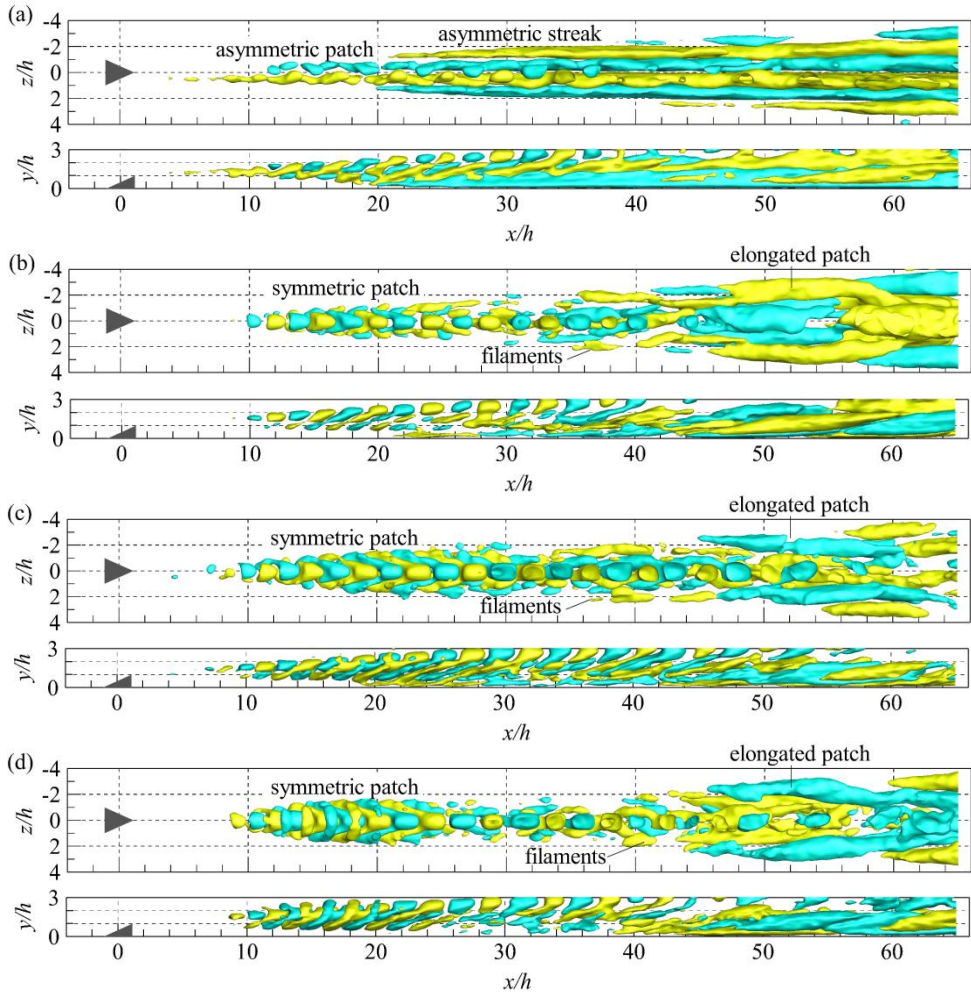


Fig. 5.9. Streamwise velocity component of POD modes at $Re_h = 460$ ($\varphi_{n,u}/u_\infty = 1.0 \times 10^{-4}$); (a)(b)(c)(d): mode 1, 2, 4 and 5.

5.5.2 Symmetry of disturbance energy

A quantitative assessment of the integrated disturbance energy (ε_{rms}) produced by the symmetric and asymmetric type of POD modes is provided. All the modes having symmetric and asymmetric disturbance distribution are selected from the first 41, 32 and 24 modes for $Re_h = 1170$, 730 and 460 respectively, taking 40% of the total energy into account. Higher order modes are neglected, as their energy becomes negligible and high frequency components are increasingly corrupted by measurement noise. The detection of the mode type is performed by means of spatial auto-correlation function of the streamwise velocity fluctuation component ($\varphi_{n,u}/u_\infty$) at selected y - z cross-plane. The correlation map showing either varicose or sinuous distribution revealing symmetry or asymmetry in the mode. Modes with a

5. Reynolds number dependence of roughness-induced transition

normalized autocorrelation coefficient higher than 0.1 are considered in the analysis. The number of symmetric and asymmetric modes at each Re_h is given in Tab. 5.2. The streamwise velocity fluctuations are reconstructed using equation (3.21). The streamwise evolution of the integrated disturbance energy is shown in Fig. 5.10. Close to the micro-ramp at all flow conditions, the disturbance energy produced by the symmetric modes grows rapidly after the appearance of K-H vortices, exhibiting remarkably higher contribution to the total integrated disturbance energy with respect to the asymmetric modes.

Tab. 5.2. Number of symmetric and asymmetric POD modes at three Re_h

| Re_h | $N_{symmetric}$ | $N_{asymmetric}$ |
|--------|-----------------|------------------|
| 1170 | 5 | 5 |
| 760 | 11 | 2 |
| 460 | 15 | 1 |

At $Re_h = 1170$, the ε_{rms} of symmetric modes reaching the maximum amplitude at $x/h = 11$, following by a rapid decrease until $x/h = 21$. Downstream from $x/h = 24$, the second ascending of the ε_{rms} occurs, increasing until the downstream extend of the domain. Differently, the ε_{rms} produced by asymmetric modes undergoes exponential growth in the range of $x/h = [7, 42]$, intensifying beyond the level of symmetric modes from $x/h = 21$. The maximum energy magnitudes reached by both modes are comparable.

At $Re_h = 730$ and 460 , although the first mode is asymmetric type, the relative energy contained is rather low ($\lambda_n/\sum\lambda_n = 4.6\%$). As more POD modes exhibit symmetric pattern (see Tab. 5.2), the integrated disturbance energy of the symmetric modes undergoes faster intensification. No obvious decrease can be observed in the whole calculated domain. The maximum magnitude of ε_{rms} produced by symmetric modes is 5 times higher than that of asymmetric mode.

In summary, at $Re_h = 1170$, although initially dominant, the disturbance produced by K-H instability rapidly decays before the inception of second growth of unstable fluctuations, which transition is associated to. It is confirmed that the K-H instability does not plays the role in triggering transition at $Re_h = 1170$. On the other hand, at lower $Re_h (< 1000)$, the unsteady disturbances of symmetric mode exhibit much faster growth with higher magnitude than asymmetric mode till the establishment of turbulence, indicating K-H instability is the incentive to transition.

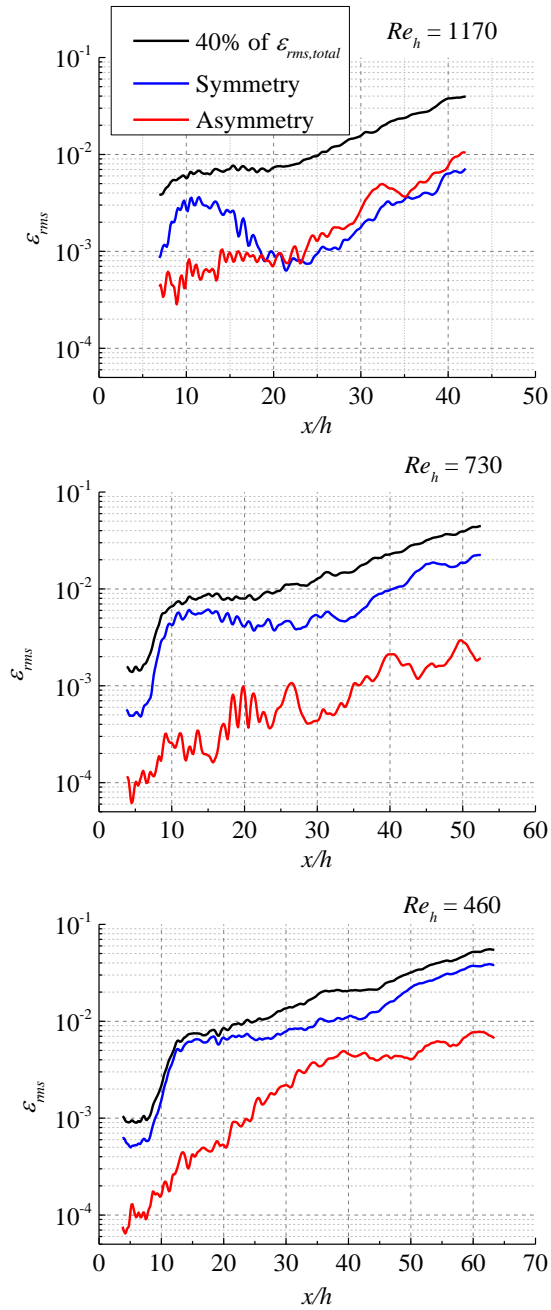


Fig. 5.10. Streamwise evolution of ϵ_{rms} produced by symmetric and asymmetric mode at three Re_h .

5.5.3 Spatial development of secondary vortex structure: low order model

In order to further understand the development of secondary vortex structure and the inception of transition, the symmetric and asymmetric eigenmodes selected in the previous section are combined and projected on the mean velocity field following equation (3.24). The small-scale structures and random turbulent features are filtered out after this procedure, clarifying the observation in the instantaneous flow field, as shown by the iso-surface of instantaneous streamwise vorticity ω_x^* in Fig. 5.11 and Fig. 5.12 at $Re_h = 1170$ and 460 respectively.

At $Re_h = 1170$, the primary and secondary streamwise vortex pair incept at the most upstream region. The secondary vortex pair is produced by increased near-wall shear below the primary pair, continuing downstream with high vorticity magnitude. The sideward upwash motion produced by the secondary vortices gives rise to the formation of low-speed regions aside (black isosurface, $u'/u_\infty = -0.04$, Fig. 5.11). The amplification of the low-speed magnitude leads to local inflectional instability and induces the sidewise hairpin vortices at $x/h = 38$, indicating the onset of turbulent wedge (Chap 4). The correlation between hairpin vortices and low-speed regions has also been observed in transitional (Brinkerhoff and Yaras 2014) and fully turbulent boundary layer (Adrian 2007, Schlatter et al. 2014, Jodai and Elsinga 2016). The observation manifests the important role of the low-speed streaks produced by the secondary vortex pair. The scenario is similar to the bypass transition process, in which secondary instability is situated on the low-speed streaks (Schlatter et al. 2008, Hack and Zaki 2014). The persistence and growth of the former structure is conducted to the amplification of perturbation and transition to turbulence.

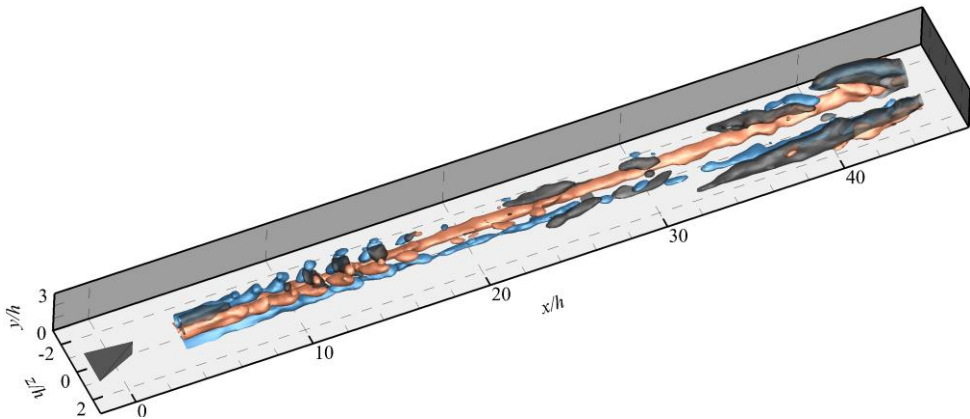


Fig. 5.11. Instantaneous streamwise vorticity at $Re_h = 1170$ after low order reconstruction; red and blue colour corresponds to clockwise and anticlockwise rotation vortices, $\omega_x^* = \pm 0.16$, low-speed region highlighted by black isosurface of $u'/u_\infty = -0.04$.

The secondary vortex structure at $Re_h = 460$ is the leg-buffer vortices formed in between of the two neighbouring hairpin legs, shown as LB1-LB5 in Fig. 5.12. As can be seen in the x - y side view, the leg-buffer structure remains at constant wall-normal location in the early evolution stage ($x/h < 30$). In order to understand the source and spanwise propagation of the leg-buffer vortices, the change rate of vorticity is estimated following the equation (Kundu and Cohen 1990),

$$\frac{D\omega}{Dt} = (\omega \cdot \nabla)V + \nu \nabla^2 \omega \quad (5.2)$$

where the first term on the right-hand side is the change of vorticity due to tilting and stretching. Further decomposition of this term, considering only the change of streamwise vorticity ω_x gives

$$(\omega \cdot \nabla)u = \underbrace{\omega_x \frac{\partial u}{\partial x}}_{S_x} + \underbrace{\left(-\frac{\partial w}{\partial x} \frac{\partial u}{\partial y}\right)}_{T_y} + \underbrace{\frac{\partial v}{\partial x} \frac{\partial u}{\partial z}}_{T_z} \quad (5.3)$$

separating the effect of vortex tilting (T_y and T_z) and stretching (S_x) terms. Due to the strong wall-normal and spanwise shear layer around the central-low speed region ($\partial u/\partial y$, $\partial u/\partial z$), the related tilting terms (T_y and T_z) dominate the change of vorticity, as illustrated along the core of LB1 and LB2 in Fig. 5.13. The leg-buffer vortices incline towards the spanwise side of the wake via vortex tilting, until reaching the outer side of the K-H vortices at $z/h = \pm 1.5$, $x/h > 24$ (see Fig. 5.12(b)). The formation of the leg-buffer vortices attributes to the spanwise shear layer ($\partial u/\partial z$) of the central low-speed region together with $\partial v/\partial x$ induced by alternating upwash and downwash motion (T_z , $x/h = [13.5, 14.2]$, LB1; $x/h = [16, 17]$, LB2). Moving outside of the K-H vortices, the spanwise velocity w becomes an important component as it influences the lateral growth of the leg-buffer vortices. The x - y cross-plane distribution of the spanwise velocity around LB1 and LB2 is shown in Fig. 5.14. A lateral jet can be observed with outward and inward velocity below and above the leg-buffer vortices, respectively. The jet spreads the leg-buffer vortices into the laminar mean shear layer ($\partial u/\partial y > 0$), through the tilting term T_y . The long streamwise range and spanwise propagation of the leg-buffer vortices leads to the growth of sideward low speed regions (see the black isosurface of $u'/u_\infty = -0.07$, Fig. 5.15). The former regions facilitate the propagation of perturbation, exhibiting as the formation of the new vortex structures sideward ($x/h = 60$), regarding as the precursor of turbulent wedge.

5. Reynolds number dependence of roughness-induced transition

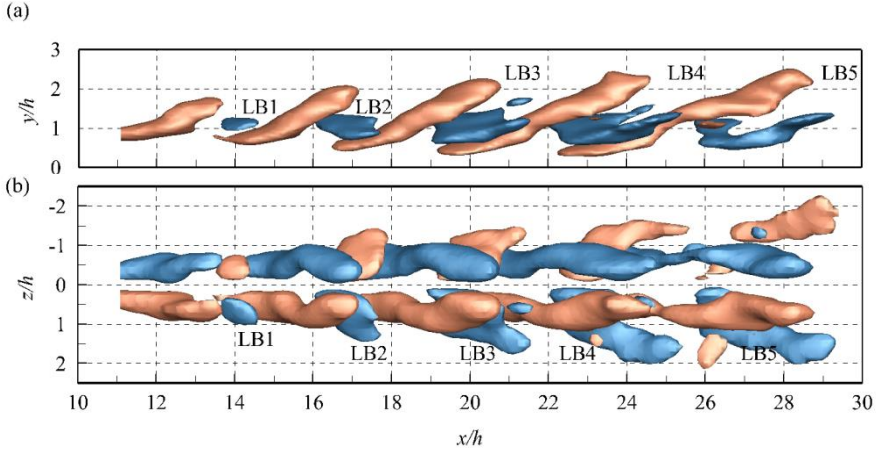


Fig. 5.12. The instantaneous streamwise vorticity at $Re_h = 460$ after low order reconstruction, side view (a) and top view (b).

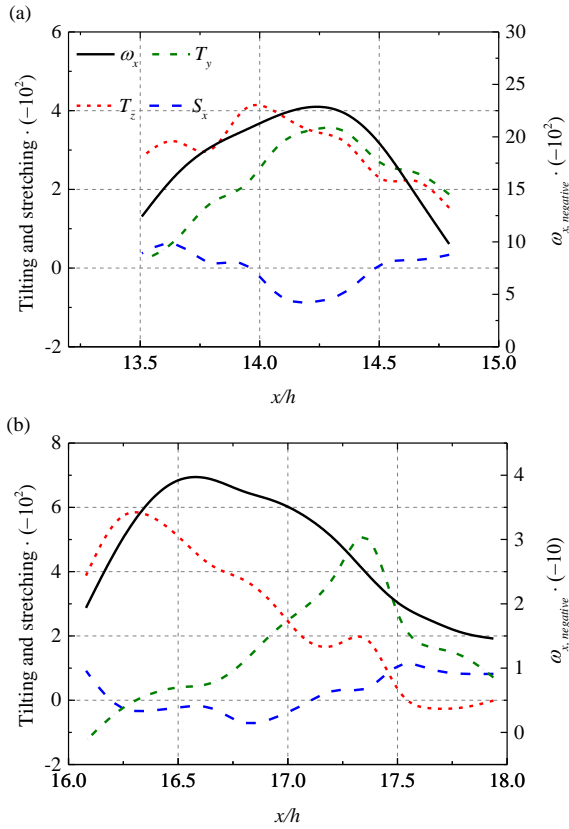


Fig. 5.13. Vorticity, tilting and stretching term along the core of selected leg-buffer vortices, LB1 (a) and LB2 (b).

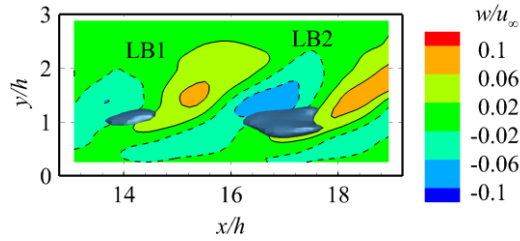


Fig. 5.14. Spanwise velocity distribution at x - y cross plane, $z/h = 0.7$; superimposed by the iso-surface of LB1 and LB2.

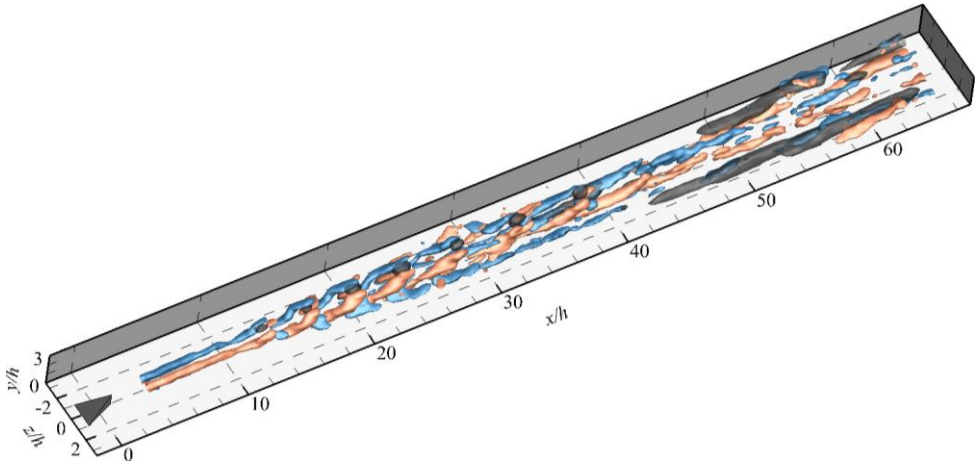


Fig. 5.15. Instantaneous streamwise vorticity at $Re_h = 460$ after low order reconstruction; red and blue isosurface clockwise and anticlockwise rotation vortices, $\omega_x^* = \pm 0.16$, low-speed region highlighted by black isosurface of $u'/u_\infty = -0.07$.

5.6 Reynolds number effect on transition mechanism

At all flow conditions considered, the micro-ramp induces strong velocity disturbances in the wake, which undergoes exponential growth and leads to boundary layer transition. The onset of transition process is significantly delayed when decreasing Re_h .

The time-averaged flow topology features with multiple pairs of counter-rotating streamwise vortices. The major difference when changing Re_h is the active range of primary vortices, which transport low momentum upward around the symmetry plane. Unlike the rapid lift-up and intensity decrease process at $Re_h = 1170$, the former vortex pair persists till the most downstream region of the measurement domain at lower Re_h , sustaining the high intensity of central low-speed region. The detached shear layer around the central low-speed region is prone to continuous growth of Kelvin-Helmholtz instability.

5. Reynolds number dependence of roughness-induced transition

In the instantaneous flow organisation, when $Re_h < 1000$, the hairpin vortices induced by Kelvin-Helmholtz (K-H) instability evolves gradually from close to the micro-ramp until the destabilization of the overall shear layer, revealing the importance of K-H instability on the transition. Differently, the K-H vortices break down rapidly at $Re_h = 1170$, losing connection with the near-wall transition process. The spanwise propagation of the wake at all flow conditions is initialized by the secondary vortex structures, inducing the growth and spread of disturbance by sideward ejection event. The local instability leads to the formation of large-scale hairpin vortices downstream, confirming to be the turbulent wedge.

Two major types of unsteady modes are obtained from the POD analysis. The symmetric POD mode pair corresponds to the shedding phenomenon of K-H vortices, and the asymmetric mode leads to a sinuous wiggling motion of the wake. The dominance of symmetric mode and related K-H instability strongly depend on Re_h . When $Re_h < 1000$, the disturbance energy produced symmetric mode increase steeply till the onset of turbulence, exhibiting considerable larger magnitude than that of asymmetric mode, revealing the dominant role of K-H instability on transition. At $Re_h = 1170$, the active range of symmetric disturbances is limited in the near wake, separating from the downstream inception of transition, indicating the insignificance of the former mode in the transition process.

6

Roughness geometry effect on transition

This chapter has been published in International Journal of Heat and Fluid Flow (Ye et al. 2016).

In this chapter, besides micro-ramp, three more roughness geometries (cylinder, diamond and hemisphere) are considered maintaining constant height and span of the element. The main target is to compare the different flow topologies and study the effect of the element shape on accelerating boundary layer transition. The tomographic PIV experiments are performed at $Re_h = 1170$. The flow behaviour is described by means of vortex topology and by statistical analysis of the velocity fluctuations. The instantaneous flow topology elucidates the mechanism of transition along its stages. A main distinction is observed between the bluff-front elements that induce a horseshoe vortex due to upstream flow separation, leading to more rapid transition and the slender micro-ramp, requiring significant longer distance for transition onset. The mechanism of sideward propagation of the turbulent non-turbulent interface features a continuous convection and generation of hairpin-like vortices and remains the common denominator among all elements considered.

6.1 Introductory remarks

The influence of roughness geometry on transition process has been recognized for a long time. Numerous research efforts have been devoted to the topic, in order to understanding the flow pattern around different types of isolated roughness elements at both subsonic and supersonic flow condition, as has been discussed in sec. 2.3.2. However, the discussion remains open regarding which aspect of the roughness geometry is of primary importance in its effectiveness in promoting transition.

The current chapter considered four different isolated roughness geometries (cylinder, diamond, hemisphere and micro-ramp) with constant span of 2mm and width of 4mm. The dimensions of the roughness elements are provided in sec. 3.4. The main objective is to compare the early stages of transition. Attention has been put to the transition process in the low-speed regime, where compressibility effects do not play a role and the topology of the flow can be studied in its details to determine the transitional flow pattern. The experiments are conducted at $Re_h = 1170$ (also sec. 3.2 for the corresponding flow condition). The cross-flow topology identifies the mean structure of streamwise vortices embedded in the near wake. The statistical evaluation of the velocity fluctuations yields the distinction between the turbulent and laminar flow regions. The details of unsteady flow activity are inspected by instantaneous visualization with the aid of the vortex detection λ_2 criterion. The main findings are summarized and visually elucidated with conceptual sketches of the streamwise vortices organization and the occurrence of hairpin-like vortices.

6.2 Near wake flow topology

The mean flow velocity and vorticity fields over different roughness elements are used to describe the near wake flow topology. The result is obtained by the ensemble average of 200 uncorrelated instantaneous snapshots. The cross-flow field is inspected at three $y - z$ planes positioned downstream of the roughness elements

($x/h = 5, 14$ and 24), as shown in Fig. 6.1. The projected streamlines on $y-z$ plane are visualized with the colour contours of streamwise velocity (u/u_∞).

The flow topology in the near wake cylinder, diamond and hemisphere differs from the micro-ramp, as it is more complex. The main difference is given by the presence of HP vortex, due to the bluff-front of the roughness elements which create strong recirculation region upstream of the elements. Full details of the micro-ramp near wake flow topology are available in sec. 4.2, featuring with primary vortex pair originated from the trailing edge (*trailing edge pair*, TRP) and secondary vortex pair (SP). A simplified model of the flow pattern in the near wake of micro-ramp is sketched in Fig. 6.2(a) for comparison.

The near wake flow pattern behind the cylinder at $x/h = 5$ (Fig. 6.1(a-1)) is dominated by a pronounced counter-rotating vortex pair (horseshoe pair, HP) away from the symmetry plane ($z/h = \pm 1.5, y/h = 0.3$). The spanwise distance between the vortices is $3h$. This vortex pair is assumed to be the trailing part of a horseshoe vortex originating from the separated region upstream of the cylinder (Baker 1979, Hu et al. 2015). The vortex wraps around the roughness element and bends downstream, resulting into two streamwise counter-rotating vortices. The conceptual flow organization associated to the horseshoe vortex is visualized with the aid of a simplified sketch in Fig. 6.2(b) (dark blue line). Going back to Fig. 6.1(a-1), lateral upwash motions are produced by the horseshoe vortices, which induce low-speed regions and evident velocity deficits at $z/h = \pm 2.0$. In the back of the cylinder, another reversed flow region induces a weaker pair of counter-rotating vortices (rear pair, RP) which push low momentum flow upwards, giving rise to a low-speed region around the symmetry plane. A saddle point is formed at $y/h = 0.6$. Downstream at $x/h = 14$ (Fig. 6.1(a-2)), the horseshoe originated vortices move upward to $y/h = 0.6$, while the spanwise location of the vortex core remains unaltered. A tertiary pair of vortices (tertiary pair, TP) is formed, which are located to the outside of the HP vortices. The whole vortex system generates five saddle points and alternating low- and high-speed regions. Further downstream at $x/h = 24$ (Fig. 6.1(a-3)), an additional vortex pair (fourth pair, FP) of even weaker vorticity magnitude is identified due the mutual induction effect of the neighbouring vortices, producing an increased number of saddle points together with the aforementioned vortical structures. The overall active area of the wake flow propagates in both wall-normal and spanwise direction. The multiple counter-rotating streamwise vortex pairs are visualized with dark blue, light blue, purple and pink lines in the simplified sketch in Fig. 6.2(b). The induced low- and high-speed regions are highlighted with grey and yellow projections on the wall.

Similar to the vortical structure downstream of the cylinder, the horseshoe vortex pair (HP) is also present downstream of the diamond at $x/h = 5$, as shown in Fig. 6.1(b-1) and the conceptual sketch in Fig. 6.2(c). The spanwise separation of the trailing vortices is $3.6h$, slightly larger than that behind the cylinder. The latter may be ascribed to the increase in effective frontal area as the front sides of the diamond induce a further lateral expansion of the separated shear layer. The development of

6. Roughness geometry effect on transition

the vortex system with secondary and tertiary vortex pairs appears to be simpler than for the cylinder. The velocity deficit close to the symmetry plane is relatively weak, no clear circulation observed and the RP vortices are barely observable (shown with the dashed blue line in Fig. 6.2(c)). Compared with the cylinder, the tertiary vortex pair (TP) makes its appearance at a more upstream location at $x/h = 5$. Travelling downstream, besides wall-normal movement, the HP vortices also propagate slightly in spanwise direction to $z/h = \pm 2.0$ and ± 2.3 at $x/h = 14$ and 24 (Fig. 6.1(b-2) and (b-3)) respectively. The wake flow shows a larger area of streamwise vortical activity (see Fig. 6.2(c)).

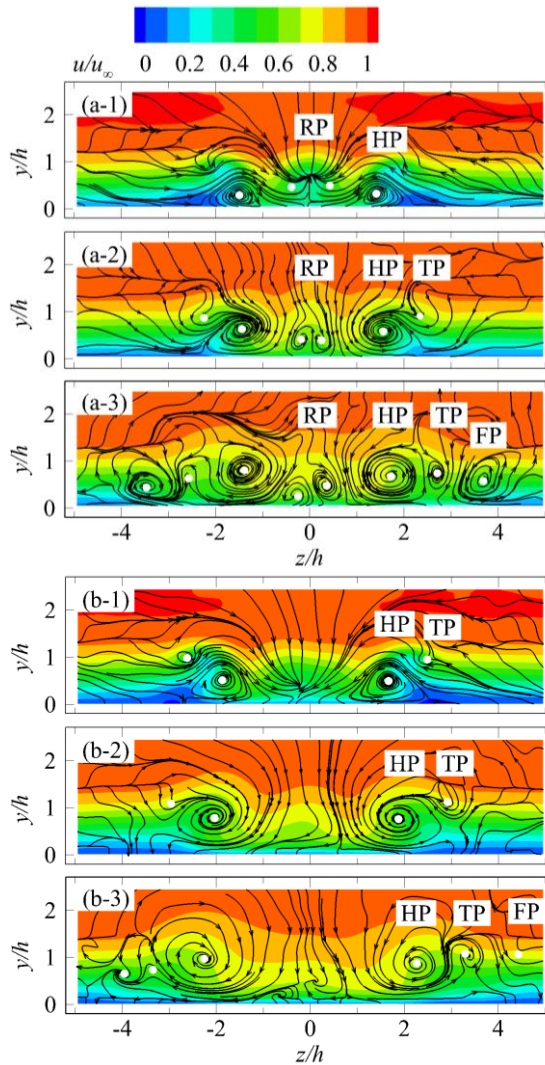


Fig. 6.1. Colour contours of time-averaged streamwise velocity (u/u_∞), continued next page.

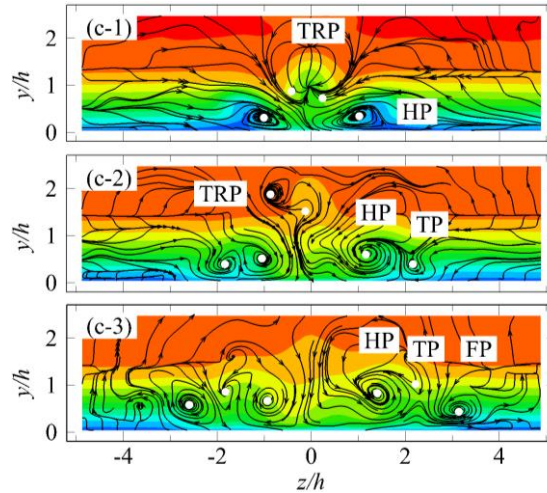


Fig. 6.1. Colour contours of time-averaged streamwise velocity (u/u_∞), superimposed with projected streamlines at three streamwise positions: (1) $x/h = 5$; (2) $x/h = 14$; (3) $x/h = 24$, behind cylinder (a), diamond (b) and hemisphere (c). HP: horseshoe pair, RP: rear pair, TP: tertiary pair, FP: fourth pair, TRP: trailing-edge pair, SP: secondary pair. White dots: time-averaged streamwise vortex cores.

In the near wake of the hemisphere at $x/h = 5$ (Fig. 6.1(c-1)), the HP vortices exhibit a notably smaller spanwise separation ($2h$), inducing two low-speed regions by the action of a lateral upwash motion. Different from the vortical structure in the wake of the cylinder and diamond, a pair of counter rotating vortices (*trailing-edge pair*, TRP) close to the symmetry plane with rotating direction opposing to the HP can be observed at $y/h = 1$. The TRP vortex is postulated to emanate from the tip region of the hemisphere (see Fig. 6.2(d)). It produces a central upwash motion such that a velocity deficit region is induced. Moving downstream, the TRP lifts up with a rapid decrease of its intensity and becomes indistinguishable at $x/h = 24$ (Fig. 6.1(c-3)). As a result, the velocity deficit is also rapidly recovered. The mutually induced tertiary (TP) and fourth (FP) vortex pair can be detected at the side of the HP vortices close to the wall from $x/h = 14$ and 24 respectively. The overall area dominated by the activity of streamwise vortices is smaller compared with that of the cylinder and the diamond element, but larger than that of the micro-ramp. Note that close to the symmetry plane, the RP cannot be inferred from inspection of the streamtraces, although the streamwise vorticity field (not present in the current paper) indicates its weak presence.

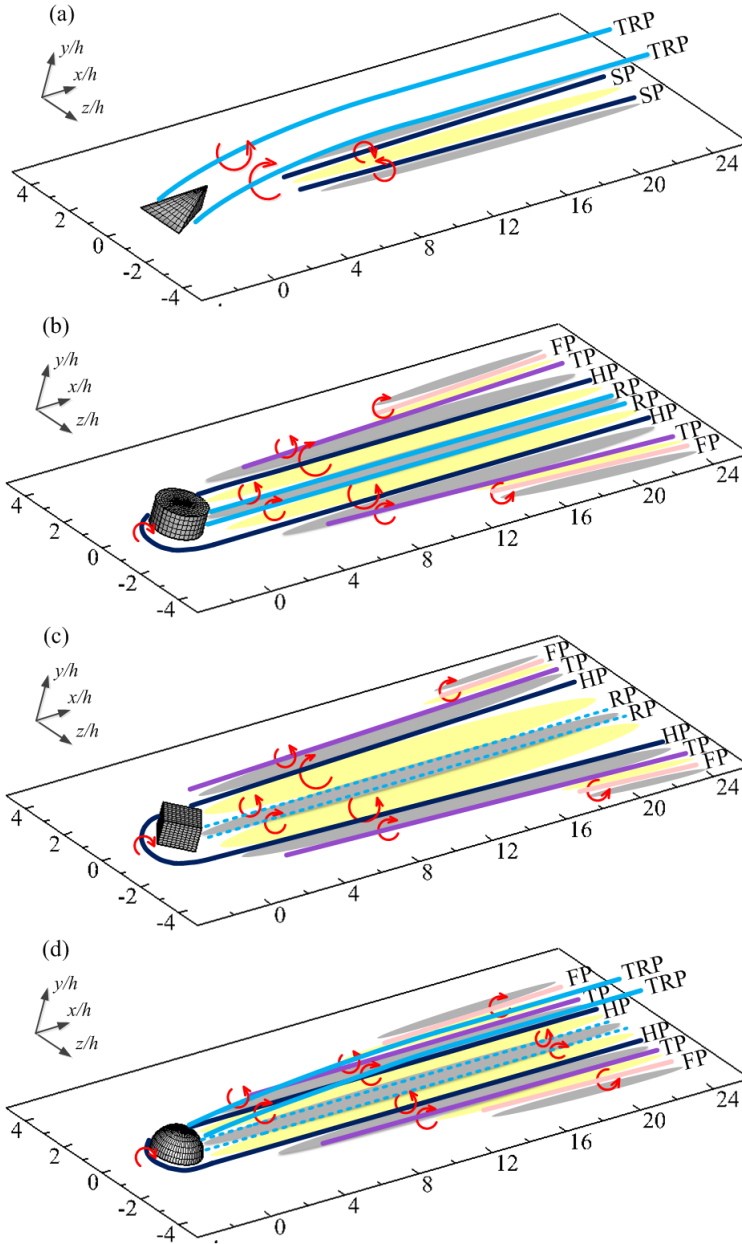


Fig. 6.2. Conceptual sketches of the wake topology behind different roughness elements. The solid and dashed lines are streamwise vortices; Grey and yellow projections on the wall indicate low- and high-speed regions respectively.

The occurrence of velocity streaks is one of the main features of the spanwise inhomogeneity of the flow past the roughness element, which shows a strong resemblance to the scenario of bypass transition (Brandt et al. 2004). The importance of such inhomogeneity can be quantified by the streak amplitude (Andersson et al. 2001), defined as:

$$Au(x) = \frac{1}{2} [\max_{y,z} (u(x, y, z) - u_{bl}(x, y, z)) - \min_{y,z} (u(x, y, z) - u_{bl}(x, y, z))] \quad (6.1)$$

where $u_{bl}(x, y, z)$ is the velocity of the undisturbed boundary layer. After its introduction, the streak amplitude has also been used to describe the evolution of the flow property in the wake of roughness element (De Tullio et al. 2013). As shown in Fig. 6.3, after a slight increase in the near wake region, the streak amplitude generally decays when moving downstream. The maximum streak amplitude for micro-ramp, cylinder, diamond and hemisphere are 41%, 40%, 39%, and 34% of the freestream velocity u_∞ respectively. As suggested in the work of Andersson et al. (2001), for a streak amplitude of $0.26u_\infty$ the sinuous mode associated to the spanwise high-shear becomes unstable (streaky instability). Instead, for a streak amplitude larger than $0.37u_\infty$, the varicose mode resulting from three-dimensional shear layer instability dominates over the sinuous mode. Accordingly, except for the hemisphere, the maximum streak magnitude of the other three roughness elements are above the upper-critical streak amplitude of $0.37u_\infty$, indicating the potential amplification of both sinuous and varicose modes close to the roughness. In the near wake of the hemisphere, the sinuous mode is assumed to dominate the growth of unstable waves. Moving downstream, the streak amplitude rapidly reduces below the upper-stability-limit ($0.37u_\infty$) from $x/h = 11$ for micro-ramp, and $x/h = 8$ for cylinder and diamond. Further downstream, the streak amplitude of the cylinder, diamond and hemisphere reach a plateau at $x/h = 40, 30$ and 40 of around $0.26u_\infty, 0.28u_\infty$ and $0.26u_\infty$, respectively. In the case of the micro-ramp, the streak amplitude decreases monotonically until the most downstream region, resulting in a magnitude of approximately $0.26u_\infty$. The minimum streak amplitude of all cases remains above or approaches the lower-amplitude-limit of $0.26u_\infty$ for the growth of the sinuous mode. Consequently, the streaky instability is postulated to dominate the growth of unsteadiness in the downstream region of roughness wake.

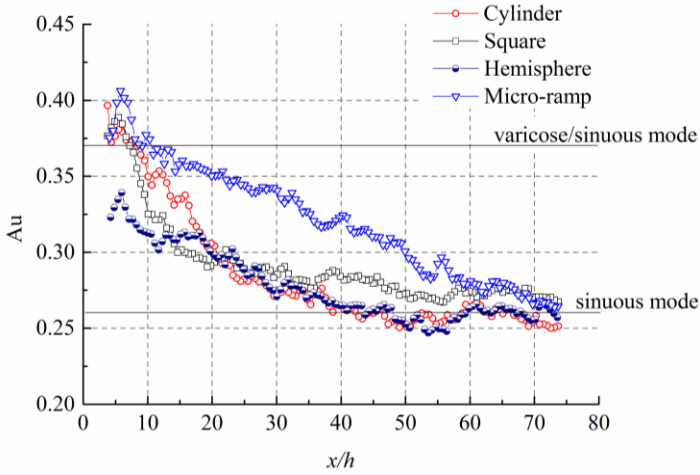


Fig. 6.3. The streamwise evolution of streak amplitude (Au).

6.3 Roughness induced velocity fluctuations

The roughness elements induce up and downwash motions in the wake, resulting in low- and high-speed regions. The increased level of shear produced in the wall-normal directions and the additional shear in the spanwise direction accelerate the growth of unstable waves, resulting in the formation of individual vortices that involve velocity and vorticity fluctuations. In order to study these, the RMS fluctuations of the streamwise velocity component ($\langle u' \rangle / u_\infty$) are extracted at six y - z cross-sections, namely $x/h = [5, 14, 24, 35, 50, 70]$ (Fig. 6.4). The y - z cross-sectional contours are superimposed on the time-averaged streamwise velocity contour lines (u / u_∞).

In the wake of micro-ramp, as discussed in sec. 4.5.1 (Fig. 4.10), a single peak of velocity fluctuations with a relatively high intensity ($0.22u_\infty$) is detected at the detached shear layer where an inflection point is induced by central upwash motion of the trailing edge vortex pair (TRP). The intensity of such peak decreases moving downstream, along with the central low-speed region undergoing a rapid decay. Nevertheless, the maximum can be traced until $x/h = 30$ before it disappears. Beneath the wake region, the central downwash motion produced by the secondary vortices (SP) transport high momentum fluid close to the wall, resulting in high wall shear and an increased level of velocity fluctuations. The upwash motion induced jointly by secondary and tertiary vortices (TP) contributes to the formation of two sideward low-speed regions and inflectional velocity profiles ($u - y$). The overall result features the inception of the sideward velocity fluctuation peaks, moving in the spanwise direction downstream.

In the near wake of the cylinder, more peaks of streamwise velocity fluctuations (I, II and III) ($x/h = 5$, Fig. 6.4(a-1)) are detected, concentrating at the edge of a central low-speed lobe and two symmetrical side-lobes. The inflectional

velocity profile ($u - y$) and a high level of flow shear are produced due to the central and lateral upwash motion induced by RP and HP, which introduce unstable conditions for laminar flow development. The magnitude of the central and lateral peaks is $0.12u_\infty$ and $0.09u_\infty$ respectively. Moving downstream, due to the wake recovery process, the shear rate at the inflectional point close to the symmetry plane decays. As a result, the magnitude of peak I decreases rapidly (less than $0.10u_\infty$ at $x/h = 14$, Fig. 6.4(a-2)), until a peak can no longer be observed from $x/h = 24$ onwards (Fig. 6.4(a-3)). The downwash motion produced by the horseshoe originated vortex pair (HP) transports high momentum flow towards the wall, resulting in high near-wall shear. Consequently, an increased level of streamwise velocity fluctuations close to the wall is observed (Fig. 6.4(a-2) and (a-3)). Comparing with the wake of micro-ramp, in which additional vortices need to develop before critical conditions are reached that destabilize the laminar regime, the flow close to the wall is destabilized close to the cylinder, due to the effect of horseshoe vortex system.

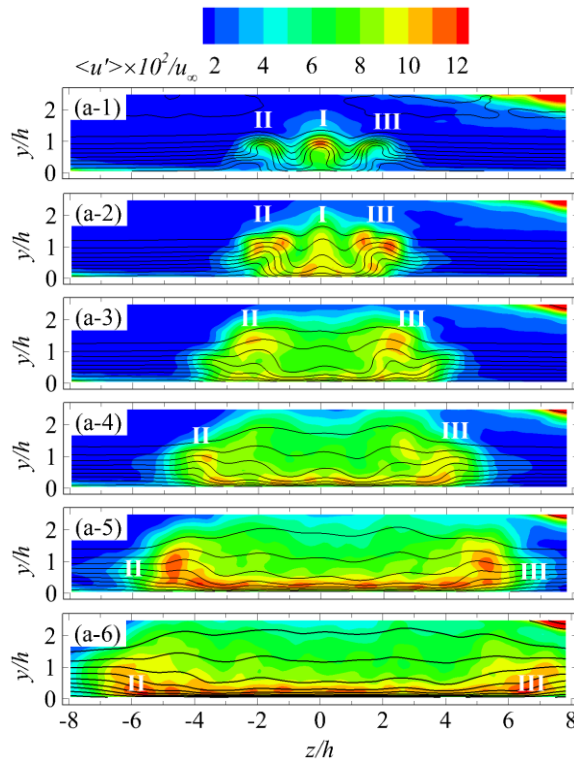


Fig. 6.4. $y - z$ cross-sectional contours of streamwise velocity fluctuations $\langle u' \rangle / u_\infty$, continued next page.

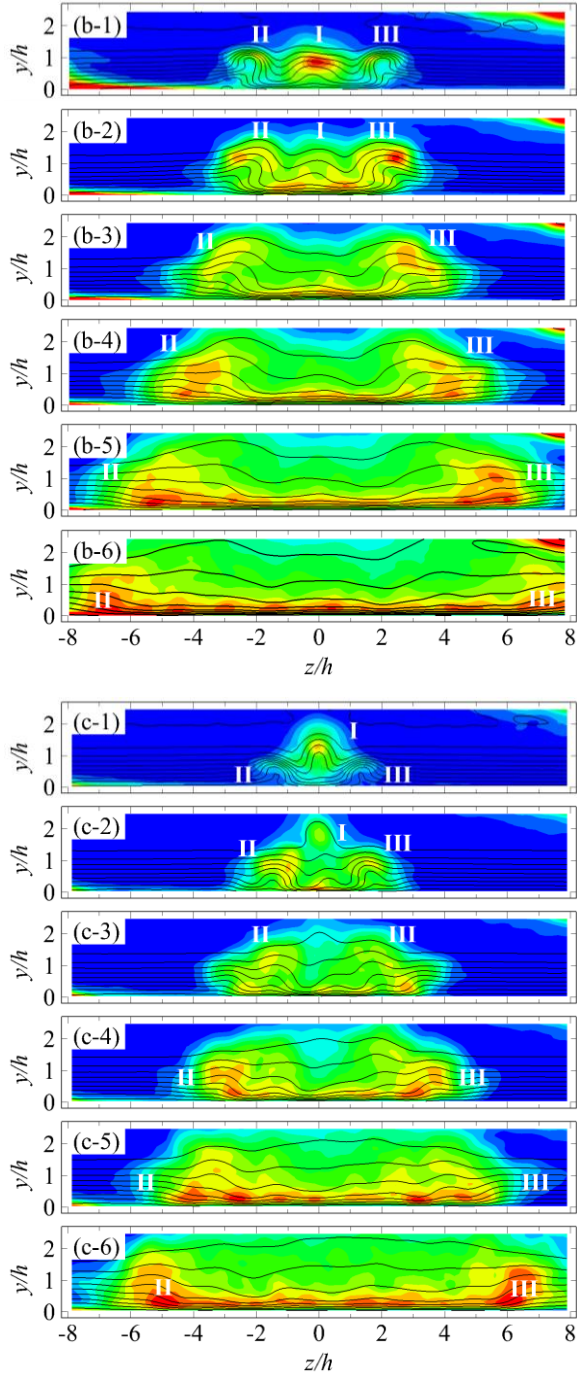


Fig. 6.4. $y - z$ cross-sectional contours of streamwise velocity fluctuations $\langle u' \rangle / u_\infty$, superimposed with contour lines of streamwise velocity u / u_∞ ; 1: $x/h = 5$, 2: $x/h = 14$, 3: $x/h = 24$, 4: $x/h = 35$, 5: $x/h = 50$, 6: $x/h = 70$; (a) cylinder, (b) diamond, (c) hemisphere.

Away from the symmetry plane, the inflectional points at the upper shear layer produced by the combined effect of the horseshoe originated (HP) and tertiary vortices (TP) remain present and contribute to the persistence of the sideward velocity fluctuation peaks (II and III, at $x/h = 14$ and 24 , Fig. 6.4(a-2) and (a-3)). A noticeable magnitude increase of peaks II and III can be observed when moving downstream. The area showing significant velocity fluctuations spreads rapidly in the spanwise direction at this stage, denoting the onset of a turbulent wedge. Peaks II and III are considered to sustain the cascade of velocity fluctuations, giving rise to laminar to turbulent transition. Unlike the relatively homogeneous distribution of streamwise velocity fluctuations at the centre of a turbulent wedge (corresponding to a fully turbulent core (Schubauer and Klebanoff 1956, Zhong et al. 2003)), two symmetrical peaks at the turbulent-non-turbulent interface of the turbulent wedge remain active till the most downstream region, indicating their role in the propagation of turbulent fluctuations towards the surrounding laminar boundary layer. A detailed analysis based on the instantaneous vortical structures contributing to the maxima of velocity fluctuations is presented in the next section. In this case, the transition process is significantly promoted comparing with micro-ramp (approximately 20 roughness heights).

Compared with the cylinder, similar turbulent structures can be observed in the near wake of the diamond and hemisphere, with triple peaks of velocity fluctuations (peaks I, II and III at $x/h = 5$, Fig. 6.4(b-1) and (c-1)), located at the interfaces of three velocity deficit regions and the freestream. Compared to II and III, peak I shows the largest magnitude of $0.13u_\infty$ and $0.11u_\infty$ for the diamond and hemispherical element, respectively. For the diamond element, peak I undergoes a faster decaying process, and can be barely observed at $x/h = 14$. In the wake of the hemisphere, besides the decrease in amplitude, peak I moves upward when travelling downstream under the action of the trailing-edge vortex pair. On the other hand, the side peaks (II and III) produced by the upwash motion of the horseshoe and tertiary vortex pair persist downstream and even increase their intensity while relatively homogeneous conditions are established in the region inside the turbulent wedge.

The formation of the turbulent wedge indicates that the late stage of transition occurs in the wake of all considered roughness elements. The spreading angle of the turbulent wedge evaluated from the present observation domain yields a slightly lower angle for the micro-ramp (4.6°) and slightly larger value for the diamond element (6.4°). The hemisphere and the cylinder exhibit a spreading angle of 5.2° and 5.5° respectively. The latter results are in fair agreement with a number of recently reported results converging around 6° (Singer 1996, Strand and Goldstein 2011, Brinkerhoff and Yaras 2014).

6.4 Instantaneous vortical structures

The onset of oscillatory motions and their growth is only represented by the time-averaged amplitude of velocity fluctuations statistics in the previous section.

The dynamical characterization of the flow in relation to transition and breakdown to turbulence requires the inspection of the evolution of the coherent structures that contribute to a high level of velocity fluctuations. The present measurements allow the inspection of the instantaneous vortex organization, detected by the λ_2 criterion (Jeong and Hussain 1995). The most prominent length scales and wavenumbers can be inferred from this analysis. The iso-surface of λ_2 is color-coded by the streamwise velocity to better discriminate between regions of accelerated and decelerated flow. The approximate location of the time-averaged streamwise vortex cores is indicated by purple lines to ease the interpretation of the flow organization.

The wake flow of the micro-ramp has been particularly explained in sec. 4.4, Fig. 4.9. Kelvin-Helmholtz rollers dominate the near wake as they are visible from $x/h = 5$ with an arc-shape (PHV) spaced at regular intervals of approximately $\lambda/h = 1.45$. When moving downstream, the size and shape of K-H vortices change from arch to hairpin, and in the end to a ring-shape, accompanied by lift-up, pairing and subsequently breakdown upstream of the formation of turbulent wedge ($x/h = [30, 50]$). New vortex structures featuring hairpin-shape with no clear periodicity are produced at turbulent non-turbulent interface of the turbulent wedge. The spanwise location of new hairpin vortices is the same as the sideward low speed regions produced by secondary and tertiary vortices in the time-averaged flow field.

6.4.1 Wake flow of the cylinder and the diamond

The wake of the cylinder and diamond exhibits a similar mean vortex topology as well as instantaneous flow pattern. Therefore only the instantaneous flow organization over cylinder is analysed in detail for the sake of conciseness (see Fig. 6.5). From the most upstream region ($x/h = [3, 5]$), the primary hairpin vortex (PHV) is visible at the location of the unstable separated shear layer close to the symmetry plane, originating from the K-H instability, as shown in Fig. 6.5(a). The initial interval of neighbouring PHV is $\lambda/h = 3.5$, which is 2.4 times of the interval found behind the micro-ramp at the same flow condition. As the growth rate of the perturbation is inversely proportional to the wavelength of the vortices (Cushman-Roisin 2014), the K-H instability is comparatively less important in the wake of cylinder. Downstream, at $x/h = 9$, the upwash motion away from the symmetry plane produced by the HP vortices and associated ejection events give rise to the formation of vortices located at the spanwise side of the convected PHV (see Fig. 6.5(b)). Instead of a complete hairpin vortex structure, the sidewise hairpin vortices (SHV) feature a cane or leg shape, which is caused by non-uniform stretching, partial tearing, cutting and connecting (Guezennec et al. 1989). The SHV occur in a periodic manner with the wavelength of $\lambda/h = 1.7$ (half of the initial wavelength of PHV). The SHV moves slightly in the spanwise direction when travelling downstream. The head portion of PHV and SHV contributes to the peaks of velocity fluctuations (I, II and III, Fig. 6.4(a)). The PHV and SHV exhibit a good degree of spanwise symmetry as the vortices appearing on the sides seem to have the same phase. This phenomenon could be explained as a process of a phase locking of the vortex system. Strong ejection events (Q2, $u' < 0, v' > 0$, visualized by the iso-surface of $u'v'/u^2_\infty = -0.002$, coloured green) at

the leg and upstream region of the head of PHV lift up the low momentum flow, inducing an inflectional velocity profile and unstable shear layer. The local inflectional profile and associated unstable behaviour leads to the formation of new hairpin-shape rollers (sub-PHV) at $x/h = 11$ (Fig. 6.5(b)) between two neighbouring PHV with lower vorticity magnitude. A similar regeneration mechanism of hairpin vortices was also observed in direct numerical simulations of a turbulent spot (Singer and Joslin 1994, Brinkerhoff and Yaras 2014) and experimental visualization of a transitional boundary layer (Guo et al. 2004). In the range of $x/h = [9, 14]$, a spanwise-symmetrical vortex packet is formed comprising two neighbouring PHV, sub-PHV and SHV. The vortex packet resembles the structure of U-shaped vortices, as proposed by Singer and Joslin (1994) and Guo et al. (2010) which consists of multiple hairpin and quasi-streamwise vortices (Fig. 6.5(b)), indicating the late stage of transition.

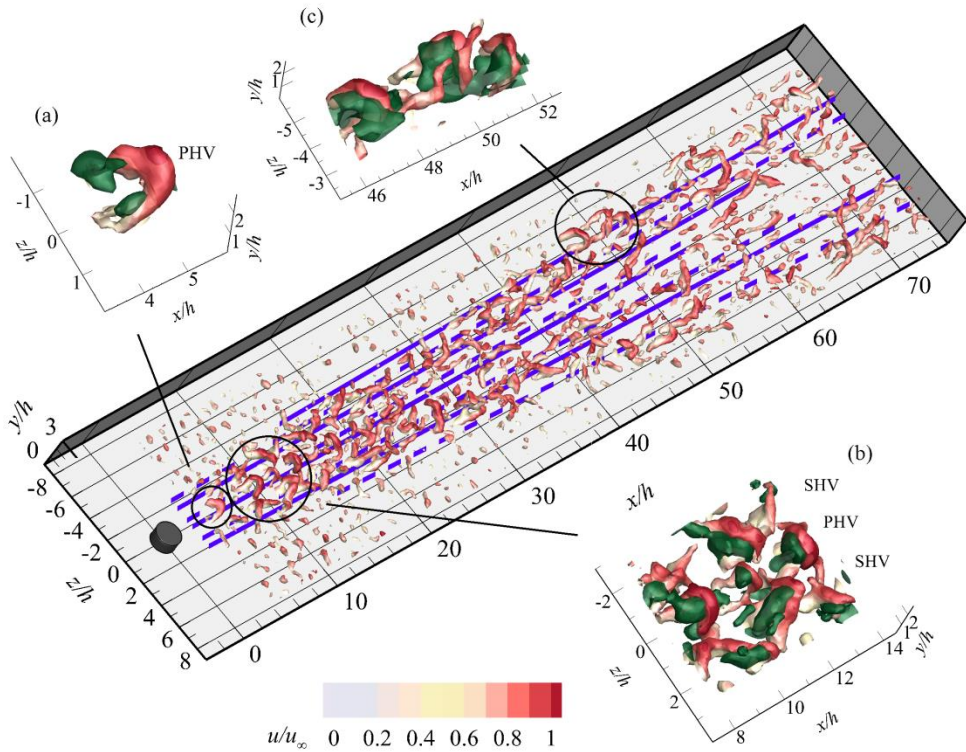


Fig. 6.5. The instantaneous flow pattern of the cylinder wake visualized by the λ_2 criterion ($\lambda_2 = -0.07$), colour coded by u/u_∞ ; Solid and dash dot purple lines: clockwise and anti-clockwise rotating streamwise vortices; the ejection event shown with green iso-surface of $u'v'/u_\infty^2 = -0.002$.

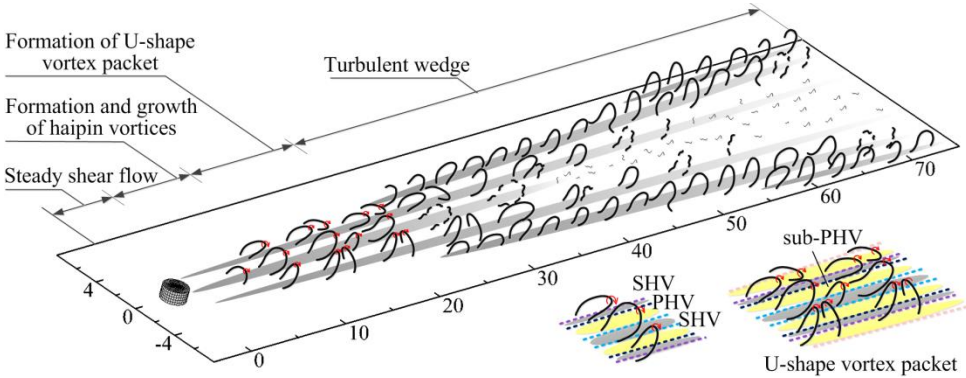


Fig. 6.6. Conceptual model of the transitional flow organization in the wake of cylinder; low- and high-speed regions: grey and yellow projections; dash lines: RP (light blue), HP (dark blue), TP (purple), FP (pink).

Moving downstream (from $x/h = 20$), the PHV loses coherence and periodicity as they appear to be distorted and break up into patches of vorticity. Later on, a similar breakdown process also occurs for the SHV. A good correspondence is observed between the spatial distribution and appearance of hairpin vortices and the low-speed regions in the time-averaged flow field. The situation is schematically depicted in the conceptual model describing the instantaneous organization of the vortical structures in Fig. 6.6. The PHV and SHV enclose the successive low-speed regions, which are produced by the time-averaged counter-rotating streamwise vortex pairs (Fig. 6.2(a)), whereas, in the high-speed regions, no evident vortical activity is detected.

6

Starting from $x/h = 30$, a chain of newly formed hairpin vortices (NHV) can be observed with strong quasi-streamwise hairpin legs aside the SHV (see Fig. 6.5(c)). The new hairpins of high intensity spread spanwise concentrating at the edge of turbulent wedge. In fact, due to its intermittent behaviour, the streamwise location where the NHV are first detected varies significantly in a range of $x/h = [14, 40]$. The location of NHV agrees with the stationary low-speed regions of the mean flow produced jointly by HP and TP vortices (see Fig. 6.6). Close to the symmetry plane, the activity of large coherent vortices is visibly weaker, indicating that the flow yields a more isotropic turbulent regime.

In the wake downstream of the diamond (see Fig. 6.7), the PHV evolves with a smaller initial wavelength of $\lambda/h = 2.5$ and SHV exhibit half the latter wavelength. The inception of the U-shape vortex structure moves closer to the diamond (Fig. 6.7(b)). Similar to the cylinder, the NHV vortices make their first appearance in the range of $x/h = [14, 40]$ (see Fig. 6.7(c)) and move downstream with increased concentration on the turbulent non-turbulent interface.

The transitional flow organization behind cylinder and diamond is summarized by the simplified model shown in Fig. 6.6. The short range with quasi-steady shear

flow is terminated by the PHV induced disturbances close to the roughness. Moving downstream, the SHV is generated at the spanwise side of the former hairpin vortices. Later, the PHV, sub-PHV and SHV together develop into the U-shape vortex packet, indicating the late stage transition. Further downstream, the NHV develops following the border of turbulent wedge, accompanied by the breakdown process of PHV and SHV.

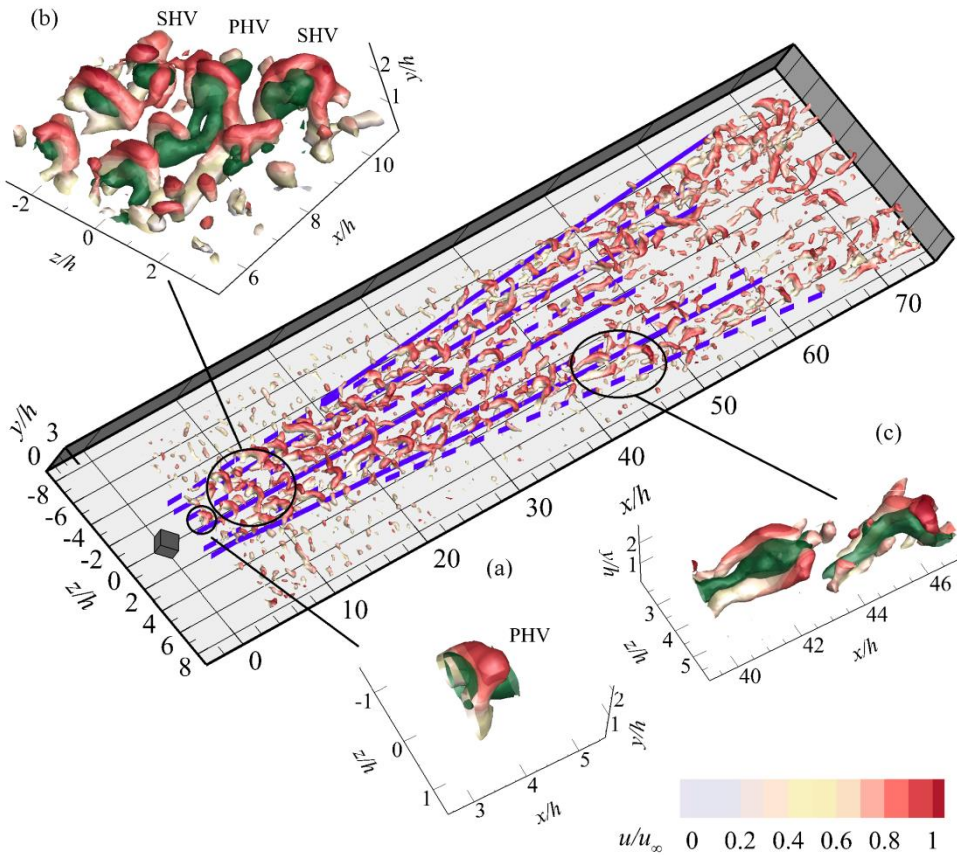


Fig. 6.7. The instantaneous flow pattern of the diamond wake visualized by the λ_2 criterion ($\lambda_2 = -0.07$), colour coded by u/u_∞ ; Solid and dash dot purple lines: clockwise and anti-clockwise rotating streamwise vortices; the ejection event shown with green iso-surface of $u'v'/u_\infty^2 = -0.002$.

6.4.2 Wake flow of the hemisphere

The primary hairpin vortices (PHV) with complete head and leg portion that shed from the hemisphere can be observed from the most upstream region in the measurement domain (see Fig. 6.8). The head portion of the PHV contributes to the

strong velocity fluctuations at the upper shear layer (corresponding to peak I, Fig. 6.4(c)), where a central low-speed region produced by the upwash in the mean flow is enclosed. The initial wavelength of the PHV is $2.5h$, which is the same as that of diamond. At the spanwise sides of the PHV, SHV are produced with arch-shape and a relatively lower vorticity. The SHV appear at the same location as the sideward low-speed regions. The head portion of SHV produces a high level of velocity fluctuations shown as peak II and III in Fig. 6.4(c).

Convecting downstream, the PHV undergoes a lift-up process, in combination with a size and shape variation ascribed to vortex tilting and stretching. At $x/h = [7, 10]$, the growth and stretching of PHV can be observed with an elongated quasi-streamwise leg portion moving close to the wall. Conversely, the head is lifted up due to the effect of a central ejection induced by the legs. The inclination angle of the hairpin is approximately 45° within this range. The wall-normal position of the hairpin head stays constant after reaching the maximum of $y/h = 2.5$, which is within the upper shear layer. Similar to the evolution of the PHV, the growing and stretching process also occurs for the SHV, which develops from an arch to a complete hairpin shape. Nevertheless, the SHV remains at a constant wall-normal position, which is similar to the relatively constant wall-normal position of the HP (see Fig. 6.2(c)).

When moving further downstream to $x/h = [12, 15]$, the head portion of PHV detaches from the leg and rises beyond the upper edge of the measurement domain. The whole PHV is torn apart into vortex fragments and rapidly decreases in intensity. Meanwhile, the SHV remains comparatively strong and develops following the spanwise propagation of the sideward low-speed regions.

Starting from $x/h = 28$, the NHV appears at the side of SHV, where the fourth streamwise vortex pair (FP) starts to be active and induces low-speed regions in combination with the tertiary pair (TP) in the mean flow. The onset location of the NHV is delayed compared with cylinder and diamond, falling within the range of $x/h = [25, 35]$. The NHV develops downstream with a spanwise propagation, but no evident periodicity is found in the formation of these vortices. Yet, a high concentration of NHV is observed at the turbulent non-turbulent interface. In the meanwhile, the vorticity magnitude of SHV decreases due to its interaction with the growing NHV. The former vortices are later observed to be fragmented.

The conceptual model (see Fig. 6.9) visualizes the instantaneous vortical structure downstream of the hemisphere, where PHV shedding directly from the tip of the hemisphere. The SHV is generated bounding the PHV. Both the PHV and SHV grow downstream and undergo tilting and stretching followed by a rapid breakdown. Further downstream, the NHV is produced at the border of the turbulent wedge after the breakdown of PHV, persisting till the most downstream region. The overall instantaneous vortex pattern also resembles a wedge shape in the downstream region.

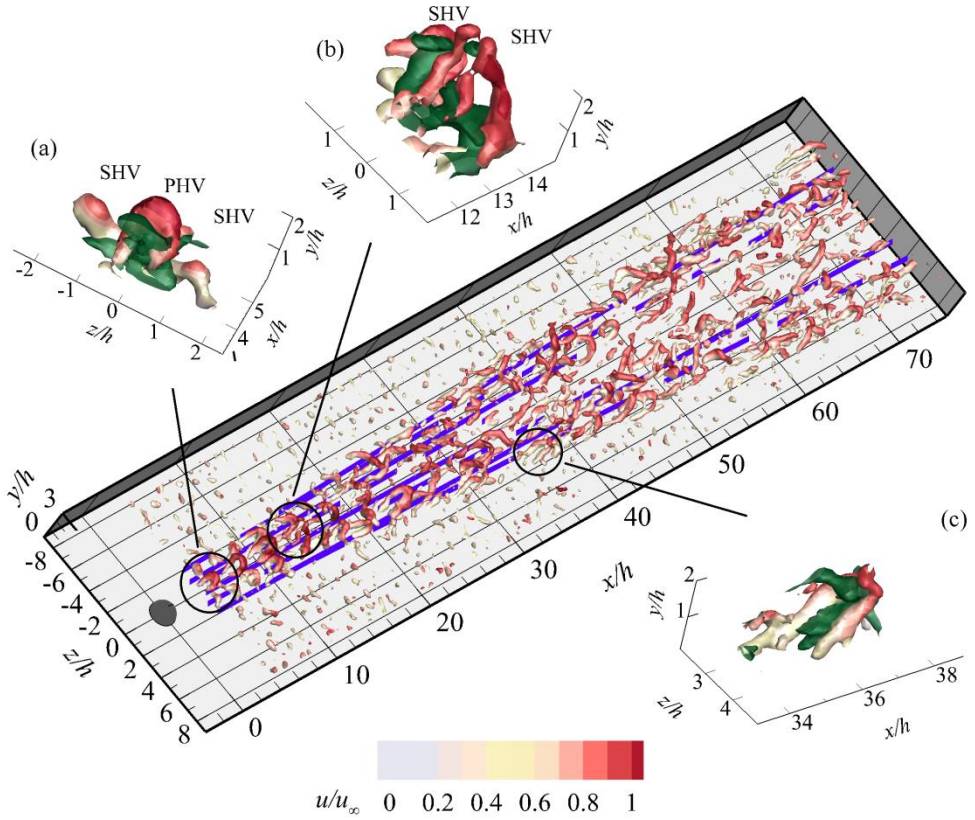


Fig. 6.8. The instantaneous flow pattern of the hemisphere wake visualized by the λ_2 criterion ($\lambda_2 = -0.07$), colour coded by u/u_∞ ; Solid and dash dot purple lines: clockwise and anti-clockwise rotating streamwise vortices; the ejection event shown with green iso-surface of $u'v'/u^2_\infty = -0.002$.

6

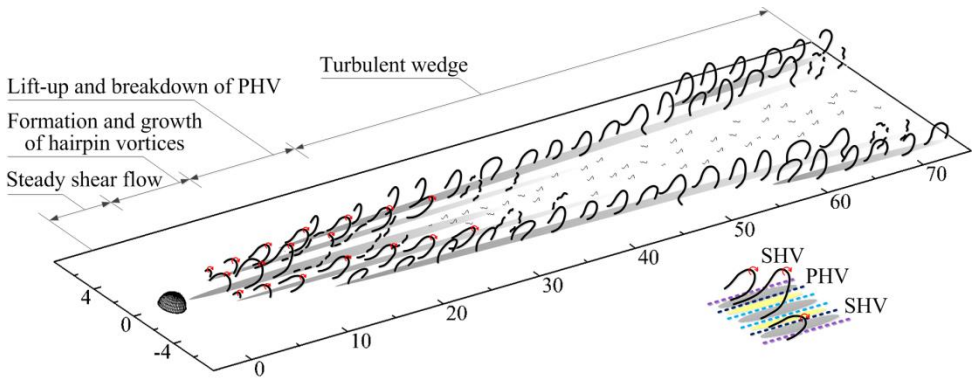


Fig. 6.9. Conceptual model of the transitional flow organization in the wake of hemisphere; low- and high-speed region: grey and yellow projections; dash lines: TRP (light blue), HP (dark blue), TP (purple).

6.4.3 Features of turbulent wedge

A general evolution stage observed in the transitional flow behind the different roughness geometries is the onset of a turbulent wedge, where the late stage transition occurs. The inception of the turbulent wedge (x_w) is significantly delayed in the wake of micro-ramp compared to the cylinder and diamond, with an intermediate behaviour for the hemisphere, revealing its geometry dependence. The features of the turbulent wedge are summarized in Tab. 6.1.

Tab. 6.1. Features of turbulent wedge

| Roughness geometry | Cylinder | Diamond | Hemisphere | Micro-ramp |
|---------------------|----------|----------|------------|------------|
| Origin (x_w/h) | [14, 40] | [14, 40] | [25, 35] | [30, 50] |
| Spreading angle (°) | 6.4 | 5.5 | 5.2 | 4.6 |

The newly generated hairpin vortices (NHV) concentrate at the boundary of the turbulent wedge, inducing strong velocity fluctuations at the turbulent-non-turbulent interface. In the core area of the turbulent wedge, large scale coherent vortical structures are barely observed, indicating a more isotropic turbulent regime. The spanwise location of the NHV coincides with the envelope of successive low-speed regions produced by the lateral or central upwash motion of one or two neighbouring streamwise vortices respectively, as presented in the time-averaged flow topology (see Fig. 6.1 and Fig. 6.2). This agreement suggests a relation between the lateral spreading of turbulent wedge and the streaky velocity distribution of the mean flow. The inception of the NHV occurs at the same location as the sideward low-speed regions. Once formed, the NHV evolve downstream following low-speed region enclosed. Further downstream, when a new low-speed region is generated sideward, the inflectional instability at the newly formed high-shear layer will trigger the formation of new NHV (Krishnan and Sandham 2006), while, the existing NHV undergo breakdown.

In summary, the lateral spreading of turbulent wedge is assisted by the successive low-speed regions, which give rise to local inflectional instability, leading to the convection and regeneration of hairpin vortices at the turbulent non-turbulent interface.

6.5 Geometry effect on the route to transition

It is found that the roughness geometry can greatly modify the wake flow topology and subsequently the onset location of transition. In the wake of all roughness elements considered (micro-ramp, cylinder, diamond and hemisphere), the rapid breakdown of PHV agrees with the decreasing level of streamwise velocity fluctuations close to the symmetry plane (peak I in Fig. 6.4), indicating that the perturbation at the separated shear layer induced by Kelvin-Helmholtz instability is only active in the most upstream region. The PHV loses the spatial connection with the downstream turbulent wedge in both streamwise and spanwise direction (also

wall-normal direction for hemisphere and micro-ramp). As a result, the K-H instability does not play a decisive role in triggering transition.

On the other hand, the sideward low-speed regions as well as the inflectional velocity ($u - y$) profiles provide a favourable condition for the growth of turbulent fluctuations (Andersson et al. 2001). As a result, a cascade of NHV in the downstream region develops from the former location, indicating the onset of transition. The topological evolution from the roughness element until transition strongly depends on roughness geometry. In the wake of bluff front elements (cylinder, diamond and hemisphere), the horseshoe vortices (HP) become active from the most upstream region. The lateral upwash motions induced by HP lead to the early formation of the sideward low-speed regions, which later evolve into quasi-parallel velocity streak distribution (Cherubini et al. 2013). In the case of a micro-ramp, the sideward low-speed regions are induced by secondary pair (SP). The later structure is created by the effect of excessive near-wall shear after the lift-up process of the TRP, delaying the arising of former low-speed regions. Consequently, the micro-ramp appears to be the least effective type of roughness in promoting transition when compared with cylinder, diamond and hemisphere.

7

Conclusions and outlooks

The three-dimensional transitional flow features behind isolated roughness element is investigated at different roughness-height based Reynolds number (Re_h), varying from critical to supercritical conditions ($Re_h = 460, 730$ and 1170). The main contributions of the study are the successful identification of the unstable vortical structures developing in the wake of roughness element and in-depth analysis of their relation with the instability mechanism, leading to transition. Tomographic PIV appears to be well-suited for the description of the vortex dominated flow behaviour. The latter is supported by a good agreement between the measurements and boundary layer theory in the undisturbed laminar region. The wide spatial range covered within the measurement domain encompasses the near wake development and the formation of a self-similar regime within a turbulent wedge. The snapshot POD method is an efficient tool of data reduction for tomographic PIV. The POD modes provide clearer insight to the unsteady flow organization and the symmetry properties of the fluctuating energy.

7.1 Transition mechanisms

7.1.1 Dominant flow feature

In the thesis, the first question to be addressed regards the identification of the flow feature dominating the wake of isolated roughness element. The micro-ramp geometry is selected as the representation of the slender-front roughness element. The time-averaged flow behind the micro-ramp exhibits a primary pair of counter-rotating streamwise vortices emanating from the trailing edge of the element at all three Re_h . The profound upwash motion due to the primary vortex pair induces a central low-speed region. The inflectional point of the velocity profile is prone to the onset of Kelvin-Helmholtz (K-H) type instability. A secondary vortex pair is formed close to the wall with opposing rotating direction with respect to the primary pair. The resultant sideward ejection events trigger the spanwise spreading of the unstable disturbances.

The first quantitative experimental observation of the transitional flow feature behind micro-ramp is provided in the thesis. Under the influence of K-H instability, the instantaneous flow field behind the micro-ramp starts with the appearance of K-H vortices in the separated shear layer close to the symmetry plane. Complex spatial evolution of the K-H vortices is observed in the wake. The onset of transition is identified by the inception of turbulent wedge, which features with the cascade of large-scale hairpin-like vortices concentrating along the spanwise sides. What the relation between K-H vortices and the laminar to turbulent transition is becomes a crucial question to be answered.

At supercritical $Re_h = 1170$, the primary vortex pair lifts up and decreases in strength, which cannot be detected from $x/h = 30$. The K-H vortices in the instantaneous flow advance from arch-shape to hairpin shape. After the lift-up process, the legs of K-H vortices connect at the bottom, assuming a ring shape. Although remaining high intensity and coherence in the near wake, the K-H vortices break down rapidly after pairing, losing spatial connection with the near wall region,

where later on turbulent wedge forms. Consequently, the K-H instability doesn't play the role in the transition process forced by micro-ramp at this flow condition.

On the other hand, the inception of hairpin vortices of the turbulent wedge coincides with the regions where the secondary and tertiary vortices induce rigorous upwash motion. The sideward low-speed regions produced offers the favourable condition for the growth of unstable fluctuations, associated to the physical mechanism of transition. The localized inflectional instability leads to the formation of hairpin vortices.

The lateral spreading of the turbulent wedge is caused by a destabilizing mechanism involving the regeneration of low-speed streaks. Consequently, a general process of the convection and regeneration of hairpin vortices is observed at the turbulent-non-turbulent interface.

7.1.2 Reynolds number effect

Despite the insignificance of K-H vortices in the transition process at $Re_h = 1170$, it remains suspicious to generally exclude K-H instability from the mechanisms related to micro-ramp induced transition, as the selection of dominant instability mode relates to flow conditions.

In fact, the relevance of K-H instability to transition is strongly influenced by Re_h . The active range of the primary vortex pair and central low-speed region increases significantly when $Re_h < 1000$. The strength and sustained range of former structures play a key role in determining the transition mechanism, as the shear layer around the central low-speed region is associated to the growth of K-H instability. In the instantaneous flow organisation, the K-H vortices evolve from the near wake until the inception of turbulent wedge, indicating its importance on transition process.

Using the POD analysis it is clearly found that the flow fluctuations growing past the micro-ramp are dominated by a symmetric mode. At higher Reynolds, the symmetric mode (K-H) quickly vanishes and symmetric and asymmetric fluctuations grow with comparable contributions. On the other hand, when $Re_h < 1000$, the disturbance energy produced by symmetric mode increases steeply till the onset of transition. The magnitude of the disturbance energy is remarkably larger than that of asymmetric mode, revealing the dominant role of K-H instability on transition.

Due to the dependence of transition mechanism on the central low-speed region at different Re_h , it is conjectured that there is a correlation between the low-speed magnitude, its sustained range and the onset location of transition, which should be taken into account for future development of criterion for transition prediction.

7.1.3 Geometry effect

After gaining a thorough understanding of the transition scenario behind the slender-front roughness element, the following step is to study the roughness

geometry effect on transition, particularly comparing the bluff-front roughness with the slender-front type. Which aspect of roughness geometry has the primary influence on transition? To answer this question, experiment are performed at $Re_h = 1170$ behind cylinder, diamond and hemisphere shape roughness to compare with micro-ramp geometry.

Behind all the roughness elements, the transition mechanism is related to the sideward ejection event, producing sideward low-speed regions. The localized inflectional instability at the spanwise sides of the wake leads to the growth of turbulent fluctuations, where transition is developed from.

The bluff-front roughness elements (cylinder, diamond and hemisphere) trip early laminar to turbulent transition comparing with micro-ramp. The horseshoe vortex is generated around bluff-front roughness, whose legs induce sideward low-speed regions, starting from the roughness location. In the wake of the micro-ramp, a longer distance is required for the lateral low-speed regions to develop, as the secondary vortex pair appears after the lift-up of the primary pair. Therefore, it can be concluded that the tripping effectiveness is strongly influenced by the frontal profile of roughness element. When designing boundary layer trip, early onset of transition is expected by increasing the incidence angle of the roughness element.

7.2 Outlooks in incompressible flow regime

7.2.1 Mechanism-based transition criterion

The close relationship between the central low-speed region and dominant transition mechanism indicate it would be instructive to establish a correlation between the low-speed magnitude, its sustained range and the onset location of transition.

In hypersonic flow regime, Van Den Eynde and Sandham (2015) observed a linear relationship between the maximum streak amplitude (Au) and the growth rate (σ) of integrated disturbance energy (e_{rms}) in the near wake of roughness element of different geometry, as

$$\sigma = 0.416Au^{\max} - 0.130 \quad (7.1)$$

However, the relationship is based on a limited number of flow conditions (freestream turbulence and Re_h). Under these flow conditions, the horseshoe vortex system upstream of bluff-front roughness only produces weak unsteadiness, which has little contribution to the transition process. More roughness height-based Reynolds number (Re_h) should be considered, ranging from subcritical to supercritical condition, to achieve a more generalized relationship. Moreover, the direct relation between transition onset location and the streak amplitude would provide a clearer guideline to predict roughness induced transition.

7.2.2 Effect of freestream turbulence

In the low speed regime, the three-dimensional roughness plays a crucial role in boundary layer receptivity to the free-stream turbulence. To the best of the author's knowledge, all studies on roughness induced transition in incompressible flow regime are performed at low turbulence inflow conditions. The study on the effect free-stream turbulence is missing. When the freestream environment contains higher level of disturbances, the flow is supposed to follow a different path of transition to turbulence.

In the bypass transition process, the free-stream turbulence level (Tu) and integral length scale (Λ) has significant influence on transition mechanism, as both parameters can modify the spanwise scale of the velocity streaks. By increasing Tu , transition can be accelerated (Brandt et al. 2004). The disturbance energy is found to be proportional to Tu (Fransson et al. 2005). The influence of FST length scale is less profound on transition Reynolds number, but exhibiting a particular trend. At low Tu , the increase of FST length scale can promote transition. Whereas at high Tu level, transition is delayed with larger FST length scale (Shahinifar and Fransson 2011).

The question mark remains on the sensitivity of roughness wake induced instability to freestream turbulence. It is of interest to produce a systematic research on the interaction between isolated roughness element and FST level and length scale.

7.2.3 Numerical simulation of roughness induced transition

Tomographic PIV has demonstrated the capability to characterize the three-dimensional transitional flow field behind isolated roughness element with high spatial resolution. It is also of great interest to know till what streamwise extent that the numerical simulation can accurately reveal the transitional flow features and related physical mechanism. Direct numerical simulation (DNS) has recently been used to detailed study the roughness induced transition in both incompressible and compressible flow regime (Choudhari et al. 2010, De Tullio et al. 2013, Iyer and Mahesh 2013, Loiseau et al. 2014, Subbareddy et al. 2014). Based on the tomographic PIV result, comparison can be made to verify the capability of DNS in characterizing roughness induced transition in incompressible flow regime. Moreover, in the current measurement, the information around the roughness element is missing, as the domain is limited by laser reflection from the roughness element. The temporal resolution is also limited. The three-dimensional result from DNS will offer a high spatial-temporal resolved description of transitional features from upstream of the roughness element until the establishment of fully turbulent boundary layer.

7.3 Outlook towards the high speed regimes

The common effect of roughness element is to promote laminar to turbulent transition of the boundary layer, increasing drag and surface heat load. The resulted aero-thermodynamic problem is of critical importance in the design of hypersonic

vehicle. Currently, the transition prediction at hypersonic speed is mostly performed with empirical correlations based on in flight and ground test. The test condition is rather limited by the operating condition of the wind tunnels. The reliability and accuracy of transition prediction method would be significantly enhanced after considering the physical mechanism involved in roughness induced transition.

The existence measurement difficulty limits the detailed characterization of the flow feature. High fidelity computational techniques such as direct numerical simulation (DNS) and large eddy simulation (LES) offer the possibility to characterize the physical mechanism of roughness induced transition with fine details in high speed flow, and help defining better physical models to predict transition (Choudhari et al. 2010, Redford et al. 2010, Bernardini et al. 2012, Iyer and Mahesh 2013, Subbareddy et al. 2014). Compared with incompressible regime, several common features have been found, including the streamwise counter-rotating vortices and the shedding phenomenon of hairpin vortices. One evident question arises: does the roughness induced transition follow the same path to transition moving from the incompressible to the compressible regime?

Further quantitative experiments are necessary to produce a better understanding of the flow topology in the proximity and downstream of the roughness element and to link these flow features to the downstream occurrence of in boundary layer transition. Preliminary investigation is performing by the author. The quantitative infrared thermography and tomographic PIV were used to study the effect of isolated roughness of micro-ramp geometry on hypersonic boundary layer transition. The local heat flux distribution and the three-dimensional velocity field were obtained to characterize the transitional flow features over the micro-ramp. The topological interpretation is aided making use of high fidelity resolution low speed experiments using tomographic particle image velocimetry in order to detect similarities and to gain more insight into the local flow topology. The onset location of transition is estimated based on the observation of the lateral spreading of wake, identifying as the onset of turbulent wedge.

7.3.1 Flow Conditions

The experiments were performed at Mach 6.5 in the Hypersonic Test Facility Delft (HTFD) at HSL of TU Delft. The operation of the wind tunnel follows the Ludwig tube concept (Schrijer and Bannink 2010) and generates a Mach 7.5 freestream having a velocity of 1030m/s without model installed. The test section has a diameter of 350mm. Constant total temperature T_0 (579K) and total pressure p_0 (28bar) were used in the experiment, reaching a freestream unit Reynolds number of $14 \times 10^6 \text{m}^{-1}$. The total duration of the flow in the test section with uniform conditions is approximately 100ms. The repeatability of the freestream flow conditions is 0.4%, characterizing by the rms fluctuations with different test runs (Schrijer and Bannink 2010).

A 1° compression ramp model (800 mm long and 350 mm wide) was installed in the symmetry plane of the test section, spreading the entire width (Fig. 7.1). A

micro-ramp with 5.5mm height (h) and 11mm span (c) is installed at $x_h = 241$ mm from the leading edge for IR thermography measurement and $x_h = 241, 281, 321$ and 361mm for tomographic PIV measurement. The Mach number at the edge of the boundary layer is 6.5. The freestream velocity is 1020m/s. The roughness-height based Reynolds number, Re_h remains constant of 7.8×10^4 at all roughness locations, which is highly supercritical (Redford et al. 2010, Bernardini et al. 2012, Bernardini et al. 2014). The origin of the coordinate system that is used in this investigation is located at the center of the micro-ramp. The x , y and z axis correspond to the streamwise, spanwise and wall-normal direction respectively.

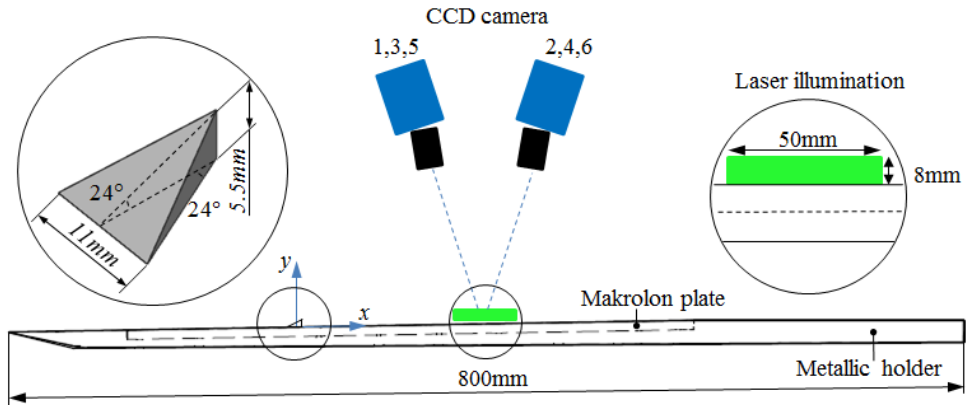


Fig. 7.1. Sketch of the model and tomographic PIV setup, top view.

7.3.2 Experimental arrangement

7.3.2.1 Infrared thermography

The infrared thermography measurements were carried out with a CEDIP Titanium 530L IR system. The camera detector has an array of MCT sensor material. The sensor has a size of 320×256 pixels and a spectral response in the range of $7.7 - 9.3 \mu\text{m}$. An integration time of $340 \mu\text{s}$ was used in the experiment to achieve a satisfactory camera sensitivity. The recording frame rate was 218Hz at full resolution. The resulted spatial resolution is approximately 1.6 pixels/mm. The tunnel was fitted with a Germanium window with a transmissivity of approximately 0.8, providing optical access to the infrared wavelength. The camera was placed in an angle of approximately 15° with respect to the window in order to prevent self-reflections. By changing the upstream and downstream inclination direction of the camera, two domains were measured with an overlap of approximately 80mm in order to capture the wake flow from the micro-ramp until the establishment of turbulent boundary layer. The IR system was calibrated using a reference black body, counting the effect of germanium window and camera inclination angle with

respect to the window on transmissivity. Spurious contributions due to ambient radiation are minimized by shielding the camera with a matt-black sheet.

The convective heat transfer is obtained from the measured transient surface temperature distribution using a one-dimensional semi-infinite wall model, in which the unsteady heat conductive equation (Fourier equation) is solved. The data reduction method is based on the work by Cook and Feldermann (Cook and Felderman 1966) and the present implementation is discussed in detail by Schrijer et al. (Schrijer et al. 2003). The measured surface heat flux q_s is non-dimensionalized using the heat flux values for an undisturbed laminar boundary layer $q_{s, laminar}$, as

$$q^* = q_s / q_{s, laminar} \quad (7.2)$$

7.3.2.2 Tomographic PIV measurement

The tomographic PIV system consists of six LaVision *Imager LX* interline CCD cameras (1628×1236pixels, 4.4μm/pixel) positioning in a rectangular configuration, as shown in Fig. 7.2. A maximum aperture angle of 40° was obtained in order to get a good reconstruction quality. The cameras were equipped with objectives of 75mm focal length and Scheimpflug adaptors to adjust the lens plane. The numerical aperture was set at $f_{\#}=8$, resulting in a focal depth of 10.5mm.

The flow was seeded with Titanium dioxide (TiO₂) with a primary crystal size of 50nm (Huntsman UV-TITAN M765) and a nominal bulk density ρ_b of 200 kg/m³. The particle is ejected to the high pressure high temperature storage tube by a custom made cyclone before the running of the wind tunnel in order to obtain relatively homogeneous particle distribution in the flow. As the fidelity of the measurement highly depends on the ability of the particle to follow the flow, the size of the particle needs to be well-controlled to reduce the particle relaxation time. In the present experiment, the particles were dehydrated before putting into the cyclone to eliminate particle agglomeration. Additional filter is applied to the cyclone to further filtrate large size particles. The resulting particle relaxation time τ_p is 1.4μs.

The tracer particles were illuminated by a Spectra Physics Quanta-Ray double pulsed Nd: Yag laser (400mJ/pulse, 532nm wavelength, 7ns pulse duration) with a thickness of 8mm. The pulse separation time was set to 0.75μs, yielding a particle displacement of 24pixels in the freestream. The measurement volume size is 50(x)×38(y)×8(z)mm³ (9h×7h×1.5h), resulting in a digital image resolution of 32.6pixels/mm. The measurement domain begins from 384mm from the leading edge. The image sequence was recorded at a frequency of 2Hz. Due to the short-duration of HTFD, only single snapshot can be captured at runtime and snapshots both before and after the runtime were also recorded. The near wake flow development was captured by moving the micro-ramp closer to the measurement domain with three steps of 40mm interval. The whole measurement extends from 23mm to 193mm downstream of the center of the micro-ramp ($x/h = [4, 35]$).

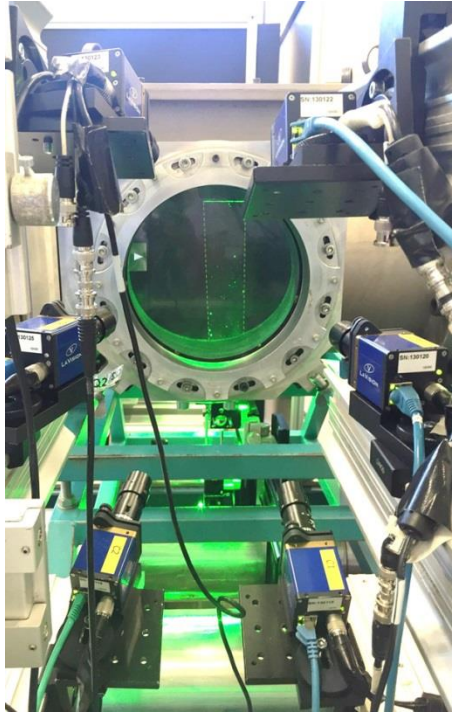


Fig. 7.2. Photography of tomographic PIV setup.

The system synchronization, calibration, data acquisition and processing were performed in LaVision Davis 8. The physical calibration was performed with a custom-made calibration target of 1mm thick at ambient pressure, establishing the relation between object and image space. Due to the density difference between the flow conditions and the ambient, the light refraction will introduce additional particle triangulation errors (Avallone et al. 2014). Further correction is needed to reduce the misalignment error by using the 3D self-calibration technique (Wieneke 2008). For each run, the first step self-calibration is performed on 20 snapshots after the runtime of the wind tunnel, during which the density is still close to vacuum. The second step volume self-calibration is based on the single snapshot at runtime to further compensate the effect of density difference. A final misalignment error of below 0.05pixel is achieved.

The raw images were pre-processed by the subtraction of pixel time-minimum and of the spatial minimum from a kernel of 31×31 pixels. Image intensity was homogenized by normalization against the local average (kernel of 51×51 pixels). The measurement volume was reconstructed using the CSMART algorithm, which reduces the reconstruction time comparing with conventional MART (Atkinson and Soria 2009). The position of the wall was determined by detecting an intensity peak in the three-dimensional reconstructed object, corresponding to a few reflection points at the surface. Spatial cross-correlation analysis was performed with a custom

software (FLUERE, Lynch (2015)) performing multi-grid and volume deformation interrogation using a final interrogation volume of $40 \times 40 \times 40$ voxels ($1.23 \times 1.23 \times 1.23 \text{mm}^3$), with an overlap of 75% between neighbouring interrogation windows. The resulting vector pitch is 0.3mm. The no-slip wall condition was applied during the iterative correlation process by setting zero velocity below the detected wall position. Outliers are detected using the normalized median filter proposed by Westerweel and Scarano (2005) and replaced with interpolated neighbouring values. Summary of tomographic PIV measurement parameters is given in Tab. 7.1.

Tab. 7.1. Parameters of tomographic PIV

| Parameter | Value |
|-------------------------------|--|
| Laser pulse separation | 0.75 μ s |
| Active sensor size | d |
| Magnification | 0.14 |
| Digital image resolution | 32.6pixels/mm |
| Object focal length, $f_{\#}$ | 75mm, 8 |
| Measurement volume | 50(x) \times 38(y) \times 8(z)mm ³ (9h \times 7h \times 1.5h) |
| Interrogation volume | 40 \times 40 \times 40voxels ($1.23 \times 1.23 \times 1.23 \text{mm}^3$) |
| Overlap factor | 75% |
| Vector pitch | 0.31mm |

7.3.3 Micro-ramp flow topology at Mach 6

In low speed flow, where compressibility effects are not considered, the time-averaged transitional wake flow topology over submerged micro-ramp features with two pairs of counter-rotating vortices in the near wake at $Re_h = 1170$ (Chap. 4), inducing alternating low- and high-speed regions. For the current conditions, the normalized surface heat flux q^* is shown in Fig. 7.3. Two high heat load regions at the side of the micro-ramp can be observed, corresponding to the high shear stress at these locations. As been observed in Fig. 4.2 and Fig. 4.15, a primary vortex pair originates from the trailing edge of the micro-ramp, inducing a lateral downwash motion and a transport of high momentum flow towards the wall at the side of the vortices, causing the increased heat flux levels. In the numerical simulation at hypersonic flow conditions, Tirtey et al. (2011) also found these dominant primary vortices in the wake of the micro-ramp. Due to the induced upwash motion, the primary vortex pair (TRP) lift up when moving downstream. The high speed regions tend to move close to each other after the lift-up process of the primary vortex pair, so as the high heat flux regions (see Fig. 7.3). The heat load magnitude undergoes a rapid decrease when moving downstream, which can be attributed to the damping of the streamwise vorticity magnitude. The former high heat load regions from either side of the micro-ramp seem to disappear at $x/h = 8$ and a single high heat flux area close to the symmetry axis is observed. This area is associated to a secondary vortex pair with an opposing rotating direction as the primary pair, transporting high-speed

flow towards the wall close to the symmetry axis. Furthermore, the lateral upwash motion induced by the secondary vortex pair produces two sideward low speed regions. As a result, low heat flux regions, shown as the dark blue streaks, can be observed at the spanwise side of the wake in the range $x/h = [3, 15]$.

Further downstream at $x/h = 22$, the width of the global high heat flux region increases from that location on. This scenario suggests the onset of a turbulent wedge. The process of breakdown to turbulence starts to occur. In the low speed flow, a tertiary pair of streamwise vortices is considered as the precursor of a turbulent wedge. The former vortex pair appears outward of the secondary pair in the downstream region, leading to new pairs of low- and high-speed regions and a spanwise propagation of the overall vortical structures.

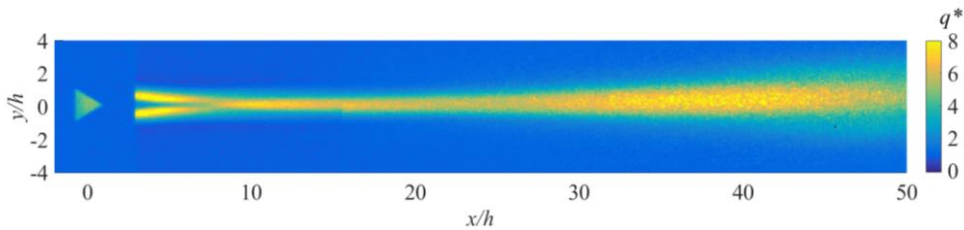


Fig. 7.3. Normalized heat flux distribution q^* behind the micro-ramp.

Preliminary tomographic PIV results yield the time-averaged velocity field of 20 uncorrelated snapshots. The y - z cross-plane contours of shear magnitude $S = [(\partial u/\partial y)^2 + (\partial u/\partial z)^2]^{1/2}$ at selected streamwise locations ($x/h = 12, 13$ and 18) are shown in Fig. 7.4, superimposing by the contour lines of streamwise velocity component (u/u_∞). At $x/h = 12$, the micro-ramp produces a detached shear layer and central low-speed region. As suggested in the conceptual sketch at low speed (Fig. 4.15), the primary vortex pair close to the symmetry plane lifts up low-momentum fluid from the wall, giving rise to the central low-speed region. Beneath the low-speed region, high-shear layer is observed indicating that high-momentum fluid is transported towards the wall by the downwash motion. The observation agrees with the single high surface heat flux area close to the symmetry plane in Fig. 7.3, confirming the presence of the secondary vortex pair in the wake of micro-ramp in hypersonic laminar boundary layer. In addition, the sideward ejection of secondary vortex pair leads to two low-speed regions outwards with relatively low intensity. Moving downstream, the central low-speed region lifts up and detaches from the boundary layer at $x/h = 13$, and cannot be detected at $x/h = 18$. The near-wall shear decreases in the downstream region, consistent with the decrease in surface heat flux in this streamwise range.

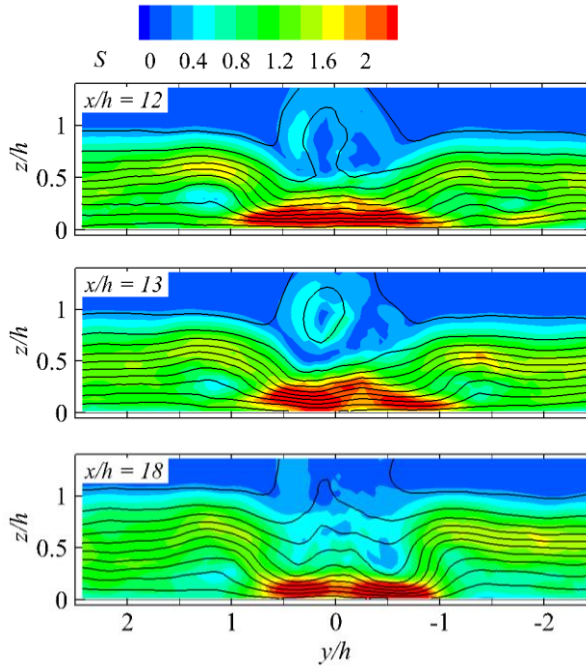


Fig. 7.4. Contour of shear magnitude $S = [(\partial u/\partial y)^2 + (\partial u/\partial z)^2]^{1/2}$ at y - z cross-planes, with contour lines of streamwise velocity (u/u_∞) from 0 to 1 with 0.1 interval.

References

- Acarlar, M. S., Smith, C. R. (1987) A study of hairpin vortices in a laminar boundary layer. Part 1. Hairpin vortices generated by a hemisphere protuberance. *J Fluid Mech* **175**: 1-41.
- Adrian, R. J., Meinhart, C. D., Tomkins, C. D. (2000) Vortex organization in the outer region of the turbulent boundary layer. *J Fluid Mech* **422**: 1-54.
- Adrian, R. J., Liu, Z. C. (2002) Observation of vortex packets in direct numerical simulation of fully turbulent channel flow. *Journal of Visualization* **5**: 9-19.
- Adrian, R. J. (2007) Hairpin vortex organization in wall turbulence. *Phys Fluids* **19**: 041301.
- Anderson, B., Tinapple, J., Surber, L. (2006) Optimal control of shock wave turbulent boundary layer interactions using micro-array actuation, *3rd AIAA Flow Control Conference*, San Francisco, CA.
- Anderson, J. (2010) *Fundamentals of aerodynamics, fifth edition*. McGraw-Hill Education, New York.
- Andersson, P., Berggren, M., Henningson, D. S. (1999) Optimal disturbances and bypass transition in boundary layers. *Phys Fluids* **11**: 134-150.
- Andersson, P., Brandt, L., Bottaro, A., Henningson, D. S. (2001) On the breakdown of boundary layer streaks. *J Fluid Mech* **428**: 29-60.
- Asai, M., Minagawa, M., Nishioka, M. (2002) The instability and breakdown of a near-wall low-speed streak. *J Fluid Mech* **455**: 289-314.
- Atkinson, C., Soria, J. (2009) An efficient simultaneous reconstruction technique for tomographic particle image velocimetry. *Exp Fluids* **47**: 553-568.
- Avallone, F., Ye, Q., Schrijer, F. F. J., Scarano, F., Cardone, G. (2014) Tomographic PIV investigation of roughness-induced transition in a hypersonic boundary layer. *Exp Fluids* **55**: 1852.
- Avallone, F., Ragni, D., Schrijer, F. F. J., Scarano, F., Cardone, G. (2016) Study of a supercritical roughness element in a hypersonic laminar boundary layer. *AIAA J* **54**: 1892-1900.
- Babinsky, H., Li, Y., Pitt Ford, C. W. (2009) Microramp control of supersonic oblique shock-wave/boundary-layer interactions. *AIAA J* **47**: 668-675.
- Baker, C. J. (1979) The laminar horseshoe vortex. *J Fluid Mech* **95**: 347-367.
- Bernardini, M., Pirozzoli, S., Orlandi, P. (2012) Compressibility effects on roughness-induced boundary layer transition. *Int J Heat Fluid Flow* **35**: 45-51.
- Bernardini, M., Pirozzoli, S., Orlandi, P., Lele, S. K. (2014) Parameterization of boundary-layer transition induced by isolated roughness elements. *AIAA J* **52**: 2261-2269.
- Berry, S. A., Bouslog, S. A., Brauckmann, G. J., Caram, J. M. (1998) Shuttle orbiter experimental boundary-layer transition results with isolated roughness. *J Spacecraft Rockets* **35**: 241-248.
- Berry, S. A., Auslender, A. H., Dilley, A. D., Calleja, J. F. (2001) Hypersonic boundary-layer trip development for Hyper-X. *J Spacecraft Rockets* **38**: 853-864.
- Berry, S. A., Horvath, T. J., Hollis, B. R., Thompson, R. A., Hamilton, H. H. (2001) X-33 hypersonic boundary-layer transition. *J Spacecraft Rockets* **38**: 646-657.

References

- Berry, S. A., Hamilton, H. H., Wurster, K. E. (2006) Effect of computational method on discrete roughness correlations for shuttle orbiter. *J Spacecraft Rockets* **43**: 842-852.
- Blinde, P. L., Humble, R. A., Oudheusden, B. W. V., Scarano, F. (2009) Effects of micro-ramps on a shock wave/turbulent boundary layer interaction. *Shock Waves* **19**: 507-502.
- Brandt, L., Schlatter, P., Henningson, D. S. (2004) Transition in boundary layers subject to free-stream turbulence. *J Fluid Mech* **517**: 167-198.
- Brinkerhoff, J. R., Yaras, M. I. (2014) Numerical investigation of the generation and growth of coherent flow structures in a triggered turbulent spot. *J Fluid Mech* **759**: 257-294.
- Cantwell, B., Coles, D., Dimotakis, P. (1978) Structure and entrainment in the plane of symmetry of a turbulent spot. *J Fluid Mech* **87**: 641-672.
- Cherubini, S., De Tullio, M. D., De Palma, P., Pascazio, G. (2013) Transient growth in the flow past a three-dimensional smooth roughness element. *J Fluid Mech* **724**: 642-670.
- Choudhari, M., Fischer, P. (2005) Roughness-induced transient growth, *35th AIAA Fluid Dynamics Conference and Exhibit*, Toronto, Ontario Canada.
- Choudhari, M., Li, F., Edwards, J. (2009) Stability analysis of roughness array wake in a high-speed boundary layer, *47th AIAA Aerospace Sciences Meeting including The New Horizons Forum and Aerospace Exposition*, Orlando, Florida.
- Choudhari, M., Li, F., Chang, C.-L., Edwards, J., Kegerise, M., King, R. (2010) Laminar-turbulent transition behind discrete roughness elements in a high-speed boundary layer, *48th AIAA Aerospace Sciences Meeting Including the New Horizons Forum and Aerospace Exposition*, Orlando, Florida.
- Citro, V., Giannetti, F., Luchini, P., Auteri, F. (2015) Global stability and sensitivity analysis of boundary-layer flows past a hemispherical roughness element. *Phys Fluids* **27**: 084110.
- Cook, W. J., Felderman, E. J. (1966) Reduction of data from thin-film heat-transfer gages - a concise numerical technique. *AIAA J* **4**: 561-562.
- Cossu, C., Brandt, L. (2004) On tollmien-schlichting-like waves in streaky boundary layers. *European Journal of Mechanics - B/Fluids* **23**: 815-833.
- Couliou, M., Monchaux, R. (2016) Spreading of turbulence in plane couette flow. *Phys Rev E* **93**: 013108.
- Craik, A. D. D. (1971) Non-linear resonant instability in boundary layers. *J Fluid Mech* **50**: 393-413.
- Crawford, B. K., Duncan Jr., G. T., West, D. E., Saric, W. S. (2013) Laminar-turbulent boundary layer transition imaging using IR thermography. *Optics and Photonics Journal* **3**: 233-239.
- Crow, S. C. (1970) Stability theory for a pair of trailing vortices. *AIAA J* **8**: 2172-2179.
- Cushman-Roisin, B. (2014) *Environmental fluid mechanics*. John Wiley and Sons, Inc, USA.
- Danehy, P., Bathel, B., Ivey, C., Inman, J., Jones, S. (2009) No PLIF study of hypersonic transition over a discrete hemispherical roughness element, *47th AIAA Aerospace Sciences Meeting including The New Horizons Forum and Aerospace Exposition*, Orlando, Florida.
- Danehy, P., Ivey, C., Inman, J., Bathel, B., Jones, S., Jiang, N., Webster, M., Lempert, W., Miller, J., Meyer, T., Mccrea, A. C. (2010) High-speed PLIF imaging of

- hypersonic transition over discrete cylindrical roughness, *48th AIAA Aerospace Sciences Meeting Including the New Horizons Forum and Aerospace Exposition*, Orlando, Florida.
- De Tullio, N., Paredes, P., Sandham, N. D., Theofilis, V. (2013) Laminar–turbulent transition induced by a discrete roughness element in a supersonic boundary layer. *J Fluid Mech* **735**: 613-646.
- Denissen, N. A., White, E. B. (2008) Roughness-induced bypass transition, revisited. *AIAA J* **46**: 1874-1877.
- Denissen, N. A., White, E. B. (2009) Continuous spectrum analysis of roughness-induced transient growth. *Phys Fluids* **21**: 114105.
- Dolling, D. S. (2001) Fifty years of shock-wave/boundary-layer interaction research: What next? *AIAA J* **39**: 1517-1531.
- Doolittle, C. J., Drews, S. D., Goldstein, D. B. (2014) Near-field flow structures about subcritical surface roughness. *Phys Fluids* **26**: 124106.
- Downs, R. S., White, E. B., Denissen, N. A. (2008) Transient growth and transition induced by random distributed roughness. *AIAA J* **46**: 451-462.
- Dryden, H. L. (1953) Review of published data on the effect of roughness on transition from laminar to turbulent flow. *J Aeronaut Sci* **20**: 477-482.
- Duguet, Y., Schlatter, P., Henningson, D. S., Eckhardt, B. (2012) Self-sustained localized structures in a boundary-layer flow. *Phys Rev Lett* **108**: 044501.
- Duguet, Y., Schlatter, P. (2013) Oblique laminar-turbulent interfaces in plane shear flows. *Phys Rev Lett* **110**: 034502.
- Durbin, P., Wu, X. (2007) Transition beneath vortical disturbances. *Annu Rev Fluid Mech* **39**: 107-128.
- Elsinga, G., Van Oudheusden, B., Scarano, F. (2006) Experimental assessment of tomographic-PIV accuracy, *13th international symposium on applications of laser techniques to fluid mechanics*, Lisbon, Portugal.
- Elsinga, G. E., Scarano, F., Wieneke, B., Van Oudheusden, B. W. (2006) Tomographic particle image velocimetry. *Exp Fluids* **41**: 933-947.
- Elsinga, G. E. (2008) Tomographic particle image velocimetry and its application to turbulent boundary layers. Doctoral thesis, Delft University of Technology, The Netherlands.
- Elsinga, G. E., Westerweel, J. (2012) Tomographic-PIV measurement of the flow around a zigzag boundary layer trip. *Exp Fluids* **52**: 865-876.
- Ergin, F. G., White, E. B. (2006) Unsteady and transitional flows behind roughness elements. *AIAA J* **44**: 2504-2514.
- Fedorov, A. (2011) Transition and stability of high-speed boundary layers. *Annu Rev Fluid Mech* **43**: 79-95.
- Fransson, J. H. M., Brandt, L., Talamelli, A., Cossu, C. (2004) Experimental and theoretical investigation of the nonmodal growth of steady streaks in a flat plate boundary layer. *Phys Fluids* **16**: 3627-3638.
- Fransson, J. H. M., Brandt, L., Talamelli, A., Cossu, C. (2005) Experimental study of the stabilization of tollmien–schlichting waves by finite amplitude streaks. *Phys Fluids* **17**: 054110.
- Fransson, J. H. M., Matsubara, M., Alfredsson, P. H. (2005) Transition induced by free-stream turbulence. *J Fluid Mech* **527**: 1-25.
- Fransson, J. H. M., Talamelli, A., Brandt, L., Cossu, C. (2006) Delaying transition to turbulence by a passive mechanism. *Phys Rev Lett* **96**: 064501.

- Fransson, J. H. M., Talamelli, A. (2012) On the generation of steady streamwise streaks in flat-plate boundary layers. *J Fluid Mech* **698**: 211-234.
- Fukuda, M. K., Hingst, W. G., Reshotko, E. (1975) Control of shock wave-boundary layer interactions by bleed in supersonic mixed compression inlets. NASA-CR-2595, FTAS/TR-75-100.
- Gad-El-Hak, M., Blackwelder, R. F., Riley, J. J. (1981) On the growth of turbulent regions in laminar boundary layers. *J Fluid Mech* **110**: 73-95.
- Ghosh, S., Choi, J.-I., Edwards, J. R. (2010) Numerical simulations of effects of micro vortex generators using immersed-boundary methods. *AIAA J* **48**: 92-103.
- Giepman, R. H. M., Schrijer, F. F. J., Van Oudheusden, B. W. (2014) Flow control of an oblique shock wave reflection with micro-ramp vortex generators: Effects of location and size. *Phys Fluids* **26**: 066101.
- Giepman, R. H. M., Louman, R., Schrijer, F. F. J., Van Oudheusden, B. W. (2016) Experimental study into the effects of forced transition on a shock-wave/boundary-layer interaction. *AIAA J* **54**: 1313-1325.
- Gregory, N. T., Walker, W. S. (1956) The effect on transition of isolated surface excrescences in the boundary layer.
- Guezennec, Y. G., Piomelli, U., Kim, J. (1989) On the shape and dynamics of wall structures in turbulent channel flow. *Phys Fluids A* **1**: 764-766.
- Guo, H., Lian, Q. X., Li, Y., Wang, H. W. (2004) A visual study on complex flow structures and flow breakdown in a boundary layer transition. *Exp Fluids* **37**: 311-322.
- Guo, H., Borodulin, V. I., Kachanov, Y. S., Pan, C., Wang, J. J., Lian, Q. X., Wang, S. F. (2010) Nature of sweep and ejection events in transitional and turbulent boundary layers. *J Turbul* **11**: 1-9.
- Hack, M. J. P., Zaki, T. A. (2014) Streak instabilities in boundary layers beneath free-stream turbulence. *J Fluid Mech* **741**: 280-315.
- Head, M. R., Bandyopadhyay, P. (1981) New aspects of turbulent boundary-layer structure. *J Fluid Mech* **107**: 297-338.
- Henningson, D. S., Spalart, P. R., Kim, J. (1987) Numerical simulations of turbulent spots in plane poiseuille and boundarylayer flow. *Phys Fluids* **30**: 2914-2917.
- Herbert, T. (1983) Secondary instability of plane channel flow to subharmonic three-dimensional disturbances. *Phys Fluids* **26**: 871-874.
- Herges, T., Kroeker, E., Elliott, G., Dutton, C. (2010) Microramp flow control of normal shock/boundary-layer interactions. *AIAA J* **48**: 2529-2542.
- Herman, G. T., Lent, A. (1976) Iterative reconstruction algorithms. *Comput Biol Med* **6**: 273-294.
- Hicks, R. M., Harper, W. R., Jr. (1970) A comparison of spherical and triangular boundary-layer trips on a flat plate at supersonic speeds. NASA-TM-X-2146.
- Hodson, H. P., Howell, R. J. (2005) The role of transition in high-lift low-pressure turbines for aeroengines. *Prog Aerosp Sci* **41**: 419-454.
- Hodson, H. P., Howell, R. J. (2005) Bladerow interactions, transition, and high-lift aerofoils in low-pressure turbines. *Annu Rev Fluid Mech* **37**: 71-98.
- Horvath, T., Tomek, D., Splinter, S., Zalameda, J., Krasa, P., Schwartz, R., Gibson, D., Tietjen, A., Berger, K. (2010) The hythirm project: Flight thermography of the space shuttle during hypersonic re-entry, *48th AIAA Aerospace Sciences Meeting Including the New Horizons Forum and Aerospace Exposition*, Orlando, Florida.

- Horvath, T. J., Berry, S. A., Merski, N. R. (2004) Hypersonic boundary/shear layer transition for blunt to slender configurations-a NASA Langley experimental perspective. RTO-MP-AVT-111.
- Howell, R. J., Ramesh, O. N., Hodson, H. P., Harvey, N. W., Schulte, V. (2000) High lift and aft-loaded profiles for low-pressure turbines. *J Turbomach* **123**: 181-188.
- Hu, B., Zhang, H., Younis, M. Y., Li, Y., Raza, M. S. (2015) Experimental investigation on the transition of separation/attachment in steady laminar juncture flows. *Exp Fluids* **56**: 1-9.
- Huang, J., Corke, T. C., Thomas, F. O. (2006) Plasma actuators for separation control of low-pressure turbine blades. *AIAA J* **44**: 51-57.
- Humble, R. A., Scarano, F., Van Oudheusden, B. W. (2007) Unsteady flow organization of compressible planar base flows. *Phys Fluids* **19**: 076101.
- Hunt, J. C. R., Wray, A. A., Moin, P. (1988) Eddies, streams, and convergence zones in turbulent flows, *Center for Turbulence Research, Proceedings of the Summer Program*, Stanford University, USA.
- Iyer, P. S., Mahesh, K. (2013) High-speed boundary-layer transition induced by a discrete roughness element. *J Fluid Mech* **729**: 524-562.
- Jeong, J., Hussain, F. (1995) On the identification of a vortex. *J Fluid Mech* **285**: 69-94.
- Jodai, Y., Elsinga, G. E. (2016) Experimental observation of hairpin auto-generation events in a turbulent boundary layer. *J Fluid Mech* **795**: 611-633.
- Joslin, R. D., Grosch, C. E. (1995) Growth characteristics downstream of a shallow bump: Computation and experiment. *Phys Fluids* **7**: 3042-3047.
- Joslin, R. D. (1998) Aircraft laminar flow control. *Annu Rev Fluid Mech* **30**: 1-29.
- Kachanov, Y. S. (1994) Physical mechanisms of laminar-boundary-layer transition. *Annu Rev Fluid Mech* **26**: 411-482.
- Kähler, C. J., Scharnowski, S., Cierpka, C. (2012) On the resolution limit of digital particle image velocimetry. *Exp Fluids* **52**: 1629-1639.
- Kegerise, M. A., King, R. A., Owens, L. R., Choudhari, M. M., Norris, A. T., Li, F., Chang, C.-L. (2012) An experimental and numerical study of roughness-induced instabilities in a mach 3.5 boundary layer. RTO AVT-200 RSM-030.
- Kirby, M., Boris, J., Sirovich, L. (1990) An eigenfunction analysis of axisymmetric jet flow. *J Comput Phys* **90**: 98-122.
- Kirchner, M. E. (1987) Laminar flow: Challenge and potential, *Research in Natural Laminar Flow and Laminar-Flow Control*, Virginia, USA.
- Klebanoff, P. S., Schubauerand, G. B., Tidstrom, K. D. (1955) Measurements of the effect of two-dimensional and three-dimensional roughness elements on boundary-layer transition. *J Aeronaut Sci* **22**: 803-804.
- Klebanoff, P. S., Tidstrom, K. D., Sargent, L. M. (1962) The three-dimensional nature of boundary-layer instability. *J Fluid Mech* **12**: 1-34.
- Klebanoff, P. S., Tidstrom, K. D. (1972) Mechanism by which a two - dimensional roughness element induces boundary-layer transition. *Phys Fluids* **15**: 1173-1188.
- Klebanoff, P. S., Cleveland, W. G., Tidstrom, K. D. (1992) On the evolution of a turbulent boundary layer induced by a three-dimensional roughness element. *J Fluid Mech* **237**: 101-187.

- Kline, S. J., Coles, D. E., Hirst, E. A. (1969) Computation of turbulent boundary layers--1968 AFOSR-IFP-Stanford conference: Proceedings, *Conference on Computation of Turbulent Boundary Layers*, California, USA.
- Krishnan, L., Sandham, N. D. (2006) Turbulent spots in a compressible boundary-layer flow. In: Govindarajan R. (ed) *IUTAM symposium on laminar-turbulent transition, fluid mechanics and its applications*. Springer Netherlands, Dordrecht, pp. 329-334.
- Krishnan, L., Sandham, N. D. (2006) On the merging of turbulent spots in a supersonic boundary-layer flow. *Int J Heat Fluid Flow* **27**: 542-550.
- Kundu, P., Cohen, L. (1990) *Fluid mechanics*. Academic, California, USA.
- Landahl, M. T. (1990) On sublayer streaks. *J Fluid Mech* **212**: 593-614.
- Lau, K. Y. (2008) Hypersonic boundary-layer transition: Application to high-speed vehicle design. *J Spacecraft Rockets* **45**: 176-183.
- Legrand, M., Nogueira, J., Tachibana, S., Lecuona, A., Nauri, S. (2011) Flow temporal reconstruction from non time-resolved data part ii: Practical implementation, methodology validation, and applications. *Exp Fluids* **51**: 861-870.
- Lengani, D., Simoni, D., Ubaldi, M., Zunino, P. (2014) POD analysis of the unsteady behavior of a laminar separation bubble. *Exp Therm Fluid Sci* **58**: 70-79.
- Lesieur, M. (2012) *Turbulence in fluids, 4th edition*. Springer Science & Business Media, Dordrecht.
- Li, Q., Liu, C. (2010) LES for supersonic ramp control flow using mvg at $m=2.5$ and $re_0=1440$, *48th AIAA Aerospace Sciences Meeting Including the New Horizons Forum and Aerospace Exposition*, Orlando, Florida.
- Lin, J. C. (2002) Review of research on low-profile vortex generators to control boundary-layer separation. *Prog Aerosp Sci* **38**: 389-420.
- Lin, N., Reed, H. L., Saric, W. S. (1992) Effect of leading-edge geometry on boundary-layer receptivity to freestream sound. In: Hussaini M. Y., Kumar A. and Streett C. L. (eds) *Instability, transition, and turbulence*. Springer New York, New York, NY, pp. 421-440.
- Loiseau, J.-C., Robinet, J.-C., Cherubini, S., Leriche, E. (2014) Investigation of the roughness-induced transition: Global stability analyses and direct numerical simulations. *J Fluid Mech* **760**: 175-211.
- Lu, F., Pierce, A., Shih, Y. (2010) Experimental study of near wake of micro vortex generators in supersonic flow, *40th Fluid Dynamics Conference and Exhibit*, Chicago, Illinois.
- Lumley, J. L. (1967) The structure of inhomogeneous turbulence. In: Yaglom A. M. and Tatarski V. I. (eds) *Atmospheric turbulence and wave propagation*. Nauka, Moscow, pp. 166-178.
- Lynch, K. P. (2015) Advances in time-resolved tomographic particle image velocimetry. Doctoral thesis, Delft University of Technology, The Netherlands.
- Lynch, K. P., Scarano, F. (2015) An efficient and accurate approach to time-resolved tomographic PIV. *Exp Fluids* **56**: 1-16.
- Melling, A. (1997) Tracer particles and seeding for particle image velocimetry. *Meas Sci Technol* **8**: 1406-1416.
- Montomoli, F., Hodson, H., Haselbach, F. (2010) Effect of roughness and unsteadiness on the performance of a new low pressure turbine blade at low reynolds numbers. *J Turbomach* **132**: 031018.

- Morkovin, M. V. (1969) On the many faces of transition. In: Wells C. S. (ed) *Viscous drag reduction: Proceedings of the symposium on viscous drag reduction*. Springer US, Boston, MA, pp. 1-31.
- Morkovin, M. V. (1988) Recent insights into instability and transition to turbulence in open-flow systems. *NASA-CR-181693*.
- Morkovin, M. V. (1990) Panel summary: Roughness. In: Hussaini M. Y. and Voigt R. G. (eds) *Instability and transition: ICASE/NASA LaRC series*. Springer US, New York, NY, pp. 265-271.
- Morton, C., Yarusevych, S., Scarano, F. (2016) A tomographic particle image velocimetry investigation of the flow development over dual step cylinders. *Phys Fluids* **28**: 025104.
- Ovchinnikov, V., Choudhari, M. M., Piomelli, U. (2008) Numerical simulations of boundary-layer bypass transition due to high-amplitude free-stream turbulence. *J Fluid Mech* **613**: 135-169.
- Perraud, J., Arnal, D., Seraudie, A., Tran, D. (2004) Laminar-turbulent transition on aerodynamic surfaces with imperfections, *RTO-AVT-111 Symposium*, Prague, Czech Republic.
- Praisner, T. J., Clark, J. P. (2004) Predicting transition in turbomachinery—part i: A review and new model development. *J Turbomach* **129**: 1-13.
- Prasad, A. K., Jensen, K. (1995) Scheimpflug stereocamera for particle image velocimetry in liquid flows. *Appl Opt* **34**: 7092-7099.
- Raffel, M., Willert, C. E., Wereley, S., Kompenhans, J. (2007) *Particle image velocimetry: A practical guide*. Springer-Verlag Berlin Heidelberg.
- Redford, J. A., Sandham, N. D., Roberts, G. T. (2010) Compressibility effects on boundary-layer transition induced by an isolated roughness element. *AIAA J* **48**: 2818-2830.
- Redford, J. A., Sandham, N. D., Roberts, G. T. (2012) Numerical simulations of turbulent spots in supersonic boundary layers: Effects of mach number and wall temperature. *Prog Aerosp Sci* **52**: 67-79.
- Reshotko, E. (1984) Disturbances in a laminar boundary layer due to distributed surface roughness. *Turbulence and chaotic phenomena in fluids: Proceedings of the international symposium*. Amsterdam, North-Holland, pp. 39-46.
- Reshotko, E. (2001) Transient growth: A factor in bypass transition. *Phys Fluids* **13**: 1067-1075.
- Reshotko, E., Tumin, A. (2001) Spatial theory of optimal disturbances in a circular pipe flow. *Phys Fluids* **13**: 991-996.
- Reshotko, E., Tumin, A. (2004) Role of transient growth in roughness-induced transition. *AIAA J* **42**: 766-770.
- Reshotko, E. (2008) Transition issues for atmospheric entry. *J Spacecraft Rockets* **45**: 161-164.
- Reynolds, O. (1883) An experimental investigation of the circumstances which determine whether the motion of water shall be direct or sinuous, and of the law of resistance in parallel channels. *Philos Trans R Soc London* **174**: 935-982.
- Rizzetta, D. P., Visbal, M. R. (2005) Numerical simulation of separation control for transitional highly loaded low-pressure turbines. *AIAA J* **43**: 1958-1967.
- Rizzetta, D. P., Visbal, M. R. (2007) Direct numerical simulations of flow past an array of distributed roughness elements. *AIAA J* **45**: 1967-1976.

- Robert, J. P. (1992) Laminar flow control-a challenge for a manufacturer, *First European Forum on Laminar Flow Technology*, DGLR-Bericht.
- Robinson, S. K. (1991) Coherent motions in the turbulent boundary layer. *Annu Rev Fluid Mech* **23**: 601-639.
- Samimy, M., Lele, S. K. (1991) Motion of particles with inertia in a compressible free shear layer. *Phys, Fluids A: Fluid Dyn* **3**: 1915-1923.
- Saric, W. S., Reed, H. L., Kerschen, E. J. (2002) Boundary-layer receptivity to freestream disturbances. *Annu Rev Fluid Mech* **34**: 291-319.
- Sayadi, T., Schmid, P. J., Nichols, J. W., Moin, P. (2014) Reduced-order representation of near-wall structures in the late transitional boundary layer. *J Fluid Mech* **748**: 278-301.
- Scarano, F., Riethmuller, M. L. (2000) Advances in iterative multigrid PIV image processing. *Exp Fluids* **29**: S051-S060.
- Scarano, F. (2013) Tomographic PIV: Principles and practice. *Meas Sci Technol* **24**: 012001.
- Schlatter, P., Brandt, L., De Lange, H. C., Henningson, D. S. (2008) On streak breakdown in bypass transition. *Phys Fluids* **20**: 101505.
- Schlatter, P., Li, Q., Örlü, R., Hussain, F., Henningson, D. S. (2014) On the near-wall vortical structures at moderate reynolds numbers. *European Journal of Mechanics, B/Fluids* **48**: 75-93.
- Schlichting, H., Krause, E. (2003) *Boundary layer theory*. Springer-Verlag Berlin Heidelberg, Germany.
- Schmid, P. J., Henningson, D. S. (2001) The viscous initial value problem. *Stability and transition in shear flows*. Springer New York, New York, NY, pp. 99-151.
- Schneider, S. P. (2001) Effects of high-speed tunnel noise on laminar-turbulent transition. *J Spacecraft Rockets* **38**: 323-333.
- Schneider, S. P. (2004) Hypersonic laminar-turbulent transition on circular cones and scramjet forebodies. *Prog Aerosp Sci* **40**: 1-50.
- Schneider, S. P. (2015) Developing mechanism-based methods for estimating hypersonic boundary-layer transition in flight: The role of quiet tunnels. *Prog Aerosp Sci* **72**: 17-29.
- Schrijer, F. F. J., Scarano, F., Van Oudheusden, B. W. (2003) Experiments on hypersonic boundary layer separation and reattachment on a blunted cone-flare using quantitative infrared thermography, *12th AIAA International Space Planes and Hypersonic Systems and Technologies*, Norfolk, Virginia.
- Schrijer, F. F. J., Bannink, W. J. (2010) Description and flow assessment of the delft hypersonic ludwig tube. *J Spacecraft Rockets* **47**: 125-133.
- Schröder, A., Geisler, R., Elsinga, G. E., Scarano, F., Dierksheide, U. (2008) Investigation of a turbulent spot and a tripped turbulent boundary layer flow using time-resolved tomographic PIV. *Exp Fluids* **44**: 305-316.
- Schubauer, G. B., Klebanoff, P. S. (1956) Contributions on the mechanics of boundary-layer transition. NACA-TR-1289.
- Serpiéri, J., Kotsonis, M. (2016) Three-dimensional organisation of primary and secondary crossflow instability. *J Fluid Mech* **799**: 200-245.
- Shahinfar, S., Fransson, J., H. M. (2011) Effect of free-stream turbulence characteristics on boundary layer transition. *Journal of Physics: Conference Series* **318**: 032019.

- Shahinfar, S., Sattarzadeh, S. S., Fransson, J. H. M., Talamelli, A. (2012) 074501revival of classical vortex generators now for transition delay. *Phys Rev Lett* **109**: 074501.
- Shin, Y.-S., Rist, U., Krämer, E. (2015) Stability of the laminar boundary-layer flow behind a roughness element. *Exp Fluids* **56**: 11.
- Singer, B. A., Joslin, R. D. (1994) Metamorphosis of a hairpin vortex into a young turbulent spot. *Phys Fluids* **6**: 3724-3736.
- Singer, B. A. (1996) Characteristics of a young turbulent spot. *Phys Fluids* **8**: 509-521.
- Sirovich, L. (1987) A debreceni déri múzeum évkönyve. *Q Appl Math* **45**: 573-582.
- Soloff, S. M., Adrian, R. J., Liu, Z. C. (1997) Distortion compensation for generalized stereoscopic particle image velocimetry. *Meas Sci Technol* **8**: 1441-1454.
- Spalart, P. R. (1988) Direct simulation of a turbulent boundary layer up to $Re = 1410$. *J Fluid Mech* **187**: 61-98.
- Strand, J. S., Goldstein, D. B. (2011) Direct numerical simulations of riblets to constrain the growth of turbulent spots. *J Fluid Mech* **668**: 267-292.
- Subbareddy, P. K., Bartkowicz, M. D., Candler, G. V. (2014) Direct numerical simulation of high-speed transition due to an isolated roughness element. *J Fluid Mech* **748**: 848-878.
- Sun, Z., Schrijer, F. F. J., Scarano, F., Van Oudheusden, B. W. (2012) The three-dimensional flow organization past a micro-ramp in a supersonic boundary layer. *Phys Fluids* **24**: 055105.
- Sun, Z., Scardino, F., Van Oudheusden, B. W., Schrijer, F. F. J., Yan, Y., Liu, C. (2014) Numerical and experimental investigations of the supersonic microramp wake. *AIAA J* **52**: 1518-1527.
- Sun, Z., Schrijer, F. F. J., Scarano, F., Van Oudheusden, B. W. (2014) Decay of the supersonic turbulent wakes from micro-ramps. *Phys Fluids* **26**: 025115.
- Tani, I., Komoda, H., Komatsu, Y., Iuchi, M. (1962) Boundary-layer transition by isolated roughness. Aeronautical Research Institute, University of Tokyo, No. 375.
- Tani, I. (1969) Boundary-layer transition. *Annu Rev Fluid Mech* **1**: 169-196.
- Thibert, J. J., Reneaux, J., Schmitt, V. (1990) Onera activities on drag reduction. *Tiré à part- Office national d'études et de recherches aérospatiales* **90**: 1053-1064.
- Tirtey, S. C., Chazot, O., Walpot, L. (2011) Characterization of hypersonic roughness-induced boundary-layer transition. *Exp Fluids* **50**: 407-418.
- Tsai, R. (1987) A versatile camera calibration technique for high-accuracy 3D machine vision metrology using off-the-shelf TV cameras and lenses. *IEEE J Robot Automat* **3**: 323-344.
- Van Den Eynde, J. P. J. P., Sandham, N. D. (2015) Numerical simulations of transition due to isolated roughness elements at mach 6. *AIAA J* **54**: 53-65.
- Van Driest, E. R., Mccauley, W. D. (1960) The effect of controlled three-dimensional roughness on boundary-layer transition at supersonic speeds. *J Aerosp Sci* **27**: 261-271.
- Van Dyke, M. (1982) *An album of fluid motion*. Parabolic Press, Stanford, California.
- Van Oudheusden, B. W., Scarano, F., Van Hinsberg, N. P., Watt, D. W. (2005) Phase-resolved characterization of vortex shedding in the near wake of a square-section cylinder at incidence. *Exp Fluids* **39**: 86-98.
- Van Rooij, R. M., Timmer, W. A. (2003) Roughness sensitivity considerations for thick rotor blade airfoils. *ASME J Sol Energy Eng* **125**: 468-478.

- Vermeersch, O., Yoshida, K., Ueda, Y., Arnal, D. (2015) Natural laminar flow wing for supersonic conditions: Wind tunnel experiments, flight test and stability computations. *Prog Aerosp Sci* **79**: 64-91.
- Violato, D., Scarano, F. (2013) Three-dimensional vortex analysis and aeroacoustic source characterization of jet core breakdown. *Phys Fluids* **25**: 015112.
- Von Doenhoff, A. E., Braslow, A. L. (1961 170) The effect of distributed surface roughness on laminar flow. In: Lachmann G. V. (ed) *Boundary Layer and Flow Control*. Pergamon, pp. 657-681.
- Wang, B., Liu, W., Zhao, Y., Fan, X., Wang, C. (2012) Experimental investigation of the micro-ramp based shock wave and turbulent boundary layer interaction control. *Phys Fluids* **24**: 055110.
- Werlé, H. (1981) Transition and separation: Visualizations in the onera water tunnel. In *its La Rech Aerospaciale, Bimonthly Bull No 1980-5 (ESA-TT-673) p 35-49 (SEE N81-26008 16-99) Transl into ENGLISH of La Rech Aerospaciale, Bull Bimestriel (Paris), no 1980-5, Sep-Oct 1980 p 331-345* **1**: 35-49.
- Westerweel, J. (1997) Fundamentals of digital particle image velocimetry. *Meas Sci Technol* **8**: 1379-1392.
- Westerweel, J., Scarano, F. (2005) Universal outlier detection for PIV data. *Exp Fluids* **39**: 1096-1100.
- White, E. B., Rice, J. M., Ergin, F. G. (2005) Receptivity of stationary transient disturbances to surface roughness. *Phys Fluids* **17**: 064109.
- White, F. M., Corfield, I. (2006) *Viscous fluid flow*. McGraw-Hill New York, New York, NY.
- Whitehead, A. H., Jr. (1969) Flow field and drag characteristics of several laminar boundary layer tripping element in hypersonic flow. NASA-TN-D-5454.
- Wieneke, B. (2008) Volume self-calibration for 3D particle image velocimetry. *Exp Fluids* **45**: 549-556.
- Wu, X., Moin, P. (2009) Direct numerical simulation of turbulence in a nominally zero-pressure-gradient flat-plate boundary layer. *J Fluid Mech* **630**: 5-41.
- Wu, X., Moin, P., Hickey, J.-P. (2014) Boundary layer bypass transition. *Phys Fluids* **26**: 091104.
- Yan, Y., Chen, C., Wang, X., Liu, C. (2014) LES and analyses on the vortex structure behind supersonic mvg with turbulent inflow. *Appl Math Model* **38**: 196-211.
- Ye, Q., Schrijer, F. F. J., Scarano, F. (2016) Boundary layer transition mechanisms behind a micro-ramp. *J Fluid Mech* **793**: 132-161.
- Ye, Q., Schrijer, F. F. J., Scarano, F. (2016) On reynolds number dependence of micro-ramp-induced transition, *18th International Symposium on the Application of Laser and Imaging Techniques to Fluid Mechanics*, Lisbon, Portugal.
- Ye, Q., Schrijer, F. F. J., Scarano, F. (2016) Geometry effect of isolated roughness on boundary layer transition investigated by tomographic PIV. *Int J Heat Fluid Flow* **61**: 31-44.
- Zhang, X. F., Vera, M., Hodson, H., Harvey, N. (2005) Separation and transition control on an aft-loaded ultra-high-lift LP turbine blade at low reynolds numbers: Low-speed investigation. *J Turbomach* **128**: 517-527.
- Zhong, S., Chong, T. P., Hodson, H. P. (2003) A comparison of spreading angles of turbulent wedges in velocity and thermal boundary layers. *J Fluids Eng* **125**: 267-274.

- Zhong, X., Wang, X. (2012) Direct numerical simulation on the receptivity, instability, and transition of hypersonic boundary layers. *Annu Rev Fluid Mech* **44**: 527-561.
- Zhou, J., Adrian, R. J., Balachandar, S., Kendall, T. M. (1999) Mechanisms for generating coherent packets of hairpin vortices in channel flow. *J Fluid Mech* **387**: 353-396.

Acknowledgements

The thesis includes the 4 years dedication of PhD work in the Group of Aerodynamics, TU Delft. It is a great period of life that I have enjoyed. During the four years, I have met a lot of nice people who supported and encouraged me in both work and life. I would like to use this section to express my acknowledgements to them.

I would like to give the first thanks to my promotors and supervisors, Prof. Fulvio Scarano and Dr. Ferry Schrijer. Fulvio and Ferry, thank you for patiently guiding and motivating me to achieve the hard and ambitious academic goals during my PhD. I really enjoyed the discussions we had every week. Your passion and enthusiasm for research also influence my attitude to work. You bring me out from my comfort zone, pushing me to be brave and blunt when facing challenges.

Thanks to Prof. Stefan Hickel, for the help in performing numerical simulation. I want to express my appreciation to Prof. Ningfei Wang from Beijing Institute of Technology, who brought me the passion to start the PhD research.

I am also grateful to all the technicians, who provided help during the experiment campaigns, Peter Duyndam, Frits Donker Duyvis, Henk-Jan Siemer, Nico van Beek, Eric de Keizer and Stefan Bernardy. Special thanks to Peter for being always available to fix the problems in HTFD. Thanks to Frits for the nice model design and expertise in solving laser problems. I appreciate the efficient administrative assistant from Colette.

Thanks to all my PhD colleagues in Aerodynamics, Theo, Valeria, Yi, Haohua, Weibo, Martin, Paul, Wouter, Peppe, Rakesh, Shaafi, Varun, Beppe, Tiago, Jan, Rogier, Mustafa, Andrea, Zeno, Liesbeth, Mirja and more, for the nice time we have during lunch and coffee break. Many thanks to Jun, for the great dinners on weekends and the times hanging out together. My gratitude to Jacopo, for being a good friend and also a full time entertainer, who brings a lot of funny stories. Thanks to Lei who kept me company during the last two month of my PhD in the office. Special thanks to Francesco and Dani for the help and experiences shared in HTFD. Thanks to Kyle, for the help and discussions in my first tomo PIV experiment.

To my dear friends in Delft, Shuanghou, Xiaojia, Xiaojun, Nan, Ye, Qingxi, Bo, Zhengzhong, Linfeng, Yannian, Fei and many more. Thanks for spending the great holiday also some working times together, reminding me of a lot of wonderful moments. Also thank you for listening to my complaints and troubles. Your understanding and suggestions make the tough times much easier. Special thanks to Zi and Jia. It is a great pleasure to have you as roommates for three years, for all the 'girl's talk' at home, and laughter we shared. Thanks to Xiangrong. It is quite a coincidence to meet someone having the same birthday. Then it becomes wonderful to celebrate all the birthdays together for four years.

Acknowledgements

To my friends in China, especially Chen, Jieli and Hui. You have been my best friends since high school. I am grateful to your support and considerations, the endless talk we had on wechat, and the wonderful times we had every time I went back to China.

To my parents, I owe the deep gratitude to you. You did the best you can to give me a great childhood. Thanks for your unconditional love, encouragement and being always supportive for all the decisions I have made. (感谢我的爸爸妈妈，一直以来给予我的关心和爱，让我在成长过程中一直都能无忧无虑。谢谢你们的信任，在我面对困境时给的鼓励，以及对我所有选择、决定的支持。我永远都爱你们！)

Qingqing Ye

Delft, May, 2017

Publications

Journal Articles

- Q. Ye, F. F. J Schrijer, and F. Scarano, "Geometry effect of isolated roughness on boundary layer transition investigated by tomographic PIV," *Int. J. Heat Fluid Fl.* 61A: 31(2016).
- Q. Ye, F. F. J Schrijer, and F. Scarano, "Boundary layer transition mechanisms behind a micro-ramp," *J. Fluid Mech.* 793: 132 (2016).
- F. Avallone, Q. Ye, F. F. J. Schrijer, F. Scarano and G. Cardone, "Tomographic PIV investigation of roughness-induced transition in a hypersonic boundary layer," *Exp. Fluids* 55:1852 (2014).
- Q. Ye, F. F. J Schrijer, and F. Scarano, "On Reynolds number dependence of micro-ramp-induced transition," Under review of *J. Fluid Mech.*
- Q. Ye, F. F. J Schrijer, and F. Scarano, "Tomographic PIV measurement of hypersonic boundary layer transition past a micro-ramp", *AIAA J.*, to be submitted.
- Q. Ye, F. F. J Schrijer, and F. Scarano, "Particle tracer response across shock wave in hypersonic flows for PIV measurement", *Meas. Sci. Technol.*, to be submitted.
- Q. Ye, F. F. J Schrijer, and F. Scarano, "Infrared thermography investigation of transitional flow over isolated roughness at high speed", *Quant. Infr. Therm. J.*, to be submitted.

Conferences

- Q. Ye, F. F. J Schrijer, and F. Scarano, "Tomographic PIV measurement of hypersonic boundary layer transition past a micro-ramp," *47th Fluid Dynamic Conference*, AIAA Aviation Forum, June 2017, Denver, USA.
- Q. Ye, "Mechanisms of boundary layer transition induced by isolated roughness," *Burgers Symposium 2017*, May 2017, Lunteren, the Netherlands.
- Q. Ye, F. F. J Schrijer, and F. Scarano, "On Reynolds number dependence of micro-ramp-induced transition," *18th International Symposium on the Application of Laser and Imaging Techniques to Fluid Mechanics*, July 2016, Lisbon, Portugal.
- K. Groot, Q. Ye, Y. Zhang, F. Pinna and B.W. van Oudheusden, "BiGlobal stability analysis of a micro-ramp wake using PIV base flows" *46th AIAA Fluid Dynamics*

- Conference*, June 2016, Washington, D.C., USA.
- Q. Ye, F. F. J. Schrijer, and F. Scarano, "Infrared thermography investigation of transitional flow over isolated roughness at high speed," *51st 3AF International Conference on Applied Aerodynamics*, April 2016, Strasbourg, France.
 - Q. Ye, F. F. J. Schrijer, and F. Scarano, "Roughness induced boundary layer transition in incompressible flow," *15th European Turbulence Conference*, August 2015, Delft, the Netherlands.
 - Q. Ye, F. F. J. Schrijer, and F. Scarano, "Geometry effect of isolated roughness on boundary layer transition investigated by tomographic PIV," *the 9th Symposium on Turbulence and Shear Flow Phenomena*, June 2015, Melbourne, Australia.
 - Q. Ye, F. F. J. Schrijer, and F. Scarano. "A tomographic PIV study on boundary layer transition induced by isolated roughness," *4th International Conference of Experiment Fluid Mechanics*, Aug 2014, Beijing, China. (**Young Researcher Award**).
 - F. Avallone, Q. Ye, F. F. J. Schrijer, F. Scarano and G. Cardone, "Tomographic PIV investigation of roughness-induced transition in a hypersonic boundary layer," *17th International Symposium on Application of Laser Techniques to Fluid Mechanics*, July 2014, Lisbon, Portugal.

Curriculum Vitae

29-09-1989 Born in Tangshan, Hebei, China

Education

- 04/2013-present Ph.D researcher in Aerodynamics,
Thesis: Mechanisms of boundary layer transition induced by isolated roughness.
Faculty of Aerospace Engineering,
Delft University of Technology, Delft, the Netherlands.
- 09/2011-03/2013 Ph.D researcher in Aerospace Propulsion Engineering,
School of Aerospace Engineering,
Beijing Institute of Technology, Beijing, China.
- 03/2011-06/2011 Exchange Student,
Aerohydrodynamics Department,
Samara State Aerospace University, Samara, Russian Federation.
- 09/2007-06/2011 Bachelor in Aerospace Propulsion Engineering (with honour)
Thesis: Aerodynamic performance of elliptical ring wing
Beijing Institute of Technology, Beijing, China.